# Influence of Doping on Multiferroic $YbMnO_3$

A thesis

Submitted for the degree of

**Doctor of Philosophy**

*By*

**Sattibabu Bhumireddi**


**School of Engineering Sciences and Technology**
**University of Hyderabad**
**Hyderabad - 500046**
**India**

**June 2016**

*Dedicated……*

*To my son Harshit*

# Declaration

I hereby declare that the work reported in this thesis is original and was carried out by me during my tenure as a PhD student at University of Hyderabad, India. This thesis has not formed the basis for the award of any degree, diploma, associateship, membership or similar title of any university or institution.

Sattibabu Bhumireddi
Date: June, 2016

School of Engineering Sciences and
Technology
University of Hyderabad
Hyderabad - 500046
India.

# CERTIFICATE

This is to certify that the thesis work entitled "**Influence of Doping on Multiferroic $YbMnO_3$**" submitted by **Sattibabu Bhumireddi** under our supervision has been carried out at the University of Hyderabad, Hyderabad, India, and this has not been submitted for any degree or diploma at this or any other University.

Dr. Dibakar Das
Associate Professor
School of Engineering Science &Technology,
University of Hyderabad, India

,

Prof. A. K. Bhatnagar
School of Engineering Science &Technology,
University of Hyderabad, India

Prof. M. Ghanashyam Krishna
Dean,
School of Engineering Science &Technology,
University of Hyderabad, India

# Summary

This prime objective of this thesis is to investigation of the effect of Mg, Sc, Ho and Er doping on the structure, magnetic order and magnetocaloric properties of the multiferroic $YbMnO_3$. Magnetoelectric coupling is observed in Mg doped $YbMnO_3$ by using neutron diffraction and is of interest for a variety of applications/devices. Large magnetocaloric effect (MCE) are observed in $Yb_{0.7}Ho_{0.3}MnO_3$, which are appreciable enough to consider these sample as magnetic refrigerants at low temperature. The thesis is divided into eight chapters.

Chapter 1 deals with a brief introduction to the multiferroic oxides ~~is~~ presented. A brief survey of the literature, highlighting the interest in pure and doped $YbMnO_3$ is reported. Materials in which the magnetic ordering can be controlled by electric field and vice-versa are called multiferroic. Such compounds have tremendous potential in practical applications such as spintronic. Rare-earth and yttrium manganites of general formula $RMnO_3$ crystallize in hexagonal structure for *R* with smaller ionic radius (*R* = Ho, Er, Tm, Yb, Lu, and Y) or in orthorhombic structure for larger ionic radius (*R* = La, Ce, Pr, Nd, Sm, Eu, Gd, Tb, and Dy) . Hexagonal $RMnO_3$ compounds are known to show simultaneously ferroelectric as well as magnetic ordering in the ordered phase. The crystal structure of hexagonal manganites consists of $MnO_5$ polyhedra in which the $Mn^{3+}$ ion is surrounded by three oxygen ions in plane and two apical oxygen ions. The Mn ions with in Mn-O plane form a triangular lattice and are coupled in terms of spins through the antiferromagnetic (*AFM*) super exchange interaction. Due to the incomplete *AFM* coupling between neighboring Mn ions in the triangular lattice, the system forms a geometrically frustrated magnetic state

In this chapter 2, describes details of synthesis and various experimental techniques carried out in this dissertation. Details of synthesis of the samples by using solid state reaction method and the experimental techniques employed to check phase purity of samples by using X-ray diffraction (XRD) and crystal structure and magnetic structure determination by using the Neutron powder diffraction (NPD) method are given. Physical Property Measurement System

(PPMS) has been used to understand the magnetic and magnetocaloric properties. Raman spectroscopy was used to understand bond length variation with doping.

In chapter 3, the structural, magnetic and magnetoelastic properties of $Yb_{1-x}Mg_xMnO_3$ (x = 0.00 and 0.05) using neutron diffraction and magnetization measurements are described. From the refinement, it is clearly seen that due to Mg substitution, the cell parameter *a* decreases marginally, while there is a slight increase in *c*. Overall the cell volume decreases for x = 0.05 sample when compared to that of x= 0.00 sample. This decrease in cell volume can be ascribed to ionic size effects, since smaller $Mg^{2+}$ (Shannon ionic radii 0.890 Å) ion replaces the slightly bigger $Yb^{3+}$ (Shannon ionic radii 0.925 Å) ion. The temperature dependence of dc magnetic susceptibility ($\chi = M/H$) of $Yb_{1-x}Mg_xMnO_3$ ($x$ = 0.00, 0.05 and 0.1) samples in zero field cooled (ZFC) and field cooled (FC) state of the sample, and in an applied field of 100 Oe are discussed. With decreasing temperature, $\chi$ increases gradually with *T*, as if following the Curie-Weiss law, however, around 200 K there is a deviation from the Curie-Weiss behaviour. At low temperatures, around 10 K, there is a sudden rise in $\chi$, as if the samples are undergoing ferromagnetic ordering. The ferromagnetic ordering has been attributed to the ordering in the $Yb^{3+}$ sub-lattice. $d\chi/dT$ data show anomaly around 85 K in $x$ = 0.00 sample, 89 K for x = 0.05 and 88 K for x = 0.1, these temperatures refer to the Neel temperatures for these compounds. Temperature dependence of the *ac* magnetic susceptibility, $\chi_{ac}(T)$, shows no signature of spin-glass behaviour of these compounds.

Temperature dependent neutron diffraction studies were carried out on polycrystalline $Yb_{1-x}Mg_xMnO_3$ ($x$ = 0.00 and 0.05) samples. For the magnetic refinement of the present ND data, the structure described by the basis vectors of the irreducible representations $\Gamma_6$ for $Yb^{3+}$ (at Wyckoff site 2*a*), $\Gamma_2$ for $Yb^{3+}$ at 4b site and $\Gamma_2$ representation for Mn at 6*c* site were used. From the Rietveld refinement of temperature dependent ND data, the structural and magnetic properties of the samples were extracted. The temperature dependence of the lattice parameters (*a* and c/*a* ratio) and unit cell volume *V* show anomalous behavior near $T_{N1} \sim 85$ K (The Mn ordering temperature) due to the magnetoelastic effect. Also all the Mn-O bond distances display considerable variation at $T_{N1}$. Magnetic measurements show that the Néel temperature ($T_N$) increases marginally from 85 *K* for $x$ = 0.00 to 89 *K* for $x$ = 0.05 sample, respectively and also studied structural magnetic properties of $Yb_{0.9}Mg_{0.1}MnO_3$ sample.

In chapter 4, specific heat and magnetocaloric properties of $Yb_{1-x}Mg_xMnO_3$ ($x$ = 0.00 and 0.05) samples are discussed. A peak in $C_p$ is obtained for both samples, it is at ~83 K for x

= 0 and at ~86 K for x = 0.05 samples and is attributed to the antiferromagnetic ordering indicating a small increase in Neel temperature due to Mg substitution. The broad feature in $C_p$ vs T at ~6.5 K is attributed to the Schottky anomaly. The estimated effective molecular fields were derived from the Schottky analysis and obtained values are $H_{mf}$ = 3.0 and 3.5 T for $YbMnO_3$ and $Yb_{0.95}Mg_{0.05}MnO_3$, respectively. High temperature shift of the Schottky anomaly with Mg doping indicates increase in the effective molecular field of Mn at the Yb 4*b* site. The data support that the idea that although molecular field is mainly responsible for the Schottky anomaly in $Yb_{1-x}Mg_xMnO_3$ but $Mn^{3+}$ spin ordering also affects it. Specific heat data also show that the ferromagnetic transition is taking place at ~2.7 K for x = 0.0 and T = 3.3 K for x = 0.05 samples due to the ordering of Yb ions at the 2*a* site, thus these compounds show multiple transitions. The data have also been analyzed to determine magnetocaloric properties of these materials. Magnetic part of the specific heat is obtained by subtracting the lattice contribution estimated using two Debye temperatures. The magnetic entropy change ($\Delta S_{mag}$) for pure and doped samples are 2.0 J $mol^{-1}K^{-1}$ and 2.1 J $mol^{-1}K^{-1}$ , respectively, while the relative cooling power (RCP ) calculate 26.1 J/mol, 27.2 J/mol for a field change of 10 T.

In chapter 5, the effect of Sc doping on structural, magnetic and magnetocaloric properties of multiferroic $Yb_{1-x}Sc_xMnO_3$ (x = 0.1 and 0.2) are described. The structural analysis shows decrease in lattice parameter *a*, decrease in cell volume of the hexagonal unit cell and decrease in the average bond length between Mn-O with the Sc substitution. Magnetic measurements show that the Néel temperature ($T_N$) increases from 90 *K* for *x* = 0.1 sample to 94 *K* for *x* = 0.2 sample. Isothermal magnetic curves show that the field variation in magnetization generates a metamagnetic transition. The maximum entropy change $-\Delta S_M^{max}$ and the relative cooling power (RCP) of $Yb_{1-x}Sc_xMnO_3$ are found to be 2.46 ± 0.40 J/mole-K and 38.5 ± 9 J /mol for *x* = 0.1 and 1.87 ± 0.31 J/mole-K and, 30.1± 8 J/mol for *x* = 0.2 with ΔH = 10 T. The rescaled magnetic entropy change curves for different applied fields collapse onto a single curve for materials with second-order phase transition.

In chapter 6, Magnetocaloric properties of polycrystalline hexagonal $Yb_{1-x}Ho_xMnO_3$ (x = 0.1, 0.2 and 0.3) compounds are studied through magnetization measurements. The maximum entropy change $|\Delta S_M^{max}|$ and the relative cooling power (RCP) of $Yb_{1-x}Ho_xMnO_3$ are found to be 3.75 ± 0.78 J/ (mole K) and 90.0 ± 27 J/mol for *x* = 0.3 at ΔH = 100 kOe. Values of both $|\Delta S_M^{max}|$ and RCP found to increase with increasing Ho content. $Yb_{1-x}Ho_xMnO_3$ seem to be potential materials for magnetic refrigeration in the low temperature region.

In chapter 7, the effect of Er doping on structural, magnetic and specific heat properties of multiferroic $Yb_{1-x}Er_xMnO_3$ (x = 0.1, 0.2 and 0.3) are given. The structural analysis shows the increase in lattice constant *a* is due to the larger ionic radius of $Er^{3+}$, however, there is slight increase in c lattice parameter. . The inverse susceptibility *vs* T of these compounds show that the magnetic Neel temperature ($T_N$) slightly changes with increasing Er content. Specific heat $C_P$ of polycrystalline hexagonal $Yb_{1-x}Er_xMnO_3$ (x =0.1 and 0.2) samples is measured over a temperature range 2–160 K in different magnetic fields. From the Schottky analysis, estimated effective molecular fields $H_{mf}$ are 3.3 and 3.0 T for samples with x = 0.1 and 0.2, respectively. Maximum values of $\Delta S_M^{max}$ are found to be 2 $J.mol^{-1}.K^{-1}$ for $Yb_{0.9}Er_{0.1}MnO_3$ and 2.1 $J.mol^{-1}.K^{-1}$ for $Yb_{0.8}Er_{0.2}MnO_3$ with 8 T field change in the vicinity of ferromagnetic ordering temperature of $Yb^{3+}$. The values of adiabatic temperature change and relative cooling power are calculated to be 5.4 K , 23.1 $J.mol^{-1}$ and 5.6 K, 23.8 $J.mol^{-1}$ with a field change of 8 T for$Yb_{0.9}Er_{0.1}MnO_3$ and $Yb_{0.8}Er_{0.2}MnO_3$, respectively, which are appreciable enough to consider these samples as magnetic refrigerants at low temperature.

Chapter 8 Summary of the all the research works carried out and described in the earlier chapters. It also provides ideas for future research in this area on the basis of results obtained in this study are reported.

# Acknowledgements

Working on this Ph.D has been wonderful and often overwhelming experience. This journey has provided me with real learning experience on the importance of multi - tasking whilst remaining focused. So it is my duty to thank each and every one, who are influential in this pivotal period of my life.

Let me start my acknowledgement with my supervisors, Prof. A. K. Bhatnagar and Dr. Dibakar Das for accepting me as a Ph.D student. I am very grateful to Prof. A. K. Bhatnagar for introducing me in to the fascinating field of material science. He is an excellent human being to work with and thanks a lot for all his encouragement, motivation and push towards my scientific research problems. It is really a great privilege for me to work under his able and pleasant guidance. Overall it has been wonderful and satisfied journey with him during my Ph.D tenure. I would like to record my gratitude to Dr. Dibakar Das for his constant help in multiferroic studies and for discussion on rare earth manganites.

I am very grateful to Dr. K.Vinod, IGCAR, Kalpakkam for his constant help for my magnetic measurements, magnetic analysis and correcting the English in the manuscripts of my journals and this thesis. Also I would like to thank Dr. Awadhesh Mani, for providing me his magnetic lab for my research work at IGCAR, Kalpakkam.

I would like to thank Dr. Vasudeva Sirugiri, center director, UGC-DAE, CSR, Mumbai Centre and his group for carrying out the neutron diffraction measurement.

I thank Dr. S. Rayprol, UGC-DAE, CSR Mumbai for learning Rietveld refinement and neutron diffraction analysis.

I would like to thank Dr. V. Ganesan, and Dr. Aloke Banerjee UGC-DAE, CSR Indore, for their warm hands helping me to utilize their lab for characterization and for analyses.

I acknowledge with gratitude to Dean and faculty members of SEST, UoH for training me to adopt good research culture.

I would like to thank my colleagues (Dr. Sendile, Dr. Raj kumar and Srinivas) and friends in the neighboring research lab for all their help during my research.

I am happy to express my gratitude for the financial support from University of Hyderabad BBL, and UGC-DAE CSR project (CRS-M-178 and 199) made me to reach my goal in crucial time.

Finaly, I would like take this opportunity to thank my family. This degree would not be possible without full support from my parents Mr. Satyam and Mrs. Demudamma, my wife Mrs. Sreelatha and my brother Mr. Tatamnaidu. My entire family has kept me motivated to finish as well and have been a source of added support.

# List of publications

**[1]. B. Sattibabu,** A. K. Bhatnagar, K. Vinod, Sudhindra Rayaprol, Awadhesh Mani, V. Siruguri and D. Das, Studies on the magnetoelastic and magnetocaloric properties of $Yb_{1-x}Mg_xMnO_3$ using neutron diffraction and magnetization measurements ***RSC Adv.*, (2016), 6, 48636-48643.**

**[2]. B. Sattibabu,** A. K. Bhatnagar, K. Vinod, Awadhesh Manic and D. Das, Large magnetocaloric effect in hexagonal $Yb_{1-x}Ho_xMnO_3$, ***Apply physics letters* (2015),107, 262904.**

**[3]. B. Sattibabu,** A. K. Bhatnagar, K. Vinod, Awadhesh Manic and D. Das, Structural, magnetic and magnetocaloric properties of hexagonal multiferroic $Yb_{1-x}Sc_xMnO_3$ (x = 0.1 and 0.2), ***RSC Adv.*, (2015), 5, 86697.**

**[4]. B. Sattibabu,** A. K. Bhatnagar, S. Shanmukharao Samatham, D. Singh, S. Rayaprol, D.Das, V. Sirugurei and V. Ganesan, Thermodynamic Properties of Multiferroic Mg doped $YbMnO_3$ ***J. alloys and compounds*, (2015), 644, 830-835.**

**[5]. B. Sattibabu,** A. K. Bhatnagar, D. Singh, S. Rayaprol, D. Das, and V.Ganesan , Specific heat and magnetocaloric studies of hexagonal $Yb_{1-x}Er_xMnO_3$, ***Materials Letters*, (2015) , 161, 419–422.**

**[6]. B. Sattibabu** and A. K. Bhatnagar, Magnetocalorc properties of $Yb_{0.9}Mg_{0.1}MnO_3$, ***Materials Letters* (2015), 158, 395–398.**

**[7]**. **B. Sattibabu,** A. K. Bhatnagar, Sudhindra Rayaprol, D. Mohan, D. Das, M.Sundararaman and V. Siruguri, Structural and magnetic properties of Mg doped YbMnO3, ***Physica B*, (2014), 448, 210–213.**

**[8]. B. Sattibabu** and A. K. Bhatnagar, Effects of Er Doping on Raman spectra and on the Structural properties of $YbMnO_3$, ***AIP Conference Proceeding*, (2015), 1665, 130025.**

**[9]. B. Sattibabu,** A. K. Bhatnagar, Sudhindra Rayaprol, D. Mohan, D. Das, M.Sundararaman and V. Siruguri, Low Temperature Magnetic Properties of Magnesium Substituted $YbMnO_3$ ***AIP Conference Proceeding* (2014), 1591, 1766-68.**

# *Contents*

# Chapter 1

# Introduction and Literature Review

## 1.1 Introduction

In multiferroics materials different ferroic orders (ferromagnetic, ferroelectric and ferroelastic) exists in the same phase [1]. In multiferroic materials the spontaneous magnetization (polarization) can be switched on by an applying external magnetic (electric) field. In addition to these, if there is a strong coupling amongst them, then it can be controlled mutually, i.e. magnetization (polarization) is controlled by electric (magnetic) field (Fig. 1.1). The present thesis is based on the research work done on some multiferroic materials in which (anti)-ferro/ferrimagnetic and ferroelectric properties coexists.

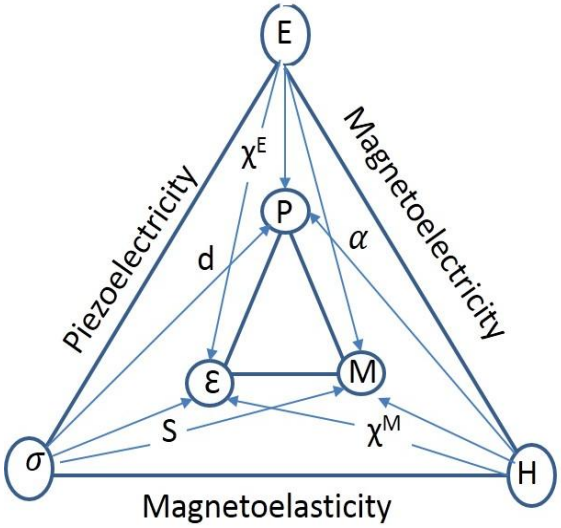


Figure 1.1: Demonstration of different ferroic properties and their interaction in materials [1].

One of the envisaged use of multiferroic materials is the manufacture of magnetic storage systems such as hard disks where ferromagnetic or ferroelectric materials are presently used. The use of a multiferroic material in these memory devices can increase in the data storage capacity/density and lower the power consumption also.

This chapter gives a brief overview of some of the fundamental and important concepts of magnetism, including brief descriptions of different types of magnetic materials and ferroelectric order(s) that are essential to form magnetoelectrics. In addition, some details of magnetic refrigeration, rare-earth manganite multiferroics, literature and motivation for pursuing this work are given. The work reported in this thesis is mostly confined to structural and magnetic properties of a rare-earth hexagonal $YbMnO_3$ and doping effects at the Yb site and from these measurements getting some other properties related to magnetic refrigeration etc.

## 1.2 Ferroelectricity

Ferroelectricity is the property spontaneous polarization of materials and the polarization can be controlled by an applied electric field. Origin of ferroelectricity lies in the absence of Centrosymmetry in the crystal structure. The well-known ferroelectric materials have $ABO_3$ formula with perovskite structure [2]. One of the examples is $BaTiO_3$. In most of the cases the B – site ions have empty *d* shell like $Ti^{+4}$, $Ta^{+5}$, $W^{+6}$. In these materials the origin of ferroelectricity is off – centering of the B - ion in oxygen octahedral, which introduces a dipole moment, as shown in fig. 1.2. The off – centering of the B ion reduces the crystal into non – centrosymmetric phase. Off – centering is the result of strong covalent bond between oxygen and empty *d* states and is part of the driving force for ferroelectricity.

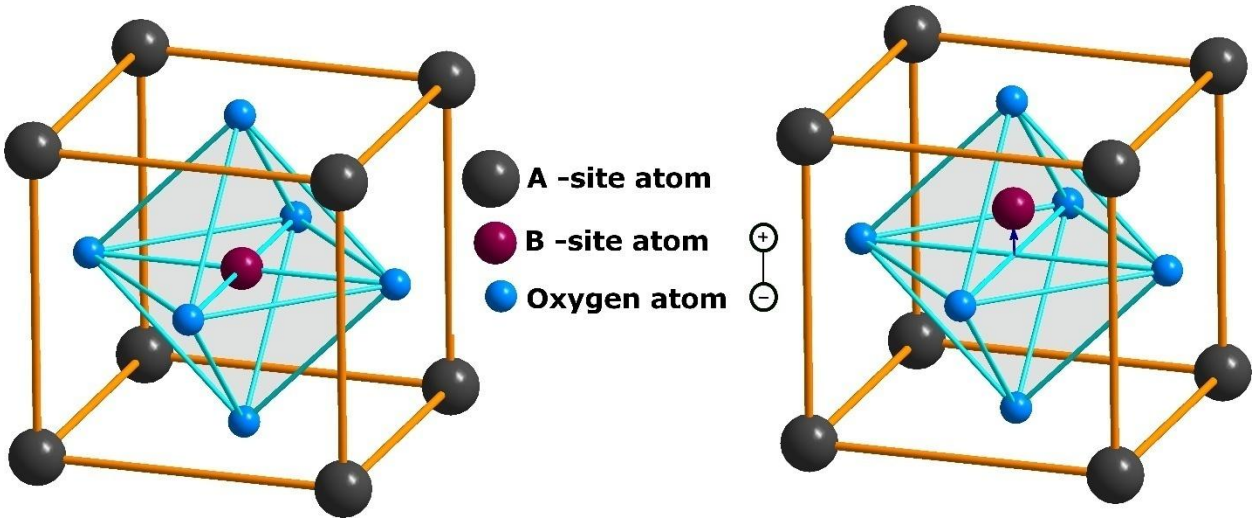


Figure.1.2: $ABO_3$ perovskite structure, displacement of B – site atom generates the dipole moment

There are other types of ferroelectrics called improper ferroelectrics. An example of improper ferroelectric is $YMnO_3$. In $YMnO_3$ though it has $ABO_3$ formula, the origin of ferroelectricity has nothing to do with $Mn^{+3}$ ions. It is caused by buckling of layered $MnO_5$ polyhedra, together with Y ions displacement form its equilibrium position, leading to a non-zero electric polarization along c – axis [3].

# 1.3 Magnetism in Solids

## 1.3.1 Magnetic Moments

The magnetic moment μ of an atom is associated with its total angular momentum J. For a single atom with only one electron, J is given by equation 1.1, where the quantum number L describes the orbital angular momentum and S is the quantum number associated with the intrinsic spin on the electron.

$$J = L + S \qquad (1.1)$$

For a material with a linear magnetic response in a small applied magnetic field, the relationship between the magnetic moment μ and total angular momentum J is given by

$$\mu = g_J \mu_B \sqrt{J(J+1)} \qquad (1.2)$$

In this equation, $\mu_B$ is the Bohr magneton, $\mu_B = {e\hbar}/{2m_e}$, and $g_J$ is the Land's g-factor, which can be expressed in terms of the quantum numbers J, L and S as follows:

$$g_J = \frac{3}{2} + \frac{S(S+1) - L(L+1)}{2J(J+1)} \qquad (1.3)$$

The magnetic susceptibility χ, the magnetic response of a material to an external stimulus, can be expressed in terms of the magnetic moment per unit volume, known as the magnetization M, and the magnetic field strength H. The magnetic flux density B is related to the magnetic field strength H by $B = \mu_0(H + M)$. As above, for a material with a linear magnetic susceptibility in a small magnetic field the following expression is obeyed ($\mu_0$ and $k_B$ are the permeability of free space and Boltzmann constants respectively):

$$\chi = \frac{M}{H} \approx \frac{\mu_0 M}{B} = \frac{\mu_0 \mu^2}{3K_B T} \qquad (1.4)$$

In fact, equation 1.4 is a statement of Curie's law, which states that magnetic susceptibility of a material is proportional to the inverse of the temperature. A system in which Curie's law is valid, where the moments tend to align with any applied magnetic field, is known as paramagnetic. The magnetic moments associated with unpaired electrons in paramagnetic

systems can be considered independent and are therefore randomly aligned in zero magnetic field. The spins are forced by applied magnetic field to align along the field direction, depending on the strength of the applied field, until all the moments get aligned and the magnetization becomes saturated. An example of a paramagnet in a small applied magnetic field is illustrated in fig.1.3.In general, the susceptibility of a paramagnetic material is very small but positive.

Diamagnetism is usually a weak effect, and most materials are diamagnetic to some degree. Unlike paramagnetism, the magnetic response of diamagnets is also largely temperature independent, and equation 1.4 is no longer valid in these materials. The magnetic moments in a diamagnetic material tend to oppose any applied magnetic field, and this is illustrated in fig.1.3. The susceptibility of diamagnetic materials is negative and usually very small, i.e., $-10^{-5}$ to $10^{-4}$,
except for a superconductor which is considered to be a perfect diamagnet at very low fields and low temperatures.

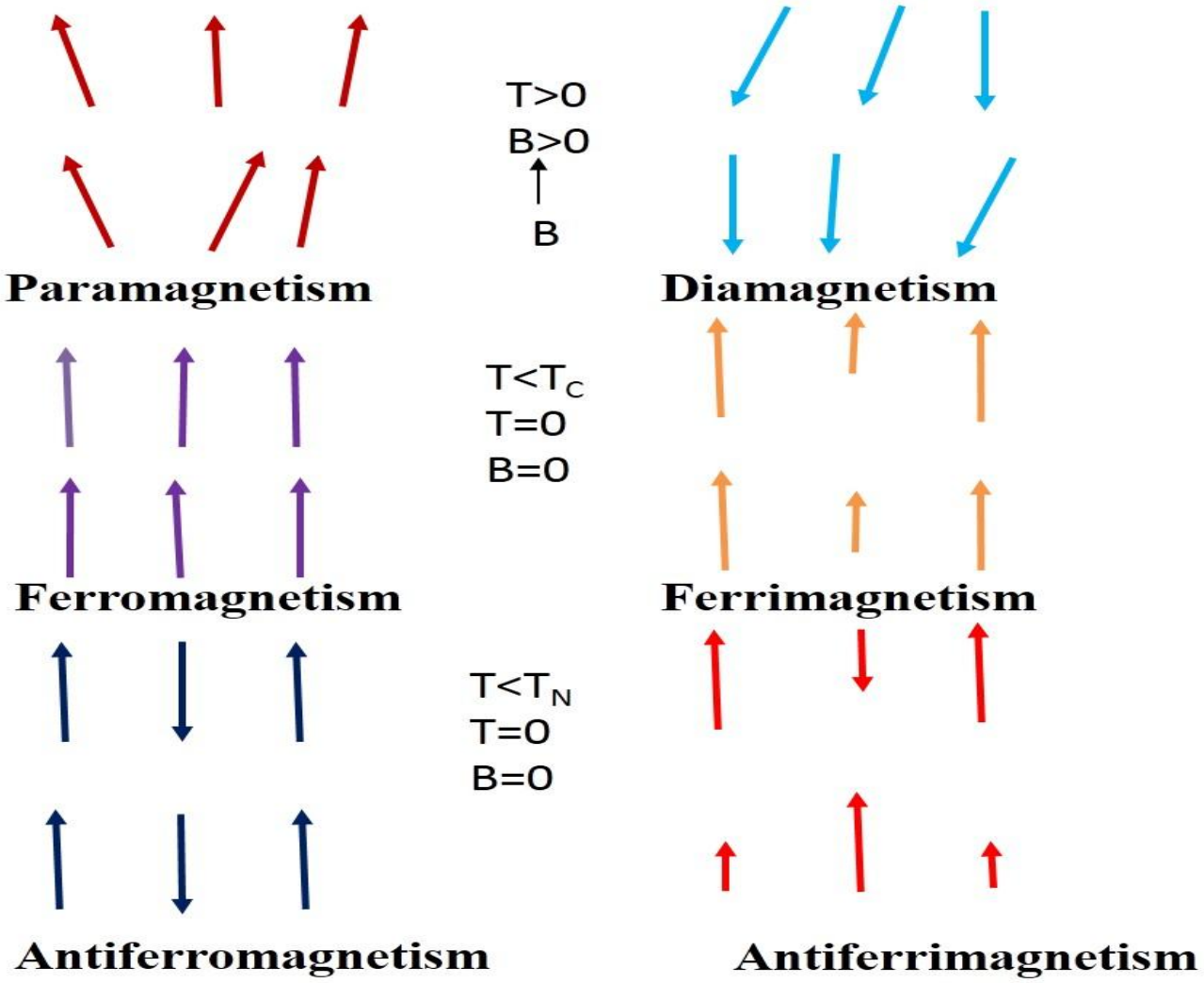


Figure.1.3: Spins arrangement in different magnetic materials.

In a ferromagnetic/ferrimagnetic material electron spins starts getting aligned below a certain temperature, so called Curie Temperature ($T_c$), and get fully aligned at T = 0 K. The magnetic susceptibility becomes magnetic field dependent and exhibit well known property of hysteresis. On the other hand, spins in an antiferromagnetic/antiferrimagnetic material get antiparallel below a certain temperature, so called Neel temperature ($T_N$), and become fully antiparallel at T = 0 K. In these materials the magnetic moments on neighboring atoms interact with each other which is not present in diamagnetic and paramagnetic materials. This interaction takes place via an exchange interaction, which will be discussed in in section 1.3.2. Depending on the details of this interaction, this results in a variety of different kinds of long-range magneticorder such as ferromagnetism, ferrimagnetism, antiferromagnetism, spiral

order, helical order and spin glass. Some of these are illustrated in fig.1.3. Ferromagnetic systems have a Curie temperature Tc below which ferromagnetism onsets. It is related to the susceptibility by the Curie-Weiss law:

$$\chi \propto \frac{1}{T-T_C} \qquad (1.5)$$

In an antiferromagnet, the critical temperature is known as the N´eel temperature $T_N$, and in this case Tc = −θ in equation 1.5. We therefore expect θ = −$T_N$. Below $T_N$, the magnetic moments lie antiparallel to their nearest neighbors [4].

## 1.3.2 Magnetic Interactions

The macroscopic magnetic effects observed are due to interactions between magnetic moments and in some cases competing interactions on similar energy scales that mean small external influences can have a large effect on the properties of the material. The magnetic dipole interactions are far too weak to account for magnetic ordering in systems that order at any temperature higher than a few Kelvin. A general introduction to magnetic interactions is presented by Blundell. [5]

## 1.3.3 Exchange Interactions

Magnetic ordering at temperatures higher than a few Kelvin finds its origin in electrostatic interactions at a quantum mechanical level. An exchange between two magnetic ions with spin $S_i$ and $S_j$ is usually described using the Hamiltonian,

$$\hat{H} = -\sum_{ij} J_{ij} S_i . S_j \qquad (1.6)$$

where $J_{ij}$ is known as the magnetic exchange constant between the spins of ion i and ion j. The magnetic exchange constant represents the strength of the magnetic interaction. A material with strong magnetic interactions displays magnetic ordering at higher temperatures. The sign of J describes whether an exchange favours a parallel alignment of two spins, a ferromagnetic

exchange (J >0), or an anti-parallel alignment of two spins, an antiferromagnetic exchange (J <0).

### 1.3.4 Superexchange

Superexchange interaction, mediated by a non-magnetic ion located between two magnetic ions, in general arranges the magnetic moments antiferromagnetically as the antiferromagnetic ordering is energetically favorable due to the Pauli exclusion principle. This is illustrated in fig. 1.4 for a single electron magnetic ion [5]. For parallel (ferromagnetic) alignment of the moments the excited states break the Pauli exclusion principle, as the two electrons in the same state having the same spin. But, the excited states with anti-parallel (antiferromagnetic) state are allowed. Hence, for the antiferromagnetic alignment, the electrons on all three sites are less confined spatially and hence they will have a lower kinetic energy. Thus antiferromagnetism is energetically favourable in such a system.

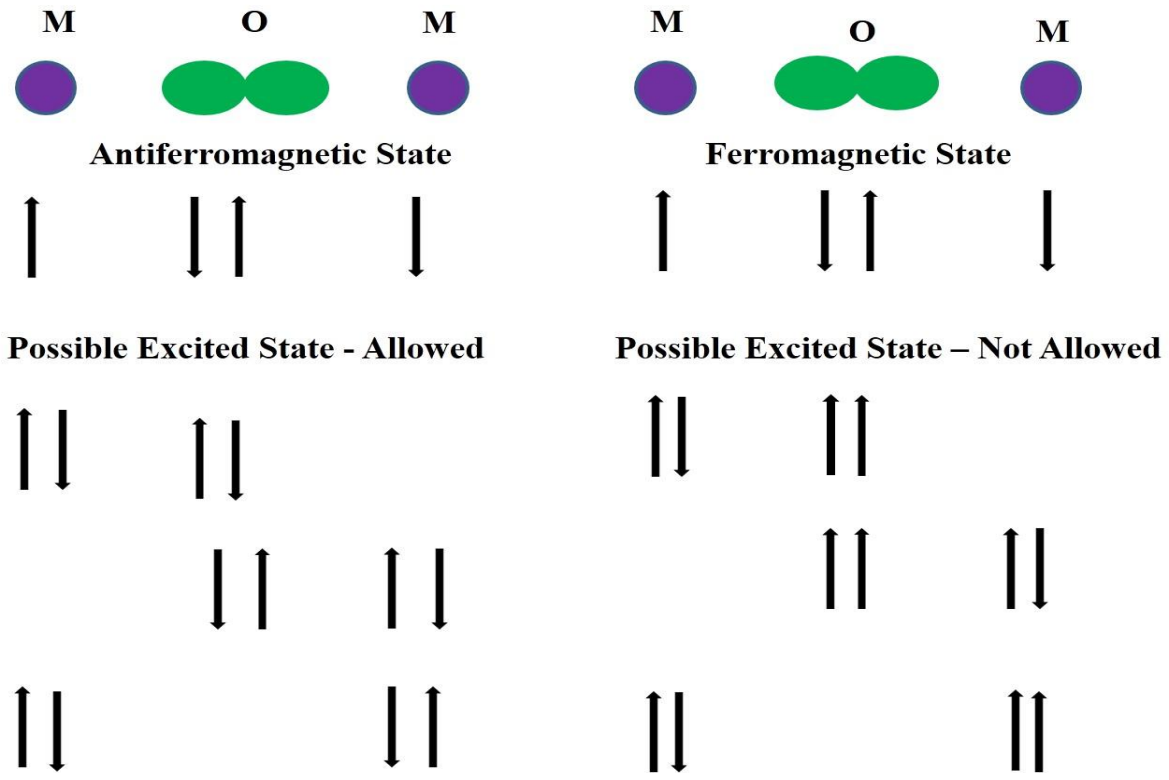


Figure.1.4**:** A diagram of the superexchange interaction when an $O^{2-}$ ion separates two single electron magnetic ions (M). Pauli exclusion principle allows the ferromagnetic excited state and restricts the antiferromagnetic arrangement of excited states.

### 1.3.5 Magnetic frustration

In some magnetic systems, competing interactions mean there is no unique ground state. The term for a system with such degenerate ground states is frustrated. Probably the most common example is geometric frustration arising from triangular arrangements of spins which are antiferromagnetically coupled [6] as shown in fig.1.5 for a two dimensional arrangement. In Fig. 1.5 three magnetic ions at the corners of a triangle and have antiferromagnetic interactions between these ions; the energy is minimized when each ion spin is aligned opposite to neighbors. After two spins become anti-parallel, the third spin is frustrated as it has two possible aligning possibilities, up and down, which have the same energy and, therefore, the third spin is unable to simultaneously minimize its interactions with both of the other two. This kind of interaction results in some interesting properties.

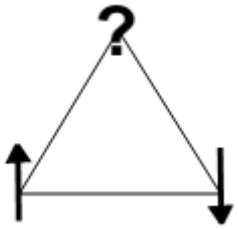


Figure 1.5: Antiferromagnetic nearest neighbor interactions on a 2D triangular lattice.

## 1.4 Magnetocaloric effect

We have carried out measurements in which we have deduced magnetocaloric effect in our samples, therefore, a short introduction to this effect is given below.

Change in magnetic field when applied to a magnetic substance induces heating or cooling effects and is termed as the magnetocaloric effect (MCE). MCE, was first discovered experimentally in Fe by Warburg in 1881 [7].

Magnetic substances have both spin degrees of freedom connected with the magnetic excitations and lattice degrees of freedom associated with phonon excitations. An external

magnetic field, when applied to a magnetic material, strongly affect the spin system, without much effect on the lattice system. The MCE can be understood considering two fundamental thermodynamic processes. Isothermal magnetization aligns magnetic moments, thus reducing the spin entropy. Since the entropy of the spin is reduced, the entropy of the lattice system must increase in order to maintain the total entropy constant, when the external magnetic field is applied adiabatically. The increase (decrease) of the lattice entropy results in increase (decrease) of the temperature of the substance. This is illustrated infig.1.6. MCE of a magnetic substance is quantitatively expressed by the isothermal entropy change, $\Delta S_T$, and/or adiabatic temperature change, $\Delta T_S$ *or* $\Delta T_{ad}$. For a ferromagnetic material, MCE is large near its spontaneous magnetic ordering temperature (the Curie temperature, $T_C$) and for a PM material MCE is large near absolute 0 K.

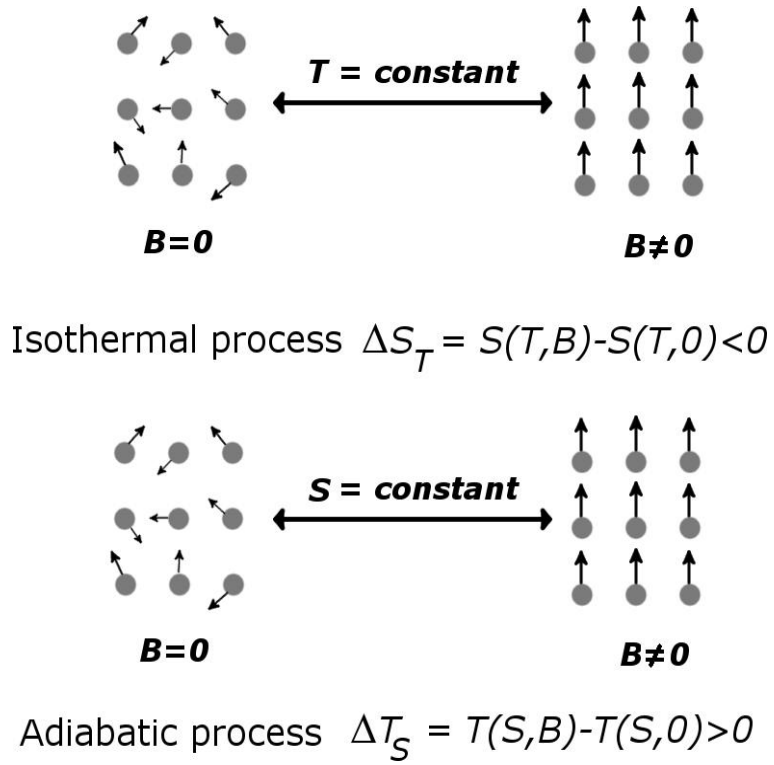


Figure.1.6: Schematic representation for application of magnetic field in two basic thermodynamic processes. Total entropy change is non-zero and negative in the isothermal process, and temperature change is non-zero and positive in the adiabatic process.

# 1.5 Magnetic refrigeration

The principle of MCE is successfully used in cooling techniques. Debye [8] in 1926 and Giauque [9] in 1927 both independently proposed magnetic refrigeration via adiabatic demagnetization. In 1933, Giauque and MacDougall achieved cooling below the liquid helium temperatures (from 3.5 K to 0.25 K) via adiabatic demagnetization refrigeration [10]. Followed by this many magnetic refrigeration based on MCE principles were reported [11-14], with the refrigeration below 20K. The idea of near room-temperature magnetic refrigeration using Gd plates were suggested in 1976 by Brown [15] and now many magnetic refrigerator prototypes have been built in laboratories over the world [16, 17].\

Analogous to a gas-compression / expansion refrigerator, magnetic refrigerators have to operate with a cycle, e.g. the Carnot cycle, the Stirling cycle or the Ericsson cycle. A typical cycle for the gaseous refrigeration includes four processes, so is the case for the magnetic refrigeration. The cycle is illustrated with the help of fig. 1.7, as follows:

• Adiabatic magnetization a → b: When a magnetic refrigerant is placed in a thermal insulated environment, applying an external magnetic field causes an increase of temperature of the refrigerant because of its MCE.

• Isofield heat extraction b → c: Then this added heat (the MCE) is removed to its surroundings by a heat-transfer medium, such as, water and helium gas. The magnetic field is kept constant to prevent the magnetic spin system from reabsorbing the heat.

• Adiabatic demagnetization c → d: Once the magnetic refrigerant is cooled sufficiently by the coolants, the magnetic field is removed adiabatically. The temperature of the refrigerant reduces due to its MCE.

• Isofield heat absorption d → a: The magnetic field is held constant, preventing the magnetic refrigerant from heating back up. The refrigerant is in thermal contact with a heat load and absorbs heat. Once the refrigerant and the heat load reach a thermal equilibrium state, the cycle finishes, and a new one begins.

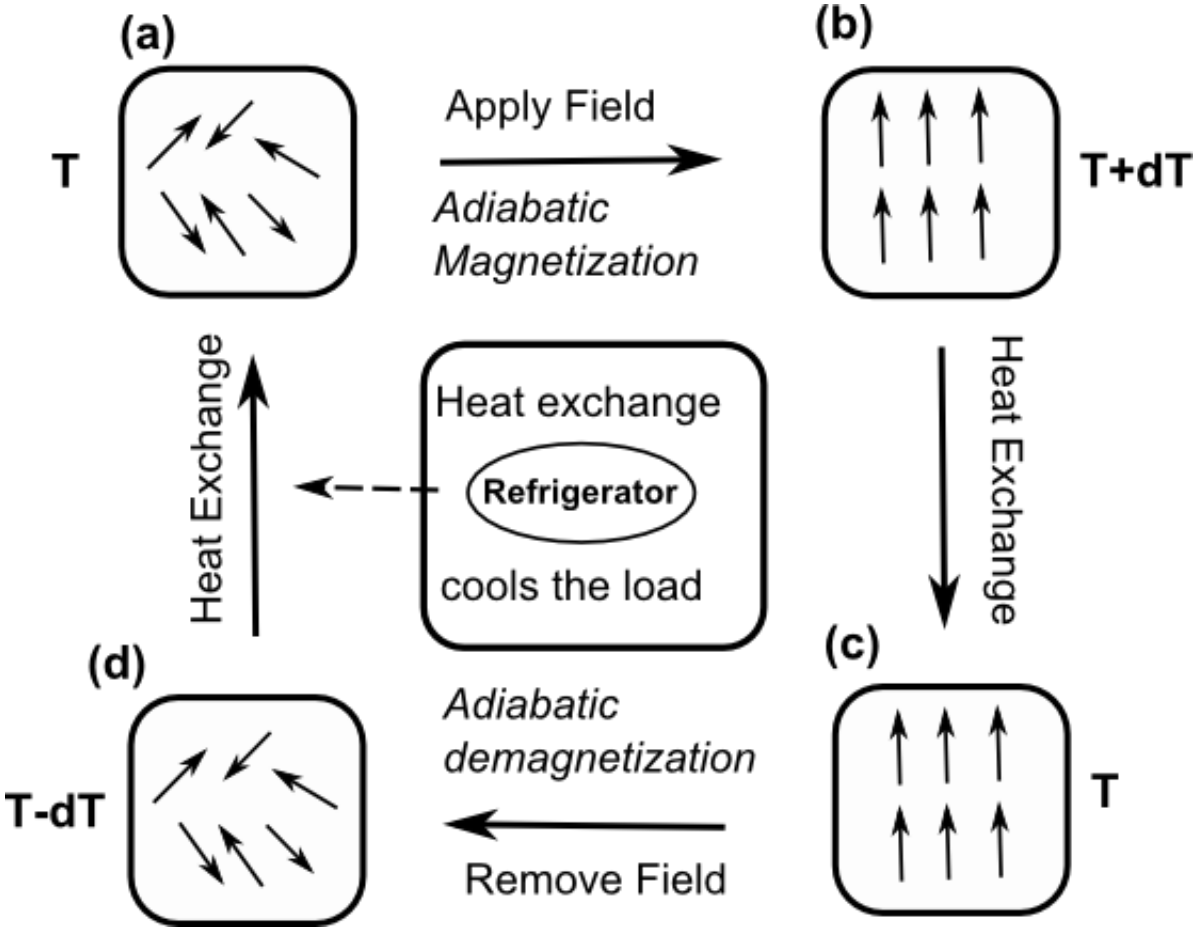


Fig. 1.7: Schematic representation of a magnetic refrigeration cycle.

## 1.6 Thermodynamic functions involved in MCE

The thermodynamic function, Gibbs free energy, which can fully describe the magnetocaloric properties of magnetic systems. When the system is at a magnetic field *B* at a temperature *T* under a pressure *p*, the Gibbs free energy *G* is given by:

$$G = U - TS + pV - MB \qquad (1.7)$$

Where *U*, *S*, *V* and *M* are the internal energy, total entropy, volume and magnetization of the system, respectively. The total differential of *G* can be written as:

$$dG = Vdp - SdT - MdB \qquad (1.8)$$

Accordingly, the parameters *S*, *V* and *M* are given by the first derivatives of *G*, as follows:

$$S(T,B,p) = -\left(\frac{\partial G}{\partial T}\right)_{p,B} \quad (1.9)$$

$$V(T,B,p) = \left(\frac{\partial G}{\partial p}\right)_{T,B} \quad (1.10)$$

$$M(T,B,p) = -\left(\frac{\partial G}{\partial B}\right)_{T,p} \quad (1.11)$$

One of the so-called magnetic Maxwell relations can be obtained by making the derivative for equations (1.9) and (1.11):

$$\left(\frac{\partial S}{\partial B}\right)_{T,p} = \left(\frac{\partial M}{\partial T}\right)_{p,B} \quad (1.12)$$

The heat capacity *C* at constant external pressure and magnetic field is represented as the second derivative of *G* with respect to temperature:

$$C_{p,B} = -T\left(\frac{\partial^2 G}{\partial T^2}\right)_{p,B} \quad (1.13)$$

Taking into account equation (1.9), equation (1.13) is written as:

$$C_{p,B} = T\left(\frac{\partial S}{\partial T}\right)_{p,B} \quad (1.14)$$

The specific heat is important for describing the first- or second-order nature of phase transitions. The heat capacity can be used to determine the magnetocaloric effect (MCE) of a magnetic material.

In terms of *T*, *B* and *p* the differential of the total entropy is written as:

$$dS = \left(\frac{\partial S}{\partial T}\right)_{p,B} dT + \left(\frac{\partial S}{\partial B}\right)_{T,p,} dB + \left(\frac{\partial S}{\partial p}\right)_{T,B} dp \quad (1.15)$$

It is seen in equation (1.15), *dS* consists of three components, the first term is due to the change of temperature, the second one is induced by the change of magnetic field and the last one is related to the change of pressure. Here it has to be noted that all the following cases are considered as reversible processes. For isothermal and isobaric processes (i.e. $dT = 0$ and $dp = 0$), only the second term is non-zero. Using the Maxwell relation (1.12), differential of magnetic field induced the entropy change in the isothermal-isobaric conditions is:

$$dS = \left(\frac{\partial M}{\partial T}\right)_{p,B} dB \quad (1.16)$$

The isothermal entropy change ($\Delta S_T$) for a field change $\Delta B = B_f - B_i$ (from an initial field $B_i$ to a final field $B_f$) can be calculated from the integral of equation (1.16):

$$\Delta S_T = \int_{B_i}^{B_f} \left(\frac{\partial M}{\partial T}\right)_{p,B} dB \qquad (1.17)$$

According to equation (1.17), the MCE of materials is proportional to $(\partial M/\partial T)_{p,B}$. Since magnetization changes rapidly at the temperature of a magnetic phase transition and slowly out of the transition region, a MCE peak located in the transition region is expected for simple ferromagnets [18].

Under adiabatic and isobaric conditions (i.e. $dS = 0$ and $dp = 0$), the left hand side and the pressure term in the right hand side of equation (1.15) are equal to zero. Using equations (1.12), (1.14) and (1.15), the differential of an adiabatic-isobaric temperature change caused by a change of magnetic field can be expressed as:

$$dT = -\frac{T}{C_{pB}} \left(\frac{\partial M}{\partial T}\right)_{p,B} dB \qquad (1.18)$$

Accordingly, the adiabatic temperature change ($\Delta T_s$ or $\Delta T_{ad}$) for a magnetic field change $\Delta B$ can be determined from the integral of equation (1.18):

$$\Delta T_s = -\int_{B_i}^{B_f} \frac{T}{C_{pB}} \left(\frac{\partial M}{\partial T}\right)_{p,B} dB \qquad (1.19)$$

## 1.6.1 Total entropy, isothermal entropy change and adiabatic temperature change

Total entropy of a magnetic substance consists of contributions from the crystalline lattice ($S_l$), from the conduction electrons ($S_e$), and from the atomic magnetic moments ($S_m$) and it can be written as:

$$S(T,B) = S_l(T,B) + S_m(T,B) + S_e(T,B) \qquad (1.20)$$

The contributions $S_l$, $S_m$ and $S_e$ generally depends on both temperature and magnetic field, and cannot be clearly separated; especially in the low temperature range (below 20 K), where the electronic contribution is much sensitive to the magnetic field. However in a simplified

approach, $S_l$ and $S_e$ are taken independent of the applied magnetic field. Hence, only the magnetic entropy contributes to the total entropy change under the magnetic field variations.

The lattice entropy is due to atomic motion. The simplest approximation to describe that is the Debye expression [19]:

$$S_l = 12N_aR\left(\frac{T}{\theta_D}\right)^3 \int_0^{\theta_D/T} \frac{x^3}{e^x-1}dx \qquad (1.21)$$

Where *Na* is the number of atoms per formula unit in a material, *R* is the gas constant and $\theta_D$ is the Debye temperature.

The electronic entropy is directly proportional to temperature with a slope given by the electronic heat-capacity coefficient $\gamma_e$:

$$S_e = \gamma_e T \qquad (1.22)$$

the magnetic entropy change for one mole of magnetic atoms is:

$$\Delta S_{m,max} = N_A K_B \ln(2J+1) = R\ln(2J+1) \qquad (1.23)$$

Where $N_A$ is the Avogadro's constant.

Fig.1.8 shows schematically total entropy as a function of temperature for a simple ferromagnet near its Curie temperature at constant applied magnetic fields, $B_i$ and $B_f$. The total entropy increases with increasing temperature at a given magnetic field and decreases with increasing field at a given temperature. The change of a magnetic field from $B_i$ to $B_f$ can cause not only a finite decrease of entropy, but also a finite increase of temperature in the material.

Two relevant processes illustrating MCE are displayed in the entropy versus temperature diagram fig 1.8. According to the diagram, when the magnetic field is applied isothermally (i.e. from state *A* to *B*), the total entropy decreases from *S* to *S′* because of the reduction of magnetic contribution; therefore, the entropy change in the process is defined as:

$$\Delta S_T(T,\Delta B) = S' - S = S\left(T,B_f\right) - S(T,B_i) \qquad (1.24)$$

Alternatively, when the magnetic field is applied adiabatically (i.e. from state *A* to *C*), the total entropy of the system keeps constant, whereas the magnetic part is reduced by applying the magnetic field, so the lattice entropy increases, resulting in a rise of temperature from *T* to *T ′*. This temperature difference at the given temperature *T* is determined by:

$$\Delta T_S(T, \Delta B) = T' - T = T\left(T, B_f\right) - T(T, B_i) \qquad (1.25)$$

And vice versa for the removal of the magnetic field in an isothermal condition and in an adiabatic condition.

Referring to equations (1.16) and (1.18), the differential of the temperature change can be written as:

$$dT = -\frac{T}{C_{p,B}} dS \qquad (1.26)$$

In equation (1.26), it is straightforward to see that the differentials of the entropy change and the temperature change have opposite signs, namely, the magnetocaloric parameters $\Delta S_T$ and $\Delta T_S$ have opposite signs.

Assuming that $T/C_p$, $B$ is a constant, which is reasonable only in the region far away from a phase transition where heat capacity is less dependent on magnetic field, thus the integral of equation (1.26) (i.e. taking equation (1.17) into (1.19) leads to:

$$\Delta T_S = -\frac{T}{C_{p,B}} \Delta S_T \qquad (1.27)$$

In equation (1.27), it can be seen that the value of $\Delta T_S$ is proportional to $T/C_p$, (for the same $\Delta S_T$) and a large $\Delta T_S$ is expected in materials with small total heat capacity. A large $\Delta T_S$ also corresponds to a large $\Delta S_T$ in a given material.

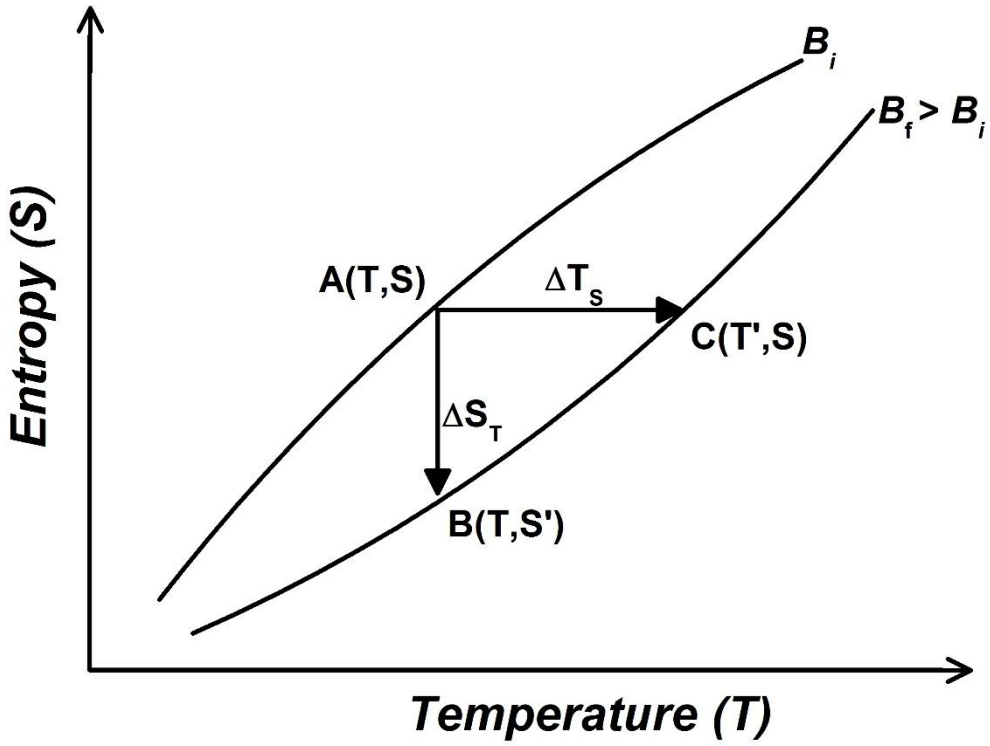


Figure.1.8: Temperature dependence of total entropy for a simple ferromagnet at constant magnetic fields *Bi* and *Bf*. Red arrowed line indicates an isothermal process from state *A* to *B*. The blue one represents an adiabatic process from state *A* to *C*.

According to figure 1.8, a true relationship between $\Delta S_T$ and $\Delta T_S$ is given by:

$$\Delta S_T(T) = -\int_T^{T+\Delta T_S} \frac{C_{p,B_f}(T)}{T} dT \qquad (1.28)$$

$$\Delta S_T(T + \Delta T_S) = -\int_T^{T+\Delta T_S} \frac{C_{p,B_i}(T)}{T} dT \qquad (1.29)$$

Where $C_{p,Bi}$ and $C_{p,Bf}$ are heat capacities at the initial field $B_i$ and the final field $B_f$, respectively. Equations (1.28) and (1.29) are simplified to equation (1.27) when $Cp,_{Bi}/T = Cp,_{Bf}/T = Cp,_B/T$ is constant.

If the magnetic phase transition under the application of a magnetic field occurs from a disordered state to an ordered state the resulting $\Delta S_T$ will be negative and $\Delta T_S$ will be positive and it is called normal MCE and for the opposite it is called inverse MCE. For example, MCE is normal in most simple ferromagnets and ferrimagnets at their Curie temperatures and in all paramagnets. Material which exhibits a stable FM phase with large net magnetization at high

temperature and a stable AFM or PM phase with small net magnetization at low temperature shows the inverse MCE.

For example, the inverse MCE in $Mn_3GaC$ compound originates from a transition from AFM to FM phase (order-order). The application of a magnetic field adiabatically causes a very small change of magnetic entropy, but a significant increase of the electronic entropy, leading to a decrease of the lattice entropy in order to keep the total entropy unchanged [20]. The negative lattice entropy change stands for a decrease of the temperature of the sample, namely,
the inverse MCE.

## 1.7 Heat capacity

Heat capacity is a fundamental physical quantity of materials. It shows the amount thermal energy $\delta Q$ a material absorb or release under a temperature change $\delta T$. The heat capacity of a substance at an arbitrary temperature $T$ is defined as:

$$C = \lim_{\delta T \to 0} \frac{\delta Q}{dT} \qquad (1.30)$$

In the case of magnetic materials, the total heat capacity at constant pressure $Cp$, includes three contributions, namely, the lattice heat capacity $C_{p,l}$ ,the electronic heat capacity $C_{p,e}$ and the magnetic heat capacity $C_{p,m}$

$$C_P = C_{p,l} + C_{p,e} + C_{p,m} \qquad (1.31)$$

Experimentally determined total heat capacity of a sample contain contributions from different physical sources and the separation the individual contributions to the total heat-capacity is very difficult. In general, the lattice heat capacity at constant volume $C_{v,l,}$ instead of $C_{p,l}$(the difference between $C_{v,l}$ and $C_{p,l}$ is very small for a solid), is estimated with the Debye model [19]. In the framework of the Debye model, the vibrations of the atomic lattice are treated as phonons in a box, and the lattice heat capacity is expressed as:

$$C_{p,l} \approx \frac{12\pi^4}{5} N_a R \left(\frac{T}{\theta_D}\right)^3 \qquad (1.32)$$

Equation (1.32) describes the heat capacity approach to zero as a $T^3$power law, which agrees well with experimental observation. The Debye model predicts correctly the heat-capacity

behavior of a solid at low and high temperatures, but due to the simple assumptions, its accuracy reduces at intermediate temperatures.

In metals, contributions from both the lattice and electronic system are present to the internal energy. The electronic contribution to heat capacity becomes dominant at very low temperatures. Taking into account of the Fermi-Dirac statistics of electrons in metals, the electronic heat capacity is given by:

$$C_{v,l} = \frac{\pi^2}{3} k_B^2 D(E_F)\mathrm{T} = \gamma_e T \qquad (1.33)$$

Where $\gamma e = \frac{\pi^2}{3} k_B^2 D(E_F$ is the electronic heat-capacity coefficient and $D(E_F)$is the electron density of states at the Fermi energy $E_F$. It has to be noted that $C_{v,e}$ is a linear function of $T$ in the whole temperature range, because the free electron heat-capacity concept is assumed to be valid even at very high temperatures.

For nonmagnetic solids, the total heat capacity at constant pressure and constant magnetic field in the low temperature region ($T \ll \theta_D$) can be represented by:

$$C_{p,B} = \gamma_e T + \frac{12\pi^4}{5} N_a R \left(\frac{T}{\theta_D}\right)^3 \qquad (1.34)$$

In order to evaluate the value of $\gamma_e$, equation (1.34) is converted to the form:

$$C_{p,B} = \gamma_e T + \frac{12\pi^4}{5} N_a R \left(\frac{T}{\theta_D}\right)^3 \qquad (1.35)$$

In order to evaluate the value of $\gamma e$, equation (1.35) is converted to the form:

$$C_{p,B}/_T \approx \gamma_e + \alpha T^2 \qquad (1.36)$$

where $\alpha = 12\pi^4 N_a R/(5\theta_D^3)$ The coefficient $\gamma e$ and the Debye temperature $\theta_D$ can be evaluated from the plot of $C_{p,B/T}$ versus $T^2$ at low temperature by taking the value of the intercept at $T$ = 0 K and the slope of the straight line, respectively.

Once the total experimental heat capacity of a magnetic solid is measured, the magnetic contribution can be deduced using equations (1.31), (1.32) and (1.33). It is a general way to obtain the magnetic heat capacity by most scientists for studying the magnetic phase transition.

## 1.8 Refrigeration capacity

Gschneidner *et al*. proposed refrigeration capacity for evaluating the cooling power of magnetic refrigerants for use in magnetic refrigeration [21]. The refrigeration capacity is defined as:

$$\mathrm{RC}^{S} = \int_{T1}^{T2} \Delta S_{ST}\,(T)dT \qquad (1.37)$$

$$\mathrm{RC}^{T} = \int_{T1}^{T2} \Delta T_{S}\,(T)dT \qquad (1.38)$$

where $T_1$ is the temperatures of the hot sink and $T_2$ is the temperatures of the cold sink. Thus, the quantity $RC^S$ indicates the amount of heat that can be exchanged between the cold and hot sinks during one ideal refrigeration cycle. The value of $RC^T$ has $K^2$ dimensions.

Later, Gschneidner *et al*. pointed out that refrigeration capacity can also be characterized by the peak MCE value and its full width at half maximum ($\delta T_{FWHM}$) [13]. So the relative cooling power is expressed as:

$$\mathrm{RCP}^{S} = \Delta S_{T,max} \times \delta T_{FWHM} \qquad (1.39)$$

$$\mathrm{RCP}^{T} = \Delta T_{S,max} \times \delta T_{FWHM} \qquad (1.40)$$

In the case of $\Delta S_T$, the value of $RCP^S$ is found to be close to 4/3 times $RC^S$.

## 1.9 Multiferroic materials

Multiferroics materials have two or more ferroic orders. The ferroic orders are ferromagnetic, ferroelectric and ferroelastic. In a vast sense anti-ferro/ferrimagnetic orders are also included in the multiferroic group. Among these materials with coexistence of magnetism and ferroelectric have great technological and fundamental importance because of their sensitivity to applied magnetic fields and coexistence of these two orders which are mutually exclusive.fig.1.9 shows the schematic view of overlap (coexistence) of magnetically and electrically polarizable materials. The existence of both ferroic orders enables the mutual control of their properties. In multiferroic materials we can control the magnetic spins by applying electric field and charge by applying magnetic field. This gives way to new

multifunctional devices which are in reduced dimensions and more sensitive due to coupling between these order parameters.

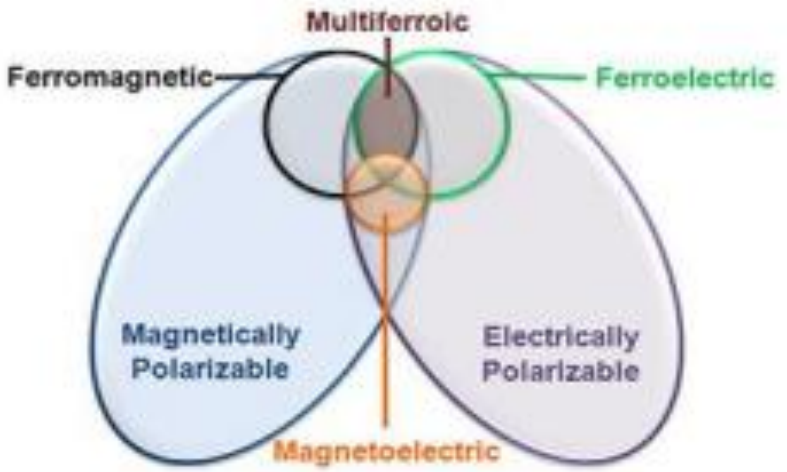


Figure.1.9: Schematic view of relation between magnetically polarizable and electrically polarizable materials [22].

## 1.9.1. Classification of multiferroics

Multiferroics are classified into different subgroups based on the involved mechanism of multiferroicity and its nature. Thus depending upon the mechanism these materials are divided into two categories namely Type 1 and Type 2 multiferroics.

**Classification of multiferroics**

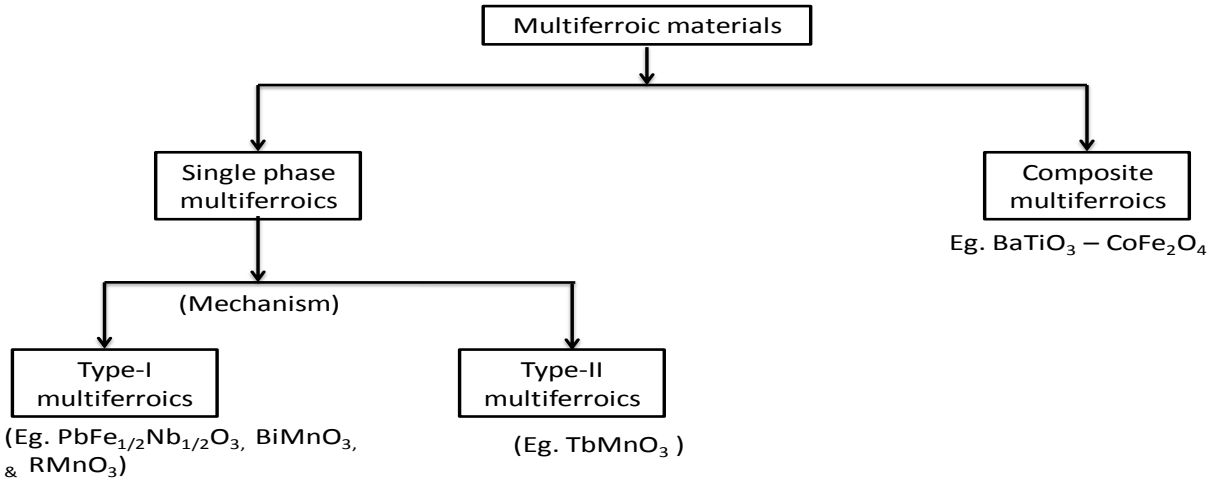


a. Type 1 multiferroics

In this class, the origin of the magnetism and ferroelectricity exists independently. The nature of coupling in such systems is weak. The origin for multiferroicity in this type can be in three ways. Firstly, multiferroicity in the materials can arise due to lone pair of electrons. This can be seen in compounds like $BiFeO_3$, $BiMnO_3$ and $PbVO_3$.Secondly due to charge ordering for example in materials like $YbFe_2O_4$, $YMnO_3$,$YbMnO_3$,$BaMF_4$ (M = 3d transition metal ion). Geometric frustration is another reason for the origin of mutiferroicity.

b. Type 2 multiferroics

In type – II multiferroics, the origin of ferroelectricity is magnetic ordering in the material. The materials falling under this type have spiral or collinear magnetic spin structure. Thus ferroelectricity in these materials is because of magnetic ordering of material. $TbMnO_3$ and $YbMn_2O_5$ etc are the examples for type 2 multiferroics.

In both cases, generally the ferroelectric temperature is much higher than the magnetic order temperature

## 1.9.2 Origin of multiferroicity

Magnetoelectric effect, which expresses the coupling between electric and magnetic fields in materials, is the induction of magnetic (electric) polarization by applying an external electric (magnetic) field. Magnetoelectric effect first predicted theoretically by Dzyloshinsky [23], and experimentally demonstrated by Astrov [24]. Magnetoelectric effect is shown by many magnetic materials [25]. Within the Landau theory framework, by the expansion of free energy for a magnetoelectric system,

$$\mathrm{F}(\vec{E},\vec{H}) = F_0 + P_i^s E_i - M_i^s H_i - \frac{1}{2}\in_0 \in_{ij} E_i E_j - \frac{1}{2}\mu_0\mu_{ij}H_iH_j - \alpha_{ij}E_iH_j - \frac{1}{2}\beta_{ijk}E_iH_jH_k - \frac{1}{2}\gamma_{ijk}H_iE_jE_k - \cdots \quad (1.41)$$

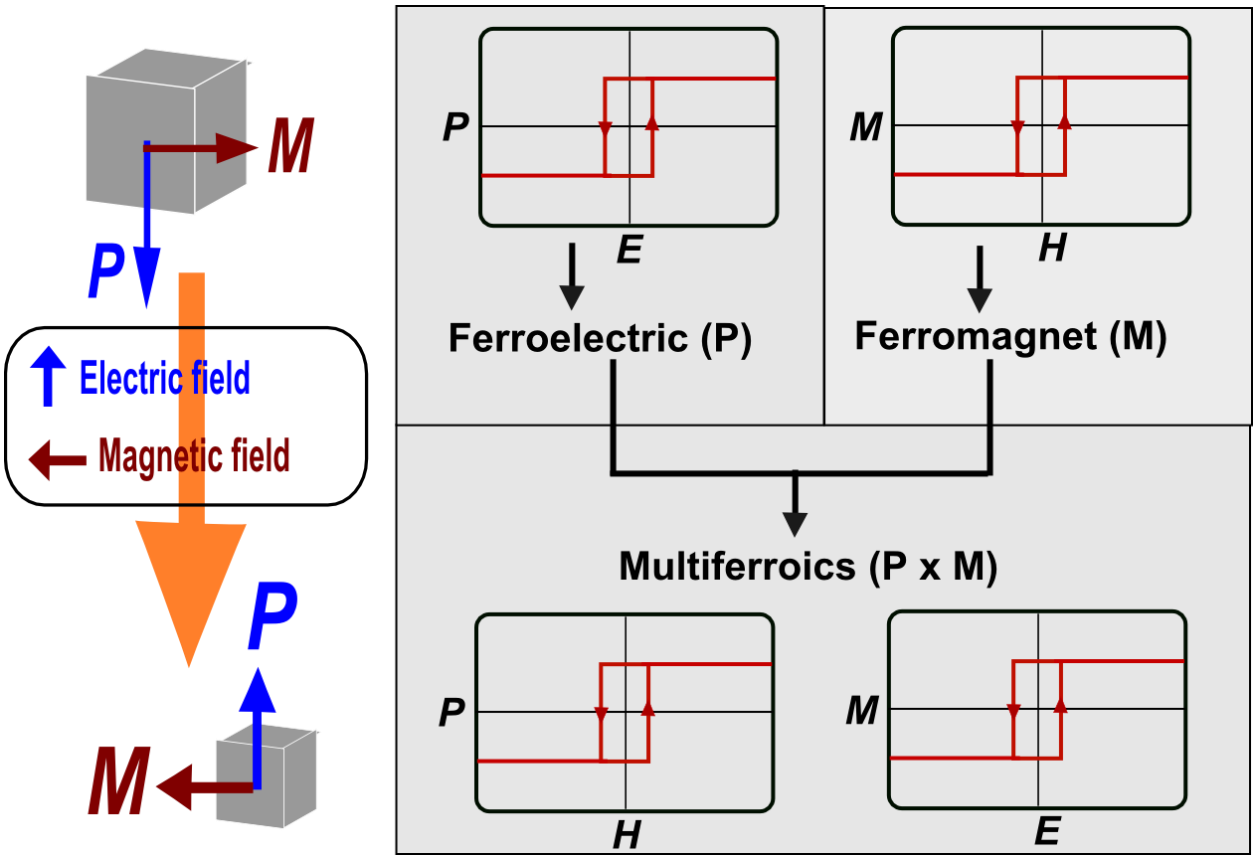


Figure. 1.10: A schematic of the ferroelectricity and ferromagnetism and multiferroics. (Reproduced from Tokura et al [26]).

where $F_0$ is the free energy in the ground state, $M^s$ and $P^s$ are spontaneous magnetization and polarization, μ0and ε0 are the magnetic and dielectric susceptibilities. The subscripts (i, j, k)

indicates components along the three spatial coordinates. The tensor α corresponds to induction of polarization (magnetization) by a magnetic (electric) field. [35].

The fist derivative of equation (1.40) gives the polarization

$$\mathrm{F}\left(\vec{E},\vec{H}\right) = -\frac{\partial F}{\partial E_i} = P_i^S + \in_0 \in_{ij} E_j + \alpha_{ij}H_j + \frac{1}{2}\beta_{ijk}H_jH_k + \gamma_{ijk}H_iE_j + \cdots \quad (1.42)$$

$$\mathrm{M}\left(\vec{E},\vec{H}\right) = -\frac{\partial F}{\partial H_i} = M_i^S + \mu_0\mu_{ij}H_j + \alpha_{ij}E_j + \beta_{ijk}E_iH_j + \frac{1}{2}\gamma_{ijk}E_jE_k + \cdots (1.43)$$

One way to improve the magneto- electric response in single-phase compounds significantly, the use of strong internal electromagnetic fields in the components to be made with great dielectric and magnetic susceptibility. It is known that ferroelelectric / ferromagnetic materials, which have the largest dielectric / magnetic susceptibility respectively. Ferroelectrics with ferromagnetism, i.e ferroelectro - magnets [31, 32], would be prime candidates for improved magnetoelectric effect . Examined except for the coexistence of ferroelectricity and ferromagnetism , materials with a strong coupling between the primary and ferroelastic and - ferromagnetic order parameter , in the class of ferromagnetic martensitic systems were also about 10 years ago [ 33 ] .

## 1.10 Rare earth manganites ($RMnO_3$)

Rare earth manganites ($RMnO_3$) with light rare earth with large ionic size R = La, Ce, Pr, Nd, Sm, Eu, Gd, Tb and Dy have pervoskite structure (Space group Pnma) at room temperature. These are well known for their Colossal Magneto Resistance (CMR) property. Whereas crystal structure of rare earth manganites ($RMnO_3$) with heavier rare earths with smaller ionic size is hexagonal structure (Space group P63cm). h – RMnO3 is antiferromagnetic, ferroelectric and has multiferroic magnetoelectric property as well. The origin of magnetoelectricity in these is quite interesting. $YMnO_3$ is well studied and prototype of h – $RMnO_3$.

## 1.11 Hexagonal $\boldsymbol{R}MnO_3$

In hexagonal multiferroics, $R$MnO$_3$, R is a rare earth element (Ho-Lu) or yttrium (Y). Even though yttrium is not a rare earth element, it also forms a hexagonal multiferroic when combined with $MnO_5$, since yttrium forms a stable trivalent cation with anionic radius similar

to rare earth materials. In this family of hexagonal structures, each $Mn^{3+}$ ion with spin = 2 is surrounded by a total of 5 oxygen ions. Three of them are in-plane and two are apical (figure 1.11) forming a bipyramid structure that looks like two tetragonal pyramids joined at their base. The triangular lattices of $Mn^{3+}$ions are formed by these $MnO_5$ bipyramids where they are "corner-linked" to each other along the in-plane oxygen ions [3]. $R^{3+}$ ions are sandwiched between these 2D triangular lattices, which are stacked alternately in *c* direction (figure 1.11). The crystal structure of these hexagonal multiferroics was first reported in 1963 [34]. These $MnO_5$ bipyramids undergo tilting to minimize their energy, which will induce ferroelectric polarization along *c* axis [35].

### 1.11.1 Magnetism in *R*$MnO_3$

The magnetic structure of *R*$MnO_3$ was first reported by Koehler *et al.* and it is antiferromagnetic due to superexchange interactions [36]. Super exchange describes the coupling between moments through a non-magnetic material. In *R*$MnO_3$ family$Mn^{3+}$ spins are coupled to each other via a non-magnetic $O^{2-}$anion. We know from the Heisenberg uncertainty principle that confining a particle to a smaller volume increases its kinetic energy. In order to minimize the kinetic energy of electrons, the wave function should expand its spatial extent, which means assigning a nonzero probability of electrons hopping between neighboring atoms. However, only hopping which are consistent with the Pauli exclusion principle are permitted. Figure 1.11 shows a schematic of electrons involved in the Mn-O-Mn superexchange process. More electron hopping modes are permitted between the $Mn^{3+}$ 3d orbitals and the $O^{2-}$orbitalif the $Mn^{3+}$ moments are anti-aligned, leading to an antiferromagnetic interaction between $Mn^{3+}$ moments mediated by the $O^{2-}$ion between them [37].

The antiferromagnetic structure of *R*$MnO_3$ is frustrated, this is due to the $Mn^{3+}$ triangular lattice structure [36]. Koehler *et al.* determined that $Mn^{3+}$ ions order in a 120◦ angle between the three moments in a triangle at low temperature (∼70K) to relieve frustration. Because adjacent layers are laterally offset from each other, the relative orientation of spins in adjacent layers affects the magnetic symmetry. The exact magnetic structure varies depending on factors such as which rare earth element occupies the space between $MnO_5$ layers, temperature and magnetic field. Multiferroism exists in *R*$MnO_3$ because of the coexistence of antiferromagnetically ordered Mn spins and the ferroelectric phase.

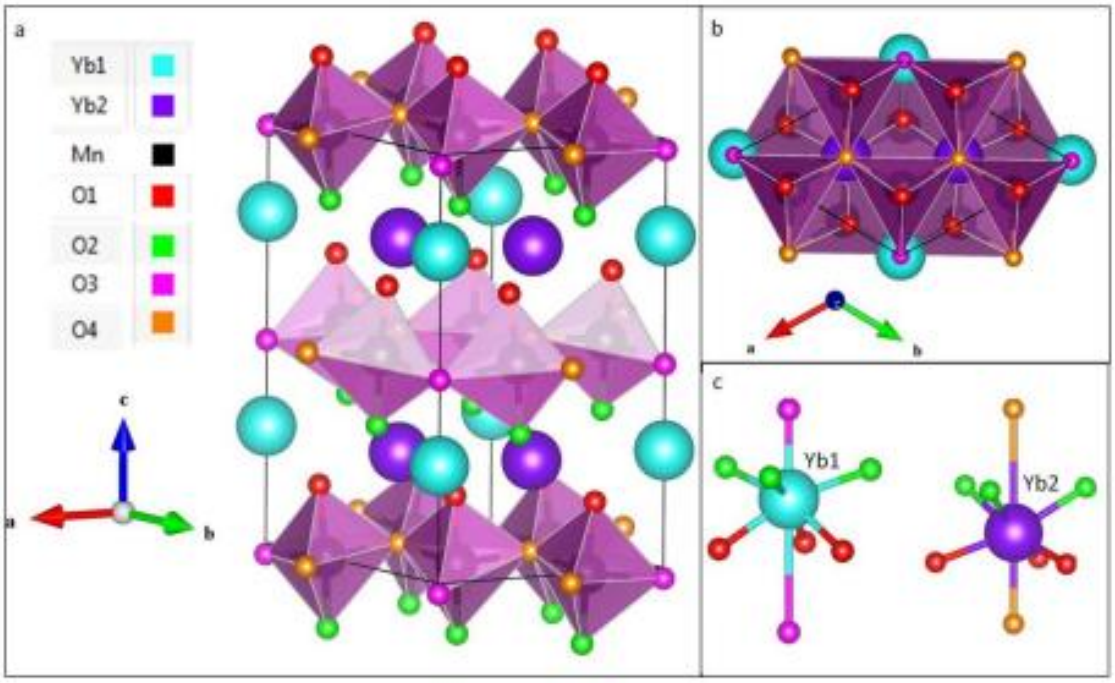


Figure. 1.11: a) Structure of h – $RMnO_3$, b) Mn – O triangular lattice, c) Oxygen ions around rare earth ion in 2a and 4b sites. Figures are constructed using VESTA Software [38]. Data for figures is taken from ref. 39.

## 1.11.2 Ferroelectricity in *R*$MnO_3$

Ferroelectricity in *R*$MnO_3$ multiferroics is due to a geometric effect. A detailed analysis of the origin of ferroelectricity in *R*$MnO_3$ was done by Bas B. Van Aken *et al.*[3],who found that the ferroelectric phase is due to the tilting of the $MnO_5$ bipyramids by displacing oxygen from its centrosymmetric position with Mn remaining at the center. This tilting of the $MnO_5$ bipyramids satisfies the hexagonal close-packing requirement and minimize the total energy of the unit cell. Tilting is accompanied by large displacement of the R-O bonds along the *c* axis due to a displacement of R atoms along the *c* axis, which leads to local antiparallel electric dipoles with different magnitudes, resulting in net ferrielectric polarization (fig 1.12). Careful structure analysis work and first principal calculation proves that Mn ions stay near to the middle of oxygen bipyramids and hence the ferroelectricity is not due to the Mn ions location. This is because off-center distortion of $Mn^{3+}$ is energetically unfavorable [3]. This structural distortion typically occurs at high temperatures for the *R*$MnO_3$ family. For example, the ferroelectric temperature $T_C$ of $YMnO_3$ was reported to be around 920 K with space group $P6_3cm$ and the centrosymmetric high temperature phase was found to be above 1270K [40, 41].

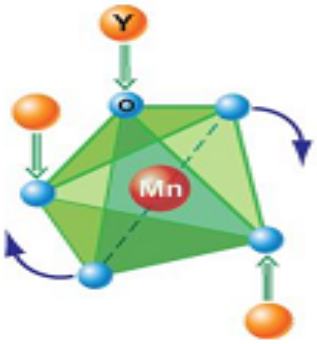


Figure. 1.12: The generation of polarization in$YMnO_3$ [3].

# 1.12 Literature review

## 1.12.1 Structure of $YbMnO_3$

M. Isobe *et al*. and Bas B Van Aken *et al*. studied the crystal structure of $YbMnO_3$ [42, 43]. Yb atoms occupy two crystallographic sites Yb(1) at 2a, Yb(2) at 4b. Mn atoms occupies 6c site. There are four equivalent sites for oxygen atoms; they are O (1) at 6c, O(2) at 6c, O(3) at 2a, O(4) at 4b. h – $YbMnO_3$ has P63cm space group at room temperature with 6 formula units per unit cell. As described earlier the structure is made of corner sharing $MnO_5$ trigonal bipyramids, which repeats along c – axis at z = 0, z = ½. $Yb^{+3}$ ions are located at the middle of separation of MnO5 polyhedra.

## 1.12.2 Properties of $YbMnO_3$

$YbMnO_3$ is antiferromagnetic with Neel temperature around ~ 85 K and ferroelectric transition ~ 900 K [39, 44]. X. Fabreges *et* al have studied its magnetic structure using neutron diffraction and Mossbauer spectroscopy [39]. They have reported that the $_{Mn}^{3+}$ moments get aligned in the ab-plane order antiferromagnetically, at the Neel temperature ($T_{N1}$= 85 K) and starts the Yb moments at the 4b crystallographic site to order due to the Mn molecular field. The Yb(4b) moments aligned along the c-axis and are antiferromagnetically (ferromagnetically) coupled along the ab-plane (c-axis). Below $T_{N2}$ 3.5 K, $Yb^{3+}$ moments at the 2a crystallographic site aligned along the ab-plane start long range ferromagnetic ordering through Yb-Yb interactions. They suggest a spin flip/reorientation of the Yb(2a) moments from ab-plane toc-axis as the source/reason for the field induced magnetictransition. Fabreges et. al. [39] reported that the best fit of the $YbMnO_3$ data was obtained assuming Γ4 representation for Mn ordering, and the ordered moment at 1.5 K was found to be 3.25μ*B*.The interaction strength

of are given as Mn – Mn > Mn – Yb > Yb – Yb. F. Yen *et* al. has constructed the magnetic phase diagram using anomalies in magnetization, dielectric constant and specific heat measurements up to 14 T [45], as is shown in fig. 2.2. At very low temperatures $T_{RE}$ = 4 K, $Yb^{+3}$ moments order and this phase is quickly suppressed by external magnetic fields. At 2 K, fields as low as 0.07 T are able to destroy the order of Yb moments. h – $YbMnO_3$ is stable in $P6_3cm$ symmetry except in low temperature and high magnetic field region. $P6_3cm$ exists beyond 14 T and the continuous transition from $P6_3cm$ to $P6_3cm$ is derived with application of higher fields.

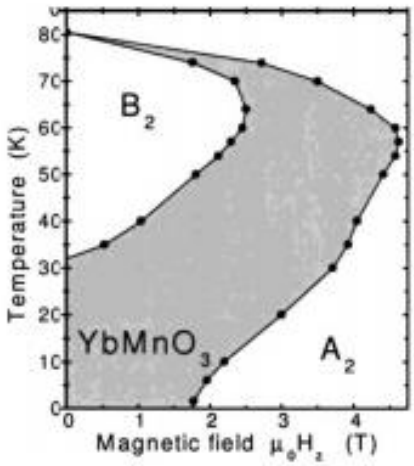


Figure. 1.13: Magnetic phase diagram of h – $YbMnO_3$ derived from the optical second harmonic generation spectroscopy. [46].

J. Fontcuberta *et al*. has observed small ferromagnetic component along c – axis of single crystal, which is observed by the hysteresis between Zero Field Cooled (ZFC) and Field Cooled (FC) susceptibility curves and small coercivity up to $T_N$ [47] and it is due to canting of $Mn^{+3}$ moments from ab plane about an angle of 0.35°.

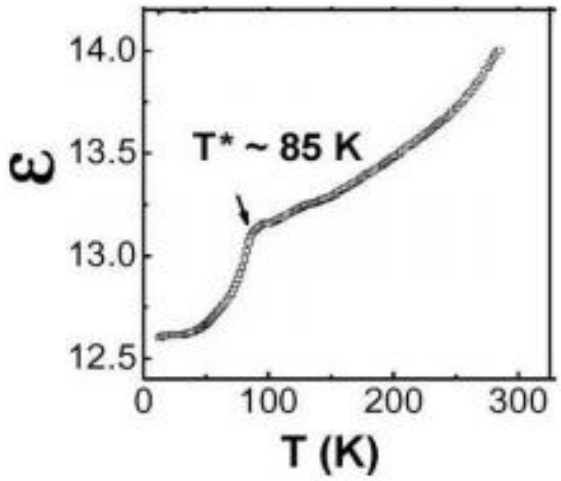


Figure. 1.14: Dielectric anomaly at the magnetic transition temperature in $YbMnO_3$ [48].

Fig. 1.14 shows the dielectric anomaly in $YbMnO_3$ around Neel temperature observed by M. C. Lin *et al.* [48]. T. Katsufuji *et al*. has explained it as due to strong p – d exchange interaction of oxygen and Mn ions [49]. T. C. Han *et al.*, T. Takahashi *et al.*, S. Kang *et al*., and several other research groups have successfully grown the h – YbMnO3 thin films by employing PLD, sol – gel techniques [50-52]. They were successfully characterized for magnetic and ferroelectric properties. Preparation of thin films is a direct application of these materials in memory devices.

N. Abramov *et al*. has studied low temperature magnetic properties of $Yb_{1-x}Ca_xMnO_3$ (x = 0.00, 0.05 and 0.10) single crystals [53]. The Neel temperature decreases slightly with Ca doping. Also specific heat at transition decrease due to decrease in number of $Yb^{+3}$ ions. Samal *et al*. has studied different physical properties of $YbMn_{1-x}Fe_xO_3$ (x = 0.00, 0.10, 0.20 and 0.30) compounds [54]. It is observed that with increasing iron concentration Neel temperature increased from 82 K to 95 K and ferroelectric loop has become more lossy. Y. J. Wu *et al*. studied the high temperature dielectric properties of $YbMnO_3$ [55]. They observed relaxation behavior because of and dipoles. The magnetic phase diagram of $YbMnO_3$ is rather complex. Results of magnetic, dielectric, and magnetoelectric measurements on single crystals of $YbMnO_3$ by Sugie et al [56] show that below $T_{N2}$ 3.5 K, long range ferromagnetic (FM) ordering of $Yb^{3+}$ moments develops and a magnetic field applied along the c-axis induces a first order magnetic transition at a critical field of H||c 35 kOe, where the magnetic ordering

along the c-axis becomes ferrimagnetic. They have identified the low temperature magnetic phase (H-T) diagram of $YbMnO_3$ with three different regions.

## 1.12.3 Room-temperature MCE materials

For room-temperature or near room temperature MCE applications magnetic materials having the Curie temperature near room temperature is required. Among the elements, rare-earth metal Gadolinium (Gd) is the only ferromagnetic element having the Curie temperature, $T_C$= 293 K, near room temperature with a quite high saturation magnetic moment of 7.63 $\mu_B$, [57]. Gd shows second-order magnetic phase transition (SOPT) at $T_C$= 293 K and the MCE properties of Gd were explored since 1976 by Brown *et al.* [15]. The magnetocaloric parameters of Gd at $T_C$ were found to be $-\Delta ST$ = 13.2 J/kg·K and $\Delta TS$ = 14 K for a field change of 7 T [15]. Presence of impurities in Gd is found to reduce its MCE [57] values. The solid solutions of Gd have been also explored, such as $Gd_{1-x}RE_x$compounds with RE = lanthanide (Tb, Ho, Er and Dy) [58–60], $Gd_{1-x}M_x$ compounds with M = other elements (Ni, Al, Pd, Rh, In, Zn and B) [61–67]. Among the above various combinations it was found that pure Gd has the better MCE characteristics suitable for room-temperature magnetic refrigeration applications.

## 1.12.4 MCE of $RMnO_3$

A. Midya, et al they reported magnetocaloric properties from magnetic measurements in $RMnO_3$($R$ = Dy, Tb, Ho, and Yb) single crystals [68]. Values of maximum entropy change ($-\Delta S_M^{max}$), the adiabatic temperature change ($\Delta T_{ad}$) and the relative cooling power (RCP) are found to be 2.3J/(mol-K),15 K and 26 J/mol for $YbMnO_3$, 5.5 J/(mol-K),11.5 K and 155 J/mol for both $DyMnO_3$, $TbMnO_3$ and 5.2 J/(mol-K),12.5 K and 144 J/mol for $HoMnO_3$ with $\Delta H$ = 80 kOe. The values of magnetocaloric parameters $DyMnO_3$ and $TbMnO_3$ are comparable in magnitude. A. Midya, et al they reported magnetocaloric properties from magnetic measurements in $HoMnO_3$ single crystals [69]. Values of maximum entropy change ($-\Delta S_M^{max}$), the adiabatic temperature change ($\Delta T_{ad}$) and the relative cooling power (RCP) are found to be 13.1 (J $kg^{-1}$), 6.5 K and 320 J/kg for $HoMnO_3$ with filed change 7 T. Mingjie Shao et al reported the magnetocaloric properties of $Dy_{1-x}Ho_xMnO_3$ ($0 \leq x \leq 1$). For $HoMnO_3$ the value of entropy change and refrigeration capacity are 12.5 J/kg K and 312 J/kg, respectively at 7 T [70].

# 1.13. Motivation and objective of present work

All these previous works have motivated us to revisit $YbMnO_3$ in polycrystalline form as well as to study the effect of doping of certain elements at the Yb site on structure, magnetic order and magneto-caloric properties. Basically our motivation for this research is as follows.

1. $RMnO_3$, in general exhibit fascinating magnetic, electric and optical properties dictated by the size of $R^{3+}$ rare earth ion. These are due to the subtle play between charge, spin, and lattice degrees of freedom.

2. Structure of $RMnO_3$ depends on size of R ion. For larger size, it has distorted orthorhombic perovskite structure whereas of smaller size R ion, it shows a hexagonal structure.

3. Among hexagonal $RMnO_3$, $YMnO_3$ is extensively studied while $YbMnO_3$ is not studied too much.

4. $YbMnO_3$ is a multiferroic material being ferroelectric below ~900 K and antiferromagnetic below ~85 K.

5. Most of studies on $YbMnO_3$ are on virgin sample and doped samples where doping is mostly done for the Mn atom.

6. Our interest is to study certain properties of un doped and doped polycrystalline $YbMnO_3$ where doping is done at the Yb site. Properties studied are structure, magnetic behavior, thermal and magnetoelectric properties.

7. The purpose of doping is to see how various properties change and if the antiferomagnetic ordering temperature and magnetocaloric effect can be enhanced by certain dopings.

8. Small ionic radius elements affect the structural change and increases the antiferromagnetic ordering temperature. RE doping is expected to enhance the magnetic and magnetocaloric properties.

9. Doping elements chosen are Mg, Ho, Sc and Er which have different ionic sizes and magnetic properties.

10. Based on the above observation the objective of the current investigation is to study the effect of Mg, Ho, Sc and Er on structural, magnetic and magnetocaloric properties of $YbMnO_3$.

## 1.14 References:

[1] H. Schmid, Ferroelectrics **162**, (1994), 317

[2] B.A. Strukov Levanyuk**,** Arkadi P.Berlin Springer (1998).

[3] Bas B. Van Aken Thomas T.M. Palstra, Alessio Filippetti and Nicola A. Spaldin Nature materials, **3**, (2004), 164.

[4] B. D. Culity and C. D. Graham, Second edition, Wiley publications.

[5] S. Blundell. Magnetism in Condensed Matter. Oxford University Press, 2001.

[6] M. F. Collins and O. A. Petrenko, Can. J. Phys. **75** (1997) 605

[7] E. Warburg, Ann. Phys. Chem., **13** (1881) 141.

[8] P. Debye, Ann. Physik, **81** (1926) 1154.

[9] W.F. Giauque, J. Amer. Chem. Soc., 49 (1927) 1864.

[10] W.F. Giauque and D. P. MacDougall, Phys. Rev., **43** (1933) 768.

[11] V.K. Pecharsky and K.A. Gschneidner Jr., J. Magn. Magn. Mater., **200** (1999) 44.

[12] K.A. Gschneidner Jr. and V.K. Pecharsky, *Rare Earths: Science, Technology and Applications III*, ed R.G. Bautista et al., Warrendale, PA: The Minerals, Metals and Materials Society, (1997) 209.

[13] K.A. Gschneidner Jr. and V.K. Pecharsky, Annu. Rev. Mater. Sci., **30** (2000) 387.

[14] K.A. Gschneidner Jr. and V.K. Pecharsky, ed D. Chandra and R.G. Bautista, Warrendale, PA: The Minerals, Metals and Materials Society, (2002) 9.

[15] G.V. Brown, J. Appl. Phys., **47** (1976) 3673.

[16] K.A. Gschneidner Jr. and V.K. Pecharsky, International Journal of Refrigeration, **31** (2008) 945.

[17] B. Yu, M. Liu, P.W. Egolf and A. Kitanovski, International Journal of Refrigeration, **33** (2010) 1029.

[18] K.A. Gschneidner Jr. and V.K. Pecharsky, Mater. Sci. Eng., **A287** (2000) 301.

[19] A.M. Tishin and Y.I. Spichkin, Condensed Matter Physics, IOP publishing, Bristol, Philadelphia, (2003).

[20] R. Burriel, L. Tocado, E. Palacios, T. Tohei and H. Wada, J. Magn. Magn. Mater. **715**, (2005) 290-291.

[21] K.A. Gschneidner Jr., V.K. Pecharsky, A.O. Pecharsky and C.B. Zimm, Mater. Sci. Forum, **69,** (1999), 315-317.

[22] L W Martin, S P Crane, Y-H Chu, M B Holcomb, M Gajek, M Huijben, C-H Yang, N

Balke and R Ramesh, J. Phys.: Condens. Matter, **20**, (2008), 434220.

[23] I. E. Dzyaloshinskii, Sov. Phys.–JETP **10**, (1960), 628.

[24] D. N. Asrov, Sov. Phys.–JETP, **11**, (1960), 708.

[25] M. Fiebig, J. Phys. D: Appl. Phys. **38**, (2005), R123.

[26] Y. Tokura, J. Magn. Magn. Mater. **310**, (2007), 1145.

[27] N. A. Spaldin and M. Fiebig, Science **309**, (2005), 391.

[28] W. Eerenstein, N. D. Mathur and J. F. Scott, NATURE **442**, (2006), 759.

[29] D. I. Khomskii, J. Magn. Magn. Mater. 306, (2006), 1

[30] S. W. Cheong and M. Mostovoy, Nat. Mater. **6**, (2007), 13.

[31] Y. Tokura, SCIENCE **312**, (2006), 1481.

[32] G. A. Smolenskiĭı and I. E. Chupis, Sov. Phy. Uspekhi **25**, (1982), 475.

[33] E. K. Salje Vol-1 (Cambridge University Press, Cambridge, 1993).

[34] H. L. Yakel, Jnr, W. C. Koehler, E. F. Bertaut, and E. F. Forrat.. Acta Crystallographica, **16(10),** (1963), 957–962.

[35] IG Ismailzade and SA Kizhaev. *FIZIKA TVERDOGO TELA*, **7**, (1965), 298–301.

[36] WC Koehler, HL Yakel, EO Wollan, and JW Cable. *Phys. Letters*, **9**, (1964).

[37] PW Anderson.. *Physical Review*, **79(2),** (1950), 350.

[38]. K. Momma *et al*., VESTA 3, J. Appl. Crystallogr., **44**, (2011), 1272.

[39]. X. Fabre ´ges, I. Mirebeau, P. Bonville, S. Petit, G. Lebras-Jasmin, A. Forget, G. Andre, and S. Pailhes,Physical Review B, **78**, (2008), 214422.

[40] Alexandra S. Gibbs, Kevin S. Knight, and Philip Lightfoot.*Phys. Rev. B*, **83**, (2011), 094111.

[41] Kazimierz ukaszewicz and Jarosawa Karut-Kaliciska. *Ferroelectrics*, **7(1),** (1974), 81–82.

[42]. M. Isobe *et al*., Structure of YbMnO3, Acta Crystallographica, **C47,** 423 (1991).

[43]. B. B. Van Aken, A. Meetsma and T. T. M. Palstra Acta Crystallographica, **E57**, (2001), i87.

[44]. Th. Lonkai, D. G. Tomuta, U. Amann, J. Ihringer, R. W. A. Hendrikx, D. M. Többens, and J. A. Mydosh, Physical Review B, **69**, (2004), 134108 .

[45]. F. Yen, C. dela Cruz, B. Lorenz, E. Galstyan, Y.Y. Sun, M. Gospodinov and C.W. Chu J. Mater. Res., **22**, (2007), 2163.

[46]. M. Fiebig, Th. Lottermoser and R. V. Pisarev, Journal of Applied Physics, **93**, (2003), 8194.

[47]. Josep Fontcuberta, Marin Gospodinov and Vassil Skumryev, Journal of Appied Physics,

**103**, (2008), 07B722.

[48]. M. C. Lin, Y. S. Chen, T. C. Han, J. G. Lin and C. H. Chen, Ferroelectrics, **380**, (2009), 38.

[49]. T. Katsufuji, S. Mori, M. Masaki, Y. Moritomo, N. Yamamoto, and H. Takagi , Physical Review B, **64**, (2001), 104419.

[50]. T. C. Han and J. G. Len, IEEE Transactions on Magnetics, **45**, (2009), 4265.

[51]. T. Takahashi, T. Yoshimura and N. Fujimura, Japanese Journal of Applied Physics **45**, (2006), 7329.

[52]. S. Kang *et al*., Journal of Korean ceramic society, **41**, (2004), 170.

[53]. N. Abramov, V. Chichkov, S. E. Lofland and Y. M. Mukovskii ,Journal of Applied Physics, **109**, (2011), 07D912.

[54]. S.L. Samal, T. Magdaleno, K.V. Ramanujachary, S.E. Lofland, A.K. Ganguli, Journal of Solid State Chemistry, **183**, (2010), 643.

[55]. Y. J. Wu *et al*., ceramics, **496,** (2010), 269.

[56] H. Sugie, N. Iwata, K. Kohn, J. Phys. Soc. Jpn., **71**, (2002), 1558

[57] S. Yu. Dan'kov, A.M. Tishin, V.K. Pecharsky and K.A. Gschneidner Jr., Phys. Rev. B, **57** (1998) 3478.

[58] S.A. Nikitin and A.S. Andreenko, Phys. Met. Metallogr., **52(1)** (1981) 55.

[59] S.A. Nikitin, A.S. Andreenko, A.M. Tishin, A.M. Arkharov and A.A. Zherdev, Phys. Met. Metallogr., **59(2)** (1985) 104.

[60] A. Smaïli and R. Chahine, J. Appl. Phys., 81 (1997) 824.

[61] C.B. Zimm, E.M. Ludeman, M.C. Severson and T.A. Herring, Adv. Cryog. Eng., **37B** (1992) 883.

[62] B.J. Korte, V.K. Pecharsky and K.A. Gschneidner Jr., Adv. Cryog. Eng., **43** (1998) 1737.

[63] K.A. Gschneidner Jr., V.K. Pecharsky and S.K. Malik, Adv. Cryog. Eng., **42** (1996) 475.

[64] A.A. Azhar, C.D. Mitescu, W.R. Johanson, C.B. Zimm and J.A. Barclay, J. Appl. Phys., **57** (1985) 3235.

[65] M.I. Ilyn, A.M. Tishin, V.K. Pecharsky, A.O. Pecharsky and K.A. Gschneidner Jr., CEC/ ICMC, Madison, (2001).

[66] V.K. Pecharsky and K.A. Gschneidner Jr., Cryocoolers, **10** (1999) 629.

[67] D. Wang, S. Huang, Z. Han, Z. Su, Y. Wang and Y. Du, Solid State Commun., **131** (2004) 97.

[68] A. Midya, S. N. Das, P. Mandal, S. Pandya and V. Ganesan, Phys. Rev. B., **84**, (2011) 235127.

[69] A. Midya, P. Mandal,S. Das, S. Banerjee, L. S. Sharath Chandra, V. Ganesan and S. Roy Barman, ,Appl. Phys. Lett. 2010, **96**, (2010), 142514.

[70] Mingjie Shao, Shixun Cao,Shujuan Yuan, Jin Shang, Baojuan Kang, Bo Lu, and Jincang ZhangAppl. Phys. Lett, **100**, (2012), 222404.

# Chapter 2

# Experimental Work

## 2.1 Introduction

In this chapter, the details is given of the synthesis, instruments used in the characterization of the samples in this thesis. Phase purity of samples is checked by using X-ray diffraction (XRD), while crystal structure, magnetic structure and magnetoelastic effect are determine using the Neutron powder diffraction (NPD) with variation of temperature. Physical Property Measurement System (PPMS) has been used to understand the magnetic and magnetocaloric properties. The present chapter gives a brief introduction of sample synthesis routes, X-ray powder diffraction, neutron diffraction and specific heat and also basics of Rietveld analysis.

## 2.2 Synthesis of $Yb_{1-x}A_xMnO_3$ (A = Mg, Ho, Sc, and Er) Samples by solid state reaction

All samples that are used in the present study prepared by conventional solid state synthesis methods. This technique have to make heating mixtures of two or more solids to a desired solid phase connection. In the present work we used high purity precursors in their oxide forms of $Yb_2O_3$ (Aldrich, purity > 99.9%), $MnCO_3$ (Aldrich, purity > 99.9%), MgO (Aldrich, purity > 99.9%), $Ho_2O_3$ (Aldrich, purity > 99.9%), $Sc_2O_3$ (Aldrich, purity > 99.9%) and $Er_2O_3$ (Aldrich, purity > 99.9%) as raw materials. These raw materials in proper stoichiometric ratio have been weighed exactly using an electronic balance. Then they are mixed in an agate mortar. An organic solvent such as acetone have been used to make better mixing of precursors. All Precursor except $MnCO_3$ are preheated to 500 °C for 5hrs before weighing to evaporate moisture. The weighed powders are mixed thoroughly using agate-motor to get homogeneity. The mixed powders are heated to 1250 °C for 15hrs and again 1300 °C for 15hrs in platinum crucibles. The heated powders are again ground and mixed thoroughly in agate-motor. The powders are pressed into pellets of diameter 10 mm and thickness 3 mm under uni-axial pressure of 750 MPa. Poly Vinyl Alcohol is used as binder in the preparation of pellets. Pressed pellets are sintered at 1400 °C for 24 hrs.

# 2.3. Sample characterization

## 2.3.1. X-ray powder diffraction

X-ray powder diffraction (XRPD) is a fast and good technique for the standard identification of phase and for crystal structure refinement. In laboratory systems, when high-speed electrons collide on a metal target like tungsten or cupper, which is connected to a high voltage transformer, kept within a sealed tube that is under vacuum, then X-rays are generated. The wavelength of the X-rays is generated characteristic of the metal target .The X-rays are collimated and directed onto the sample, which has been ground to a fine powder. The diffracted beam is detected and then processed electronically to give a count rate as a function of diffraction angle.

### 2.3.1.1 Principle

As the wavelengths of X-ray are of the order of inter planar spacing, they can be used to investigate the material structure by diffracting from the material. Let us consider a three dimensional simple atomic system where the atoms are arranged periodically in all dimensions shown in fig 2.1. When an x-rays impinge on a periodic structure, they get scattered and have certain phase relation between them. This phase relation leads to destructive or constructive interference. The condition for constructive interference in XRD is successfully given by W H Bragg and W L Bragg, famously known as Bragg's law in equation 2.1,

$$n\lambda = 2d_{hkl} \sin \theta_{hkl} \qquad (2.1)$$

where n is the order of reflection, λ is the wavelength of X –rays, $d_{hkl}$ is the inter-planar spacing of planes with Miller indices [h, k, l] and $\theta_{hkl}$ is the incident x-ray beam angle.

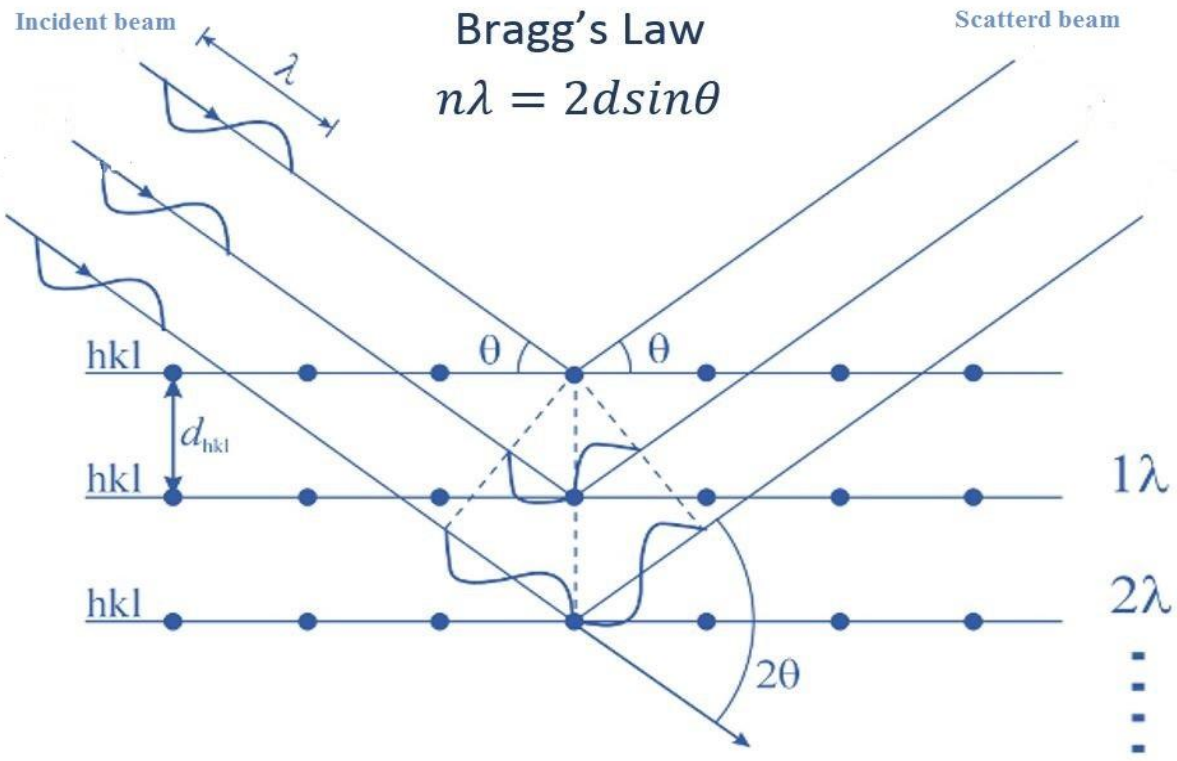


Figure. 2.1: Representation of the Braggs diffraction condition [2].

### 2.3.1.2 Experimental setup

In this study, the XRPD measurements were carried out using X'Pert PRO x-ray diffraction system from PAN analytical system and Bruker Model No. D8 Advanced diffractometer. The Bruker D8 diffractometer operates using Bragg-Brentano geometry, Cu Kα radiation and an energy-dispersive solid-state detector. XRD measurements were taken on powdered samples for both the routine phase analysis and for crystal structure refinement. The data were analyzed using the powder cell software. Structural Rietveld refinement were performed with the software package FULLPROF[3] on data taken with typical scans at a step size of 0.02 degrees (2θ) and a counting time of 5 seconds per step.

## 2.3.2 Neutron scattering

### 2.3.2.1 Theoretical background

X-ray and neutron scattering work are complementary techniques due to their different atomic scattering mechanisms. The interaction of atoms/ions in a material with X-rays and neutrons differ in many aspects and hence the diffraction patterns for a given material taken with X-rays and neutron differ considerably. Interaction of charge less neutrons with matter is short ranged and the neutrons penetrate deep into solids. Unlike the X-ray atomic scattering

factor which increases with atomic number as sown in fig 2.2 and 2.3, there is no general trend throughout the periodic table for the atomic scattering factor for neutrons, due to the complex nature of nuclear interactions. Also, neutron scattering depends on atomic nuclei, making the neutron scattering length to differ among different isotopes of the same element.

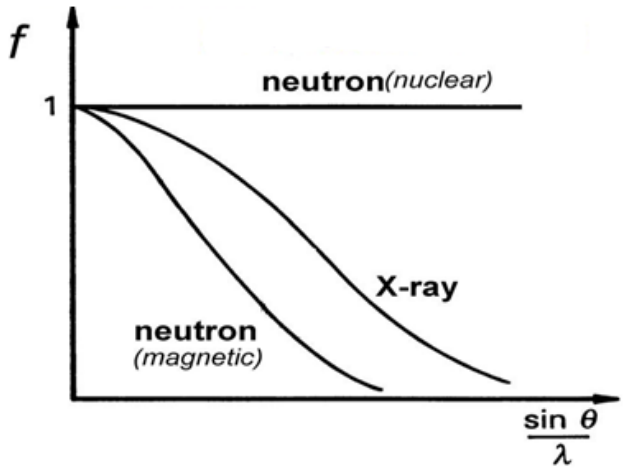


Fig. 2.2: The atomic form factor for x-ray, neutron (nuclear and magnetic) against angle.

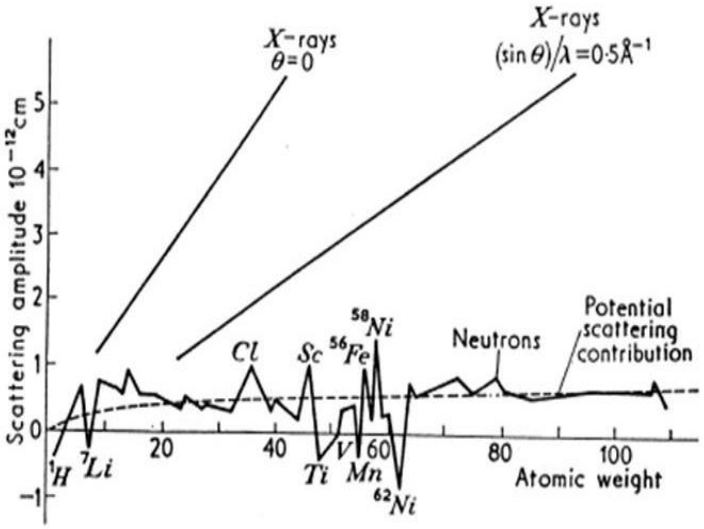


Figure.2.3: The neutron scattering amplitude versus atomic weight

The nuclear magnetic moment of the neutron can interact with the magnetic dipole moments associated with unpaired electron spins in magnetic samples. Hence, when a sample becomes

magnetic, new peaks can appear in the neutron diffraction pattern. The position and intensity of the magnetic Bragg peaks are related to the direction and strength of the magnetic moments. Hence neutron diffraction can be used to resolve the arrangement/ordering of the atomic magnetic moments in a magnetically ordered system.

Wave length λ associated with the wave nature of the neutron is given by

$$\lambda = \frac{h}{\sqrt{2mk_BT}} \qquad (2.2)$$

where h is the Planck's constant and m is the mass of the neutron. The wavelength λ corresponding to the temperature of T ≈ 300 K is nearly 2 A ˚, which is comparable to the average inter atomic distance in a solid. Therefore the thermal neutrons are suitable to determine both the atomic and magnetic structure of materials.

## 2.3.2.2 Neutron scattering theory

In a neutron scattering experiment a collimated (usually monochromatic) beam of neutrons is incident on a target sample, scatters through some interaction with the sample, and the energy spectrum of the scattered neutrons is measured using detectors in one or a range of directions.

We first consider a neutron with an initial wave vector $\boldsymbol{k}_i$ incident on a sample and which is then scattered by the sample into a state with a final wave vector $\boldsymbol{k}_f$. The angle between $\boldsymbol{k}_i$ and $\boldsymbol{k}_f$ through which the neutron is scattered is labelled $2\theta$.This event is shown in figure 2.4. The transfer of momentum to the sample is then $\hbar\boldsymbol{Q}$, where $\boldsymbol{Q}$ is known as the *scattering vector* and is defined as,

$$Q = k_i - k_f \qquad (2.3)$$

These three vectors ($\boldsymbol{k}_i$, $\boldsymbol{k}_f$, $\boldsymbol{Q}$) together form the scattering triangle, also shown in fig. 2.4. In an inelastic scattering event the neutron loses (or gains) energy during the process, and the energy transfer is given by

$$E_T = \hbar\omega = E_i - E_f = \frac{\hbar^2}{2m_n}(k_i^2 - k_f^2)\,, \qquad (2.4)$$

Where $E_i$ and $E_f$ are the initial and final energies of the neutron, and $m_n$ is the mass of the neutron.

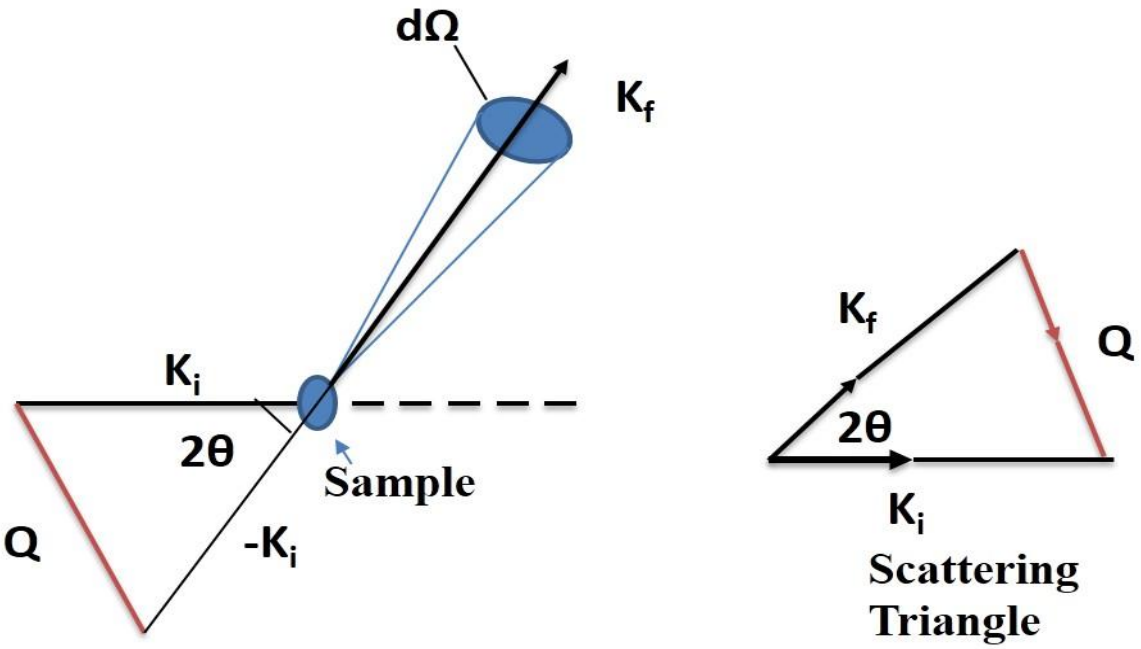


Figure..2.4: Schematic representation of a neutron scattering experiment. Incident neutrons with wave vector $\boldsymbol{k}_i$ are scattered into a final state $\boldsymbol{k}_f$ by the sample. The scattering triangle defines the scattering wave vector $\boldsymbol{Q} = \boldsymbol{k}_i - \boldsymbol{k}_f$. $d\Omega$ is the unit of solid angle subtended by the detector.

To characterize the interaction between a neutron and what it is scattering from, it is important to understand the concept of the scattering cross-section. There are three important cross-sections. The first is known as the total scattering cross section, defined as [4,7],

$$\sigma_{tot} = \frac{(total\ number\ of\ neutrons\ scattered\ per\ second\ in\ all\ directions)}{\emptyset_0} \qquad (2.5)$$

where $\Phi_0$ is the flux of the incident neutrons. It is useful to know the number of neutrons incident in a certain angular direction and this is characterised by the differential cross-section

$$\frac{d\sigma}{d\Omega} = \frac{(total\ number\ of\ neutrons\ scattered\ per\ second\ into\ d\Omega\ in\ the\ direction\ \theta,\emptyset)}{\emptyset d\Omega} \qquad (2.6)$$

where dΩ is the solid angle in the direction θ, φ, the spherical polar coordinates. This is the cross-section that is usually measured in elastic neutron scattering (where the neutron does not change energy during the scattering process). The final cross section takes into account the

energy of the scattered neutrons in a certain direction. This is called the partial differential cross-section,

$$\frac{d^2\sigma}{d\Omega dE_f} = \frac{(total\ number\ of\ neutrons\ scattered\ per\ second\ in\ the\ d\Omega\ in\ the\ direction\ \theta,\emptyset\ with\ energe\ E_f\ and\ E_f{+}dE_f)}{\emptyset d\Omega dE_f} \qquad (2.7)$$

Where $E_f$ is the final energy of the neutron after it has scattered. This cross-section is usually measured in inelastic neutron scattering, where the neutron does change energy during the scattering process. The calculation of these cross-sections is essential in the analysis of data from neutron scattering experiments and the theory of neutron scattering has accounted for these terms for every type of experiment.

Another important term in neutron scattering is known as the scattering length. A neutron is thought of as a plane wave with the wave function,

$$\varphi_i = e^{ikz} \qquad (2.8)$$

where the neutron's wavenumber k is related to its wavelength λ by $k = 2\pi/\lambda$. After the neutron interacts with a nucleus via the strong nuclear force, its wave function becomes a spherical wave in addition to the incident wave,

$$\varphi_f = -b\frac{e^{ikz}}{r} + e^{ikz} \qquad (2.9)$$

where r is the distance from the nucleus and b is the scattering length. There is a negative sign in this equation so that the majority of scattering lengths for the different elemental nuclei have a positive value of b. The scattering length cannot be calculated without a complete theory of the strong nuclear force, so it has to be determined empirically. If the scattering length is complex, this means the nucleus can absorb neutrons. It should be noted that different isotopes of the same element can have completely different values for b. This idea can be expanded to include magnetic scattering, which arises from the interaction between the magnetic moment of the neutron and the magnetic moment distribution of an unpaired electron, giving a magnetic scattering length.

### 2.3.2.3 Elastic nuclear neutron scattering

In elastic neutron scattering, $| k_i | = | k_f |$ and the scattering vector Q has to be equal to a reciprocal lattice vector of the sample, H for constructive interference in a perfect crystal. The reciprocal lattice vector is often defined in terms of the Miller indices h, k and l such that, $H = ha^* + kb^* + lc^*$, where $a^*$, $b^*$ and $c^*$ are the unit vectors of the reciprocal lattice. It can be shown that,

$$|Q| = 2|ki|\sin\theta \qquad (2.10)$$

Where $2\theta$ is the scattering angle. This is most commonly known as Bragg's Law and can also be expressed in the familiar form,

$$n\lambda = 2d \sin\theta \qquad (2.11)$$

where n is an integer, $\lambda$ is the neutron wavelength and d is the distance between two atomic layers in the material ($d = 2\pi/|Q|$).

The total cross-section for elastic scattering, of all types, can be expressed as a sum of the intensities,

$$\sigma = I_{nuclear} + I_{magnetic} + I_{interference} + I_{chiral} \qquad (2.12)$$

where the first term is the contribution from a lattice of nuclei, the second term is from the magnetic moment distribution in the lattice, the third term is the magnetic nuclear interference term and the final term is known as the chiral term, which is only non-zero for certain complicated magnetic structure, e.g. a helicoidally magnetic structure. The third and fourth terms are only relevant in polarized neutron scattering experiments and the third term will be discussed in a later section. The fourth term is outside the scope of this thesis as no chiral magnetic structures have been studied.

In equation 2.12, the nuclear term only refers to the coherent scattering from a nucleus and it is this term that is of interest in a measurement of the crystal structure of a material. The neutron can also scatter incoherently giving rise to an isotropic background in the data. For some nuclei the incoherent term can be very large giving a high background. One such example is vanadium, where the scattering is almost entirely incoherent, giving a nearly isotropic elastic scattering signal. This makes it useful for calibrating detectors.

Coherent elastic scattering in crystals only occurs when the scattering vector is equal to a reciprocal lattice vector, as this is the requirement for constructive interference in the scattering. The coherent nuclear elastic differential cross-section for a given scattering vector is,

$$\frac{d\sigma}{d\Omega} = N_0 \frac{(2\pi)^3}{V_0} \sum_H \delta(Q - H)|F_N(Q)|^2 \qquad (2.13)$$

where $N_0$ is the number of unit cells the neutrons interact with, $V_0$ is the volume of a unit cell and the nuclear structure factor,

$$F_N(Q) = \sum_j b_j \, e^{iQ.r_j} e^{-W_j(Q,T)} \qquad (2.14)$$

which sums over all the atoms j in the unit cell, with $r_j$ the position of atom j, $b_j$ the scattering length of atom j and $e^{-Wj(Q,T)}$ the Debye-Waller factor of the atom j. The Debye-Waller factor is a function of temperature and scattering vector and it takes into account the small thermal fluctuations in the position of an atom. The Debye-Waller factor represents the probability that the atom will be in its equilibrium position during the scattering process. Derivations and further
discussion on these equations is given in many books on neutron scattering [4-7].

## 2.3.2.4 Magnetic elastic scattering

The second term in equation 2.12 is due to the interaction of the magnetic moment of the neutron with the magnetic moment arising from unpaired electrons in the sample. Since the magnetic ions form a lattice superimposed on the nuclear lattice, there are a number of similarities between the two cross-sections. The main differences arises from the fact that the magnetic moment of an electron in a material has a large distribution of its scattering potential, unlike a nucleus which only scatters when the neutron is very close to it. Another difference is that a neutron only scatters from a magnetic moment when that moment is aligned perpendicular to the scattering vector Q. The differential cross-section for elastic magnetic scattering is written as,

$$\frac{d\sigma}{d\Omega} = N_m \frac{(2\pi)^3}{V_0} \sum_H \delta(Q - H)|F_{M\perp}(Q)|^2 \qquad (2.15)$$

where $N_m$ is the number of magnetic ions, $V_0$ the volume of the sample, the delta function is zero unless the scattering vector Q is equal to a reciprocal lattice vector of the magnetic lattice H and,

$$F_{M\perp} = \hat{Q} \times F_{M\times}\hat{Q} \qquad (2.16)$$

where $F_M$ is the magnetic structure factor, which in the dipole approximation is,

$$F_M(Q) = \gamma r_0 \sum_j f_j(Q)\mu_j \, e^{iQ.r_j} e^{-W_j(Q,T)} \qquad (2.17)$$

with $\gamma = 1.9132$ the gyromagnetic ratio, $r_0 = 2.8\times10^{-15}$m the classical radius of the electron and $\mu_j$ the magnetic moment of the $j^{th}$ ion. These two equations demonstrate that scattering from a magnetic ion only occurs when there is a component of the magnetic moment perpendicular to the scattering vector.

The magnetic structure factor is the Fourier transform of the magnetization density (M) in a unit cell.

$$F_M(Q) = \int M(r) e^{iQ.r}\, dr \qquad (2.18)$$

with the integral performed over the entire magnetic unit cell. This means that at Q = 0, F(0) = $\int M(r)\, dr$ the total magnetic moment of the unit cell.

## 2.3.2.5 High resolution powder neutron diffractometer

The neutron diffraction measurements presented in this thesis were carried out using Multi-PSD, high resolution neutron powder diffractometer at Dhruva Reactor, Mumbai, designed and developed [8] by UGC-DAE CSR Mumbai Centre, India(Fig. 2.5). The instrument employs open beam geometry doubly bent perfect and asymmetrically cut Si single crystal to enable high flux at the sample position and good resolution over wide scattering angular range. It is possible to change the wavelength of monochromatic beam by computer controlled goniometer within couple of minutes. The usable wavelengths on this instrument are 1.1 Å, 1.48 Å, 1.76Å & 2.31 Å. The standard wavelength is 1.48 Å. For all the neutron diffraction measurements reported in this thesis a wavelength of 1.48 Å was used.

The diffractometer is equipped with a cryogen free magnet (CFM) driven by closed cycle refrigerator (CCR). Using this CFM, neutron diffraction measurements can carried out at any

temperature from 1.6K to 300K and magnetic fields up to 7 Tesla. The neutron results presented in this thesis were measured using this CFM.

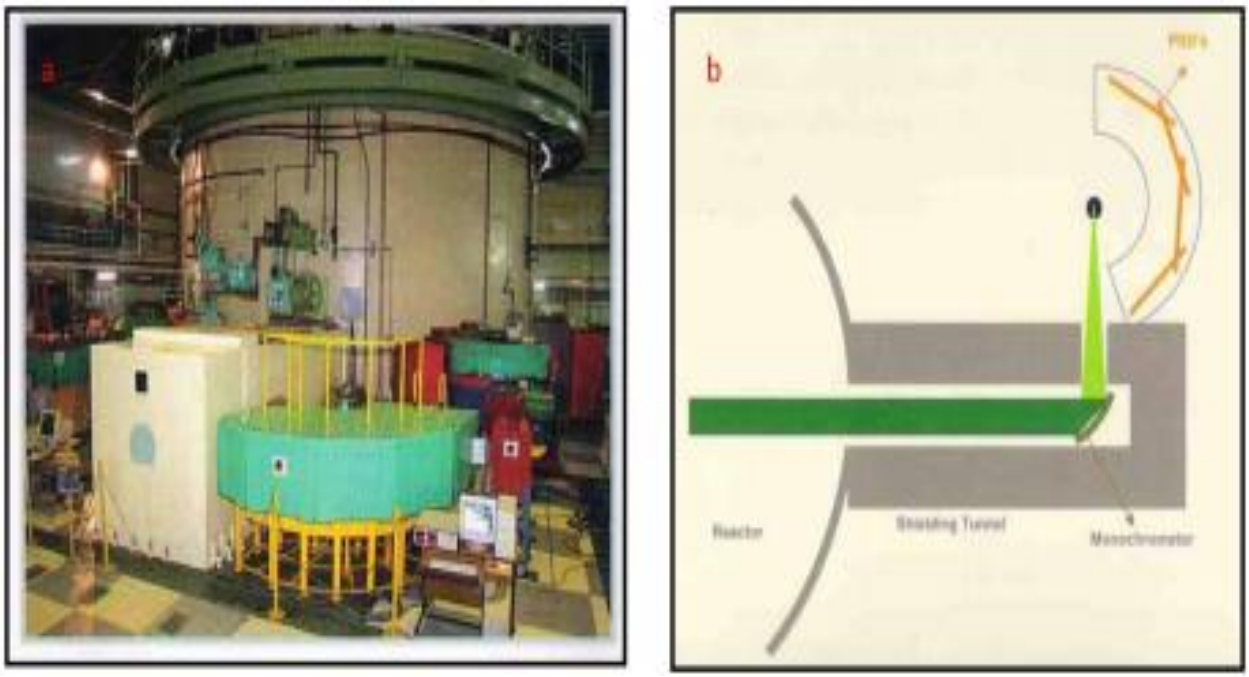


Fig. 2.5: a) Neutron diffraction facility at UGC-DAE CSR, Mumbai center. b) Schematic of neutron beam path from reactor to detectors [9].

The powder samples were filled with Vanadium sample holder, which then attached to sample holder that is inserted into the CFM. Sample is cooled by the Helium gas that is flowing through the sample chamber. This diffractometer is equipped with oscillating radial collimator (ORC) between the CFM and the detectors, which eliminates contamination from the CFM shrouds apart from reducing general background and improving S/N ratio.

## 2.3.3 The Rietveld Method

The Rietveld method, developed by Hugo Rietveld in middle 1960s [10], is used in the structure analysis. In Rietveld method integrated intensities (or structure factors) are extracted from the experimental data (or observed data). And this extracted data and all structural, instrumental parameters are refined by fitting a calculated profile to the observed data. The Rietveld method is used to refine the neutron/x-ray diffraction patterns and extensively used in the structural characterization of materials. The neutron/x-ray diffraction pattern of a power material have well defined peaks which reflect the lattice parameters, type and positions of constituent atoms of the material etc. In the Rietveld method, the expected diffraction profile

for the material is generated based on the initial/assumed material structural parameters (lattice parameters, atom type and atom positions of the material etc) and experimental parameters. Comparing with the experimentally measured diffraction profile, the model parameters are refined by least square method, to get the best match between the generated profile and the experimentally measured diffraction profile.

The profile functions used in this thesis are specified. The Gaussian function implies a normal distribution, and would be the expected peak shape for a perfect crystal with a single long-range ordering or only instrumental line broadening. The Lorentzian function implies homogeneous broadening by some physical mechanism. The combination of the two broadening mechanisms is a Voigt function, approximated to a Pseudo-Voigt for computational purposes. More complicated functions are possible, including those that allow for asymmetric line broadening. Peak broadening may also be due to strain in the sample, which can also be incorporated in the refinement model. The mathematical peak profile functions are,

Gaussian G(X) $$y = y_0 + \frac{A}{\omega\sqrt{\pi/2}} e^{-2\frac{(x-x_c)^2}{\omega^2}}$$

Lorentzian L(x) $$y = y_0 + \frac{2A}{\pi}\frac{w}{4(x-x_c)^2+w^2}$$

Pseudo-Voigt $$y = (1-\eta)G(x) + (\eta)L(x)$$

The peaks are described by the offset $y_0$, peak area A, peak centre $x_c$, full width half maximum w and mixing coefficient η. The FWHM w is related to the Gaussian width ω by $\omega = w/\sqrt{\ln(4)}$.

The least squares residual, S, which is to be minimized, is defined as,

$$S_y = \sum_K w_i\,(y_i - y_{ci})^2 \qquad (2.19)$$

Where $y_i$ is the observed intensity at the $i^{th}$ step of the diffraction pattern, $y_{ci}$ is the calculated intensity at the $i^{th}$ step and $w_i = 1/y_i$. is a weighting factor for the $i^{th}$ data point. The calculated intensity, $y_{ci}$ is determined using the following equation

$$y_{ci} = S\sum_K L_K|F_K|^2\,\emptyset(2\theta_i - 2\theta_k)P_K A + y_{bi} \qquad (2.20)$$

where $y_{bi}$ is the background intensity and 'S' is the scale factor. The letter K denotes a given Bragg reflection (h k l), $F_K$ is the structure factor of the $K^{th}$ Bragg reflection, $L_K$ contains the Lorentz polarization and multiplicity factors, $P_K$ is the preferential orientation function, $\phi$ is the reflection profile function and A is the absorption factor.

### 2.3.3.1 Agreement factors

In the Rietveld method the parameters are refined until the residual is minimized and the quality of the agreement between observed and calculated profile are defined through a set of R-values given as
[10].

$$R - Bragg\ factor, R_B = \frac{\sum|I_K(obs) - I_K(cal)|}{\sum I_K(obs)} \quad (2.21)$$

$$R_{wp} - Weighted\ pattern, R_{wp} = \left[\frac{\sum w_i(y_i - y_{ci})^2}{\sum w_i y_i^2}\right]^{1/2} \quad (2.22)$$

$$R - \ pattern, R_p = \frac{\sum_i |y_i - y_{ci}|}{\sum_i y_{ci}} \quad (2.23)$$

For n number of data points and m number of refined parameters, the expected profile value is,

$$R_{exp} = \left[\frac{(n-m)}{\sum w_i |y_{ci}|^2}\right]^{1/2} \quad (2.24)$$

Also the Goodness of fit defined as $\chi^2 = (R_{wp}/R_{exp})^2$. $\chi^2$ should converge to 1 for a good fit.

### 2.3.3.2Magnetic refinement

Several methods exist for the quantitative analysis of neutron diffraction data from magnetic systems. The most accurate method is that of representational theory, which a detailed symmetry analysis of the system is carried out. The method involves a high level of group theory, and hence has not been used in this thesis. Magnetic and nuclear structures are not usually refined simultaneously. Rather, the nuclear structure is refined at a temperature where the sample is paramagnetic or using X-ray data and then fixed during the refinement of the data taken in the magnetic regime.

## 2.3.4. Magnetic properties

### 2.3.4.1. Physical Property Measurement System (PPMS)

Magnetization, AC Susceptibility, DC resistivity and specific heat are carried out using PPMS-6000 with a maximum field of 9T (Quantum Design). The principle and operation of each technique will be discussed below [11].

### 2.3.4.2 Vibrating Sample Magnetometer (VSM)

The VSM option for the PPMS (Quantum design, U.S.A) consists essentially of a VSM vibrator assembly for vibrating the sample, suitable detection coil set and the associated electronics for driving the linear motor transport and detecting the response from the pickup coils. Magnetization changes of the order of $10^{-6}$ emu is able to resolve by the system. The measurement is based on the detection of the voltage induced on a pickup coil due to magnetic flux changes around the coil by the vibrating sample.

The time-dependent induced voltage is given by,

$$V_{Coil} = {}^{d\emptyset}/_{dt} = ({}^{d\emptyset}/_{dz})({}^{dz}/_{dt}) \qquad (2.25)$$

where Φ – is the magnetic flux enclosed by the pickup coil, *z* - vertical position of the sample with respect to the coil, and *t* - time. For a sample having DC magnetic moment m oscillating sinusoidally with amplitude of oscillation *A*, the voltage induced in the pickup coil is

$$V_{coil} = 2\pi fCmA\sin(2\pi ft) \qquad (2.26)$$

## 2.3.4.3 AC Measurement System (ACMS)

The ACMS option has the capability to be used both DC magnetometer or an AC susceptometer. The ACMS contains an AC-drive coil set that provides an alternating excitation field and a detection coil set that inductively responds to the combined sample moment and excitation field. The copper drive and detection coils are situated within the ACMS insert,

concentric with the superconducting DC magnet of the PPMS. The drive coil is wound longitudinally around the detection coil set. The field amplitude that can be applied depends on the frequency of the ac field and the temperature within the PPMS probe, but, at any temperature, the drive coil can generate alternating fields of up to ±10 Oe in a frequency range of 10 Hz to 10 kHz. Both the amplitude and phase of this response are reported. Alternatively, the ACMS can report the in-phase and quadrature components of the sample's response. The dynamic or ac susceptibility $\chi_{ac}$ = dM/dH, where dM is amplitude of change in magnetic moment and dH the amplitude of alternating field.

## 2.3.4.4 Specific heat measurement

The heat-pulse technique is a standard method for determining heat capacities and widely used by many researchers. The details of the measurements principle of this technique can be found elsewhere [12]. Heat capacity data can give information on lattice, electronic and magnetic properties of materials. Low temperature heat capacity measurements, well below the Debye temperature, give information on the electronic and magnetic energy levels of materials.

The PPMS heat capacity option measure the heat capacity at constant pressure

$$C_P = \left(\frac{dQ}{dT}\right)_P \qquad (2.27)$$

Though adiabatic process and relaxation methods are widely used to measure specific heat, it is very difficult to achieve perfect adiabatic conditions. Hence, quasi-adiabatic heat pulse technique is preferred. Using this, accurate and precise measurements are possible. Nevertheless, this method demands large sample mass. Hence, for the precise but less accurate with small amount of samples (~5-20 mg), relaxation technique is preferred. The required base temperature $T_b$ is stabilized prior to the applying heat pulse. By using heater, a heat of $Q_{in}$ is supplied continuously. Through the supporting wires, heat loss $Q_{loss}$ occurs. In order to minimize the heat leaks through the wires, the same wires are used for the sensors and heater. Then heat flow equation can be written as,

$$Q_{in} = C_p dT + Q_{loss} \qquad (2.28)$$

$Q'_{in} = dQ_{in}/dt = I^2R$ is the heat input per unit time; $C_p$ is the heat capacity of the platform + sample. $Q_{loss} = K(T-T_b)$ is loss of heat at a given time where K is the conductance of the

supporting wires. Assuming almost no changes in the resistance of heater wire and the conductance of the supporting wires for small changes in *T*, the heat flow equation can be re-written as

$$dT/dt + KT/C_p + (-KT_b/C_p - I^2R/C_p) = 0 \qquad (2.29)$$

After supplying heat to the plat form, platform temperature rises from $T_b$ to $T_b+\Delta T$. In the steady state condition, dT/dt=0, and hence heat supplied is equal to the heat loss which leads to the condition $I^2R = K\Delta T$. In this way K can be calculated.

From the differential equation 2.29, the solution for temperature at a given time is as follows

$$T(t) = T_b + \Delta T(1- \exp(-t/\tau)) \qquad \text{(heating cycle)}$$

$$T(t) = T_b + \Delta T\exp(-t/\tau) \qquad \text{(cooling cycle)}$$

Where $\tau = C_p/K$ is the relaxation time of the calorimeter.

This is called the single $\tau$ method. Generally $2\tau$ method is preferred over single $\tau$ method, where two relaxations are assumed. First one between the sample and the platform through grease and the other is between the platform and the surrounding.

For adiabatic conditions, $Q_{loss} = 0$, then $Q_{in}=C_pdT$ or $I^2R = C_pdT/dt$

Hence, $C_p = I^2Rdt/dT$

Specific heat measurement is carried out in the following manner. At first, specific heat of grease (Apizon-N) is measured. This is designated as an 'Addenda'. As a next step, the sample is mounted on the platform attached to grease which is used as a thermal link between the platform and the sample. Now, the total heat capacity of the sample+platform is measured at required temperatures. Then, the data of addenda is fitted over the measured temperature range. Now, the sample heat capacity is achieved by subtracting the addenda data from the total heat capacity at each temperature of interest.

## 2.4 References:

[1] B. D. Cullity, Elements of x-ray diffraction, Addison-Wesley publishing company, New York, USA, 1956.

[2] http://fys.kuleuven.be/iks/nvsf/experimental-facilities/x-ray-diffraction-2013- bruker-d8-discover

[3] Juan Rodríguez-Carvajal, *Physica B* **192**, (1993), 55.

[4] W. Marshall and S. W. Lovesey, Theory of thermal neutron scattering: the use of neutrons for the investigation of condensed matter (Clarendon Press, Oxford, 1971).

[5] G. E. Bacon, Neutron Diffraction (Clarendon Press, Oxford, 1975).

[6] Y. A. Izyumov, V. E. Naish and R. P. Ozerov, Neutron Diffraction of Magnetic Materials (Springer, New York, 1991).

[7] G. L. Squires, Introduction to the theory of thermal neutron scattering (Dover Publications, New York, 1996).

[8] V. Siruguri, P. D. Babu, M. Gupta, A. V. Pimpale and P. S. Goyal, Pramana, J. Phys.**71**,(2008), 1197-1201.

[9] National Facility for Neutron Beam Research, BARC technical broucher, edited by D. Sen, V. K. Aswal, R. Mukhopadhyay and S. L. Chaplot.

[10] E. Jansen, W. Schafer and G. Will, J. Appl. Crystallogr. **27**, (1994), 492.

[11] PPMS-6000 (Quantum Design) User's Manual Part Number 1081-400 C1.

[12] V.K. Pecharsky, J.O. Moorman and K.A. Gschneidner Jr., Rev. Sci. Instrum., **68** (1997) 4196.

# Chapter 3

## *Structural, magnetic, and neutron diffraction study of polycrystalline $Yb_{1-x}Mg_xMnO_3$*

## 3.1 Introduction

Materials in which the magnetic ordering can be controlled by electric field and vice-versa are called multiferroic. Such compounds have tremendous potential in practical applications such as spintronic. Rare-earth and yttrium manganites of general formula $RMnO_3$, crystallize in hexagonal structure for *R* with smaller ionic radius (*R* = Ho, Er, Tm, Yb, Lu, and Y) [1] or in orthorhombic structure for larger ionic radius (*R* = La, Ce, Pr, Nd, Sm, Eu, Gd, Tb, and Dy) [2]. Hexagonal $RMnO_3$ compounds are known to show simultaneously, ferroelectric as well as magnetic ordering in the ordered phase. The crystal structure of hexagonal manganites consists of $MnO_5$ polyhedra in which the $Mn^{3+}$ ion is surrounded by three oxygen ions in plane and two apical oxygen ions. The Mn ions with in Mn-O plane form a triangular lattice and are coupled in terms of spins through the antiferromagnetic (*AFM*) super exchange interaction. Due to the incomplete *AFM* coupling between neighboring Mn ions in the triangular lattice, the system forms a geometrically frustrated magnetic state [3-5].

In hexagonal compounds, because of the frustration of Mn spins, antiferromagnetic ordering takes place around 80 K while ferroelectric ordering takes place around 900 K. The Magneto-electric (ME) coupling is evidenced by observation of anomalies in the dielectric constant [6] or specific heat [7] at the magnetic transition temperature.

The detailed crystal structure [8] and magnetic structure [9] of $YbMnO_3$ were studied using neutron diffraction and Mössbauer spectroscopy [9]. Samal*et al*. have studied the magnetic, dielectric and ferroelectric properties of Fe doped $YbMnO_3$ [10]. They reported that the magnetic transition temperature increased from 82 K to 95 K and the ferroelectric loop became more lossy with increasing iron (Fe) content. The $Mn^{3+}$ moments get aligned in the *ab*-plane to produce antiferromagnetic order at ($T_{N1}$ = 85 K, the Neel temperature) while the Yb moments at the *4b* crystallographic site order due to the Mn molecular field [9]. Further, $Yb^{3+}$ moments at the *2a* crystallographic site show long range ordering through Yb-Yb interactions below $T_{N2}$ ~ 3.5 K [9,11]. Also, below $T_{N2}$ ~ 3.5 K, a magnetic field applied along the c-axis

induces magnetic transition at a critical field of H||c ~ 35 kOe [11] due to the spin flip/reorientation of the Yb(2a) moments [9].

Among rare earth manganites $YbMnO_3$ has been not so much studied. There have been many studies on the effect of substitution at Mn site of $YbMnO_3$, whereas we have concentrated on the Yb sites substitutions. This chapter describes the effects of the partial replacement $Yb^{3+}$ by $Mg^{2+}$ on the structural and magnetic properties of $YbMnO_3$. The interesting behavior of $YbMnO_3$ motivated us to study the magnetic structure and spin lattice coupling of $YbMnO_3$ and $Yb_{0.95}Mg_{0.05}MnO_3$ compounds using neutron diffraction as well.

## 3.2. Experimental

Polycrystalline samples of $Yb_{1-x}Mg_xMnO_3$ ($x$ = 0.00, 0.05 and 0.1) were prepared by the standard/conventional solid-state reaction method using high purity (purity better than 99.9%) $Yb_2O_3$, $MnCO_3$, and MgO powders. The high purity powders of $Yb_2O_3$, $MnCO_3$, and MgO were stoichiometrically weighed, thoroughly mixed and then calcined in air at 1200 $^0$C for 24 h. For better homogenization an intermediate grinding is done. After calcinations the mixture was cold pressed into pellets, sintered at 1450 $^0$C in air for 24 hours and slowly cooled to room temperature for sufficient oxygenation.

The phase purity was checked by the powder x-ray diffraction (*XRD*) taken on ground powder samples. Brüker D8 Advance *X-ray* powder diffractometer using Cu-Kα radiation was used for the powder Xrd measurements. In addition, the neutron-diffraction (ND) measurements were taken on powder samples at the UGC-DAE Consortium for Scientific Research at the National Facility for Neutron Beam Research NFNBR, Dhruva reactor, Mumbai, India [12]. The neutron-diffraction (ND) measurements were done with a neutron wavelength of 1.48 Å. Neutron diffraction (ND) measurements were performed at different temperatures between 2.5 K and 300 K. Temperature and magnetic field dependence of dc and ac susceptibility measurements were done a vibrating sample magnetometer (PPMS-VSM). Magnetization curves (M–H) measured at 2.5 K, 50 K and 100 K with applied magnetic fields up to 5T. All the magnetization measurements were performed on a vibrating sample magnetometer (PPMS-VSM) in the temperature range 2 to 300 *K* in 100 *Oe* applied *dc* magnetic field, in both zero field cooled (*ZFC*) field cooled (*FC*) state of the samples.

## 3.3 Results and Discussions

### 3.3.1 X-ray diffraction of $Yb_{1-x}Mg_xMnO_3$ (x = 0.00 and 0.05)

In Fig. 3.1 room temperature powder *XRD* patterns of $YbMnO_3$ and $Yb_{0.95}Mg_{0.05}MnO_3$ are shown. The samples studied here are single phase and the measured patterns can be indexed according to the hexagonal structure with $P6_3cm$ space group (JCPDS NO.38-1246) and refined using FULL PROF[13].

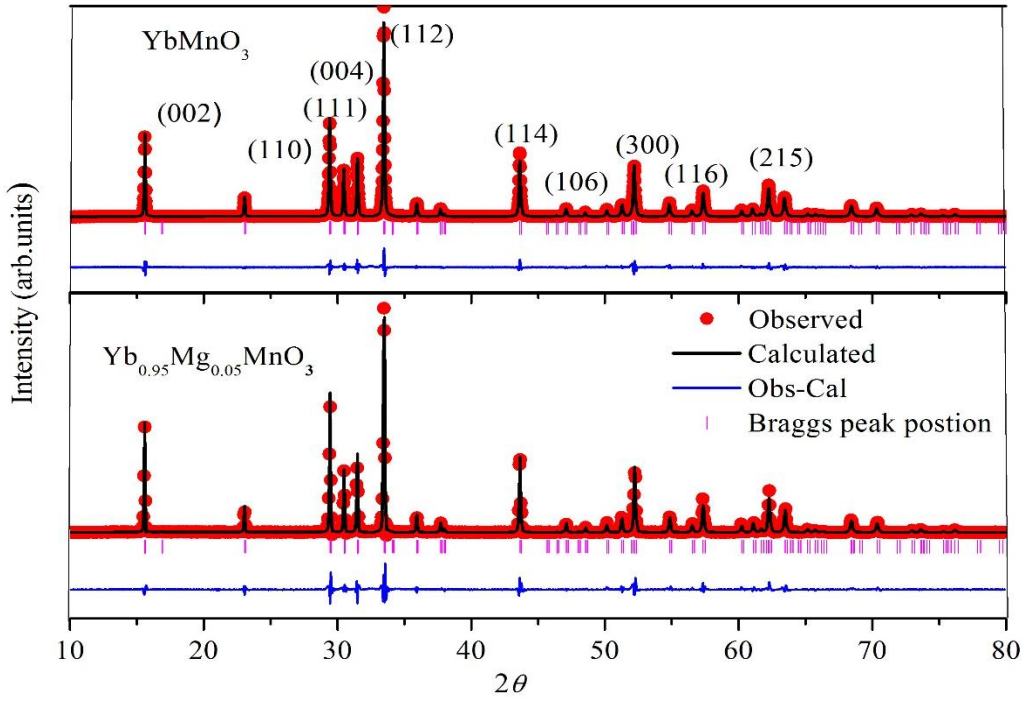


Figure.3.1: Rietveld refinement of room temperature X-Ray diffraction (XRD) data of $Yb_{1-x}Mg_xMnO_3$ ($x$ = 0.00 and 0.05) samples indexed in space group $P6_3cm$

The various obtained structural parameters and reasonable agreement factors are given in the Table 3.1.The lattice parameters and unit cell volume obtained from X-ray diffraction of $YbMnO_3$agrees with the earlier reported values [9]. Mg substitution results in decrease in cell parameters *a*, volume and cell parameter *c* increases for x = 0.05, which can be attributed to the difference in ionic radii of $Mg^{+2}$ (0.890 Å) and $Yb^{+3}$ (0.925 Å).In Table 3.2 shows magnesium substitution for ytterbium affects structural distortion which can be observed as changes in the Mn-O bond length Mn-O-Mn bond angles and distortion of $MnO_5$ polyhedron. Distortion in $MnO_5$due to substitution of Mg at A-site can be understood as: $Mn^{+3}$ (ionic radius

0.58 Å) changes to $Mn^{+4}$(ionic radius 0.53 Å), which is also smaller in size. Hence we can expect overall decrease in unit cell volume.

Table 3.1: Refined crystallographic parameters and reliability factors of$Yb_{1-x}Mg_xMnO_3$ ($x$ = 0.0 and 0.05) from XRD

| | $x$ = 0.0 | $x$ = 0.05 |
|---|---|---|
| $a$ (Å) | 6.0671 (4) | 6.0621 (4) |
| $c$ (Å) | 11.3519 (4) | 11.3558 (4) |
| $V$ (Å$^3$) | 361.886 (2) | 361.414 (2) |
| $R_P$ | 5.06 | 7.31 |
| $R_{wp}$ | 6.82 | 11.5 |
| Bragg $R$ Factor | 4.50 | 5.93 |
| $R_{exp}$ | 1.96 | 2.74 |

Table 3.2: Main bond distances (*A*˚) and angles (˚) for $MnO_5$ polyhedra of $Yb_{1-x}Mg_xMnO_3$ (*x* = 0.0 and 0.05) from XRD

| | *x* = 0.0 | *x* = 0.05 |
|---|---|---|
| Mn-O1 | 1.8532 | 1.8400 |
| Mn-O2 | 1.8366 | 1.7998 |
| Mn-O3 | 1.9033 | 1.9772 |
| Mn-O4 | 2.1017 | 2.0564 |
| <Mn-O> | 1.9237 | 1.9184 |
| $\Delta$ ($10^{-4}$) | 24.14 | 23.21 |
| Mn-O3-Mn 9 | 119.5 (7) | 118.7 (13) |
| Mn-O4-Mn | 118.6 (2) | 119 (2) |

## 3.3.2 Room temperature Neutron powder diffraction

In Fig. 3.2 the Rietveld refinement patterns of the neutron powder diffraction (*NPD*) data is shown for both *x* = 0.00 and 0.05 samples. The good agreement between observed (black scattered points) and calculated profile (red continuous line) is indicated by the difference line (blue color). Refined values of lattice parameters and discrepancy factors for $YbMnO_3$ and $Yb_{0.95}Mg_{0.05}MnO_3$ are shown in Table 3.3. The values obtained for x= 0.00 sample are in good agreement with those reported in the literature [9].

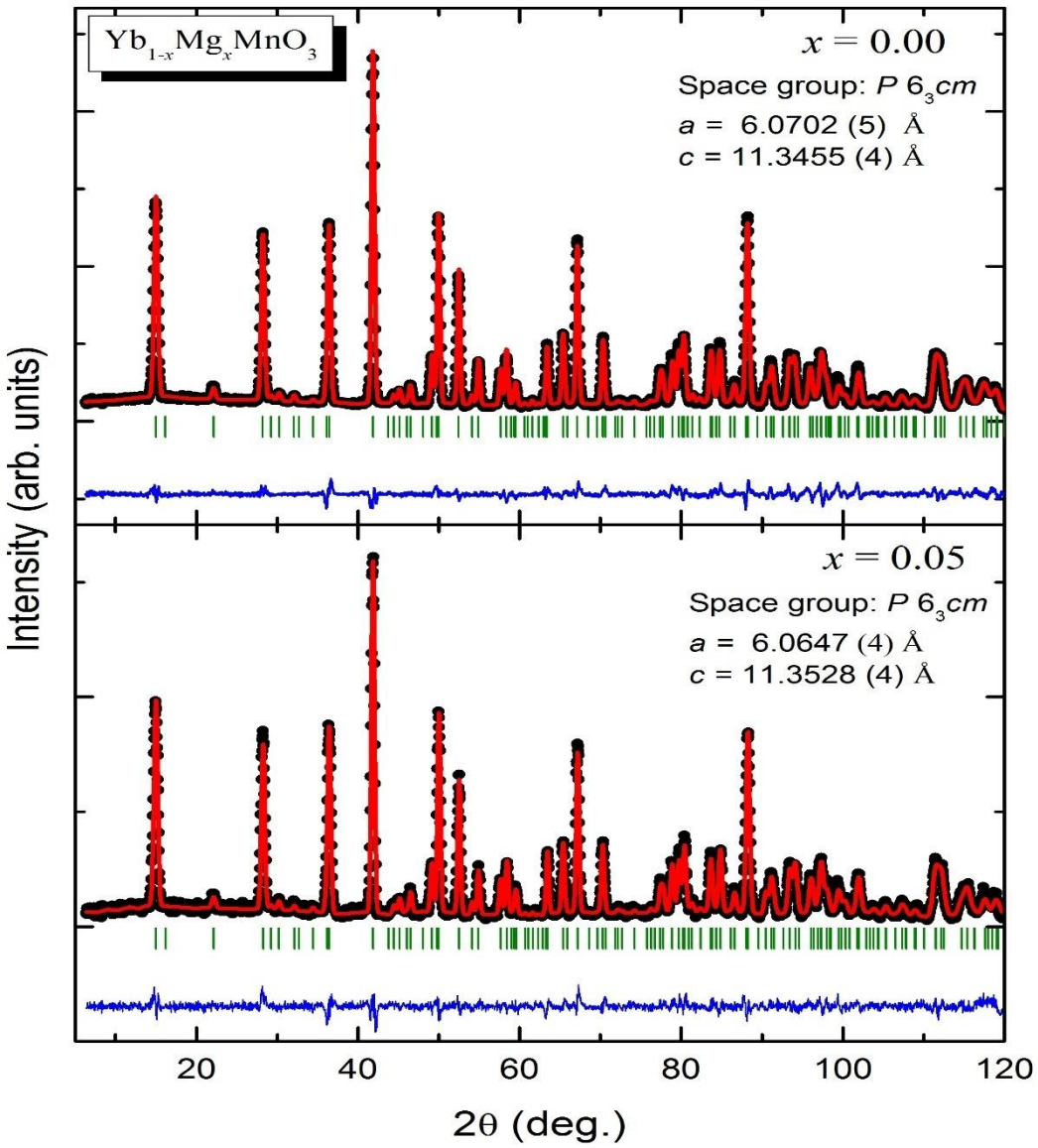


Figure.3.2: Rietveld refinement of room temperature neutron diffraction data of $YbMnO_3$ and $Yb_{0.95}Mg_{0.05}MnO_3$ samples.

From the values shown in the Table 3.3, it is clearly seen that due to Mg substitution, the cell parameters, *a* decreases marginally, whereas there is slight increase in *c*. Overall the cell volume decreases for x = 0.05 sample when compared to x = 0.00 sample. This decrease in cell volume can be ascribed to ionic size effects, since smaller $Mg^{2+}$ (Shannon ionic radii ~ 0.890Å) replaces a slightly bigger $Yb^{3+}$ (Shannon ionic radii ~ 0.925Å) ion. The observed decrease in cell volume shows that $Mg^{2+}$ does indeed replace $Yb^{3+}$ in the doped *x* = 0.05 sample. As the average *A*-site (i.e., Yb site) radius changes from *x* = 0.00 to 0.05, it is expected that the tolerance factor will also change. It is well known for manganites that the average *A*-site radius

plays a crucial role in maintaining the valence state(s) of Mn ions at B-site. Therefore, as the divalent Mg is substituted at $Yb^{3+}$ site, it will not only induce chemical pressure effect but also change the valence of Mn ions from $Mn^{3+}$ towards a mixed-valence state. Presence of $Mn^{4+}$ ion in $MnO_5$ polyhedra results in Jahn-Teller distortions and this also contributes to variations in lattice parameters, similar explanation was given by Jeuvrey*et al.,* for $YMn_{1-x}Cu_xO_3$compounds [14].

Table 3.3: Structural parameter after the Rietveld refinement of NPD for $YbMnO_3$ and $Yb_{0.95}Mg_{0.05}MnO_3$ at room temperature.

| **$Yb_{1-x}Mg_xMnO_3$** | $x$ = 0.00 | $x$ = 0.05 |
|---|---|---|
| $a$ (Å) | 6.0702(5) | 6.0647(4) |
| $c$ (Å) | 11.3455(4) | 11.3528(4) |
| $V$ (Å$^3$) | 362.052(2) | 361.869(2) |
| $\chi^2$ | 3.32 | 4.03 |
| $R_P$ | 5.51 | 9.21 |
| $R_{wp}$ | 7.25 | 12.6 |
| $R_B$ | 4.45 | 4.73 |
| $t$ (Å) | 0.8315 | 0.8334 |

*'t' is the tolerance factor (given as: $t=r_{Yb}+r_o/2^{1/2}(r_{Mn}+r_o)$).*

Some selected bond distances of Yb-O and Mn-O for x = 0.00 and 0.05 samples are listed in the table 3.4. The value of *a* decrease in Mg doped sample when compared to that in pristine sample. This change is ascribed to the decrease in the average ab-plane i.e Mn-O3 and Mn-O4 bond lengths. The Mn-O1 and Mn-O2 bond lengths are along the c-axis, and exhibit minor change on doping. The average Mn-O distance in $MnO_5$ units are significantly shorter in doped sample compared to pure $YbMnO_3$.

Table 3.4: Selected bond distances and bond angles for$YbMnO_3$ and $Yb_{0.95}Mg_{0.05}MnO_3$.

| **Parameter** | **x = 0.00** | **x = 0.05** |
|---|---|---|
| Mn-O1 | 1.8582 | 1.8892 |
| Mn-O2 | 1.8823 | 1.8746 |
| Mn-O3 | 1.9647 | 1.9816 |
| Mn-O4(x 2) | 2.0752 | 2.0675 |
| <Mn-O> | 1.9451 | 1.9532 |
| ∑Radii | 1.96 | 1.96 |
| Yb1-O1(x 3) | 2.2726 | 2.2436 |
| Yb1-O2(x 3) | 2.3029 | 2.2190 |
| Yb1-O3 | 2.370 | 2.4110 |
| Yb2-O1(x 3) | 2.2473 | 2.2795 |
| Yb2-O2(x 3) | 2.2581 | 2.2641 |
| Yb2-O4 | 2.3713 | 2.3692 |
| <Yb1-O1, O2> | 2.2877 | 2.2313 |
| <Yb2-O1, O2> | 2.2527 | 2.2718 |
| <Yb-O> | 2.3223 | 2.319 |
| ∑Radii | 2.305 | 2.305 |
| Mn-O3-Mn (°) | 119.345(2) | 119.894(3) |
| Mn-O4-Mn (°) | 118.248(2) | 117.665(3) |
| $\Delta(10^{-4})$ | 19.08 | 15.77 |

*$\Delta$ is the distortion of $MnO_5$ polyhedra.*

It is expected that the $MnO_5$ polyhedra will play important role in the magnetic properties observed in the both samples. Mn-O bond lengths are in agreement with the sum of the ionic radii [15]. Moreover, in the $YbO_7$ polyhedron, the Yb-O distance are larger in x = 0.00 sample than x = 0.05 sample, as expected due to the larger ionic radius of $Yb^{3+}$ when compared to $Mg^{2+}$. Also, the average Yb-O distance are close to the sum of the ionic radii.

## 3.3.3 Magnetic properties

### 3.3.3.1 Dc Magnetic susceptibility

The effect of Mg doping in $YbMnO_3$ have been observed in magnetization measurements also. Fig. 3.3 shows temperature dependence of dc magnetic susceptibility ($\chi$ = M/H)) of $Yb_{1-x}Mg_xMnO_3$ (x = 0.00 and 0.05) samples in zero field cooled (ZFC) and field cooled (FC) state of the sample, and in an applied field of 100 Oe, however, around 200 *K* there is a deviation from the Curie-Weiss behavior. At low temperatures, around 10*K*, there is a sudden rise in$\chi$, as if the samples are undergoing ferromagnetic ordering. The ferromagnetic ordering has been attributed to the ordering in the $Yb^{3+}$ sub-lattice [9]. On further decreasing temperature, $\chi_{ZFC}$(T) for both *x* = 0.00 and 0.05 samples exhibits another peak around 3 *K*, and bifurcation between ZFC and FC curves. This bifurcation is believed to arise due to competition between ferromagnetic and anti-ferromagnetic sub-lattice in the presence of the field.

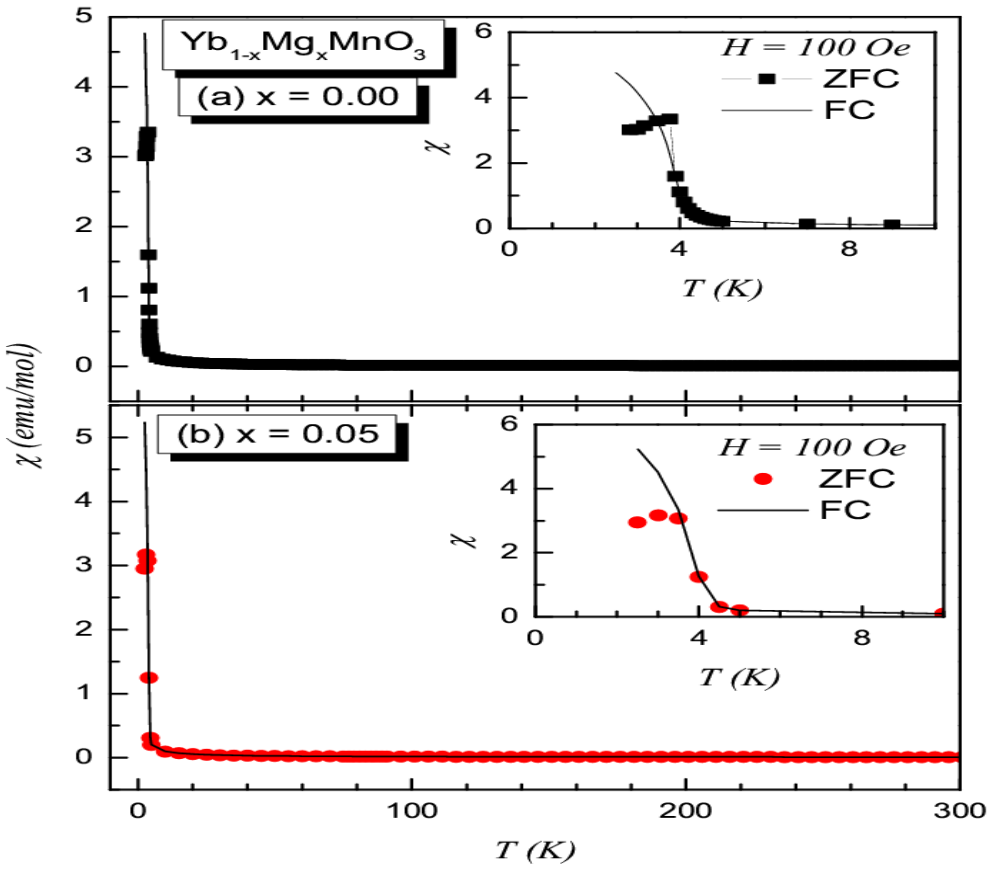


Figure.3.3: Temperature dependence of the DC susceptibility of the samples (a) $YbMnO_3$ and (b) $Yb_{0.95}Mg_{0.05}MnO_3$ with ZFC/FC mode. The inset shows low temperature behaviors of the samples with ZFC & FC mode.

It is difficult to figure out any long-range magnetic order in the plot of $\chi(T)$. The magnetization data of our polycrystalline sample agrees well with the single-crystal data of $YbMnO_3$ measured along the ab-plane [16]. Therefore, we use the first derivate of the $\chi(T)$ curves (see Fig.3.4) for both samples to find out the temperature at which antiferromagnetic ordering sets in. As shown in the figure, anomaly is observed around 85 *K* in $x = 0.00$ sample, while in the case of $x = 0.05$, the $T_N$ increases to 89 *K*. The ordering in both the compounds may be due to a canted spin ordering of the $Mn^{3+}$ ions [17]. The increase in $T_N$ for $x = 0.05$ sample can be explained on the basis of smaller cell volume, which might lead to strong exchange interactions and therefore higher ordering temperatures [9].

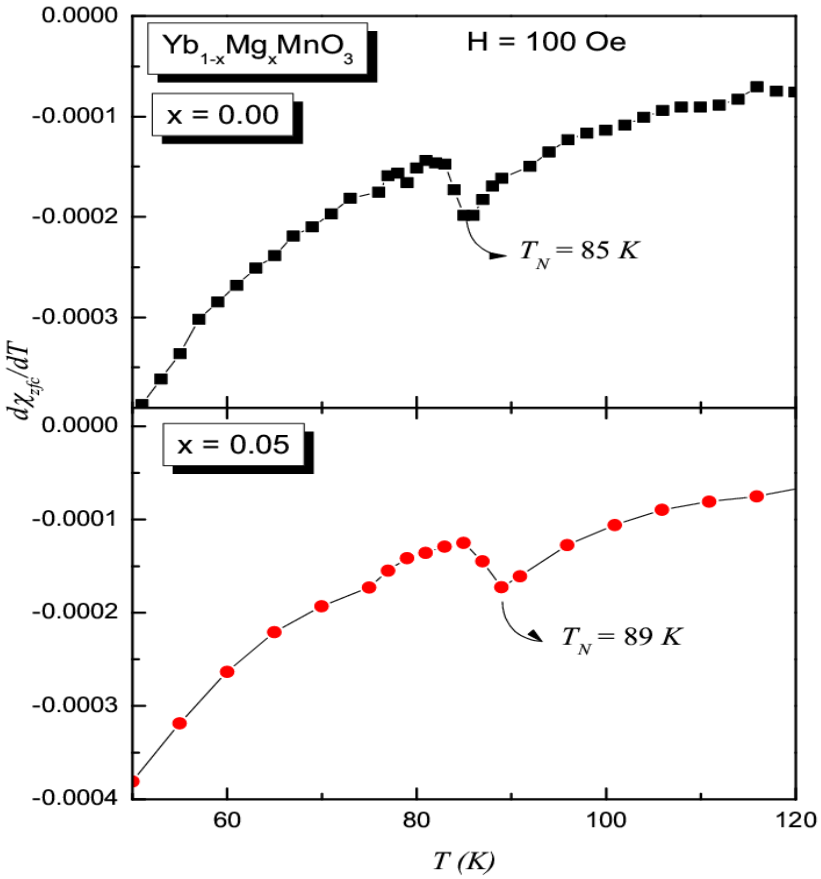


Figure.3.4: dχ/dT as function of temperature of the samples $YbMnO_3$ and $Yb_{0.95}Mg_{0.05}MnO_3$ with ZFC mode.

The plot of inverse magnetic susceptibility is shown in Fig. 3.5. The inverse susceptibility data exhibits linear behavior above 200 *K*, and can be fitted by using the Curie-Weiss law $\chi = C/T-\theta_p$. The paramagnetic Curie temperature ($\theta_p$) and effective magnetic moment ($\mu_{eff}$) are calculated from the Curie-Weiss fit. The values of $\theta_p$ obtained for $x = 0.00$ and 0.05 samples are -219 *K* and -182 *K*, respectively. The value of $\theta_p$ for $x = 0.00$ sample is in good

agreement with the reported values [9]. The negative $\theta_p$ implies predominant antiferromagnetic interactions.

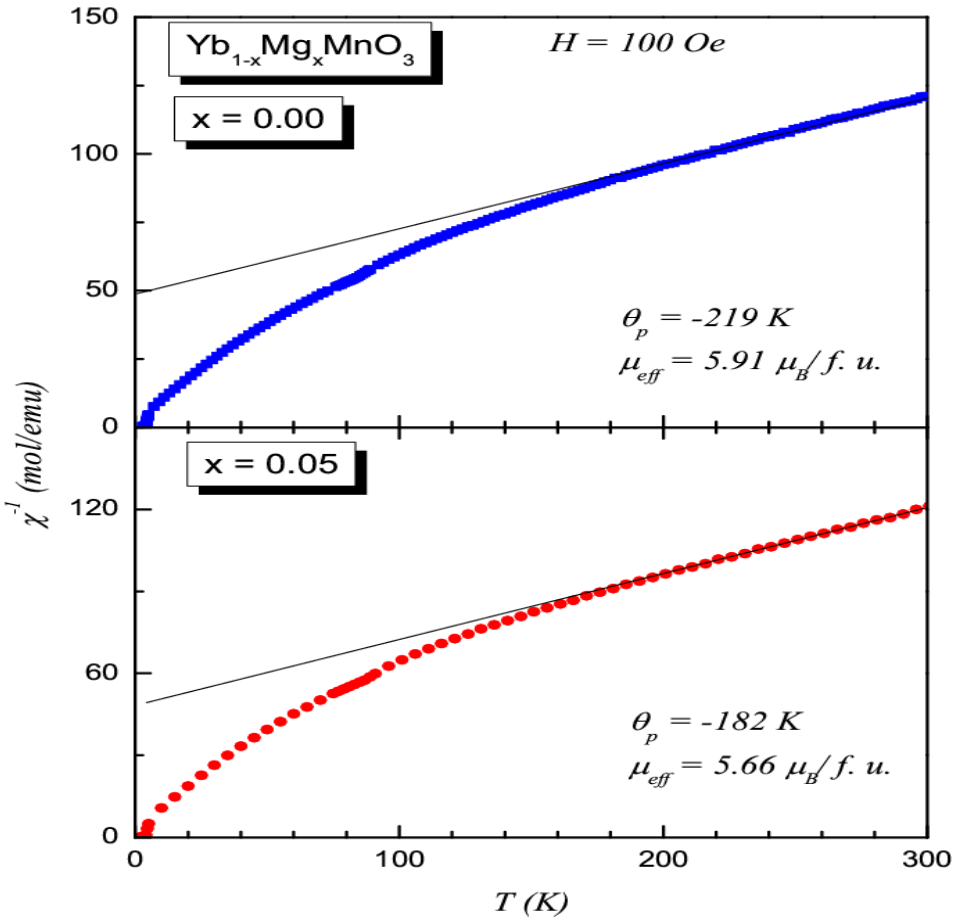


Figure.3.5: Inverse magnetic susceptibility of $YbMnO_3$ and $Yb_{0.95}Mg_{0.05}MnO_3$ with Curie-Weiss fit.

. The frustration factor *f*, defined as $|\theta_p|/T_N$ was calculated for both the compounds. The value of *f* for *x* =0.00 and 0.05 sample are 2.58 and 2.04, respectively. *f* decides the frustration of Mn spins in triangular lattice and it is slightly decreased for *x* = 0.05 sample. The effective moment $\mu_{eff}$ is 5.91$\mu_B$ ($\mu_B$ is Bohr magneton) for $YbMnO_3$ which is close to the value 6.1 $\mu_B$ reported by Fabreges *et al.*[9]. In case of the x = 0.05 sample, the observed value of $\mu_{eff}$ is 5.66$\mu_B$ for $Yb_{0.95}Mg_{0.05}MnO_3$ obtained from the equation $\mu_{eff} = (7.99C)^{0.5}$, where C is Curie-Weiss constant. Since Mg is nonmagnetic, a decrease in the magnetic moment is expected.

### 3.3.3.2 A.C magnetic susceptibility

The temperature variations of real part of $\chi_{ac}$ ($\chi'$) and its dependence on frequency for $Yb_{1-x}Mg_xMnO_3$(x = 0.00 and 0.05) samples are shown in Fig.3.6.The purpose of these measurements is to investigate, if there is any spin glass behavior in these compounds. A similar behavior is noticed for 17 Hz and 71 Hz, that is no dependence on frequency, which we take as indicative that there is no spin glass behavior. We also observe a sudden increase in $\chi'$ at low temperatures which is suggested due to ordering of $Yb^{+3}$sublattice.

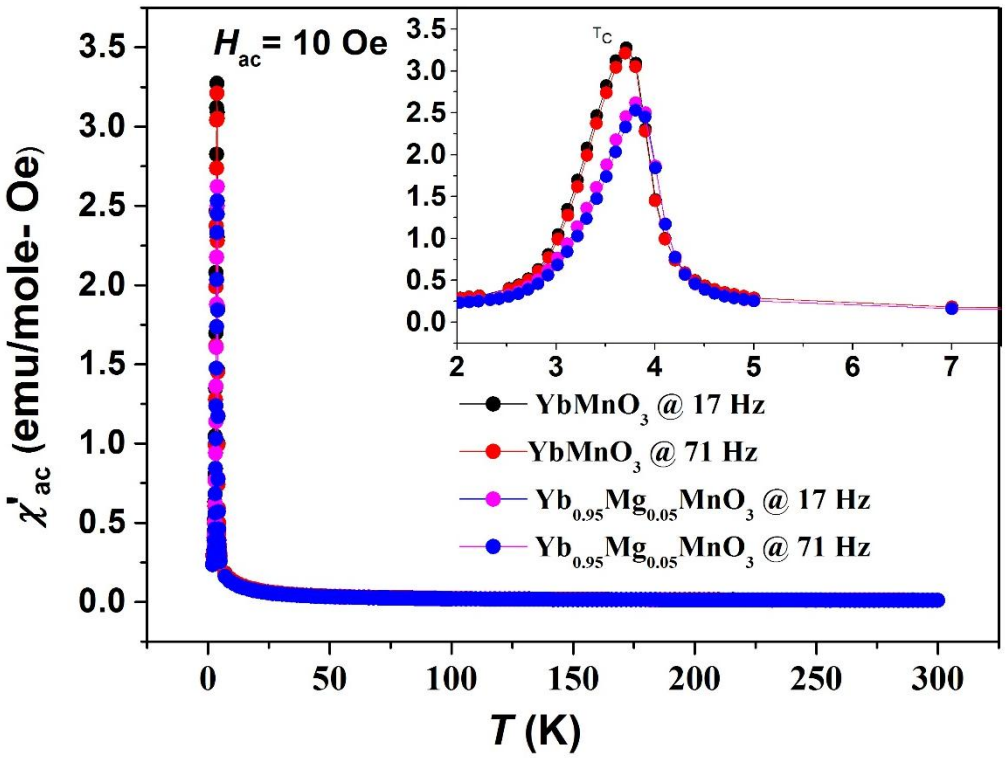


Figure. 3.6: Real part of a.c Susceptibility ($\chi'_{ac}$) of $Yb_{1-x}Mg_xMnO_3$ ($x$ = 0.00 and 0.05) samples at frequencies 17 Hz and 71 Hz. Inset shows low temperature behavior

### 3.3.3.3 M – H Analysis

Fig. 3.7 shows the *M* vs. *H* behavior of $Yb_{1-x}Mg_xMnO_3$(x= 0.00 and 0.05) samples. *M* versus *H* plot obtained at 100 K, which is above $T_N$ of both samples, is linear indicating the paramagnetic behavior of these samples and at a temperature of 50 K, which is below $T_N$, is non-linear indicating the antiferromagnetic nature. However, the *M* versus *H* plot obtained at 2.5 K exhibits hysteresis with no saturation magnetization up to 5T, as shown in inset Fig. 3.7.We can see that the magnetization has decreased for $Yb_{0.95}Mg_{0.05}MnO_3$compared to that of

$YbMnO_3$and is attributed to the doping of non-magnetic $Mg^{+2}$ion into magnetic lattice and the change in $Mn^{+3}/Mn^{+4}$ions. The decrease in total magnetization, when the temperature is increased from 2.5 K to 50 K, indicates a reduced contribution from $Yb^{+3}$sub-lattices. At 100 K total magnetization is lower than the values obtained at 50 K and 2.5 K, because as temperature rises thermal fluctuations on spins dominate and hence over all contribution to magnetization is decreased. The clear picture of hysteresis and is due to the ferromagnetic like ordering of the $Yb^{+3}$sublattices shown in inset fig3 [9]. From Fig. 3.7 we can see a step like increase in magnetization taken at 2.5 K, which we speculate due to the rotation of $Yb^{+3}$spins.

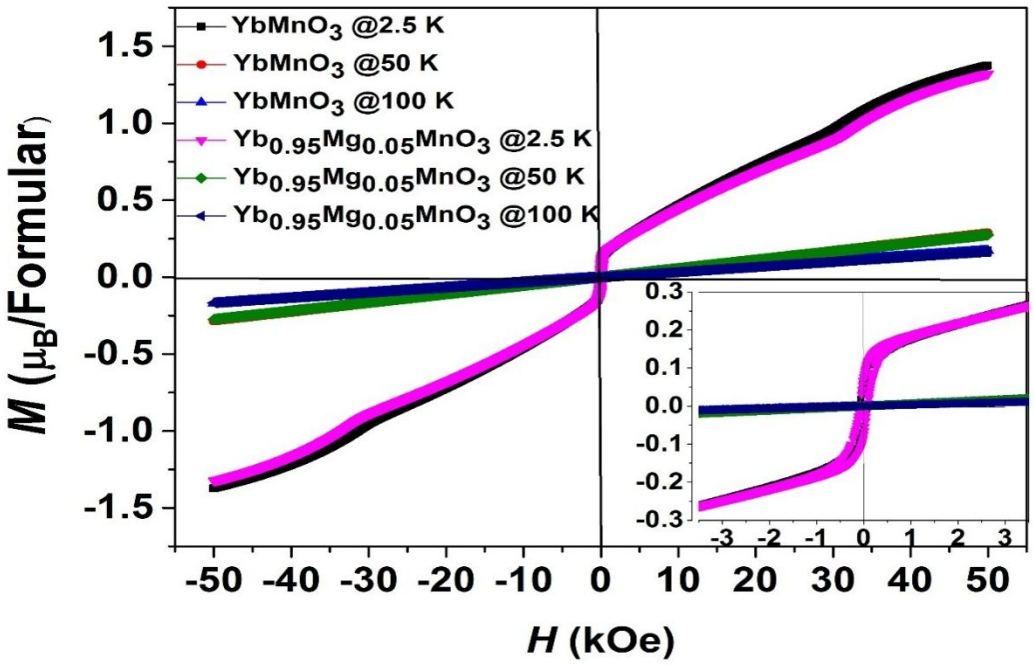


Figure 3.7: Magnetic-field dependence of the magnetization for $Yb_{1-x}Mg_xMnO_3$ ($x$ = 0.00 and 0.05) at different temperatures.

## 3.3.4 Low temperature neutron diffraction analysis

We have performed ND measurements of $Yb_{1-x}Mg_xMnO_3$ (x = 0.00 and 0.05) at a series of temperatures near the Mn ordering temperature and at room temperature with incident neutron wavelength λ = 1.48 Å. In above section 3.3.2, room temperature ND results that show subtle structural changes in parameters like cell volume, bond lengths and angles and polyhedral distortions in these samples. The nuclear structure peaks can be described by a single phase with space group $P6_3cm$ at all temperatures. The temperature variation of the ND patterns is shown in Fig. 3.8(a). The figure shows that the intensity of the (102) and (101) Bragg positions increases below $T_{N1}$ ~ 85 K and the intensity of (100) Bragg position increases below

$T_{N2}$ ~ 3.5 K, where the nuclear reflections are forbidden by the $P6_3cm$ symmetry. The temperature variations of the integrated intensities of typical Bragg peaks (100), (101), and (102) are shown in Fig. 3.8(b).

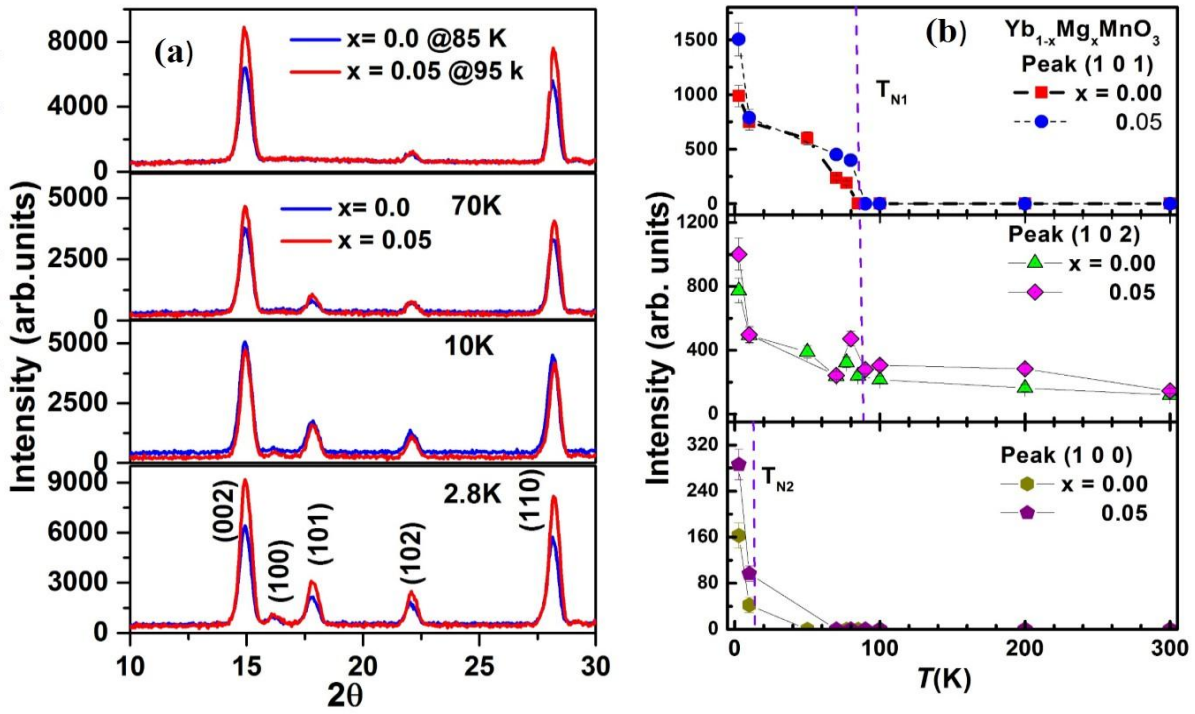


Figure.3.8: (a) Neutron diffraction patterns (b) Integrated intensities of the (100), (101), and (102) reflections between 2.8 K and 100 K of $Yb_{1-x}Mg_xMnO_3$ (x = 0.0 and 0.05).

Strong changes occur in the integrated intensities of these Bragg peaks around antiferromagnetic transition $T_{N1}$~ 85 K and ferromagnetic transition $T_{N2}$ ~ 3.5 K which correspond to the long range magnetic ordering of Mn and Yb ions, respectively. It is further observed that the intensity onset/start of corresponding Bragg peaks intensity slightly shift to higher temperature for x = 0.05 sample. The (100) and (101) Bragg peaks differ slightly from each other for temperature dependences. The (101) peak intensity rises abruptly below 85 K while the (100) peak intensity remains rather weak down to about 10 K then suddenly increases below 10 K. The observed temperature dependences suggest that the (101) and (100) peak intensities are controlled by the Mn and Yb orderings, respectively, while the (102) Bragg peak seems to have contributions from both orderings [9]. The observed temperature dependences of the (101) peak in $YbMnO_3$ is similar to that of the (100) peak in $YMnO_3$ [3, 5], whereas the Mn order does not induce a strong (101) magnetic peak in $YMnO_3$ which indicates that the Mn order is affected by the nature of the R ion.

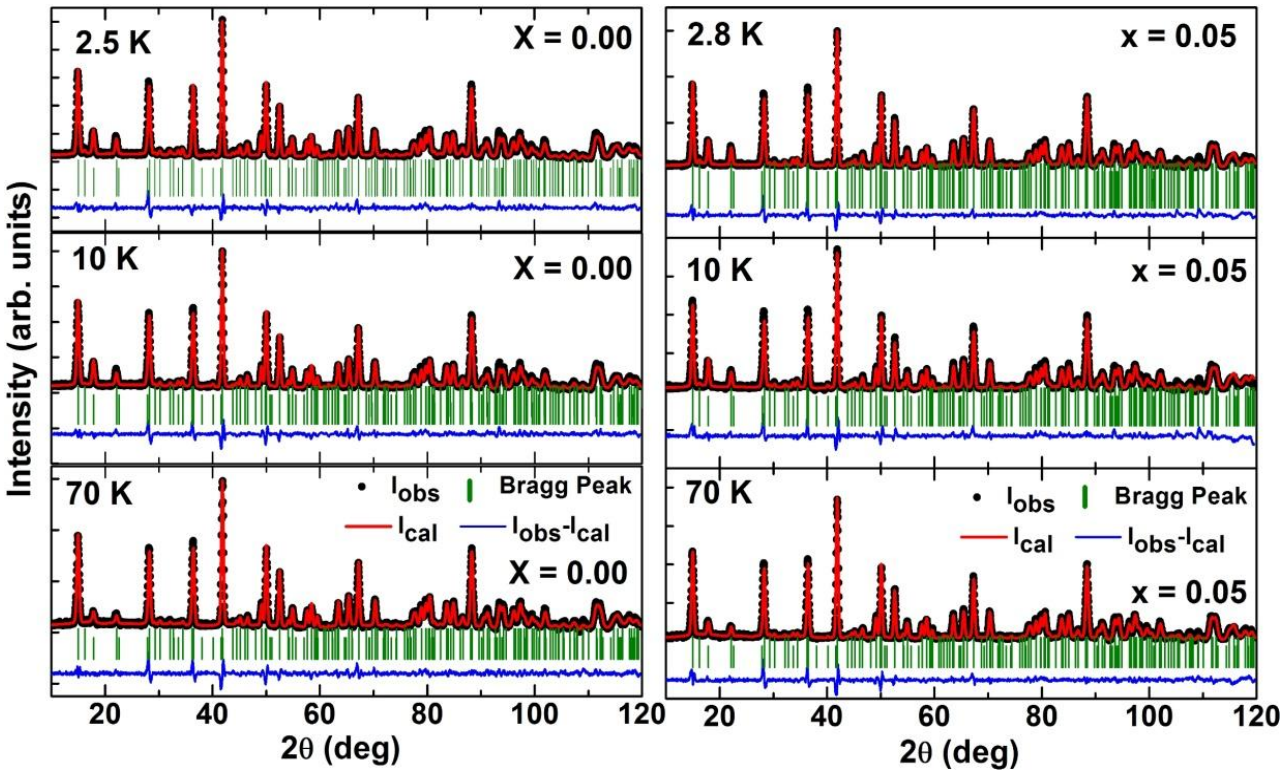


Figure.3.9: Rietveld refinement of temperature dependent ND data of $Yb_{1-x}Mg_xMnO_3$ (x = 0.00 and 0.05) at 2.5 K,10 K and 70 K.

Table.3.5: Atomic positions after Rietveld refinement of temperature dependent neutron diffraction

| **Atom (Wyckoff position)** | **$YbMnO_3$** | | | | **$Yb_{0.95}Mg_{0.05}MnO_3$** | | | |
|---|---|---|---|---|---|---|---|---|
| | **2.8 K** | **10 K** | **70 K** | **300 K** | **2.8 K** | **10 K** | **70 K** | **300 K** |
| Yb1/Mg 2(a) (0, 0, z) Z | 0.27642 | 0.27363 | 0.28158 | 0.27988 | 0.28015 | 0.28007 | 0.27763 | 0.28209 |
| Yb2 4(b) (1/3, 2/3, z) Z | 0.23378 | 0.23162 | 0.23424 | 0.23382 | 0.23502 | 0.23487 | 0.23399 | 0.23504 |
| Mn1/Mn2 6(c) (x, 0, 0) X | 0.33545 | 0.33795 | 0.33639 | 0.32581 | 0.33647 | 0.341 | 0.33251 | 0.32896 |
| O1 4(c) (x, 0, z) X | 0.31127 | 0.30871 | 0.30951 | 0.30693 | 0.30985 | 0.30562 | 0.30431 | 0.30329 |
| Z | 0.1651 | 0.16496 | 0.16489 | 0.16257 | 0.16404 | 0.16846 | 0.16741 | 0.16467 |
| O2 4(c) (x, 0, z) X | 0.63925 | 0.63792 | 0.63853 | 0.64225 | 0.63952 | 0.6456 | 0.64307 | 0.64732 |
| Z | 0.33257 | 0.33311 | 0.33209 | 0.33297 | 0.33265 | 0.33306 | 0.33431 | 0.33074 |
| O3 2(a) (0, 0, z) Z | 0.47583 | 0.47189 | 0.48239 | 0.48702 | 0.47385 | 0.47169 | 0.48899 | 0.49534 |
| O4 4(b) (1/3, 2/3, z) Z | 0.02241 | 0.02133 | 0.02478 | 0.02513 | 0.0216 | 0.02486 | 0.02883 | 0.02835 |
| Bragg R-factor | 5.85 | 6.28 | 7.16 | 6.23 | 6.73 | 9.47 | 7.47 | 8.19 |
| Rf- factor | 4.57 | 5.16 | 5.59 | 5.91 | 5.11 | 7.70 | 5.27 | 5.08 |

Figure 3.9 shows Rietveld refinement of temperature dependent ND data for selected temperatures (2.5 K, 10 K and 70 K) which confirm the hexagonal structure of $Yb_{1-x}Mg_xMnO_3$ in the space group $P6_3cm$.Temperature variation of atomic position shown in table 3.5.With

regard to the experimental observations, and analysis, six different irreducible representations are possible with $k$ =0 according to magnetic group theories as shown in fig 3.10 [3, 9]. Only four unidimensional irreducible representations seem to be particularly favorable among all the hexagonal manganites known to date. For example, the magnetic peaks of $YMnO_3$ can be explained by either $\Gamma_1$ or $\Gamma_3$ representations while those of $ErMnO_3$ are compatible with $\Gamma_2$ or $\Gamma_4$ representations Fabreges et. al. [9] demonstrated Γ4 representation for Mn ordering in YbMnO3, and the ordered moment at 1.5 K was found to be 3.25μB. The in-plane Mn magnetic moment is perpendicular to the crystallographic a and b axes for Γ1 and Γ4 and parallel to the crystallographic a and b axes for Γ2 and Γ3 configurations. The inter-plane moments are coupled antiferromagnetically for Γ1 and Γ2 ferromagnetically for Γ3 and Γ4 [5]. For the magnetic refinement of the present ND data, the structure described by the basis vectors of the irreducible representations $\Gamma_6$ for $Yb^{3+}$ (at Wyckoff site 2*a*), $\Gamma_2$ for $Yb^{3+}$ at 4b site and $\Gamma_2$ representation for Mn at 6*c* site were used [9]. From the Rietveld refinement of temperature dependent ND data, the structural and magnetic properties of the samples were extracted and selected data are shown in Figs.(3.9 -3.12).

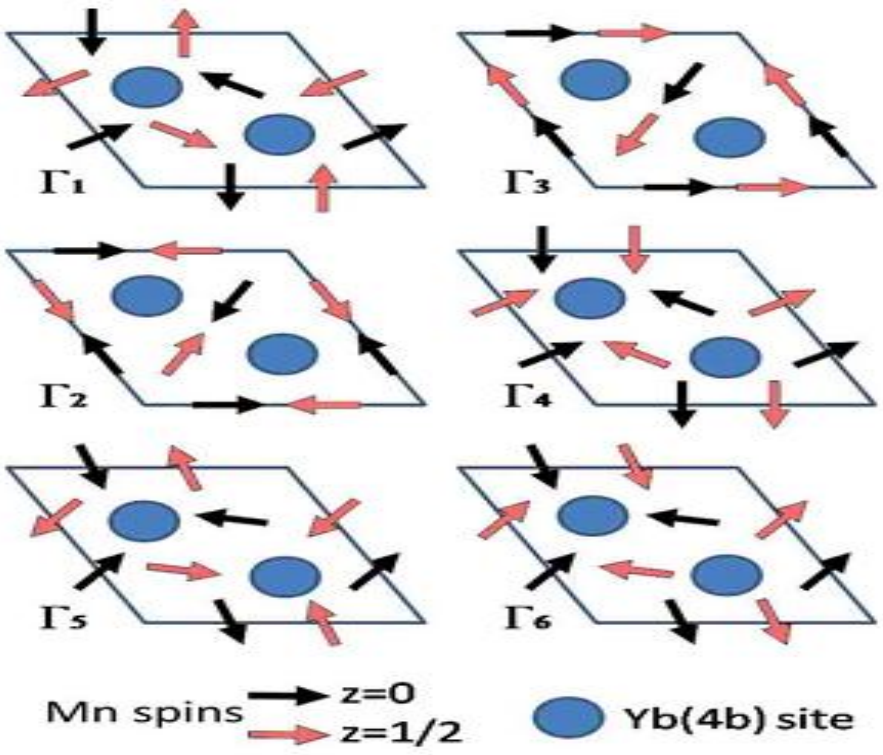


Figure 3.10: Mn spin orders in hexagonal $RMnO_3$ [9].

Figures 3.11a, 3.11b and 3.11c show the temperature dependence of the lattice parameters *a*, *c/a*, and the unit cell volume *V* of $Yb_{1-x}Mg_xMnO_3$. In general, the lattice

parameter *a* and unit cell volume *V* decrease and *c/a* increases with decreasing temperature except near the magnetic transition temperatures ($T_{N1} \approx 85$ K, $T_{N2} \approx 3.5$ K for x = 0.00 and $T_{N1} \approx 89$ K, $T_{N2} \approx 3.5$ K for x = 0.05). Close to the magnetic transition temperatures all the lattice parameters (*a*, *c/a*, and *V*) show anomalous variation [18-20] as a sudden change in value/slope from the background.

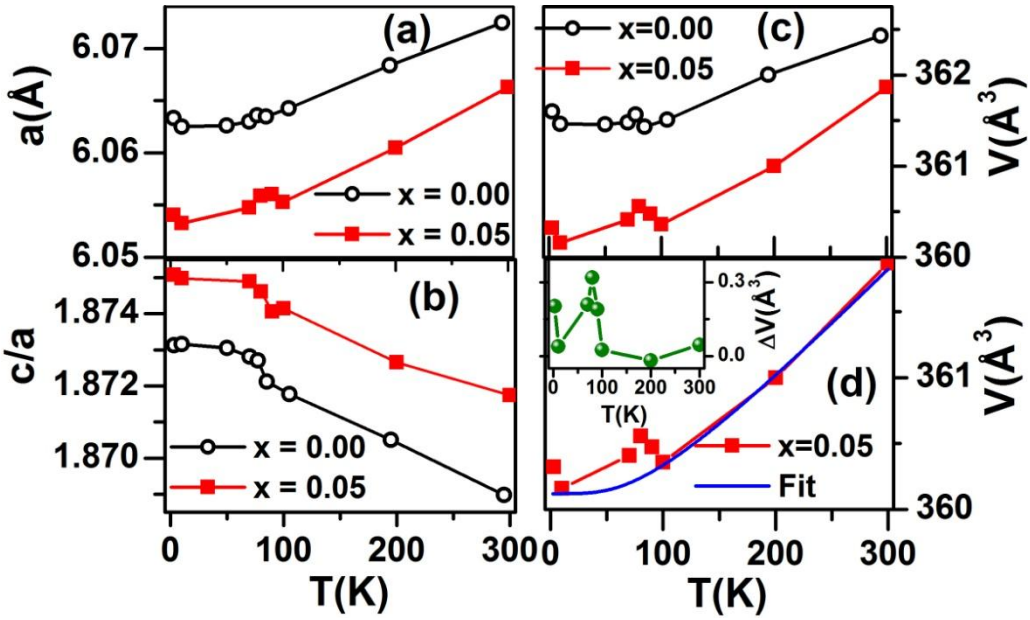


Figure .3.11:Temperature dependence of lattice parameters for $YbMnO_3$ and $Yb_{0.95}Mg_{0.05}MnO_3$: (a): lattice parameter *a*, (b): *c/a* ratio and (c): unit cell volume *V*. (d) Temperature dependence unit cell volume data for $Yb_{0.95}Mg_{0.05}MnO_3$ (red square+line) fitted to Debye–Gruneisen equation (blue line). Inset of (d) shows the temperature dependence of the lattice strain $\Delta V$ obtained by subtracting the background (fit curve) from the measured *V*.

This anomaly in lattice parameters near the magnetic transition temperatures implies strong spin-lattice coupling and consequently a magnetoelastic coupling [19,21]. The magnetoelastic effect is clearly visible in the temperature variation of the unit cell volume *V* data as shown in Fig. 3.11d. This figure shows the temperature dependence of experimentally measured cell volume (red square symbol + line) and the calculated unit cell volume (blue solid line) in the absence of the magnetic transition for the $Yb_{0.95}Mg_{0.05}MnO_3$ sample. The temperature dependence of the cell volume in the absence of magnetic transition is calculated based on the Debey–Gruneisen approximation [22].The measured unit cell volume *V* in the paramagnetic state ($T > T_{N1}$) is fitted to the Debey–Gruneisen equation and using the fit parameters (from the high temperature region fitting) the cell volume for low temperature ($T < T_{N1}$) nonmagnetic phase is calculated and is shown (blue line in the figure) in Fig. 3.11d. By

subtracting the calculated volume for the nonmagnetic phase from the measured data, we determined the volume strain $\Delta V$ and is plotted in the inset of Fig. 3.11d. The maximum volume magnetorestriction ($\Delta V/V$) near the magnetic transition temperature ($T_{N1}$) is found to be ~ 0.09% for the $Yb_{0.95}Mg_{0.05}MnO_3$. The magnitude of spontaneous magnetostriction is comparable to that of multiferroic hexagonal manganite $YMnO_3$ and $HoMnO_3$ [18, 23].

Variation of different Mn-O bond lengths for both $YbMnO_3$ and $Yb_{0.95}Mg_{0.05}Mn0_3$ are shown in Figs. 3.12a, 3.12b and 3.12c as a function of temperature. The Mn-O4 and Mn-O3 bond distances show significant variation at $T_{N1}$. The Mn-O4 bond length shows decrease below $T_{N1}$ while the Mn-O3 bond length shows increase below $T_{N1}$. The Mn-O1 and Mn-O2 bond lengths do not show significant changes with temperature. The difference between Mn-O3 and Mn-O4 bond lengths ($\Delta L$) which reflects the change of the average Mn position along the *x* direction from its neutral position, varies with temperature as shown in Fig. 3.12d. Figs.3.12e, 3.12f and 3.12g show the variation of Mn *x* position, O3 *z* position and O4 *z* position in the unit cell as a function of temperature for both $YbMnO_3$ and $Yb_{0.95}Mg_{0.05}Mn0_3$. The figures clearly show the systematic variations in atomic positions as the sample cools through $T_{N1}$. In Figs. 3.12h, 3.12i and 3.12j temperature dependence of the polyhedral distortion ($\Delta$), the tilting angle and the buckling angle are shown for the

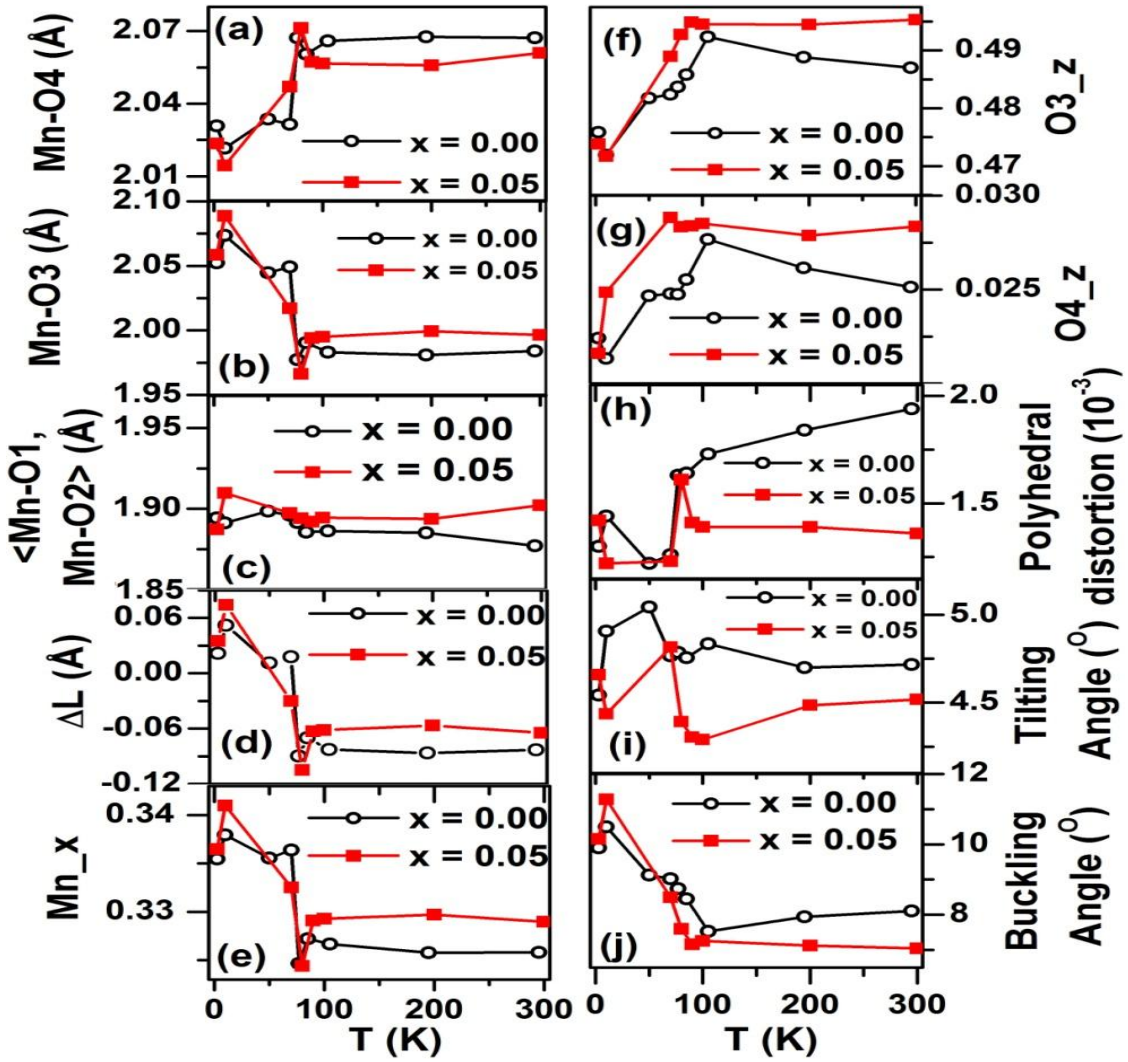


Figure.3.12: Temperature dependence of various structural parameters for $YbMnO_3$ and $Yb_{0.95}Mg_{0.05}MnO_3$: Left panel : (a): Mn-O4 bond length, (b): Mn-O3 bond length, (c): the average apical bond length (<Mn-O1,Mn-O2>), (d): ΔL, difference between Mn-O3 and Mn-O4 bond lengths and (e): Mn *x* atomic position in the unit cell. Right panel : (f), (g): O3 *z* and O4 *z* atomic positions in the unit cell. (h) : polyhedral distortion (Δ), (i) : tilting angle and (j) : the buckling angle for the $MnO_5$ polyhedra.

Samples showing clear signatures at the magnetic transition temperatures. These results of variation of temperature dependence of different structural parameters near the magnetic transition temperature clearly indicate strong magnetoelastic coupling in the $YbMnO_3$ system.

Figure 3.13(a) shows the magnetic structure of $YbMnO_3$ from the Rietveld refinement. Figure 3.13(b) shows the temperature dependence of the ordered Mn and Yb magnetic moments extracted from the neutron diffraction data refinement. Below $T_{N1}$, for both

compounds, ordered Mn moment increases with decrease in temperature. The value of saturated moment

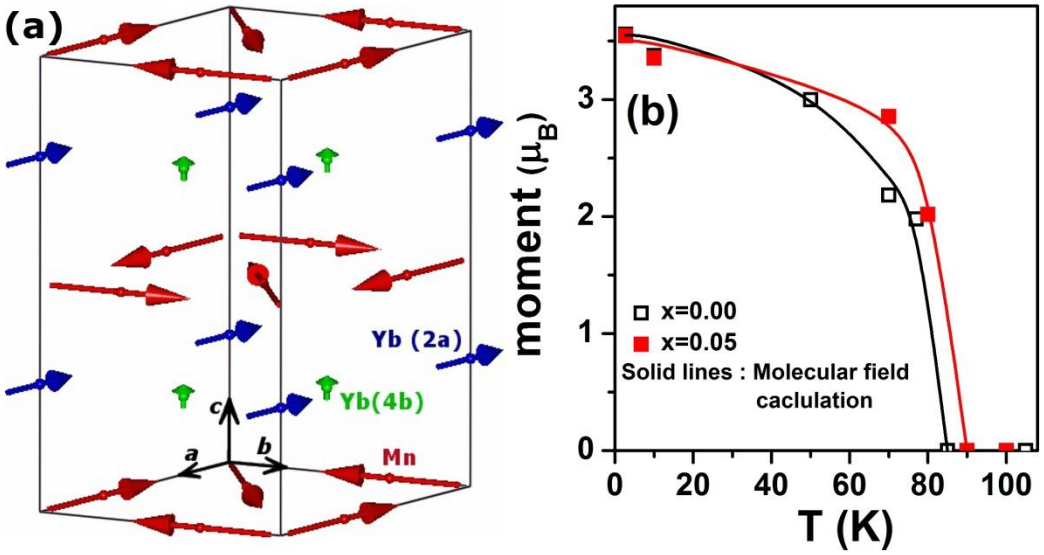


Figure3.13: (a) Magnetic structure of $YbMnO_3$ form the Rietveld refinement. (a). Temperature dependent ordered magnetic moment of Mn for $Yb_{1-x}Mg_xMnO_3$ (x = 0.00 and x = 0.05). Symbols (open for x = 0.00 and closed for x = 0.05) represents data points and solid lines represent fit to mean-field equation.

is 3.55 $\mu_B$ for both the samples which is smaller than 4 $\mu_B$ for $Mn^{3+}$. In the Fig. 3.13(b) symbols show the data points and the solid lines show the fit to the data using a self-consistent mean-field calculation described in [9]. Following [9], we used the expression $m_{Mn}(T) = m_{sat} B_2\left(\frac{g\mu_B S\lambda_0 m_{Mn}(T)}{k_B T}\right)$ to fit the observed moment versus T for both the samples. Here $B_2(x)$ is the Brillouin function for S = 2 and $\lambda_0$ is the molecular field constant representing Mn-Mn exchange [9]. Best fit to the experimental data points are obtained with $m_{sat}$ = 3.55 $\mu_B$ and $\lambda_0$ = 20 for undoped $YbMnO_3$ and with $m_{sat}$ = 3.55 $\mu_B$ and $\lambda_0$ = 26 for Mg doped $YbMnO_3$. These results suggests that with Mg doping at the Yb site, the geometrical frustration for the antiferromagnetic interaction for the triangular lattice of $Mn^{3+}$ ions is reduced and the exchange interaction is strengthened due to the Mg doping. Compared with the undoped $YbMnO_3$, higher value of $T_{N1}$ (89 K for x=0.05 and 85 K for x=0.00), reduced unit cell volume (shown in figure 3.11c) and reduced frustration parameter (2.045 for x=0.05 and 2.576 for x=0.00) for the Mg doped sample supports this fact. The Yb moment values at 2.8 K are found to be $m_{Yb(4b)}$ =

1.404 $\mu_B$, $m_{Yb(2a)}$ = 1.4697 $\mu_B$ for x = 0.00 and $m_{Yb(4b)}$ = 1.307 $\mu_B$, $m_{Yb(2a)}$ = 1.387 $\mu_B$ for x = 0.05.

## 3.3.5 Structural and magnetic properties of $Yb_{0.9}Mg_{0.1}MnO_3$

### 3.3.5.1 X-Ray diffraction

Room temperature powder XRD pattern of $Yb_{0.9}Mg_{0.1}MnO_3$ is shown in Fig.3.14. The XRD confirms that it is single phase compound and the measured pattern can be indexed according to the hexagonal structure with $P6_3cm$ space group. It is to be noted that due to a breakdown in the neutron diffraction equipment, sample with x = 0.1 could not be run.

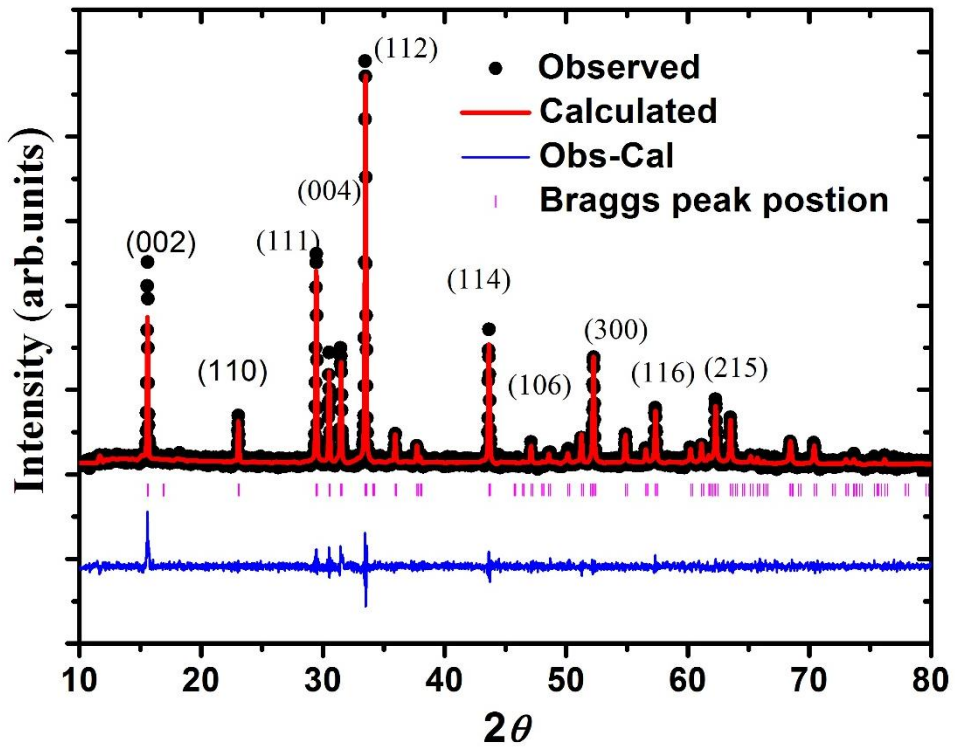


Figure.3.14: Rietveld refinement results on the XRD pattern of the $Yb_{0.9}Mg_{0.1}MnO_3$ sample.

## 3.3.5.2 Magnetic properties

Fig.3.15 shows the dependence of susceptibility versus temperature in ZFC and FC mode for $Yb_{0.9}Mg_{0.1}MnO_3$ systems, measured in a field of 100 Oe with increasing temperature from 2 to 300 K. A deviation of ZFC from FC in $\chi(T)$ is shown as the inset in Fig.3.15, which indicates that the sample is undergoing ferromagnetic ordering at ~3.5K. This ferromagnetic ordering has been attributed to the ordering in the $Yb^{3+}$sublattice [9]. Fig.3.16 shows $1/\chi$ vs T up to 300 K. It is difficult to pin point magnetic transition clearly from this curve, therefore, $d\chi/dT$ is plotted which is shown as the inset in figure 3.15b. The $d\chi/dT$ vs T shows an anomaly at ~ 88 K which refers to the antiferromagnetic canted spin ordering of the $Mn^{3+}$ions, i.e. Neel temperature $T_N$.

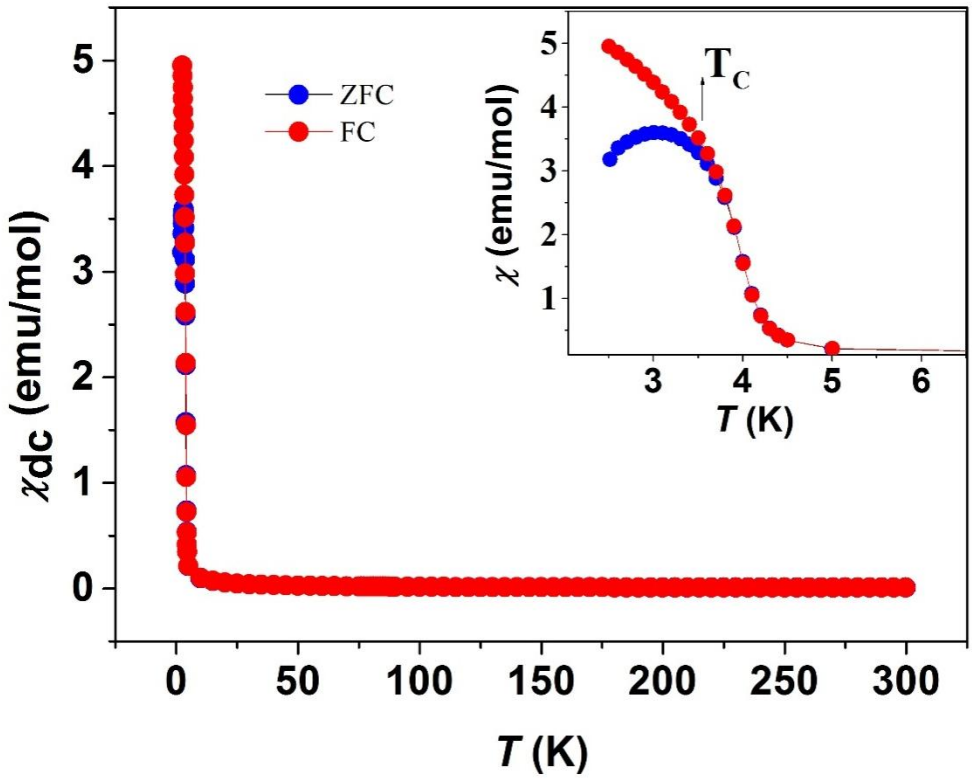


Figure.3.15: Temperature dependence of dc susceptibility with ZFC/FC mode for $Yb_{0.9}Mg_{0.1}MnO_3$. Inset shows low temperature behavior.

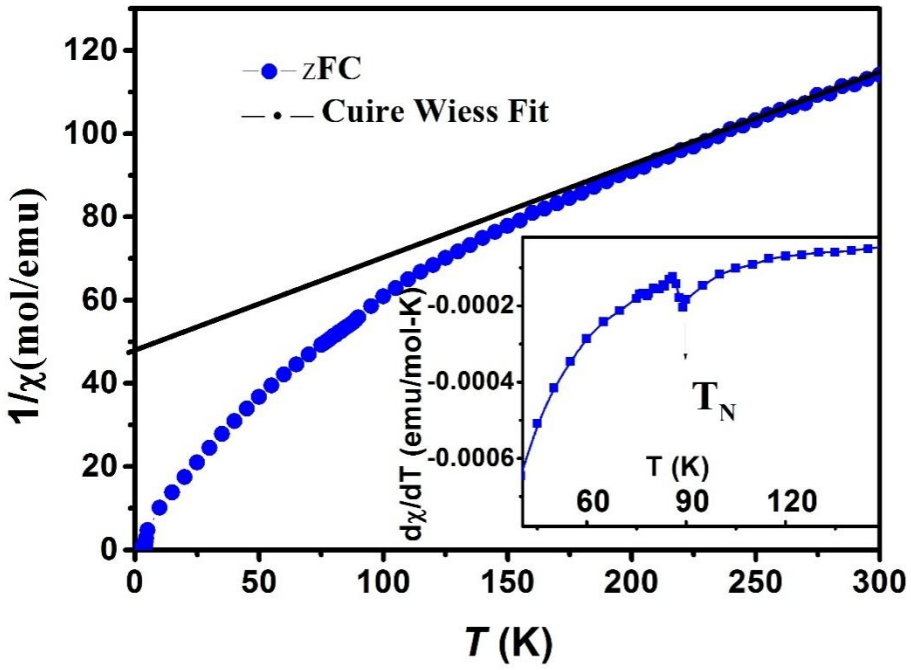


Figure.3.16: Inverse magnetic susceptibility with Curie-Weiss fit for $Yb_{0.9}Mg_{0.1}MnO_3$. Inset shows first derivative of the magnetic susceptibility.

Fig. 3.16 shows the paramagnetic Curie–Weiss (CW) behavior between 200 and 300 K. A Linear fit of the data yields Weiss temperature ($\theta_{CW}$) = −221 K in good agreement with the earlier reported value [9] and Curie constant = 0.219 emu/mol. Calculated $\theta_{CW}$ for $Yb_{0.9}Mg_{0.1}MnO_3$is much higher than $T_N$. This difference in the values of $\theta_{CW}$ and $T_N$ is an evidence of the magnetic frustration in these compounds. This is expressed by the frustration parameter, $f = |\theta_{CW}|/T_N = 2.5$ for $Yb_{0.9}Mg_{0.1}MnO_3$ and is lower than that of $YbMnO_3$. The effective moment $\mu_{eff} = 6.04\mu_B$ is obtained from curie constant. This value is close to the theoretical value of $\mu_{eff} = (0.9\mu^2_{Yb} + 0.9\mu^2_{Mn^{3+}} + 0.1\mu^2_{Mn^{4+}})^{1/2} = 6.45\mu_B$ calculated from only the spin value for the $Mn^{3+}$ion ($4.90\mu_B$),$Mn^{4+}$ ion ($3.87\ \mu_B$) and the $Yb^{3+}$ ion ($4.54\ \mu_B$).

## 3.4 Conclusion

We report in this work detailed investigations of the structural, magnetic and magnetoelastic properties of $Yb_{1-x}Mg_xMnO_3$ (x = 0.00 and 0.05) using neutron diffraction and magnetization measurements. The lattice parameter *a* and unit cell volume *V* decreases continuously with decreasing temperature but close to the Neel temperature $T_{N1} \approx 85$ K, the Yb ordering temperature $T_{N2} \approx 3.5$ K for x = 0.00 and $T_{N1} \approx 89$ K,$T_{N2} \approx 3.5$ K for x = 0.05 show a magnetoelastic or magnetostriction anomaly. Anomalous variations near the magnetic transition temperatures are observed in the temperature dependence of other structural parameters such as bond lengths, atomic positions etc and also studied structural magnetic properties of $Yb_{0.9}Mg_{0.1}MnO_3$ sample.

## 3.5 References:

[1] M. A. Gilleo, Acta Crystallogr. **10** (1957) 161.

[2] H. Yakel, W. C. Koehler, E. F. Bertaut, F. Forrat, Acta Crystallogr. **16** (1963) 957.

[3] A. Munoz, J. A. Alonso, M. J. Martinez-Lope, M. T. Casais, J. L. Martinez, M. T. Fernandez-Diaz, Phys. Rev. B **62** (2000) 9498.

[4] K. Katsufuji, M. Masaki, A. Machida, M. Moritomo, K. Kato, E. Nishibori, M. Takata, M. Sakata, K. Ohoyama, K. Kitazawa, H. Takagi, Phys. Rev. B **66** (2002) 134434.

[5]M. C. Sekhar, S. Lee, G. Choi, C. Lee, J.G. Park, Phys. Rev. B **72** (2005) 014402.

[6] Z. J. Huang, Y. Cao, Y. Y. Sun, Y. Y. Xue, and C. W. Chu, Phys. Rev. B**56**, (1997), 2623

[7] .T. Katsufuji, S. Mori, M. Masaki, Y. Moritomo, N. Yamamoto,and H. Takagi, Phys. Rev. B **64**, (2001), 104419

[8] F. Bertaut, F. Forat, and P. Fang, Compt. Rend. **256**, (1963), 1958

[9]X. Fabreges, I. Mirebeau, P. Bonville, S. Petit, G. Lebras-Jasmin,A. Forget, G. Andre, and S. Pailhes, Phys. Rev. B **78**, (2008), 214422

[10]S.L. Samal, T. Magdaleno, K.V. Ramanujachary, S.E. Lofland and, A.K. Ganguly, J. Solid State Chem., **183**, (2010), 643.

[11] H. Sugie, N. Iwata, K. Kohn, J. Phys. Soc. Jpn., **71**, (2002), 1558.

[12] A V Pimpale, B A Dasannacharya, V Siruguri, P D Babu and P S Goyal,Nucl. Instrum. Methods A, **481**, (2002), 615.

[13] J. Rodríguez-Carvajal, Physica B **192**,(1993) 55.

[14] L. Jeuvreya, O. Pen, A. Moure, C. Moure, J. Mag. Magn. Mater. **324** (2012) 717.

[15] A. Munoz, J. A. Alonso, M. J. Martınez-Lope, M. T. Casais, J. L. Martinez, M. T. Ferna´ndez-Diaz, Phys. Rev. B **62,** (2000) 950.

[16] Josep Fontcuberta, Marin Gospodinov, and Vassil Skumryev, J. Appl. Phys. **103** (2008), 07B722.

[17] Yun-Hui Huang, MarritKarppinen, Naoki Imamura, Hisao Yamauchi, John B. Goodenough, Phys. Rev. B **76,** (2007), 17440.

[18].T. Chatterji, B. Ouladdiaf, P. F Henryand D. Bhattacharya, J. Phys.: Condens. Matter, **24,** (2012), 336003.

[19] S. Lee, A. Pirogov, J. H. Han, J.-G. Park, A. Hoshikawa, and T. Kamiyama, Phys. Rev. B,**71**, (2005), 180413(R ).

[20] A. K. Singh , S. Patnaik S. D. Kaushik and V. Siruguri, Phys. Rev. B, ,**81**, (2010), 184406.

[21] S. Rayaprol, V. Siruguri, A. Hoser, C. Ritter, and E. V. Sampathkumaran, Phys. Rev. B, , **90**, (2014), 134417.

[22] T. Chatterji, T.C Hansen , S.A.J. Kimber, and D. Bhattacharya, Solid Sate Comunications, **180, (**2014),46-51.

[23] T. Chatterji, G. N. Iles B. Ouladdiaf, and T.C Hansen, J. Phys.: Condens. Matter, **22, (**2010),3160

# Chapter 4

## *Specific heat, and magnetocaloric effect of polycrystalline $Yb_{1-x}Mg_xMnO_3$*

## 4.1 Introduction:

Magnetocaloric effect (MCE) based refrigeration has higher energy efficiency over the conventional vapor compression refrigeration and considerable research interest is there in exploring new materials with better MCE properties. The guidelines for such a material are that it should have low heat capacity and exhibit a large entropy change at the ferromagnetic (FM) to paramagnetic (PM) transition temperature or field induced metamagnetic transition from antiferromagnetic (AFM) to FM states with a minimal hysteresis. Recently, rare-earth manganites are being investigated extensively for their potential as multiferroic and magnetocaloric materials. $YbMnO_3$ has a hexagonal lattice with space group $P6_3cm$ in which $Mn^{3+}$ ions are located at site 6c and $Yb^{3+}$ are situated at two different sites 2a and 4b, which leads to interesting properties [1,2,3].

Abramov *et al*. [4] have reported two peaks in heat capacity measurements of Ca doped $YbMnO_3$at low temperatures, one sharp at the transition temperature and one broad at slightly higher temperature. The sharp peak is attributed to the ferromagnetic (FM) ordering in the basal plane due to Yb in site 2*a*and the broad peak, centered at 6 K ,is consistent with the Schottky anomaly related to the Zeeman splitting of the Yb moments due to the Mn molecular field. They further observed that(1) Ca doping slightly decreased the Néel temperature and (2)a decrease in magnitude of the sharp peak which they attributed to a decrease in number of $Yb^{+3}$ ions. Measurements of heat capacity of $YbMnO_3$ and $YbMn_{0.7}Ga_{0.3}O_3$ single crystals by Abramov et al [5] showed that the substitution of Mn by non-magnetic $Ga^{3+}$ ions led to reduced Mn magnetic interactions and, therefore, suppressed the magnetic ordering of Yb in both 2*a* and 4*b* positions. The effect of Mg doping on structure and magnetism of multiferroic $YbMnO_3$ has been discussed in the chapter 3. It was observed that with 5% Mg content magnetic transition temperature is raised from 85 K to 89 K. However, the low temperature specific heat of pure and Mg substituted $YbMnO_3$ and its magnetic field dependence have not been explored in detail so far.

In this chapter, the thermodynamic properties of polycrystalline $YbMnO_3$ and Mg doped $YbMnO_3$ with and without external magnetic fields have been reported to understand their magnetocaloric properties with the help of detailed analysis of the specific heat data. Magnetic entropy change ($\Delta S_{mag}$), adiabatic temperature change ($\Delta T_{ad}$) and relative cooling power (RCP) are presented for the respective compounds here. The results on the magnetocaloric effect of these compounds derived from the isothermal magnetization data to assess its potential as a low temperature refrigerant are also presented.

## 4.2. Experimental

Polycrystalline samples of $Yb_{1-x}Mg_xMnO_3$ (x = 0.0, 0.05 and 0.1`) were prepared by the standard solid-state reaction method. The details of synthesis is discussed in chapter 3.2. Specific heat was measured by the relaxation method using a PPMS (M/S Quantum Design, USA), having a superconducting magnet of 14 T, from 2 K to 160 K. The magnetization measurements were performed using a Cryogenic Inc. (UK) make vibrating sample magnetometer operating at 20.4 Hz. Magnetization isotherms were measured at different temperatures in fields up to 100 kOe near the low temperature ordering transition.

## 4.3 Results and Discussions

### 4.3.1 Specific heat

Specific heat ($C_P$) of pure and Mg doped samples, $Yb_{1-x}Mg_xMnO_3$ as a function of temperature are displayed in figure. 4.1. The high temperature peak observed at $T_N$~83 K for $x$= 0.0 and at ~86 for $x$= 0.05 is related to the antiferromagnetic (AFM) transition and, therefore, these temperatures are to be taken as Neel temperatures ($T_N$) for these samples which are in good agreement with magnetization measurements (although slightly less)as discussed in chapter 3. The zoomed part of low temperature data of $C_p$ is shown in the figure. 4.2. At lower temperature ~2.7 K, specific heat of $YbMnO_3$ shows a break in slope or a very small smeared peak which refers to the ferromagnetic transition, however, sample $Yb_{0.95}Mg_{0.5}MnO_3$ shows a pronounced peak at 3.3 K, which is also identified as long range magnetic ordering Curie temperature $T_c$, which confirms strong coupling between the Mn and Yb magnetic sub systems [6]. These values of $T_c$ are consistent with earlier magnetization results.

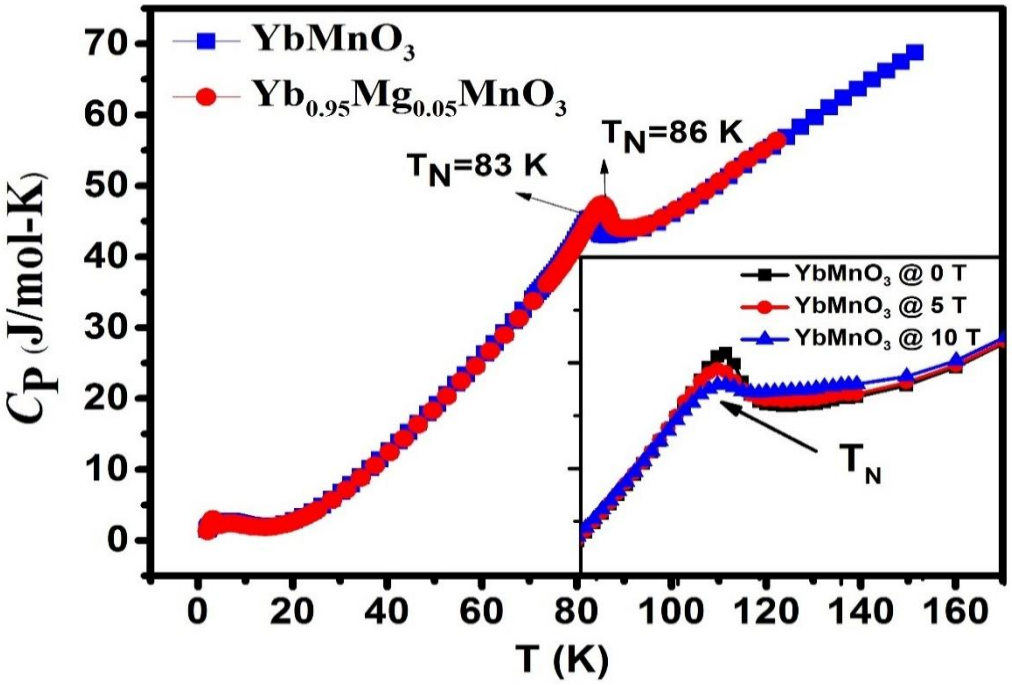


Figure 4.1: The temperature variation of specific heat of $Yb_{1-x}Mg_xMnO_3$($x$=0 and 0.05). nset shows at Neel temperature with different magnetic field of $YbMnO_3$.

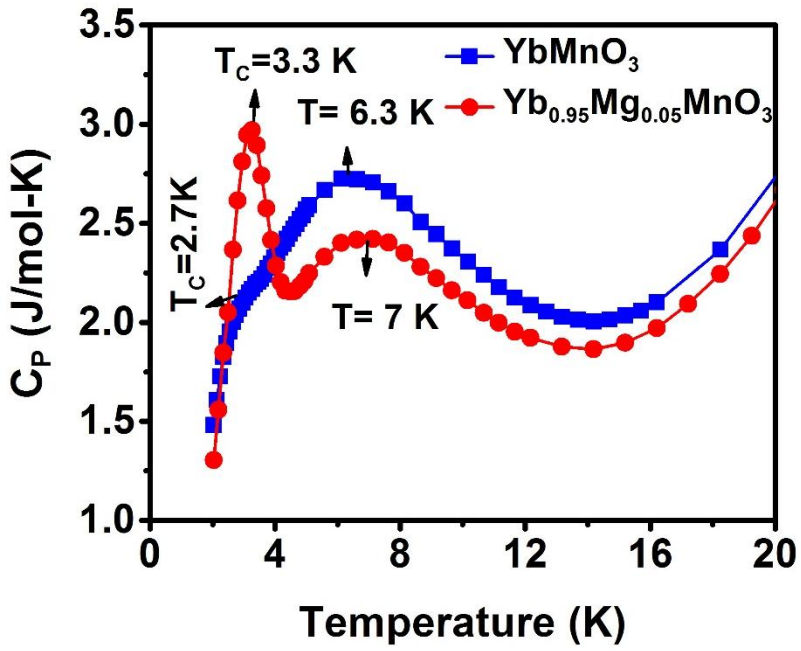


Figure4.2: Low temperature behavior of specific heat of $Yb_{1-x}Mg_xMnO_3$($x$=0 and 0.05).

Just above $T_c$, a broad hump is observed for both samples, which are speculated to be Schottky anomalies [4] due to Yb in site 4*b* in the Mn molecular field as shown in figure 4.2. The broad peak of the Schottky anomaly is shifted to high temperatures (7 K) compared to pure

compound (6.3 K), indicating an increase in the molecular field of Mn at the Yb4*b* site. Figure 4.3 shows magnetic field dependence of specific heat as a function of magnetic field for both samples in the temperature range 2 – 20 K. It is seen that the Schottky anomaly shifts to higher temperature on application of magnetic field and smears out at higher fields and seems to disappear at ~10 tesla (T) magnetic field.

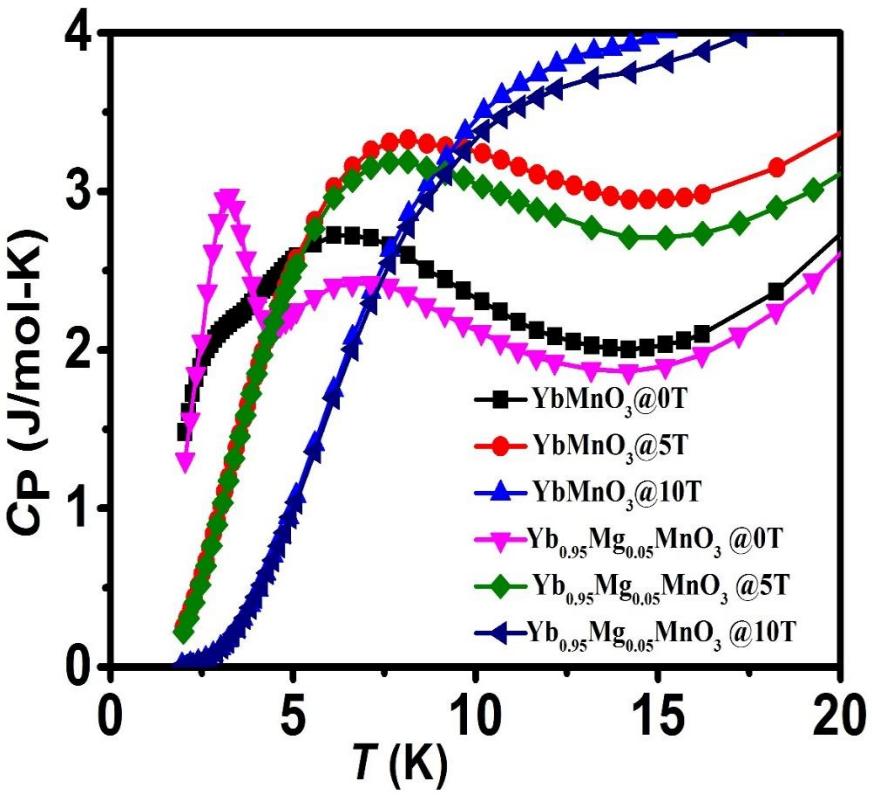


Figure. 4.3: Low temperature behavior of specific heat of $Yb_{1-x}Mg_xMnO_3$ ($x$= 0and0.05) with variation of magnetic field.

The Schottky anomaly for these samples is due to the Zeeman like splitting of crystal fields in ground state multiplet of the $Yb^{3+}$ions [4, 5]. Assuming that the effective moment of $Yb^{3+}$ions in the ground state is $\mu_{Yb}$ and that the splitting of the doublet is $\Delta_{Sch} = 2\mu_{Yb}H_{mf,}$ contribution from a two level Schottky function should fit the specific heat data at low temperatures (T <15 K). The Schottky function [5] for a two level system has been used as,

$$C_p(T) = C_S(T, \Delta_{Sch}) + C_0(T), \qquad (4.1)$$

$$C_{Sch}(T,\Delta_{Sch}) = nN_A k_B \left(\frac{\Delta_{Sch}}{k_B T}\right)^2 \left[\frac{\exp\left(\frac{\Delta_{Sch}}{k_B T}\right)}{\left(1+\exp\left(\frac{\Delta_{Sch}}{k_B T}\right)\right)^2}\right], \quad (4.1a)$$

$$C_0(T) = aT + bT^2 + cT^3, \quad (4.1b)$$

to fit the data between 5 and 15 K. In the above relations, n is the coefficient of the contribution from the Schottky effect ($n$=2/3 for Yb 4b sites), $N_A$ is the Avogadro number, and $k_B$ is the Boltzmann constant. $C_0$(T) is chosen to describe the phonon and magnon contributions. The fits are shown in figure 4.4 by continuous lines. The values of Schottky gaps $\Delta_{Sch}$ obtained by fitting are 0.873 (~10 K) for $x$ = 0.0 sample and 1.0648meV (~12 K). for $x$ = 0.05 sample. Using $\mu_{Yb}$ = 1.77$\mu_B$ [6], the calculated values of $H_{mf}$ are found to be 3.0 T and 3.5 T for $YbMnO_3$ and $Yb_{0.95}Mg_{0.05}MnO_3$, respectively. The increase of $\Delta_{Sch}$ with Mg doping indicates slight increase in energy level splitting because of the weakening of the Mn-Mn interactions. This result also hints to the fact that the Schottky anomaly is also affected by the internal field created by Mn spin ordering. The larger molecular field for x =0.05 sample results in higher $T_N$ as observed. These molecular field and Schottky gap values are nearly the same as reported values in literature [4,5].

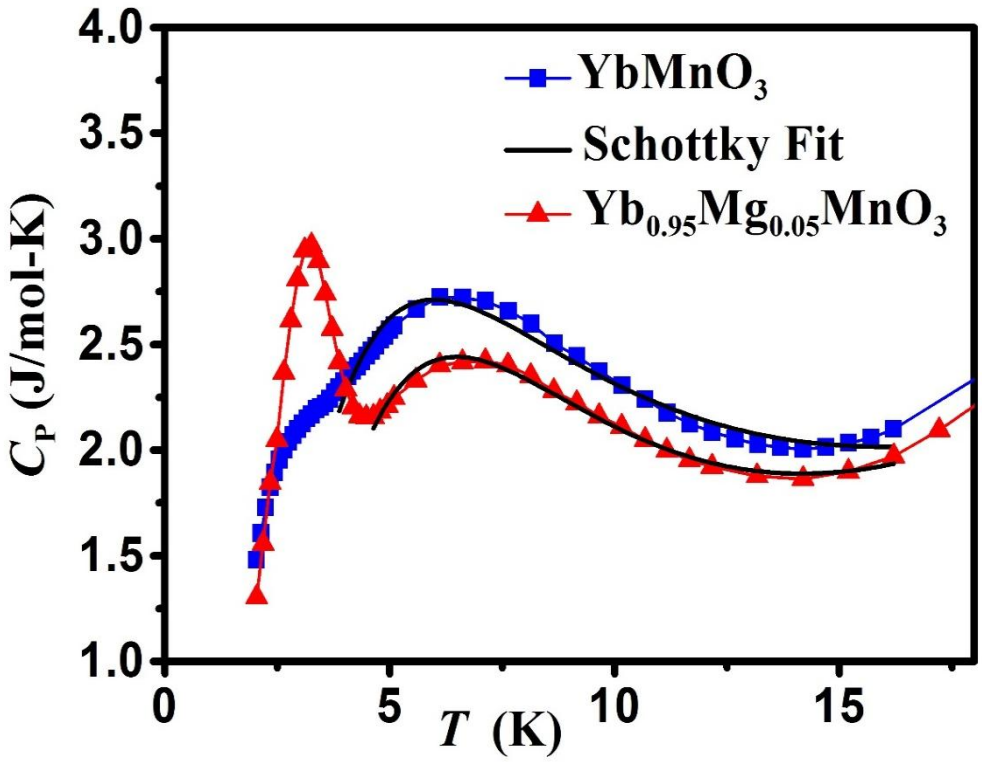


Figure. 4.4: Schottky fitting with theoretical model of $Yb_{1-x}Mg_xMnO_3$ ($x$=0 and 0.05).

$C_{mag}/T$ versus T curves for $YbMnO_3$ and $Yb_{0.95}Mg_{0.05}MnO_3$ are shown in Fig.4.6 and 4.8, respectively, where $C_{mag}$ is magnetic specific heat. $C_{mag}$ is obtained by subtracting lattice contribution ($C_{ph}$) from the total specific heat $C_p$. Here, electronic contribution is assumed to be zero as each compound exhibits electrically insulating behavior. The $\lambda$-shape type behavior of specific heat is observed at $T_N$ as shown in figure 4.6 and 4.8 indicating a second order phase transition. There is a sharp increase in $C_{mag}/T$ at about 18 K and shows a sharp peak at lower temperatures (~3 K) indicative of ferromagnetic transition as observed in $C_p$ vs T also (Fig. 4.2). $C_{ph}$ is estimated using the Debye model which uses Bloch-Gruneisen integral,

$$C_{ph} = 9nR\left(\frac{T}{\theta_D}\right)^{\theta_D/T}\int_0 \frac{x^4 e^x}{\left(e^x-1\right)^2}dx \qquad \textbf{(4.2)}$$

Here $n$= 5 is the number of atoms per formula unit. R = 8.314 $J.mol^{-1}.K^{-1}$ is the ideal gas constant, and $\theta_D$is Debye temperature. $C_{ph}$ is estimated with two Debye temperatures, $\theta_{D1}$ for heavy (Mn+RE) elements and $\theta_{D2}$ for light (O2) [7]. In this case, the Debye temperatures are chosen such that the calculated data closely match with the experimental data at high

temperatures. For $YbMnO_3$, $\theta_{D1}$ = 345 K and $\theta_{D2}$ = 755 K and for $Yb_{0.95}Mg_{0.05}MnO_3$, $\theta_{D1}$ = 332 K and $\theta_{D2}$ = 745 K, respectively, indicating slight decrease in these due to the Mg substitution. The lattice contribution to specific heat for each compound (x = 0.0, and x = 0.05) along with total $C_p$ is shown in the figures 4.5 and 4.7.

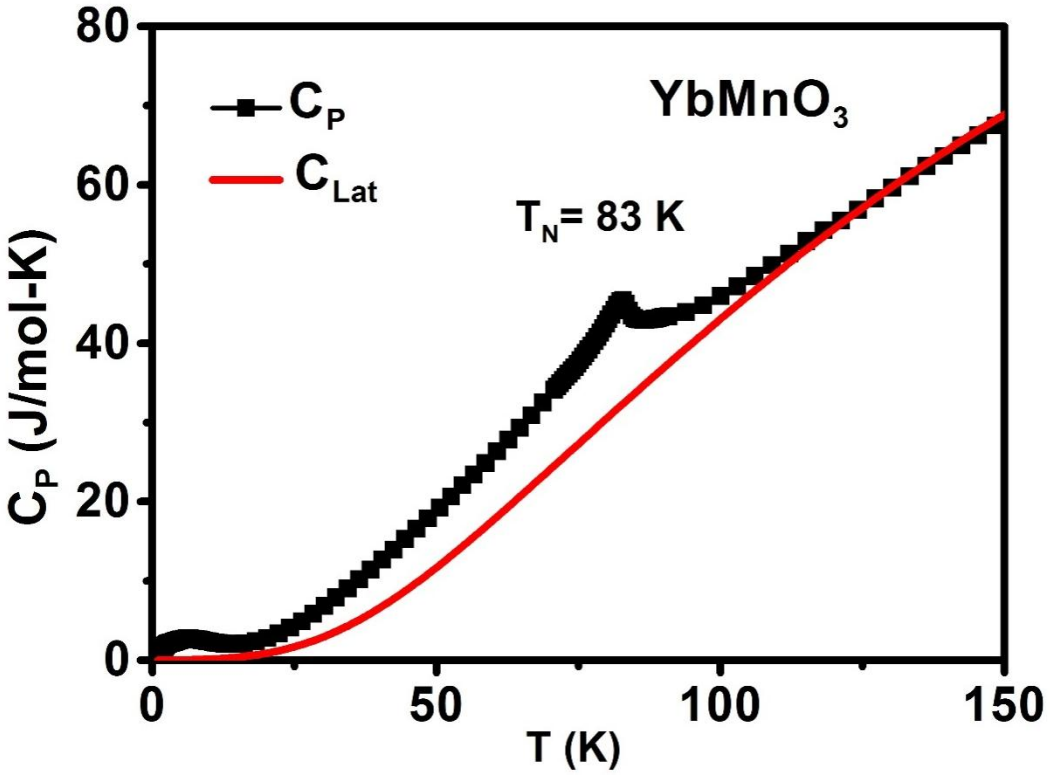


Figure. 4.5: Specific heat of $YbMnO_3$with phonon estimate lines using Debye temperatures

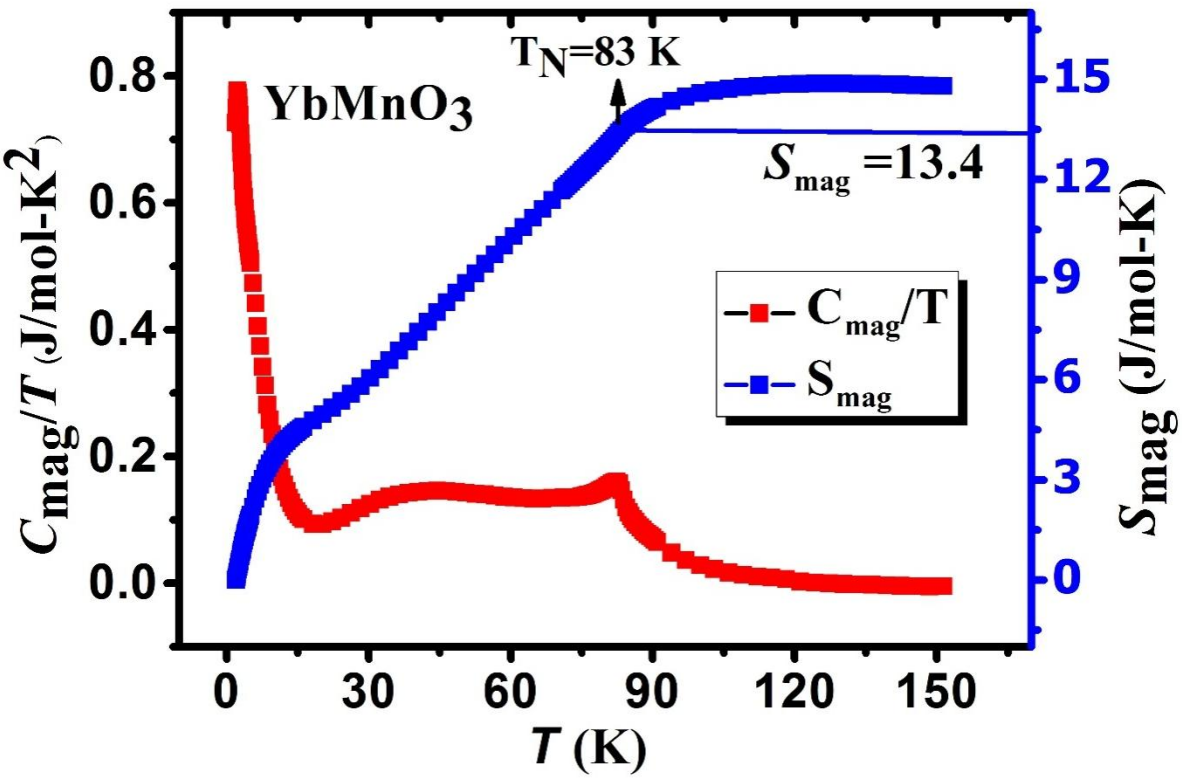


Figure. 4.6:(Left scale) The magnetic contribution to the specific heat $C_{mag}/T$, (Right scale) the magnetic entropy contribution, $S_{mag}$ as a function of temperature of $YbMnO_3$.

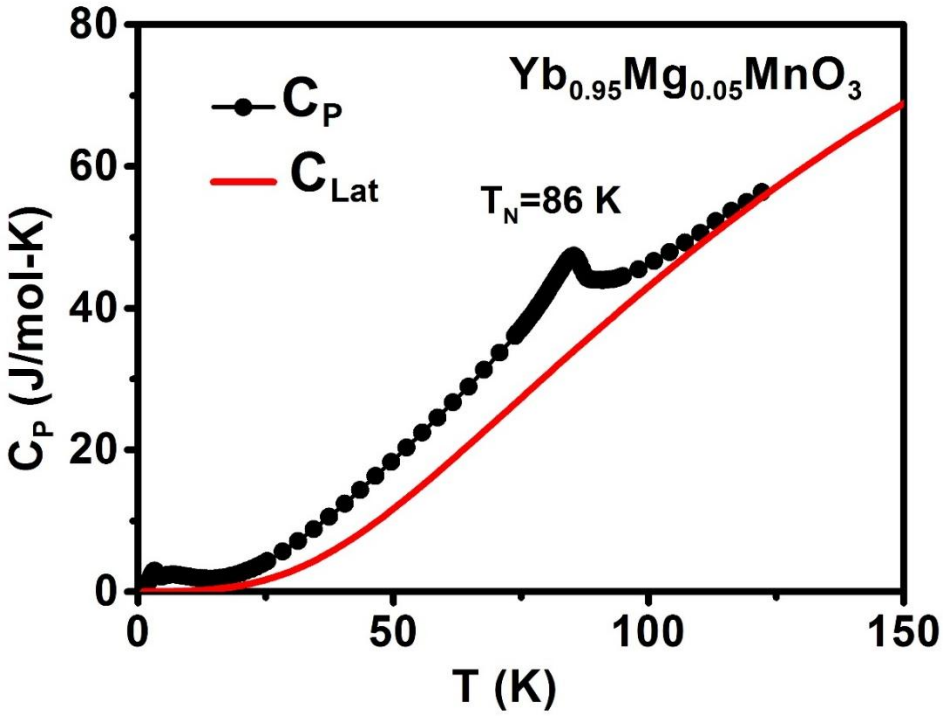

Figure.4.7: Specific heat of $Yb_{0.95}Mg_{0.05}MnO_3$with phonon estimate lines using Debye temperatures

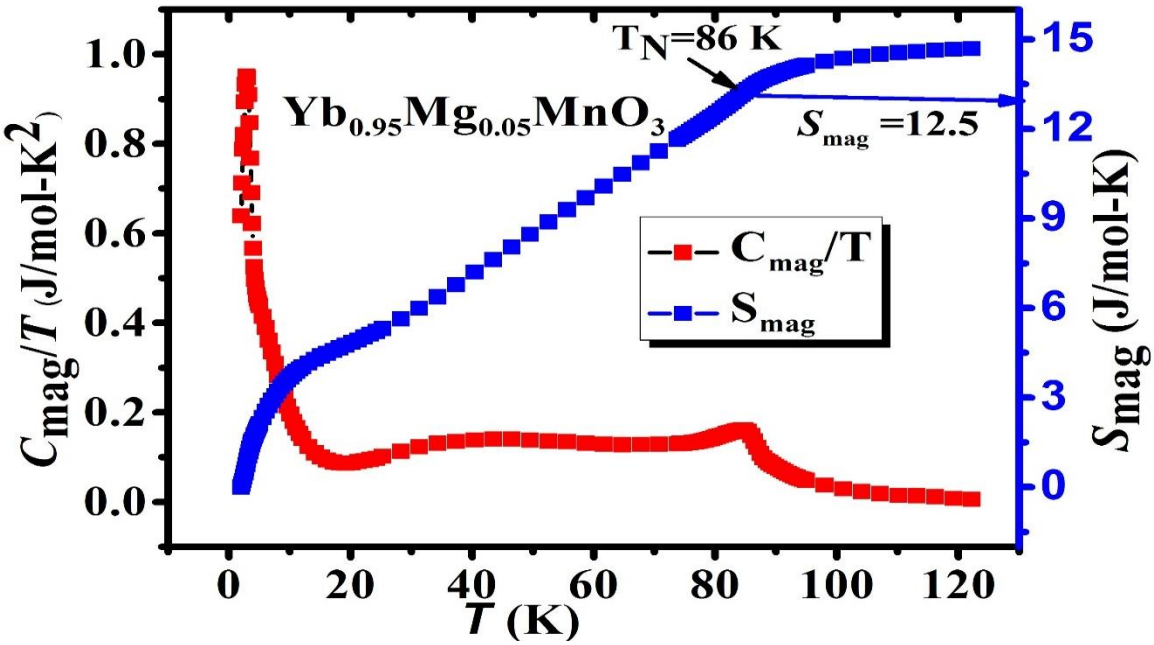


Figure. 4.8:(Left scale) The magnetic contribution to the specific heat $C_{mag}/T$, (Right scale) the magnetic entropy contribution, $S_{mag}$ as a function of temperature of $Yb_{0.95}Mg_{0.05}MnO_3$.

The magnetic entropy is calculated using the formula,

$$S_{mag} = \int_{T_1}^{T_2} \frac{C_{mag}}{T} dT \,. \qquad (4.3)$$

$S_{mag}$ Vs. T are shown in figures 4.6 and 4.8, which show that $S_{mag}$ increases rapidly up to ~ 15 K, then increase with T becomes smaller and shows saturation above 100 K. The calculated values of $S_{mag}$ at $T_N$are 13.4 $J.mol^{-1}.K^{-1}$ for $YbMnO_3$ and 12.5 $J.mol^{-1}.K^{-1}$for $Yb_{0.95}Mg_{0.05}MnO_3$, in absence of an external magnetic field. These values are very close to the theoretically estimated [$S_{mag}$= R*ln*(2S+1)] value, which is 13.4 $J.mol^{-1}.K^{-1}$for S=2 of $Mn^{3+}$. It is seen that $S_{mag}$ decreases on substitution of Mg at the Yb-site. This is consistent with decrease in

frustration factor as discussed in chapter 3 from magnetization data. However, the values of $S_{mag}$ at their respective Curie temperatures are 0.7 and 1.3 $J.mol^{-1}.K^{-1}$ for $YbMnO_3$ and 5% Mg doped $YbMnO_3$, respectively.

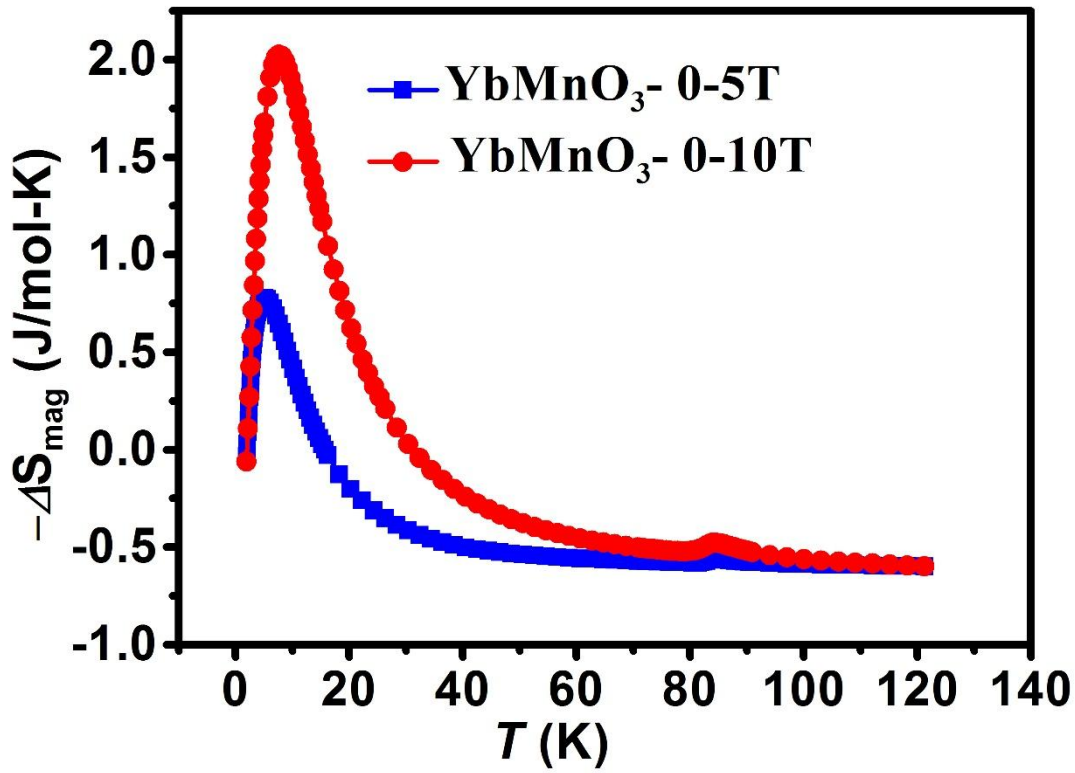


Figure.4.9: Temperature variation of magnetic entropy change for different field changeforYbMnO$_3$.

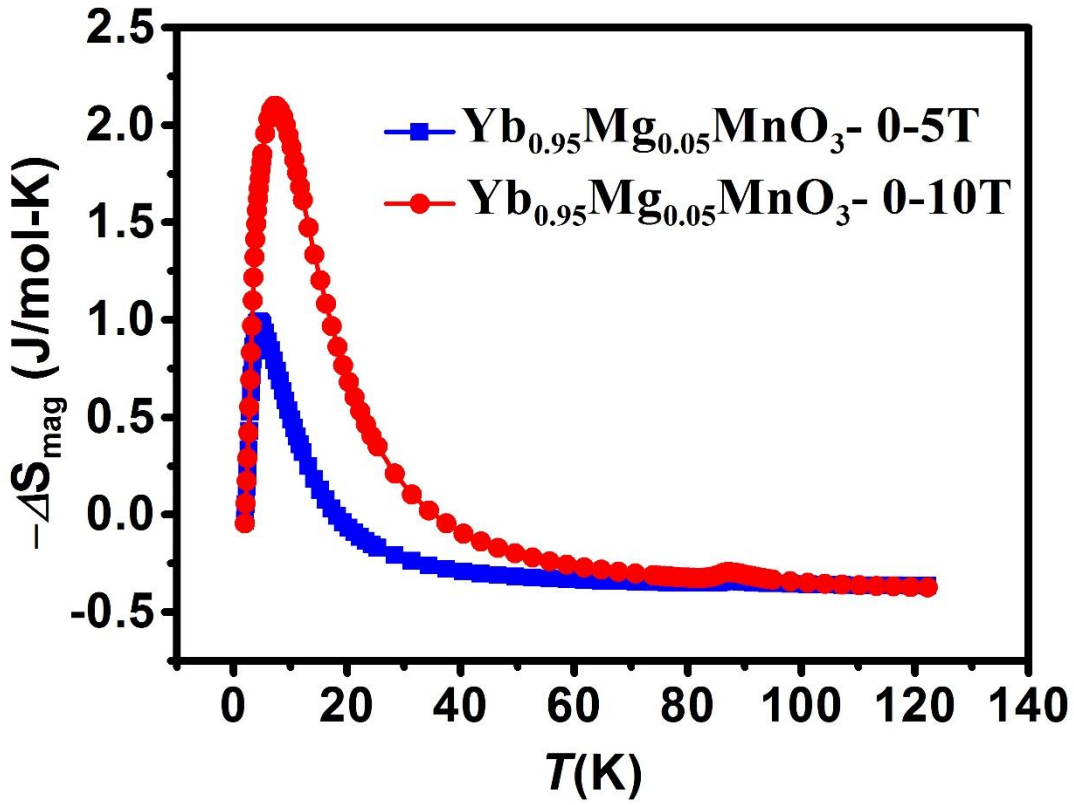


Figure.4.10: Temperature variation of magnetic entropy change at different field changefor $Yb_{0.95}Mg_{0.05}MnO_3$.

The magnetocaloric effect (MCE) is also calculated for these samples using the above data. The effect of magnetic field on specific heat of these samples is shown in the inset fig4.1 and fig 4.3. It is observed that the applied magnetic fields not only suppress the magnitude of specific heat at $T_N$ but also smear it out, which can be seen from the broadening of the peak at $T_N$. $T_N$ is shifted to slightly low temperatures and $T_C$ is shifted to slightly higher temperatures. To determine MCE, it is necessary to estimate $\Delta S_{mag}$, which represents the change in magnetic entropy in a magnetic field. $\Delta S_{mag}$ is estimated by subtracting $S_{mag}$ field curves from the zero field curve, i.e., $\Delta S_{mag} = S_{mag}(H) - S_{mag}(0)$. Typical curves obtained are shown for 5T&10T in figures 4.9 and 4.10 for $YbMnO_3$and$Yb_{0.95}Mg_{0.05}MnO_3$, respectively. $\Delta S_{mag}$ shows a peak ataround~5 K for both samples then it decreases. It also shows a very small peak at ~$T_N$ for both samples. The larger magnetic field shifts the maximum to a slightly higher temperature. The maximum values of $\Delta S_{mag}$ are 0.8 $J.mol^{-1}.K^{-1}$ (5 T), 2.0 $J.mol^{-1}.K^{-1}$ (10T) for $YbMnO_3$ and 1.0$J.mol^{-1}.K^{-1}$ (5T), 2.1$J.mol^{-1}.K^{-1}$(10 T) for $Yb_{0.95}Mg_{0.05}MnO_3$, respectively. There is a slight increase in $\Delta S_{mag}$ value in the doped sample compared to that of the parent compound but it is not that significant. In each compound, $\Delta S_{mag}$ value increases with the magnetic field. These

values are in agreement with the reported values in the literature which are~2.3 J mole$^{-1}$K$^{-1}$at H=8 T for single crystal $YbMnO_3$ [8].

The adiabatic change in temperatures ($\Delta T_{ad}$) is calculated from the above data. The plots of $\Delta T_{ad}$ vs. T are shown in figures 4.11 and 4.12 and show similar behavior as $\Delta S_{mag}$ vs T although peaks are broader. The peak values of $\Delta T_{ad}$ are ~ 1.7 K and ~6.4 K for $YbMnO_3$, ~2 K and ~7 K for $Yb_{0.95}Mg_{0.05}MnO_3$ with 5 T and 10T magnetic field change, respectively.

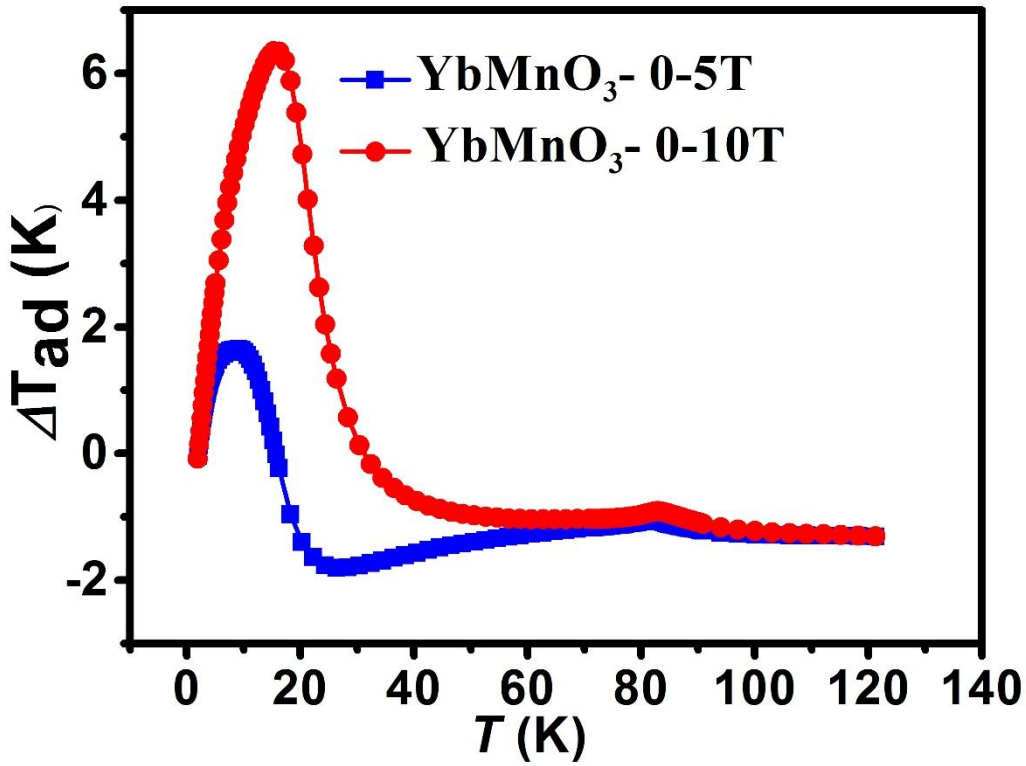


Figure.4.11: Temperature variation of adiabatic temperature change at different field change of $YbMnO_3$.

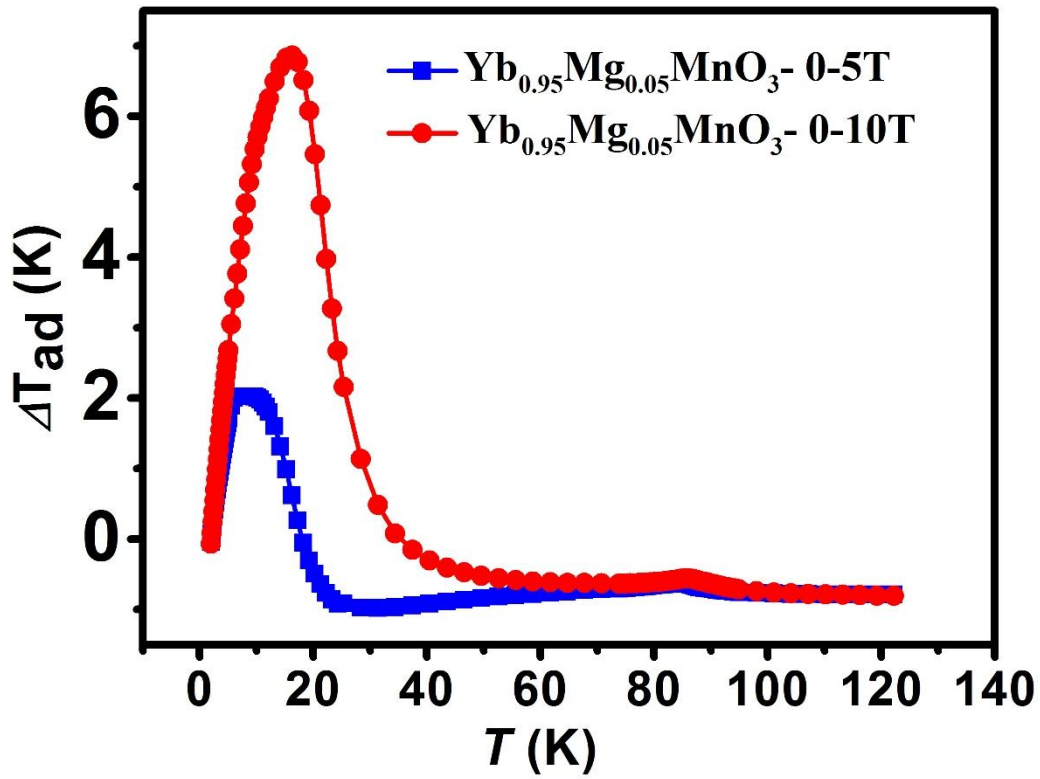


Figure.4.12: Temperature variation of adiabatic temperature change for different field change of $Yb_{0.95}Mg_{0.05}MnO_3$.

Relative cooling power (RCP) of a magnetic refrigerant is a measure of how much heat is transferred between the hot and cold sinks in one ideal refrigeration cycle [8]. RCP can be estimated by using the following formula [9],

$$RCP = \left|\Delta S_{mag}^{\max}\right| \times \left|\delta T_{FWHM}\right|, \qquad (4.4)$$

Where $\delta T_{FWHM}$ is the Full Width at Half Maximum of the $|\Delta S_{mag}|$ versus T curve. The estimated RCP values are 6.0 J.mole$^{-1}$ (5 T) and 26.1 J.mole$^{-1}$ (10 T) for $YbMnO_3$, 7.0 J.mol$^{-1}$ (5 T) and 27.2 J.mol$^{-1}$ (10 T) for $Yb_{0.95}Mg_{0.05}MnO_3$, respectively are in agreement with the RCP value of 26 J.mol$^{-1}$ for $YbMnO_3$ single crystal [8]. This shows that polycrystalline $YbMnO_3$ is equally good for magnetocaloric applications.

## 4.3.2Specific heat of $Yb_{0.9}Mg_{0.1}MnO_3$

Specific heat of $Yb_{0.9}Mg_{0.1}MnO_3$is shown in fig.4.13. from 2 to 160 K which clearly shows a peak at ~ 86 K and is indicative of the antiferromagnetic transition temperature $T_N$, which is slightly different than the value observed by magnetic measurements. In order to estimate the magnetic entropy near $T_N$, the phonon contribution is subtracted from the total specific heat. Lattice specific heat is calculated using the Debye formula, A good fit is only obtained when two Debye temperatures, $\theta_{D1}$ = 346 K and $\theta_{D2}$ = 765 K are used for the fitting.

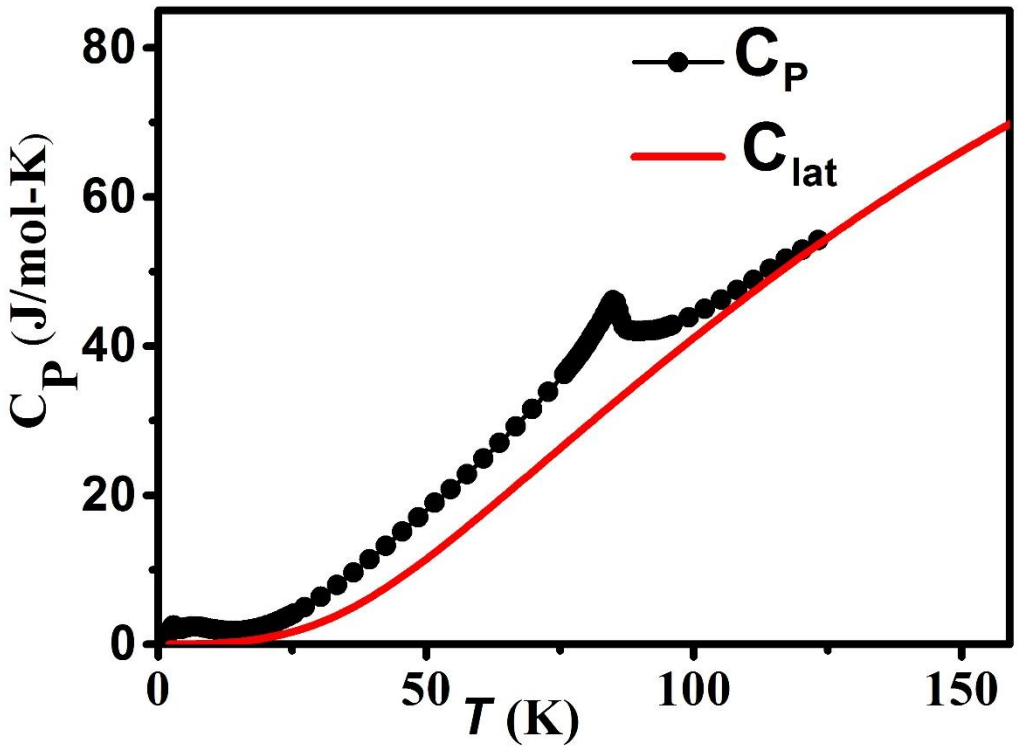


Figure.4.13: Temperature dependent specific heat and the phonon estimate line using Debye temperatures as discussed in text for $Yb_{0.9}Mg_{0.1}MnO_3$.

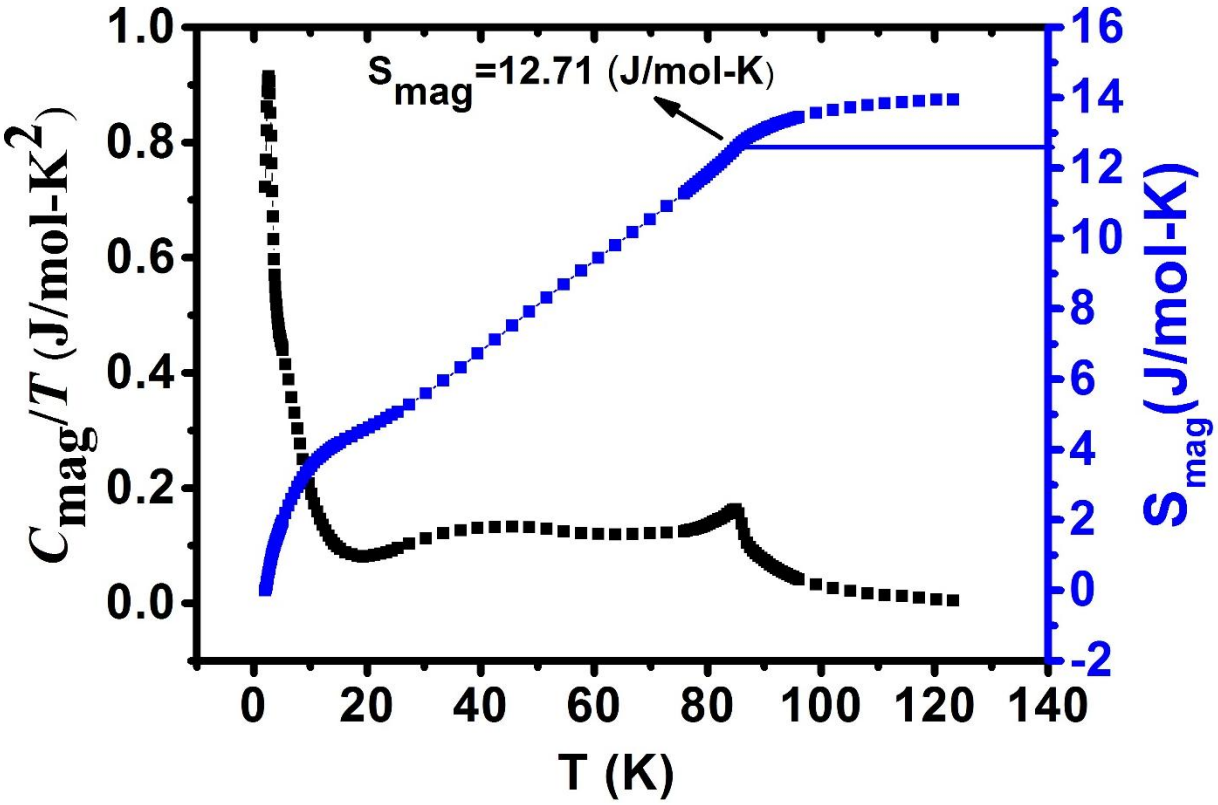


Figure. 4.14:(Left scale) The magnetic contribution to the specific heat $C_{mag}/T$, (Right scale) the magnetic entropy contribution, $S_{mag}$ as a function of temperature of $Yb_{0.9}Mg_{0.1}MnO_3$.

$C_{mag}$ is obtained after subtracting off the phonon contribution showing from the total specific heat. $C_{mag}/T$ versus T is shown in Fig. 4.14 (Left scale), which also shows a peak at $T_N$ as expected. The total magnetic entropy, $S_{mag}$, versus T is calculated and is shown in Fig.4.14 (Right scale). At $T_N$, $S_{mag}$ value for $Yb_{0.9}Mg_{0.1}MnO_3$ is 12.7 J/mol-K which is close to the theoretical value of $S_{mag}$ = 13.4 J/mol K, calculated using the relation $S_{mag} = R\ln(2S+1)$. A Schottky anomaly is also observed at ~6.7 K due to $Yb^{3+}$ ions in 4b site in the Mn molecular field [4].The value of the energy splitting due to the molecular field of Mn is given by $\Delta_{sch} = 2\mu_{Yb}H_{mf}$, where $\mu_{Yb}$is the moment of Yb in the 4b site, and $H_{mf}$ is the effective molecular field at Yb 4b sites. This splitting was estimated for the sample by fitting the $C_p$ data (Fig. 4.16) using the above formula.

A smaller anomaly in $C_p$ at FM ordering at 3.5 K is seen, which appears to be only related to total number of $Yb^{3+}$ ions. The application of a magnetic field considerably changes the behavior of $C_p$ at low T. The FM transition at ~3.5 K, due to the ordering of $Yb^{3+}$ ions at

2a sites, is suppressed by the field, and eventually disappear, while the Schottky shift to higher temperature as shown in Fig.4.15.

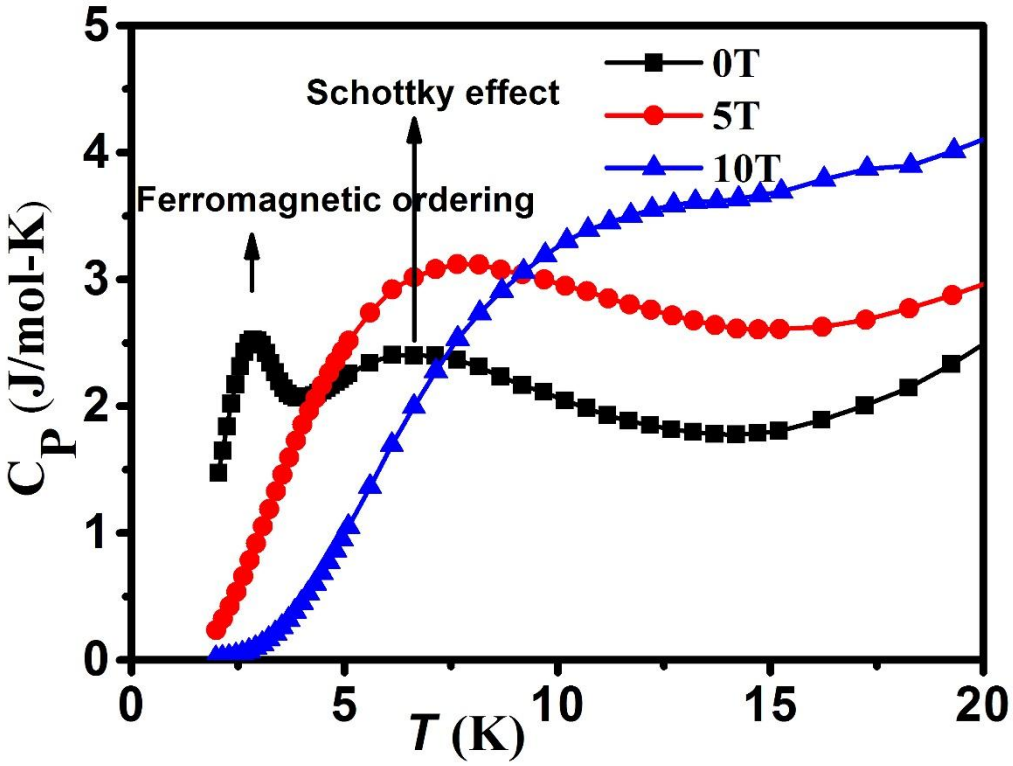


Figure. 4.15: Low temperature behavior of specific heat of $Yb_{0.9}Mg_{0.1}MnO_3$with variation of magnetic field.

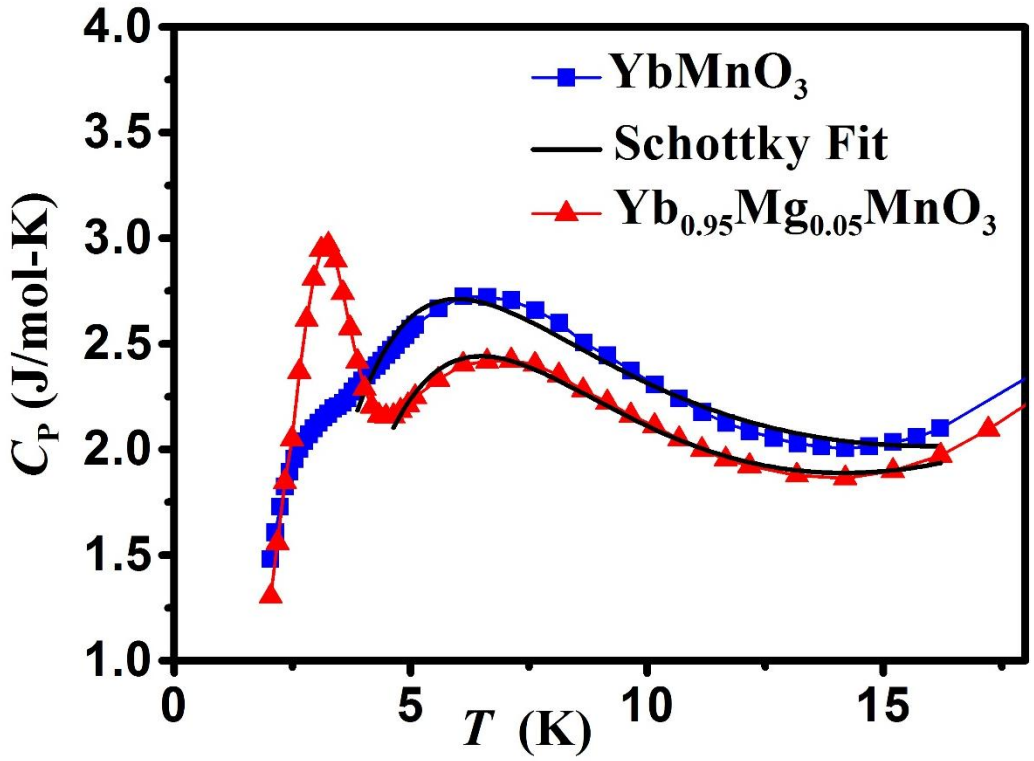


Figure. 4.16: Low temperature behavior of specific heat of $Yb_{0.9}Mg_{0.1}MnO_3$ with schottky fitting with theoretical model.

The magnetic entropy change ($\Delta S_{mag}$) and adiabatic temperature change ($\Delta T_{ad}$) for the compound $Yb_{0.9}Mg_{0.1}MnO_3$ are shown in fig 4.17 and 4.18 for 5 T, and 10 T magnetic field change. $\Delta S_{max}$ is found to increase with an increase in the applied magnetic field and maximum $\Delta S_{max}$ for 5 T and 10 T are 0.85 J $mol^{-1}K^{-1}$ and 1.98 J $mol^{-1}K^{-1}$, respectively. $\Delta S_{mag}$ maximum in Fig. 4.17 does not coincide with the transition temperature. The position of the maximum shifts from 4.4 to 7.4 K when $\Delta H$ increases from 5 to10T. $\Delta T_{ad}$ is obtained from the isentropic difference between the entropy curves S(0,T) and S(H,T). $\Delta T_{ad}$ versus T is plotted in Fig.4.18 for different fields. The peak value of $\Delta T_{ad}$ is nearly 7 K and 16 K for $\Delta H$ = 5 T and 10 T, respectively.

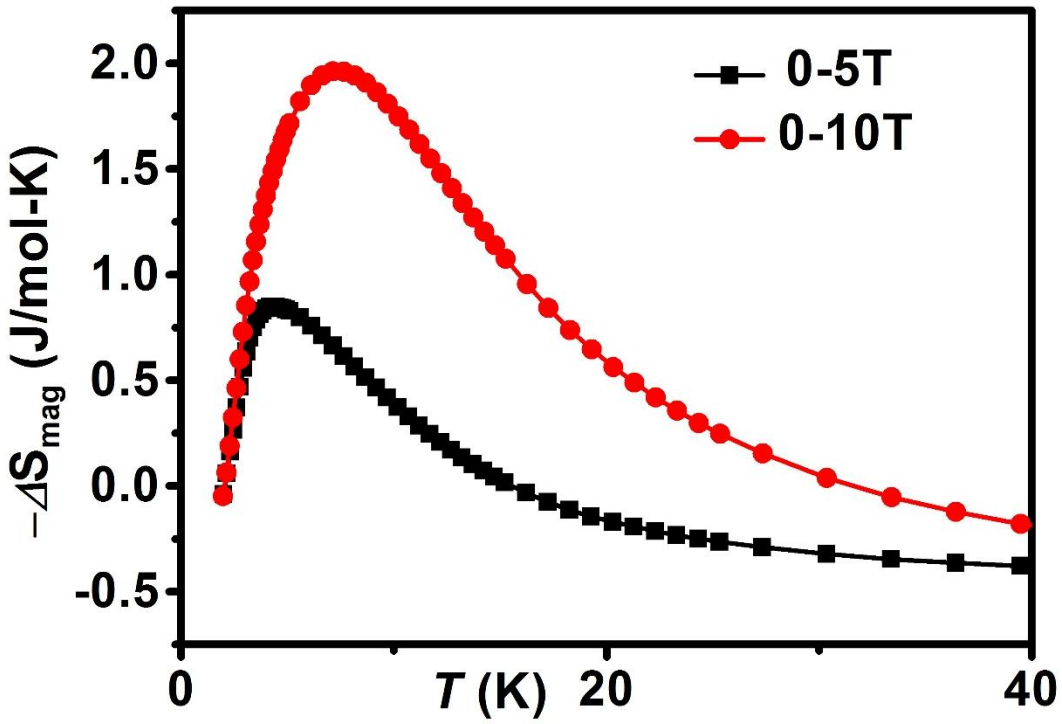


Figure. 4.17: Temperature variation of magnetic entropy change with different field change for $Yb_{0.9}Mg_{0.1}MnO_3$.

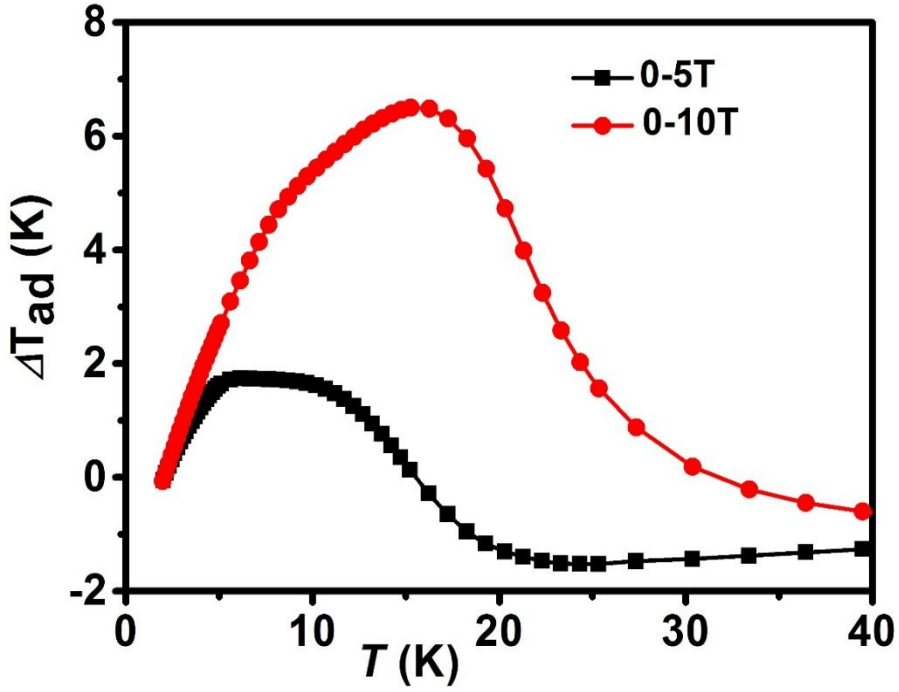

Figure. 4.18: Temperature variation of adiabatic temperature change with different field change for $Yb_{0.9}Mg_{0.1}MnO_3$.

The relative cooling power (RCP) is calculated to determine the cooling efficiency of $Yb_{0.9}Mg_{0.1}MnO_3$of equation 4.4. The RCP values of $Yb_{0.9}Mg_{0.1}MnO_3$, for $\Delta H = 5T$ and 10T, are found to be 6 J/mol and 26 J/mol, respectively.

## 4.3.3. Magnetocaloric effect:

In chapter 3, magnetization results of $Yb_{1-x}Mg_xMnO_3$ ( x = 0.00 and x = 0.05)have been discussed, which shows ferromagnetic ordering in $Yb^{3+}$ sub-lattice at low temperature around 3 K, and antiferromagnetic ordering of $Mn^{3+}$ around 85 K. In fig. 4.19, isothermal magnetization M (H) data have been shown for $Yb_{1-x}Mg_xMnO_3$ (x = 0.00 and x = 0.05) samples measured at various temperatures around the Yb ordering transition temperature $T_{N2}$. The field-induced magnetic transition can be clearly seen as a change slope around 35 kOe in the M-H curves for $T < T_{N2}$.

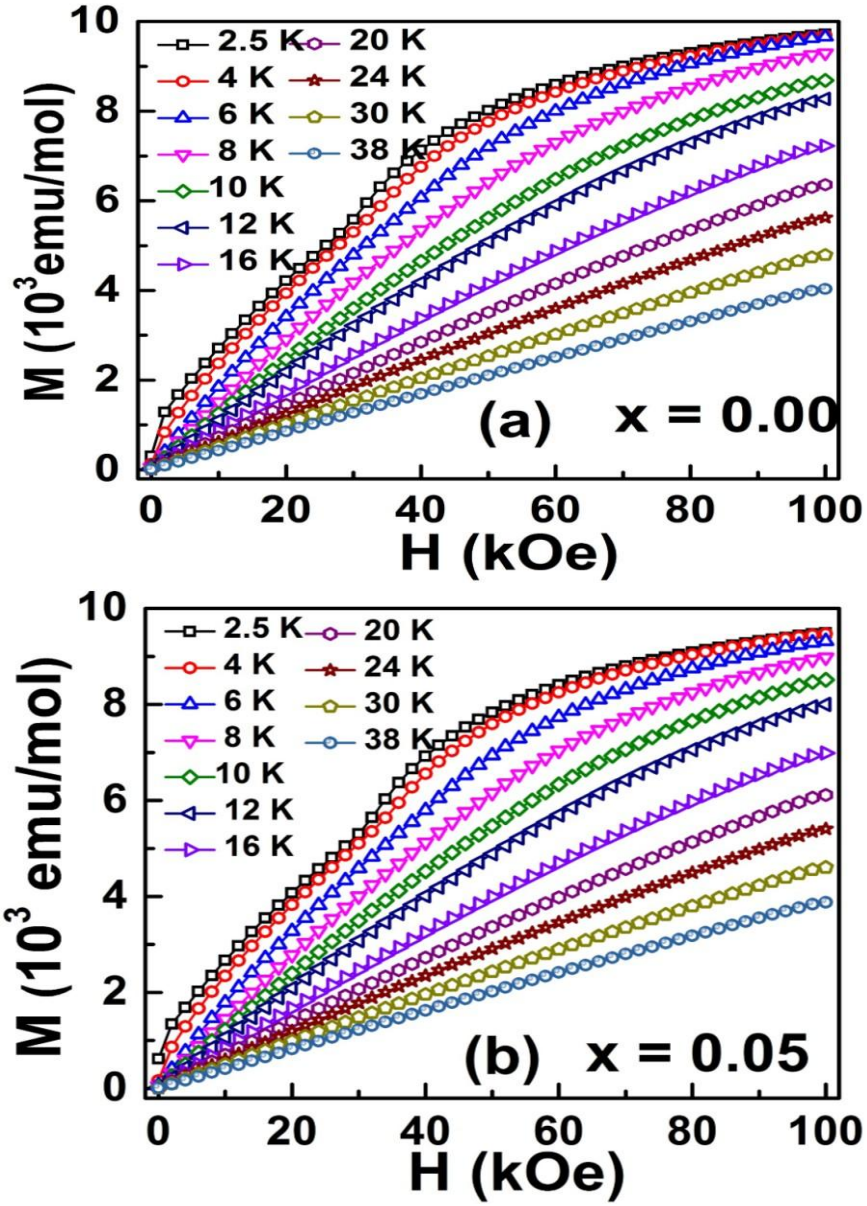


Figure.4.19: Field dependence of isothermal magnetization for $Yb_{1-x}Mg_xMnO_3$.(a) x = 0.00 and (b) x = 0.05.

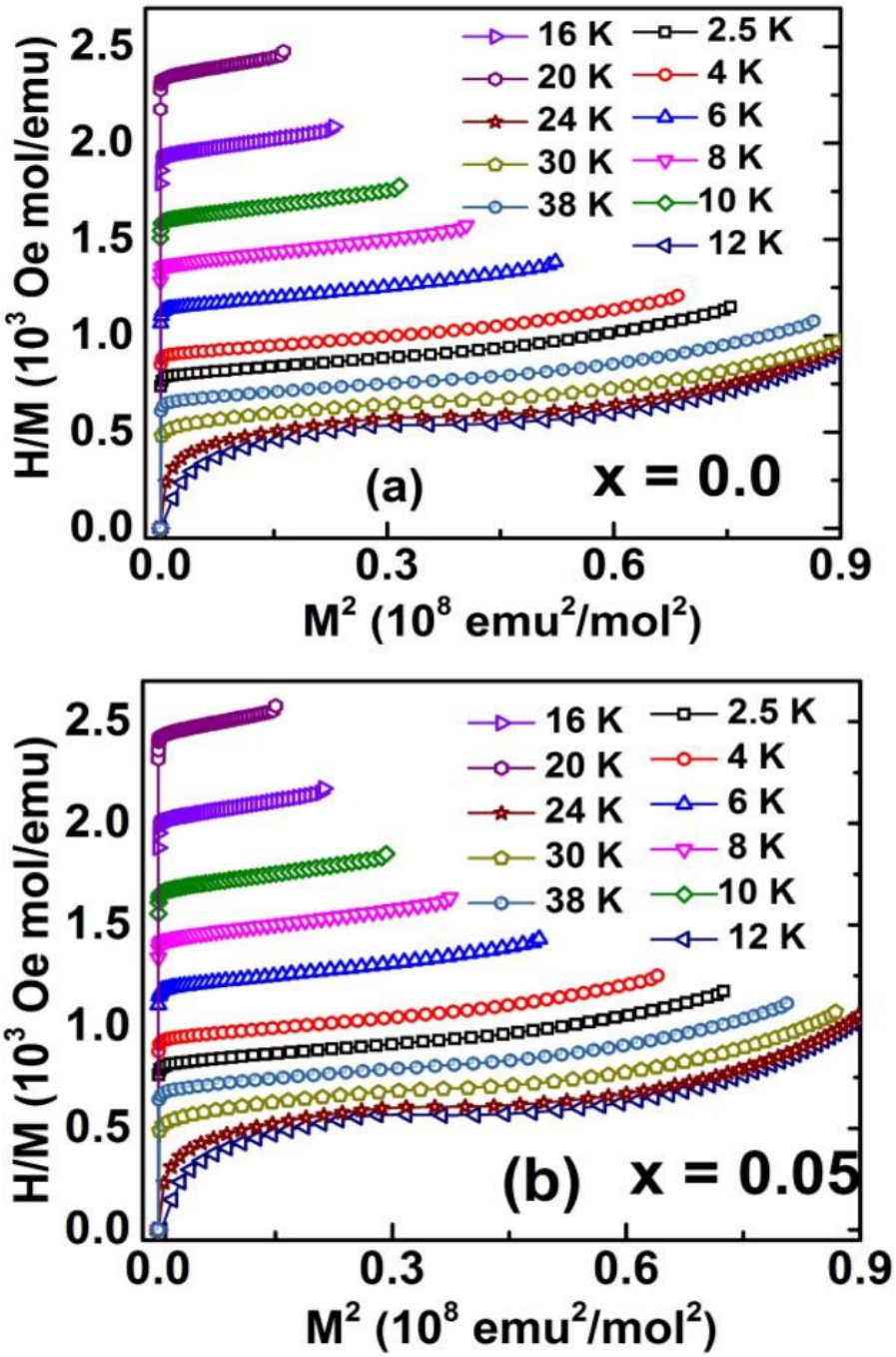


Figure.4.20: The Arrott plots of H/M vs $M^2$ at various temperatures for $Yb_{1-x}Mg_xMnO_3$ (a) x = 0.00 and (b); x = 0.05 samples.

To understand the magnetic phase transition, the *M*(*H*) data have been transformed into Arrott plots, H/M versus $M^2$ as shown in Fig. 4.20 [10]. Data of both samples show positive slopes in the full $M^2$ ranges, which is expected for a second-order phase transition [19].

From the M vs H curves magnetic-entropy change ($\Delta S_M$) can be obtained from Maxwell's thermodynamic relationship [20]:

$$\left(\frac{\partial M}{\partial T}\right)_H = \left(\frac{\partial S}{\partial H}\right)_T \qquad (4.5)$$

When the field is applied from 0 to H, the resulting $\Delta S_M$ is given by

$$\Delta S_M(T,H) = \int_0^H \left(\frac{\partial M}{\partial T}\right)_H dH \qquad (4.6)$$

Eq. (4.6) can be approximated by the equation (4.7) for magnetization measured at discrete field and temperature intervals [13]:

$$\Delta S_M(T_{av})_{\Delta H} = \frac{\delta H}{2\delta T}\left(\delta M_1 + 2\sum_{k=2}^{n-1}\delta M_k + \delta M_n\right) \qquad (4.7),$$

with the uncertainty in $\Delta S_M(T_{av})_{\Delta H}$ as,

$$\sigma\left|\Delta S_M(T_{av})_{\Delta H}\right| = \frac{1}{2\,|\,\delta T\,|}\left\{\begin{array}{l} |\,\delta H\left(\sigma M_1 + 2\sum_{k=2}^{n-1}\sigma M_k + \sigma M_n\right) \\ +\left(|\,\delta M_1\,|\,\sigma H_1 + 2\sum_{k=2}^{n-1}(|\,\delta M_k\,|\,\sigma H_k) + |\,\delta M_n\,|\,\sigma H_n\right) \\ +2\left|\Delta S_M(T_{av})_{\Delta H}\right|\times(\sigma T_u + \sigma T_l)\,| \end{array}\right\}$$

where, $\delta T = T_u - T_l$ is the temperature difference between the two isotherms measured at $T_u$ and $T_l$ with the magnetic field varying from $H_1$ to $H_n$ in constant steps of δH. $\delta M_k = M(T_u)_k - M(T_l)_k$ is the difference in the magnetization at $T_u$ and $T_l$ for each magnetic field $H_k$. For the calculation of relative error in the entropy change, following [13], the accuracy of magnetization measurements are taken as 0.5% and the accuracy of the magnetic field as 0.1%. The manufacturer quoted temperature stability of 0.25% is used as the error for temperatures. In general, the relative error in the calculated entropy change is 10-20% except at very high fields and low temperatures (H ~ 10 T, T < 4 K).

Values of $-\Delta S_M$ for different $\Delta H$ as a function of temperature determined under an applied magnetic field up to 100 kOe are presented in Fig. 4.21 The $-\Delta S_M$ is positive in the entire temperature range for both samples. The curves present a characteristic shape with a broad maximum in the vicinity of the FM transition of the Yb moments. The magnitude of the peak increases with increasing value of $\Delta H$ for each composition and the position of the maximum shifts from 3 to 9 K when the magnetic field change increases from 1 to 100 kOe. The values of the peak $-\Delta S_M^{max}$ of $Yb_{1-x}Mg_xMnO_3$ are 3.02 ± 0.37 J/(mol-K) for x = 0.00, and 2.63 ± 0.36 J/(mol-K) for x = 0.05 with $\Delta H$ = 100 kOe. The magnitude of maximum $-\Delta S_M$ ($-\Delta S_M^{max}$) increases with increasing magnetic field [14].

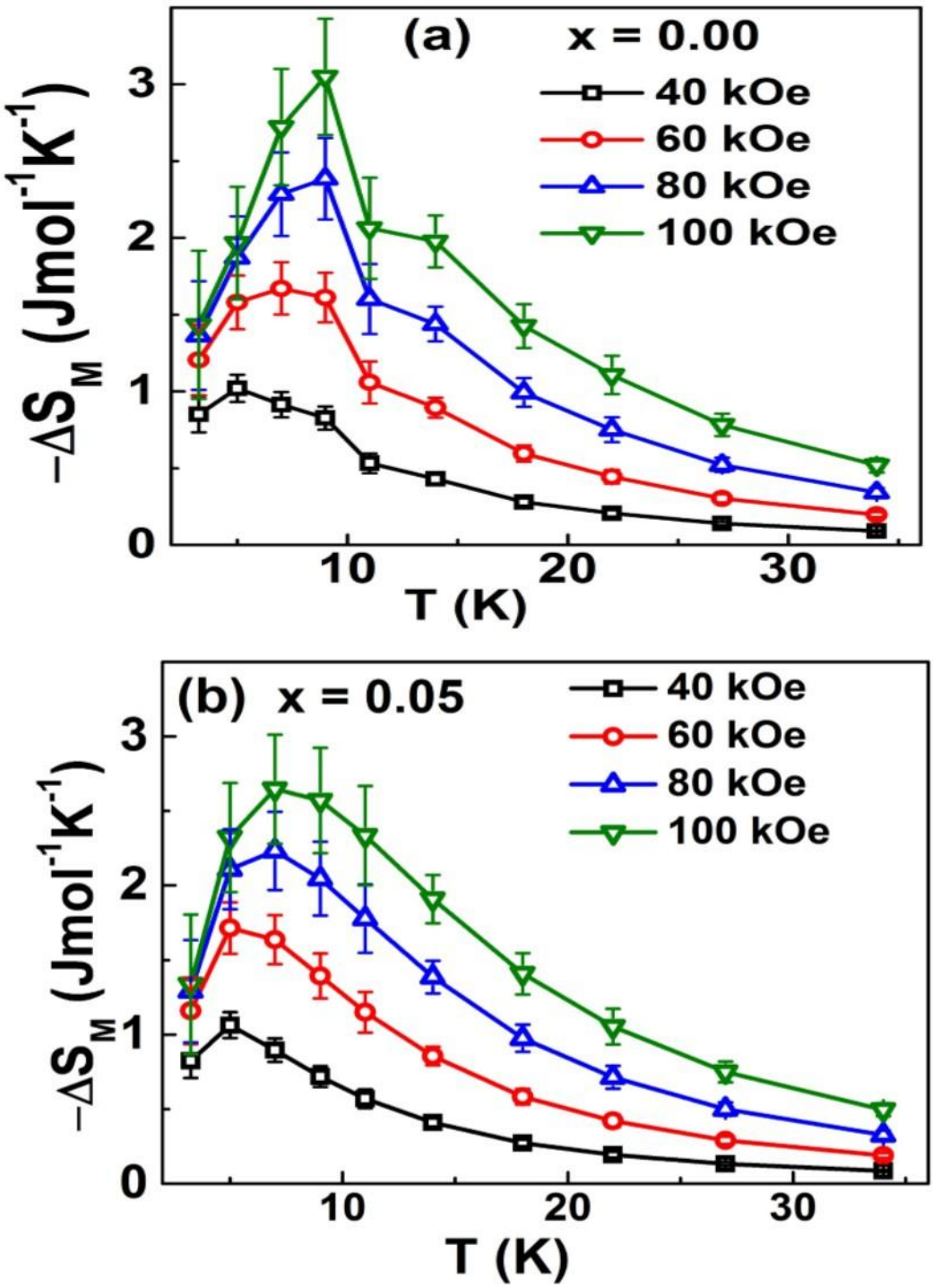


Figure.4.21: Temperature variation of magnetic entropy change ($\Delta S_M$) for $Yb_{1-x}Mg_xMnO_3$ (a) x=0.00 and (b) x = 0.05.

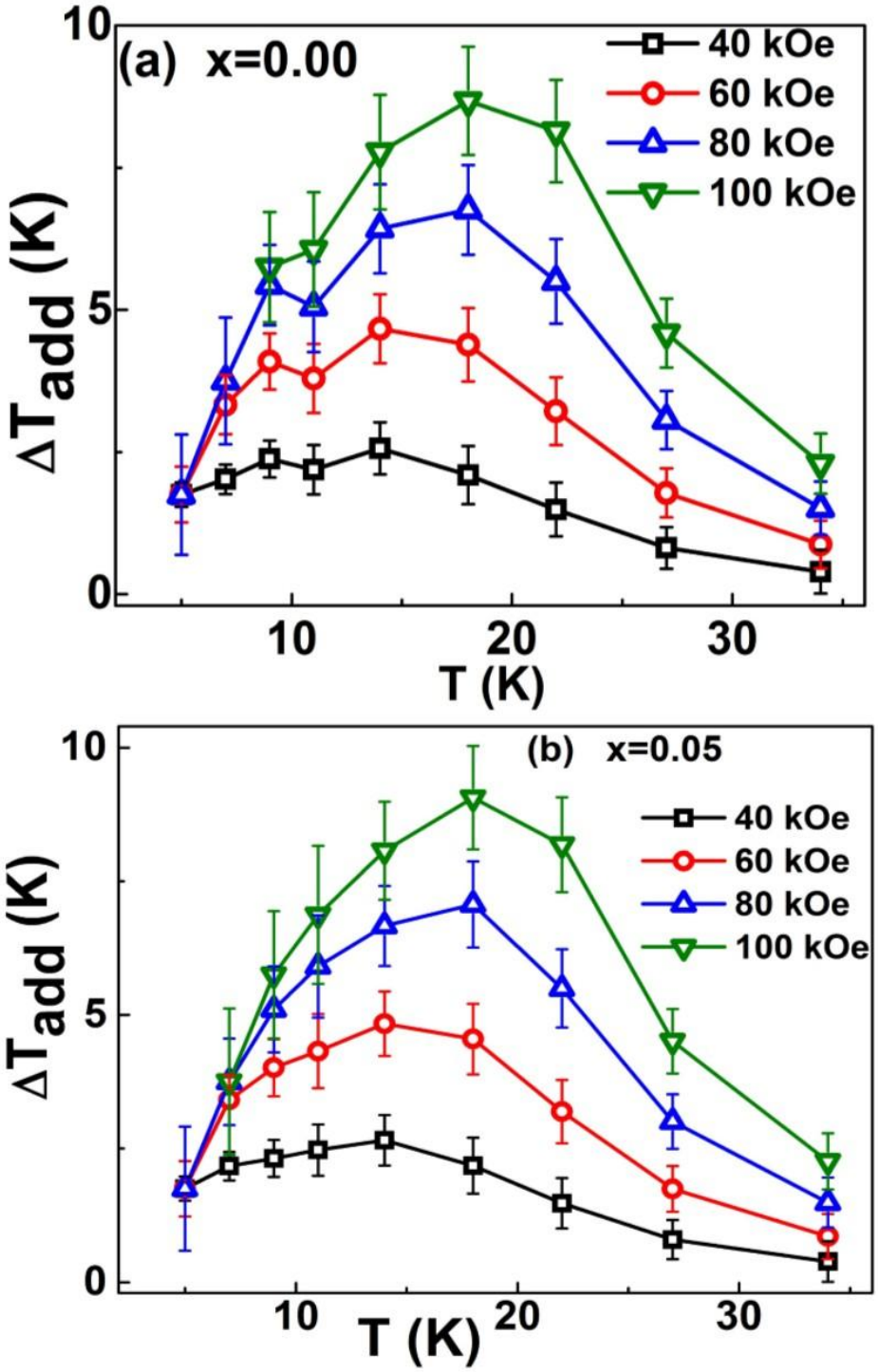


Figure.4.22: Temperature variation of adiabatic temperature change ($\Delta T_{ad}$) for different field change for $Yb_{1-x}Mg_xMnO_3$ (a) x=0.00 and (b) x=0.05.

The adiabatic temperature rise $\Delta T_{ad}$ is determined from the magnetization and heat capacity measurements as functions of temperature and magnetic field. The specific heat data ($C_P$) of $Yb_{1-x}Mg_xMnO_3$ (x = 0.00 and 0.05) as a function of temperature is discussed in 4.3.1.

The total entropy *S (*0, *T)* under zero magnetic field can be calculated from the heat capacity data as,

$$S(0,T) = \int_0^T \frac{C(0,T)}{T} dT, \qquad (4.8)$$

$\Delta T_{ad}$ is the isentropic difference between S(0, T) and S (H,T). S(H,T) is obtained by subtracting the corresponding $\Delta S_{mag}$(H,T) data (calculated from the magnetization data above) from S(0,T) [14,15]. The temperature dependence of $\Delta T_{ad}$ is plotted in fig. 4.22 for

Table.4.1. Comparison of different magnetocaloric properties of $Yb_{1-x}Mg_xMnO_3$ (x = 0.00 and 0.05) samples with reported data in the literature.

| **Composition** | **$T_{Peak}$ (K)** | **ΔH (kOe)** | **$\Delta S_M^{max}$ (J $mol^{-1}K^{-1}$)** | **ΔTad(K)** | **RCP (J/mol)** | **Ref.** |
|---|---|---|---|---|---|---|
| **$YbMnO_3$** | ~7 | 100 | 3.02 ± 0.37 | 8.6 ±0.95 | 41 ± 9 | Present |
| **$Yb_{0.95}Mg_{0.05}MnO_3$** | ~7 | 100 | 2.63 ± 0.36 | 9.06 ± 0.96 | 40.0 ± 10 | Present |
| **$YbMnO_3$(Singlecrystal)** | ~ 9 | 80 | ~ 2.3 | ~15 | ~ 26 | [8] |
| **$HoMnO_3$(Single crystal)** | ~ 12 | 80 | ~ 5.2 | ~12.5 | ~ 144 | [8] |
| **$DyMnO_3$(Single crystal)** | ~ 12 | 80 | ~ 5.5 | ~11.5 | ~ 155 | [8] |
| **$HoMnO_3$(Single crystal)** | ~ 9.5 | 70 | ~3.5 | ~6.5 | ~86 | [14] |

different fields. The peak of the curve corresponds to $\Delta T_{ad}$~8.6 ± 0.95K for x = 0.00 and ~9.06 ± 0.96 K for x = 0.05 for a field change of 100kOe. The MCE values (magnitudes of $|-\Delta S_M|$ and $\Delta T_{ad}$) determined from magnetization measurements is slightly higher compared to that determined from the heat capacity measurements in the section 4.3.1, and this result is due to the difference in measurement conditions [16]; magnetization measurements are done under

isothermal conditions while heat capacity measurements are done under adiabatic or semi/quasi adiabatic conditions. Also the temperature steps (ΔT) used for magnetization and heat capacity measurements are different. For comparison, the magnetocaloric data are listed in Table 4.1 of various magnetic materials that could be used as magnetic refrigerants.

In addition to the values of $\Delta S_M$ and$\Delta T_{ad}$ the relative cooling power RCP is also evaluated to determine the cooling efficiency of these material. RCP is a measure of the quantity of heat transferred by the magnetic refrigerant between hot and cold sinks and is defined in eq 4.4.The RCP values of $Yb_{1-x}Mg_xMnO_3$ are 30 ± 6 J /mol, and 29.0 ± 6 J/mol with ΔH = 80 kOe for x = 0.0 and 0.05 respectively. These values are higher than single crystal $YbMnO_3$ (RCP = 26 J/mole with ΔH = 80kOe) [8]. The RCP values increase with increasing field for both compounds.

For second order transitions $-\Delta S_M^{\max} = -kM_S(0)h^{2/3} - S(0,0)$, where h is the reduced field just around $T_C$ $\left[h = (\mu_0\mu_B H)/(K_B T_C)\right]$, k is a constant, Ms(0) is the saturation magnetization at low T and S(0, 0) is a reference parameter [28]. Fig.8(a) shows the linear dependence of $-\Delta S_M{}^{\max}$ versus $h^{2/3}$ which implies the second order transition for $Yb_{1-x}Mg_xMnO_3$ (x = 0.0 and 0.05).

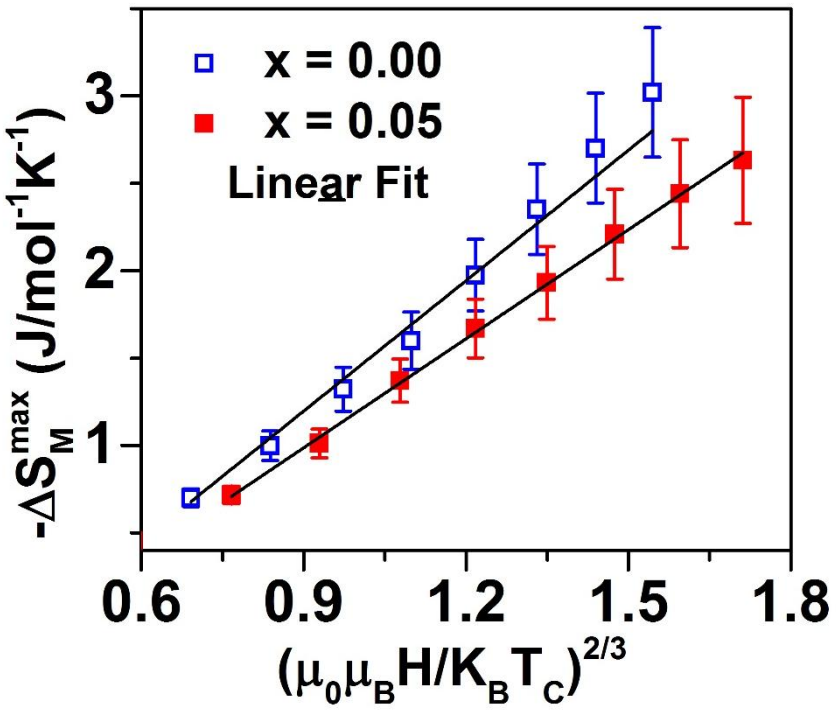

Figure.4.23: Temperature dependence of magnetic entropy change $-\Delta S_M^{max}$ vs $h^{2/3}$for $Yb_{1-x}Mg_xMnO_3$ (x = 0.0 and 0.05). Symbols correspond to data points and the solid lines are linear fit to the data.

For a second order transition, the phenomenological universal curve, suggested by Franco and Conde [18], converges the $\Delta S_M$ versus temperature data on a single universal curve if ($-\Delta S_M/\Delta S_M^{max}$) versus a *rescaled* temperature (θ) is plotted, where θ is defined in Eq. 4.9 below,

$$\theta = -\frac{T-T_C}{T_{r1}-T_C}, \qquad T \le T_C \qquad 4.9(a)$$

$$\theta = \frac{T-T_C}{T_{r2}-T_C}, \qquad T > T_C \qquad 4.9(b)$$

Where $T_{r1}$ and $T_{r2}$ are temperatures of the two reference points. For the present study, $T_{r1}$ and $T_{r2}$ are selected such that $\Delta S_M(T_{r1,2}) = 1/2\ \Delta S_M^{max}$ [19]. Figure 4.24 shows the dependence of $-\Delta S_M/\Delta S_M^{max}$ versusθ for typical field changes for $Yb_{1-x}Mg_xMnO_3$ (x = 0.00 and 0.05). It can be clearly seen that the experimental points of the samples distribute on one universal curve that can be well fitted by the Lorentz function [19]

$$\left|\frac{\Delta S_M}{\Delta S_M^{max}}\right| = \frac{1.00}{1.00+(\theta-0.00)^2} \qquad (4.10),$$

where the solid line in fig. 4.24 represents the curve corresponding to Eq. 4.10.

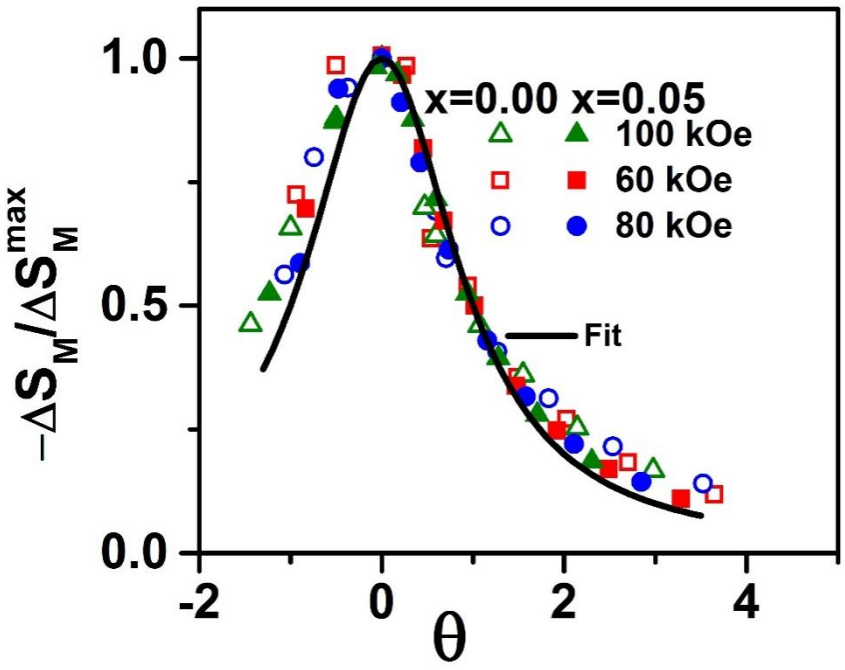

Figure.4.24: The universal curve behavior of the normalized entropy change curves as a function of the rescaled temperature for different magnetic field for $Yb_{1-x}Mg_xMnO_3$ (x = 0.0 and 0.05). Symbols correspond to data points and the solid line is the curve representing equation 4.10.

## 4.3.4 Conclusion

The temperature variation of specific heat (Cp) of single phase$Yb_{1-x}Mg_xMnO_3$ (x = 0 and 0.05) has been studied. A peak in $C_p$ is obtained for both samples, it is at ~83 K for x = 0 and at ~86 K for x = 0.05 samples and is attributed to the antiferromagnetic ordering indicating a small increase in Neel temperature due to Mg substitution. The broad feature in $C_p$ vs T at ~6.5 K is attributed to the Schottky anomaly. The estimated effective molecular fields from the Schottky analysis are $H_{mf}$ = 3.0 and 3.5 tesla for $YbMnO_3$ and $Yb_{0.95}Mg_{0.05}MnO_3$, respectively. High temperature shift of Schottky anomaly with Mg doping indicates increase in effective molecular field of Mn at the Yb 4*b* site. The data supports the idea that although molecular field is mainly responsible for the Schottky anomaly in $Yb_{1-x}Mg_xMnO_3$, $Mn^{3+}$ spin ordering also affects it. Specific heat data also shows that the ferromagnetic transition is taking place at 2.7 K for x = 0.0 and T = 3.3 K for x = 0.05 samples due to Yb 2*a* site, thus these compounds show multiple transitions. The data has also been analyzed to determine magnetocaloric properties of these materials. Magnetic part of the specific heat is obtained by subtracting the lattice contribution estimated using two Debye temperatures. The magnetic entropy change ($\Delta S_{mag}$) for pure and doped samples are 2.0 J $mol^{-1}K^{-1}$ and 2.1 J $mol^{-1}K^{-1}$respectively, while the calculated relative cooling power (RCP ) are26.1 J/mol and 27.2 J/mol for a field change of 10 tesla.

Polycrystalline hexagonal $Yb_{0.9}Mg_{0.1}MnO_3$ has also been examined for its magnetic, and magnetocaloric properties. Antiferromagnetic ordering of the Mn sublattice occurs at $T_N$ = 88 K. At low temperature (~3.5 K), the compound shows ferromagnetic (FM) ordering attributed to Yb in site 2a. A Schottky anomaly related to the Yb moments is observed due to Mn molecular field at temperature ~6.7 K. The values of isothermal magnetic entropy change, 1.98 J $mol^{-1}K^{-1}$, adiabatic temperature change 16 K and relative cooling power 26 J/mol for a field change of 10 T are also significantly for $Yb_{0.9}Mg_{0.1}MnO_3$ as a magnetic refrigerant at low temperatures.

Isothermal magnetization curves measured near the Yb long range ordering temperatures indicate a field induced magnetic transition with applied field. Isothermal magnetic entropy

change ($-\Delta S_M$) is calculated from the magnetization curves measured for different temperatures. Values of maximum entropy change ($-\Delta S_M^{max}$), the adiabatic temperature change ($\Delta T_{ad}$) and the relative cooling power (RCP) for these compounds are found to be 3.02 ± 0.37 J/(mol-K), 8.6 ± 0.95 K and 41 ± 9 J/mol for x = 0.00, and 2.63 ± 0.36 J/(mol-K), 9.06 ± 0.96 K and 40.0 ± 10 J/mol for x = 0.05, respectively, for ΔH = 100 kOe. $\Delta S_M^{max}$ versus $h^{2/3}$ shows that these compounds exhibit a second order transition.

## 4.4 References:

[1] H. Yakel, W. C. Koehler, E. F. Bertaut, and F. Forrat, Acta Crystallogr **16**,(1963), 957.

[2] S. C. Abrahams,ActaCrystallogr. B**57**,(2001), 485.

[3] I. K. Jeong, N. Hurb, and Th. Proffen, J. Appl. Crystallogr **40**,(2007), 730.

[4] N. Abramov, V. Chichkov, S. E. Lofland and Ya. Mukovskii, J. Appl. Phys. **109** (2011) 07D912.

[5] N. Abramov, S. Lofland, and Ya. Mukovskii, phys. status solidi B, **1-3** (2012) 48318.

[6] X. Fabreges, I. Mirebeau, P. Bonville, S. Petit, G. Lebras-Jasmin, A. Forget, G. Andre, and S. Pailhes, Phys. Rev. B **78** (2008) 214422.

[7] D. G. Tomuta, S. Ramakrishnan, G. J. Nieuwenhuys and J. A. Mydosh,J. Phys.: Condens. Matter, **13** (2001) 4543.

[8] A. Midya, S. N. Das, P. Mandal,S. Pandya and V. Ganesan, Phys. Rev. B**84**, (2011) 235127.

[9]K. A. Gschneidner, Jr. and V. K. Pecharsky, Annu. Rev. Mater. Sci. **30**, (2000) 387.

[10] A. Arrott and J. Noakes, Phys. Rev. Lett. **19**, (1967), 786.

[11] B. K. Banerjee, Phys. Lett. **12**,(1964),16.

[12] A.H. Morrish, The Physical Principles of Magnetism Wiley, New York, 1965 (Chapter3).

[13] V.V. Pecharsky and K.A. Gschneidner, J. Appl. Phys.,**86**,(1999), 565.

[14] A. Midya, P. Mandal,S. Das, S. Banerjee, L. S. Sharath Chandra, V. Ganesan and S. Roy Barman, ,Appl. Phys. Lett. **96**, (2010), 142514.

[15] V. K. Pecharsky and K. A. Gschneidner, , Jr, Phys. Rev. Lett., **78**,(1997) 4494.

[16] M. Foldeaki, W. Schnelle,E.Gmelin, P. Bernard, B.Koszegi, A. Giguere, R. Chahine, and T. K. Bose, , J. Appl. Phys. **82**,(1997),309.

[17] H. Oesterreicher and F.T. Parker, J. Appl. Phys. **55, (**1984), 4334.

[18] V. Franco and A. Conde, Int. J Refrig. **33**,(2010), 465.

[19] Q. Y. Dong, H. W. Zhang, J. R. Sun, B. G. Shen, and V. Franco, J. Appl. Phys, **103**,(2008), 116101.12.

# Chapter 5

## *Structural, magnetic, and magnetocaloric effect of polycrystalline $Yb_{1-x}Sc_xMnO_3$*

## 5.1 Introduction:

Materials with simultaneous presence of more than one ferroic property (multiferroics) with a strong coupling between them have been the subject of tremendous research activity in recent years. Control of electric polarization by the application of magnetic field and inducing magnetic ordering by the application of electric field in these materials are expected to lead to next generation multifunctional devices for applications in information storage processes, spintronics, multiple-state memories, magnetoelectric sensors, etc. [1–4]. One typical example of multiferroic materials is hexagonal manganites $R\mathrm{MnO_3}$ with space group $P6_3cm$, for elements at the rare-earth *R* site with a relatively small ionic radius, e.g., Ho, Er, Tm, Yb, Lu, Y, and Sc which exhibit a strong coupling between electric and magnetic dipoles [5–7].In these hexagonal manganites, Mn ions form a natural two dimensional edge-sharing triangular network, which becomes magnetically frustrated with an antiferromagnetic nearest-neighbor interaction [8,9].

Among rare earth hexagonal manganites $YbMnO_3$ has been studied only occasionally. The crystal structure of $YbMnO_3$ comprises layers of corner-sharing $MnO_5$ trigonal bipyramids with two apical (O1, O2) oxygen atoms and a triangular base of nonequivalent O3 and O4 oxygen atoms.Yb atom occupies two crystallographic sites (in Wyckoff notations), 2a and 4b of space group $P6_3cm$. The Yb–O displacements give rise to a ferroelectric moment along the *c*-axis ($T_C$= 990 K), the $Mn^{3+}$ moments order at the Neel temperature ($T_N$ = 85 K) and below Tc ~ 5 K, the magnetic moments of the $Yb^{3+}$ions are completely ordered [10]. Most of the studies in such multiferroic manganites focus on their magnetic and ferroelectric behavior, but less work has been undertaken on exploring their magnetocaloric effect (MCE) properties. MCE describes the reversible change in temperature of a material under adiabatic condition produced by the magnetic entropy change $\Delta S_M$ due to the variation in applied magnetic field [11-13].

In the present investigation, effect of Sc substitution on structural, magnetic and magnetocaloric properties of $Yb_{1-x}Sc_xMnO_3$ (x = 0.1 and 0.2) system is studied. In order to successfully use multiferroic materials in practical applications, the most important criterion is that the coupling between the ferroelectric and magnetic ordering should occur close to room temperature. Thus, it is necessary to enhance the low antiferromagnetic ordering $T_N$ of $YbMnO_3$ through chemical doping. In chapter 3 on divalent Mg ion doped $YbMnO_3$, it is shown that $T_N$ increases marginally with doping. The increase in $T_N$ can be explained on the basis of smaller cell volume (Mg has small ionic radii), which may lead to strong exchange interactions and therefore higher ordering temperatures. Hence, it is of significance to search for other effective dopants. Hexagonal $ScMnO_3$ exhibits an antiferromagnetic (AFM) transition at 139 K [14] and $Sc^{3+}$ has small ionic radius compare to that of $Yb^{3+}$. The large field induced magnetization observed in $Yb_{1-x}Sc_xMnO_3$ is worth us to investigating the magnetocaloric behavior in this system.

## 5.2 Experimental Details

Polycrystalline samples of $Yb_{1-x}Sc_xMnO_3$ (x = 0.1 and 0.2) were synthesized by the conventional solid state reaction method. High-purity (purity better than 99.9%) $Yb_2O_3$, $Sc_2O_3$ and $MnCO_3$, powders are obtained from M/s Sigma-Aldrich. The precursors $Yb_2O_3$ and $Sc_2O_3$ powders are preheated at 500 K for 5 h to remove any absorbed moisture. Stoichiometric proportions of $Yb_2O_3$, $Sc_2O_3$ and $MnCO_3$ powders are thoroughly mixed, and then calcined in platinum crucibles at 1150 $^0$C in air for 24 h with an intermediate grinding for homogenization. The calcined mixture is cold pressed into pellets at approximately $5\times10^7$ Pa pressure and then sintered at 1350 $^0$C in air for 20 hours. Finally, all samples are slowly cooled to room temperature for sufficient oxygenation. The phase purity of each sample is checked by powder x-ray diffraction (XRD) using a Bruker D8 Advance X-ray powder diffractometer operating with the Cu-Kα radiation. The magnetization measurements, performed in a Cryogenic Inc. (UK) make vibrating sample magnetometer operating at 20.4 Hz. The temperature dependence of magnetic moment was measured for zero-field cooled (ZFC) and field cooled (FC) conditions at a magnetic field of 1000 Oe. The magnetization isotherms in fields up to 10 T were measured, at different temperatures in the vicinity of low temperature ordering transition.

# 5.3 Results and Discussion

## 5.3.1 Structural characterization

The X-ray diffraction patterns and the Rietveld refinement of polycrystalline samples $Yb_{1-x}Sc_xMnO_3$( x = 0.1 and 0.2) are shown in Fig. 5.1. Both samples are in single phase and the measured patterns can be indexed to the hexagonal phase with $P6_3cm$ space group (JCPDS NO.38-1246). Refined values of lattice parameters and discrepancy factors for $Yb_{1-x}Sc_xMnO_3$( x = 0.1 and 0.2) are shown in Table 5.1 along with corresponding values for $YbMnO_3$.It is clearly seen that due to Sc substitution, the relative cell parameter c/a increases. Overall the cell volume decreases. The decrease in lattice constant *a* and cell volume is due to the smaller ionic radius of $Sc^{3+}$ [Shannon radius = 0.87Å for coordination number (CN) = 8] than $Yb^{3+}$ (Shannon radius = 0.985 Å for CN = 8).As the average *A*-site (i.e., Yb site) radius changes with Sc content, it is expected that the tolerance factor will also change.

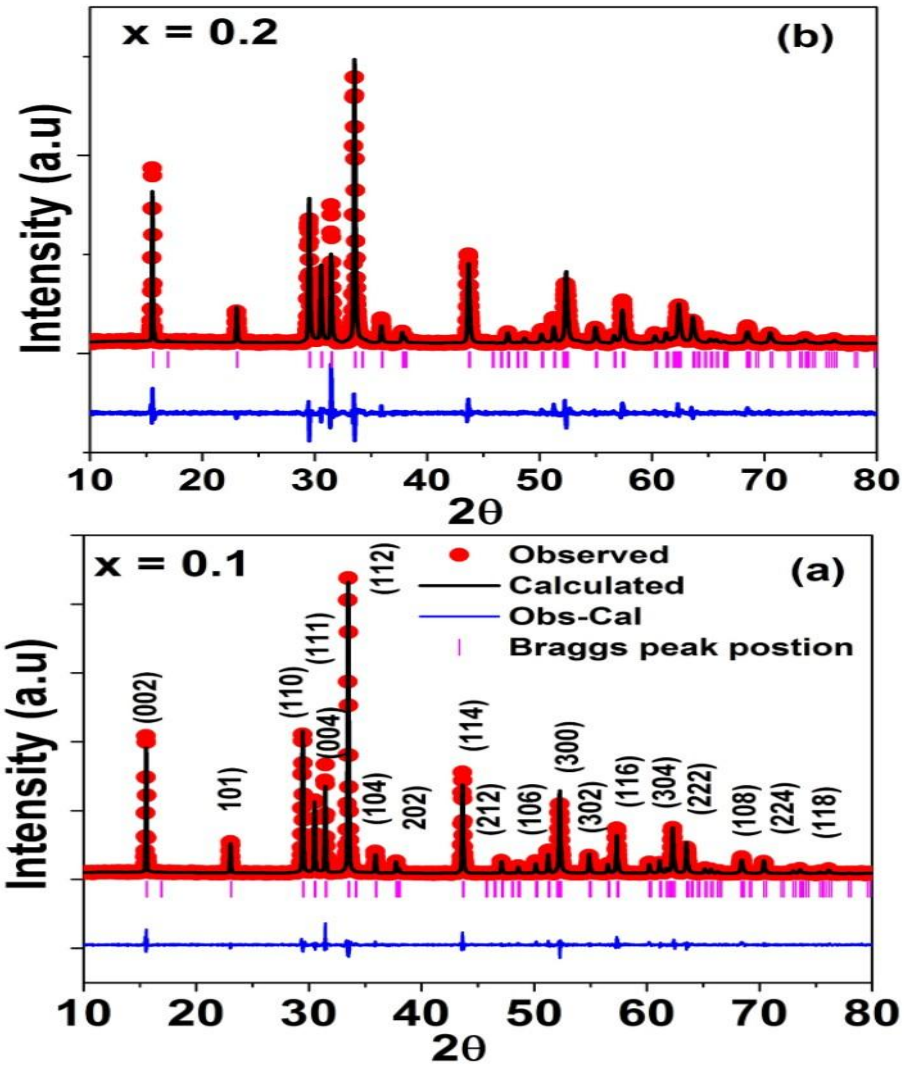

Figure.5.1: Rietveld refinement of room temperature XRD pattern of $Yb_{1-x}Sc_xMnO_3$ (a) x = 0.1 and (b) x = 0.2 samples indexed in space group P63cm.

Some selected bond distances and bond angles of $Yb_{1-x}Sc_xMnO_3$ ($x$ = 0.1 & 0.2) as well as those of $YbMnO_3$ are given in Table 5. 2. The value of *a* decreases in Sc doped sample when compared to that in $YbMnO_3$ sample. This change is ascribed to the decrease in the average *ab*-plane i.e., Mn-O3,Mn-O4onSc doping. The average Mn-O distances in $MnO_5$ units are significantly shorter in the doped samples compared to pure $YbMnO_3$. In the hexagonal phase the $Mn^{3+}$ion is fivefold coordinated, forming a trigonal bipyramid polyhedral environment. Polyhedral distortions Δ are calculated using the following formula [15],

$$\Delta = \frac{1}{N}\sum_{n=1}^{N}\left(\frac{d_n - \langle d \rangle}{\langle d \rangle}\right)^2 \qquad (5.1)$$

Where N is the coordination number (N = 5), $d_n$ is the individual distance between Mn and the $n^{th}$ nearest oxygen neighbor, and <d> is the average distance value.

Table 5.1**.** Refined crystallographic parameters and reliability factors of Rietveld refinement for $Yb_{1-x}Sc_xMnO_3$ ($x$ = 0.1 & 0.2) samples at room temperature.

| **$Yb_{1-x}Sc_xMnO_3$** | $x$ = 0.1 | $x$ = 0.2 | Compared for$YbMnO_3$in Chap 3 |
|---|---|---|---|
| *a* (Å) | 6.0577(4) | 6.046(4) | 6.0671 (4) |
| *c* (Å) | 11.362(4) | 11.3575(4) | 11.3519 (4) |
| *V* (Å$^3$) | 361.07(2) | 359.542(2) | 361.886 (2) |
| *c/a* | 1.8756 | 1.8785 | 1.8710 |
| $\chi^2$ | 4.12 | 5.97 | - |
| $R_P$*(%)* | 6.55 | 6.67 | 5.06 |
| $R_{wp}$*(%)* | 8,28 | 8.86 | 6.82 |
| $R_B$*(%)* | 4.05 | 5.34 | 4.50 |
| *t* (Å) | 0.846 | 0.842 | 0.850 |

*'t' is the tolerance factor, given as: $t=((r_{Yb+Sc}+r_o)/\sqrt{2}(r_{Mn}+r_o))$.*

Table.5.2.Main bond distances (Å) and angles for $MnO_5$ polyhedra in $Yb_{1-x}Sc_xMnO_3$ (x = 0.1 and 0.2)

| **Parameter** | ***x* = 0.1** | ***x* = 0.2** | Compared for$YbMnO_3$in Chap 3 |
|---|---|---|---|
| Mn-O1 | 1.8442 | 1.8434 | 1.8532 |
| Mn-O2 | 1.8019 | 1.8011 | 1.8366 |
| <Mn-O1, O2> | 1.823 | 1.822 | 1.845 |
| Mn-O3 | 1.9104 | 1.9067 | 1.9033 |
| Mn-O4 | 2.0931 | 2.0891 | 2.1017 |
| <Mn-O3, O4> | 2.002 | 1.9979 | 2.0025 |
| <Mn-O> | 1.9125 | 1.9099 | 1.9237 |
| ∑Radii | 2.00 | 2.00 | 2.00 |
| Yb1-O1(X3) | 2.3781 | 2.3745 | - |
| Yb1-O2(X3) | 2.4719 | 2.4676 | - |
| Yb1-O3 | 2.3251 | 2.3242 | - |
| Yb2-O1(X3) | 2.1853 | 2.1816 | - |
| Yb2-O2(X3) | 2.2765 | 2.2733 | - |
| Yb2-O4 | 2.4439 | 2.4729 | - |
| <Yb-O> | 2.3468 | 2.349 | - |
| ∑Radii | 2.405 | 2.405 | - |
| Mn-O3-Mn (°) | 118.644(3) | 118.64(6) | 119.5 (7) |
| Mn-O4-Mn (°) | 119.04(3) | 119.038(5) | 118.6 (2) |
| $\Delta(10^{-4})$ | 27 | 26.5 | 24.14 |

*$\Delta$ is the distortion of $MnO_5$ polyhedra.*

The distortion parameter is nearly constant with the Sc content in the hexagonal phase. In general, the Sc doping does not notably affect the structure of the $MnO_5$ polyhedron, in agreement with the weak changes of the trigonal bipyramidal crystal field, which is proved by the fact that the $Mn^{3+}$ions ($3d^4$) remain in the high spin state (S=2) throughout the whole doping range. TheMn-O bond lengths are in agreement with the sum of the ionic radii [14]. Moreover, in the $YbO_7$ polyhedron, the Yb-O distances are larger in x = 0.1 sample than in x = 0.2 sample, as expected due to the larger ionic radius of $Yb^{3+}$ when compared to $Sc^{3+}$. Also, the average Yb-O distances are close to the sum of the ionic radii.

## 5.3.2. Magnetic behaviors

Fig. 5.2 and 5.4 shows the temperature dependence of the susceptibility $\chi = M/H$ of $Yb_{1-x}Sc_xMnO_3$ (x = 0.1 and 0.2) measured at a magnetic field $H$ =1000 Oe. The susceptibility strongly increases with the decrease in the temperature at about 5 K. In the fig 5.3(a) and 5.5(a), we have shown zero field cooled (ZFC) and field cooled (FC) curves in the low-temperature region below 10 K. Near about 5.5 K both the curves show an anomaly with a sudden increase in magnetization with decreasing *T*. This abrupt change corresponds to the ferromagnetic (FM) ordering of $Yb^{3+}$ moments at the *2a* crystallographic sites through Yb-Yb interactions [16]. A second anomaly (a kink) is observed at 90 K for x = 0.1 and 94 K for x= 0.2, as shown in the 5.3(b) and 5.5(b), which correspond to the AFM ordering of the $Mn^{3+}$ moments and represent Neel temperatures ($T_N$) for these samples. Further, from the Rietveld refinement study itis observed that the average bond distance between the manganese and oxygen atoms decreases with increases in Sc content. This increases the covalence of Mn–O bonds and results stronger exchange interaction. It may be noted that lattice parameter *a* decreases with the Sc content and the magnetic interaction occurs in the *a–b* plane of the hexagonal manganites. Therefore, the increase in covalence of Mn–O accounts for both the increase in magnetic ordering temperature and the decrease in the lattice parameter *a*. The increase in $T_N$ from 85 K for $YbMnO_3$ to 94 K for $Yb_{0.8}Sc_{0.2}MnO_3$ sample also can be explained on the basis of smaller cell volume, which might lead to strong exchange interactions and therefore higher ordering temperatures.

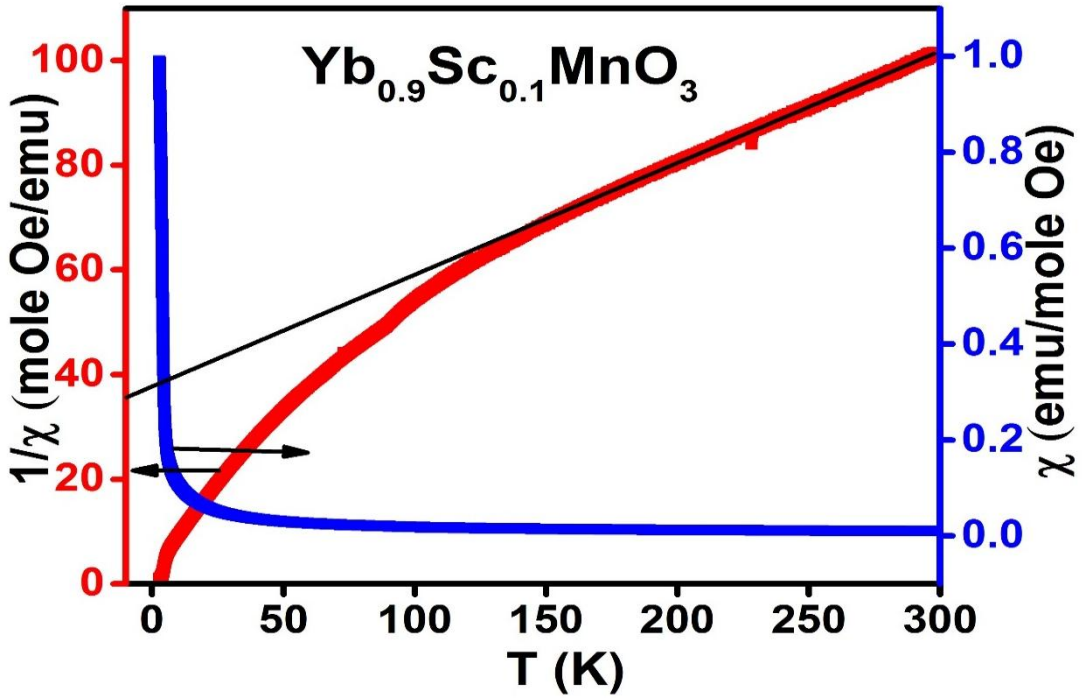


Figure.5.2: Temperature dependence of 1/ χ with Curie-Weiss fit and χ (H = 1000 Oe) of $Yb_{0.9}Sc_{0.1}MnO_3$.

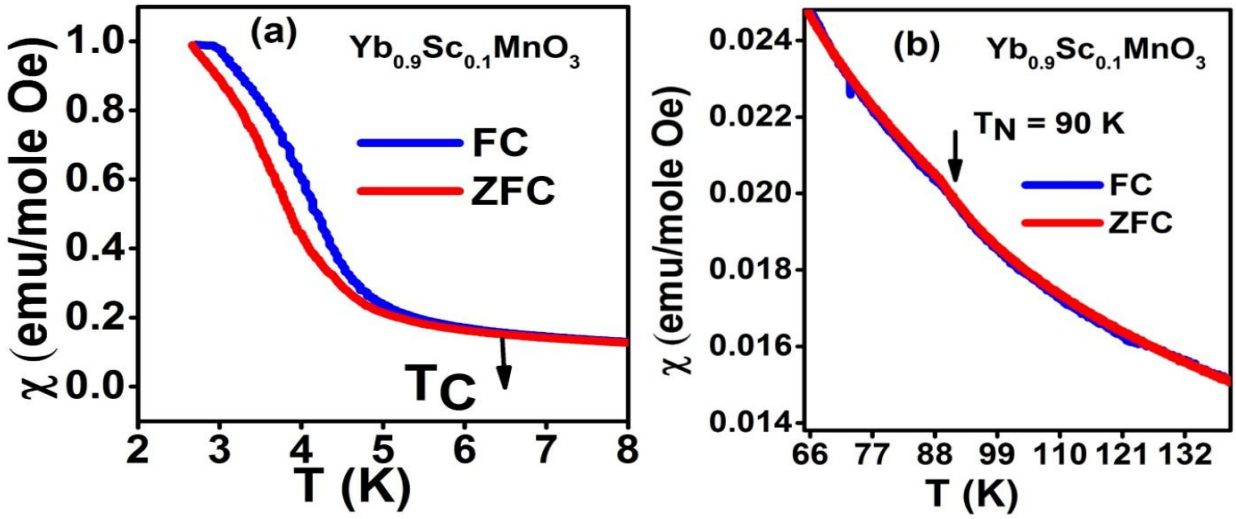


Figure 5.3: (a) ZFC and FC curves of *T* near the FM transition of $Yb^{3+}$. (b) ZFC and FC curves of *T* near the AFM transition of $Mn^{3+}$.of $Yb_{0.9}Sc_{0.1}MnO_3$.

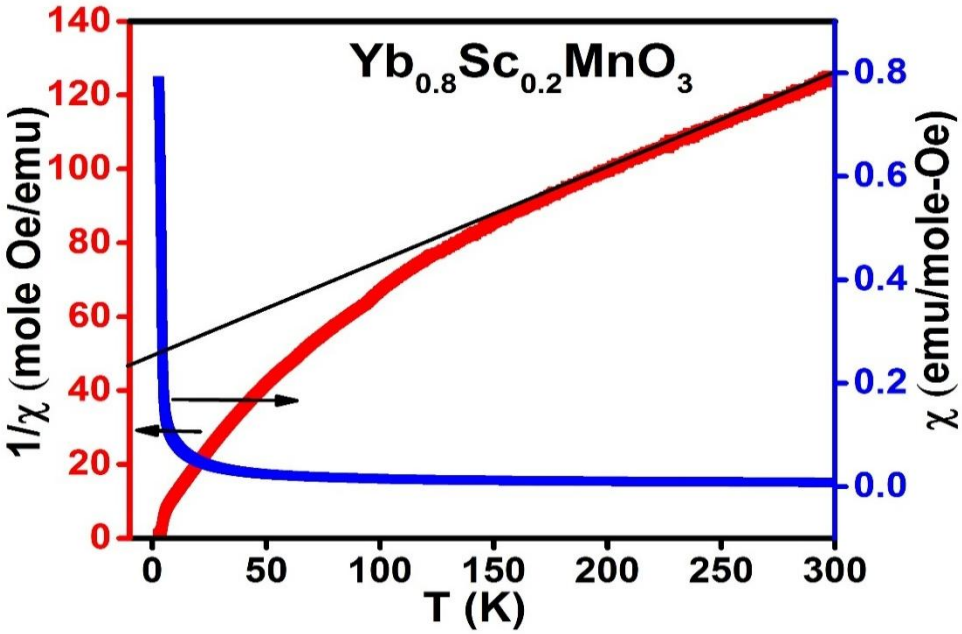


Figure.5.4: Temperature dependence of 1/ χ with Curie-Weiss fit and χ (H = 1000 Oe) of $Yb_{0.8}Sc_{0.2}MnO_3$.

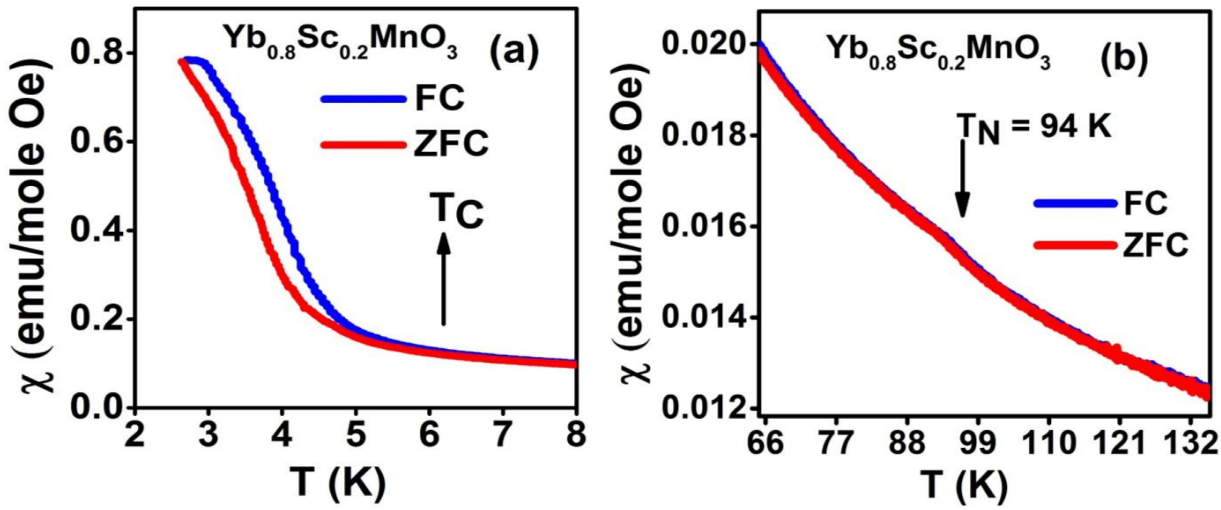


Figure 5.5: (a) ZFC and FC curves of *T* near the FM transition of $Yb^{3+}$. (b) ZFC and FC curves of *T* near the AFM transition of $Mn^{3+}$.of $Yb_{0.8}Sc_{0.2}MnO_3$.

Temperature variation of inverse magnetic susceptibility is plotted in fig.5.2 and 5.4 which show that the Curie–Weiss (CW) law is well obeyed in temperature interval between 200 and 300 K in paramagnetic phase. It fits well to the Curie-Weiss law $\chi = C/(T-\theta_{cw})$. The values of paramagnetic Curie temperature ($\theta_{cw}$) and effective magnetic moment ($\mu_{eff}$) are calculated from this Curie-Weiss fit which are listed in Table 5.3.The negative Weiss temperature indicates presence of the antiferromagnetic interaction in these compounds. The

experimental effective magnetic moments of $Yb_{1-x}Sc_xMnO_3$ (x = 0.1 and 0.2) samples are obtained from the relation $\mu_{eff} = (7.99C)^{0.5}$, where C is the Curie–Weiss constant. It is seen that the effective moment ($\mu_{eff}$ ) decreases with increases in nonmagnetic Sc content. The experimental values of $\mu_{eff}$ are in reasonable agreement with the calculated values using the following formula: $\mu_{eff} = ((1-x)\mu^2_{Yb} + \mu^2_{Mn})^{1/2}$, where x is the Sc concentration while $\mu_{Yb}$ and $\mu_{Mn}$ are the effective magnetic moment of $Yb^{3+}$ ( $\mu_{Yb} = 4.53\mu_B$) , and $Mn^{3+}$ ($\mu_{Mn} = 4.9\ \mu_B$), respectively. The ratio $f = |\theta_{CW}/T_N|$, which is a measure of geometric frustration, is around 2.05. It is smaller for Sc doped samples when compared to that of $YbMnO_3$, which indicates that the magnetic coupling between Yb and Mn moments in presence of Sc relieves the frustration effect as the magnitude of the magnetically coupling between Yb and Mn ions is the most important factors for the geometrical frustration.

Table.5.3.The magnetic parameter of $Yb_{1-x}Sc_xMnO_3$ (x = 0.1 and 0.2) estimated from CW. Also listed are magnetocaloric effect (MCE) parameters: $\Delta S_M^{max}$and RCP with reported values.

| | **From Curie-Wiess fit** | | | | | **MCE** | | | |
|---|---|---|---|---|---|---|---|---|---|
| | $\mu_{eff}^{Exp}(\mu_B)$ | $\mu_{eff}^{Theor}(\mu_B)$ | $\theta_{CW}$(K) | $T_N$(K) | $f = \lvert\theta_{CW}/T_N\rvert$ | $\Delta H$(T) | $\Delta S_M^{max}$ ($Jmol^{-1}\ K^{-1}$) | RCP ($J\ mol^{-1}$) | |
| **x = 0.1** | 6.1 | 6.5 | -182 | 90 | 2.02 | 5 | 1.32 | 13.8 | |
| | | | | | | 10 | 2.43 | 38.5 | |
| **x = 0.2** | 5.6 | 6.3 | -193 | 94 | 2.05 | 5 | 1.01 | 10.2 | |
| | | | | | | 10 | 1.88 | 30.1 | |
| **Reported values for $YbMnO_3$** | | | | | | | | | |
| Chapter 3 | 5.91 | 6.68 | -219 | 85 | 2.57 | 8 | 2.3 | 26 | Ref 18 |
| Ref 16 | 6.1 | 6.68 | -220 | 85 | 2.58 | 10 | 2 | 26 | Chap 3 |
| Ref 17 | 6.40 | 6.68 | -166 | 82 | 2.02 | - | - | - | |

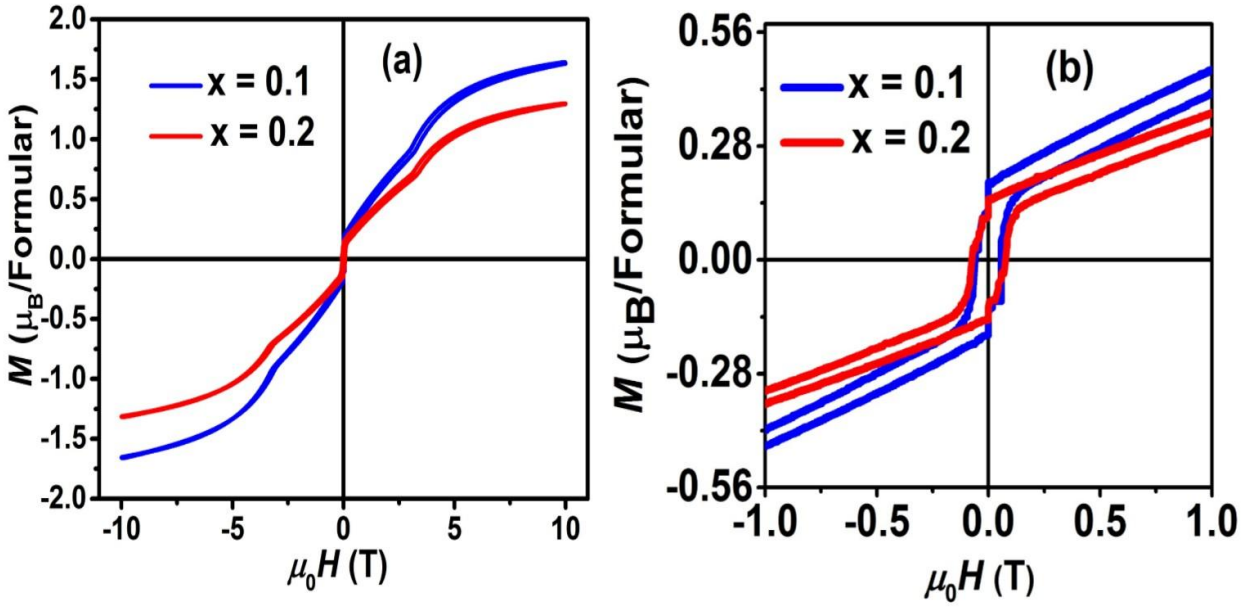


Figure.5.6: Magnetization behavior of $Yb_{1-x}Sc_xMnO_3$ (x = 0.1 and 0.2) (a)up to 10 tesla (b) up to 2 tesla.

The isothermal magnetization (M-H) curves of $Yb_{1-x}Sc_xMnO_3$ (x = 0.1 and 0.2) measured at 2.5 K are shown in Fig.5.6 (a). Both the samples show a small magnetic hysteresis loops as low fields indicating a weak ferromagnetic (FM) behavior due to $Yb^{3+}$[16,19]. At 2.5 K, the ferromagnetic (FM) behavior is observed with corresponding coercivity (Hc) around 500 Oe. A change in Sc concentration slightly changes coercivity but retentivity decreases with increase in the Sc content as shown in the fig. 5.6(b). The isothermal magnetization (M-H) at 2.5 K also shows a noticeable sudden increase in magnetization around 30 kOe, similar results are observed in $RMnO_3$ in general and is attributed to a magnetically induced phase transition where the $Mn^{3+}$ ions ordering changes from AFM to FM along the c-axis, while along the ab-plane the ordering remains unchanged to AFM [19-22]. Further, M does not saturate up to 100 kOe. As for $Yb_{0.9}Sc_{0.1}MnO_3$ and $Yb_{0.8}Sc_{0.2}MnO_3$, the magnetization at 100 kOe is 1.6$\mu_B$ and 1.3$\mu_B$, respectively. The magnetization of these samples decreases with increasing Sc concentration, which is nonmagnetic.

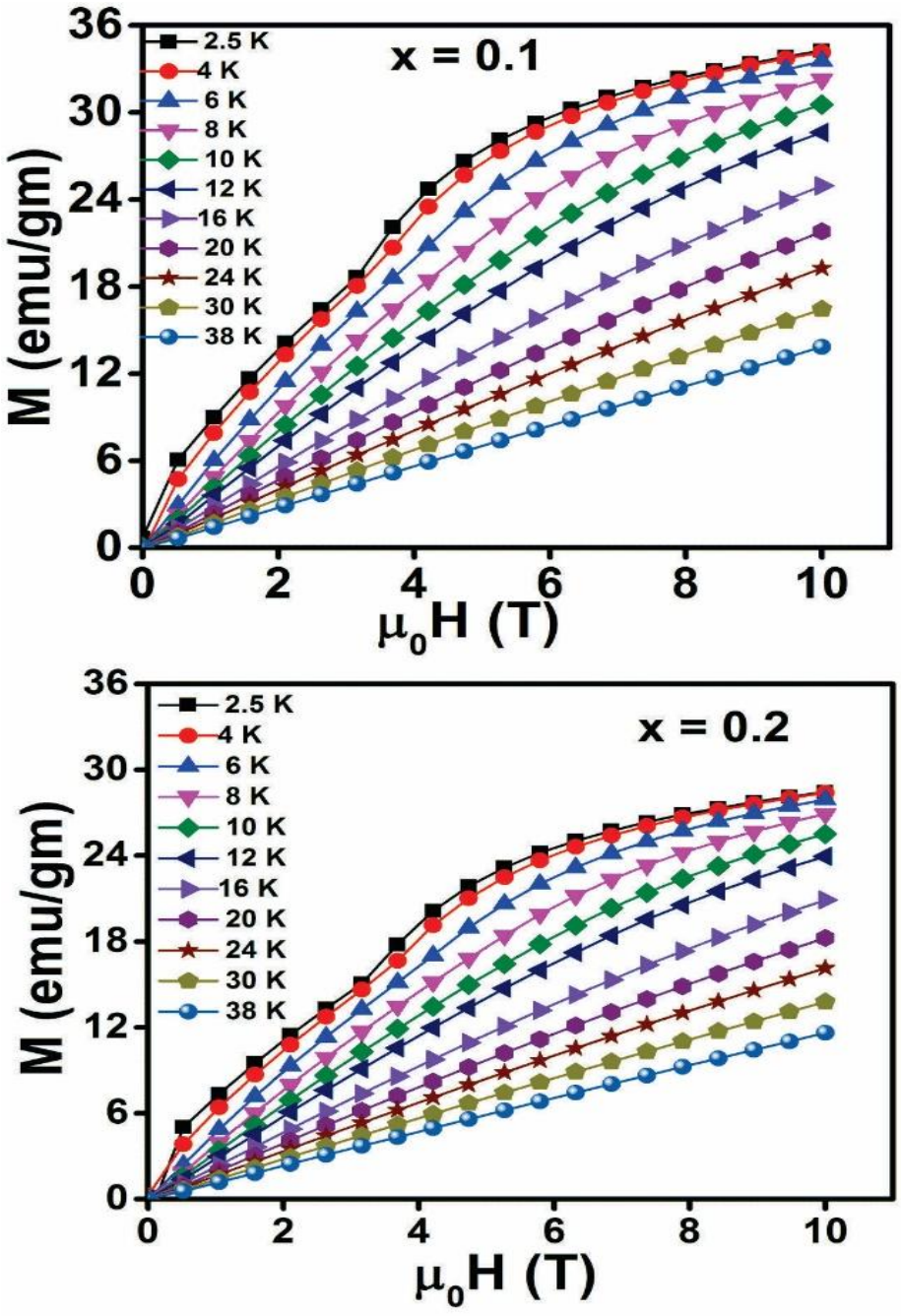


Figure.5.7: Field dependence of isothermal magnetization for $Yb_{1-x}Sc_xMnO_3$ (x = 0.1 and 0.2) at some selective temperatures.

To explain the role of applied magnetic field on metamagnetic transition, the isothermal magnetization curves as a function of magnetic field for $Yb_{1-x}Sc_xMnO_3$ (x = 0.1 and 0.2) were measured in applied fields of up to 10 T in the temperature range of 2– 40 K. Fig. 5.7 shows the typical isothermal magnetization curves of $Yb_{1-x}Sc_xMnO_3$ (x = 0.1 and 0.2), which upholds a field-induced metamagnetic transition [18]. The isotherms vary almost linearly in the low-

field region and depending upon the temperature the slope changes at a critical field *Hc* without any indication of saturation. From these plots it is seen below *T*c, *M* increases slowly with *H* in the low field region, slope changes at a critical field *Hc* and then increases slowly with further increase in *H*.

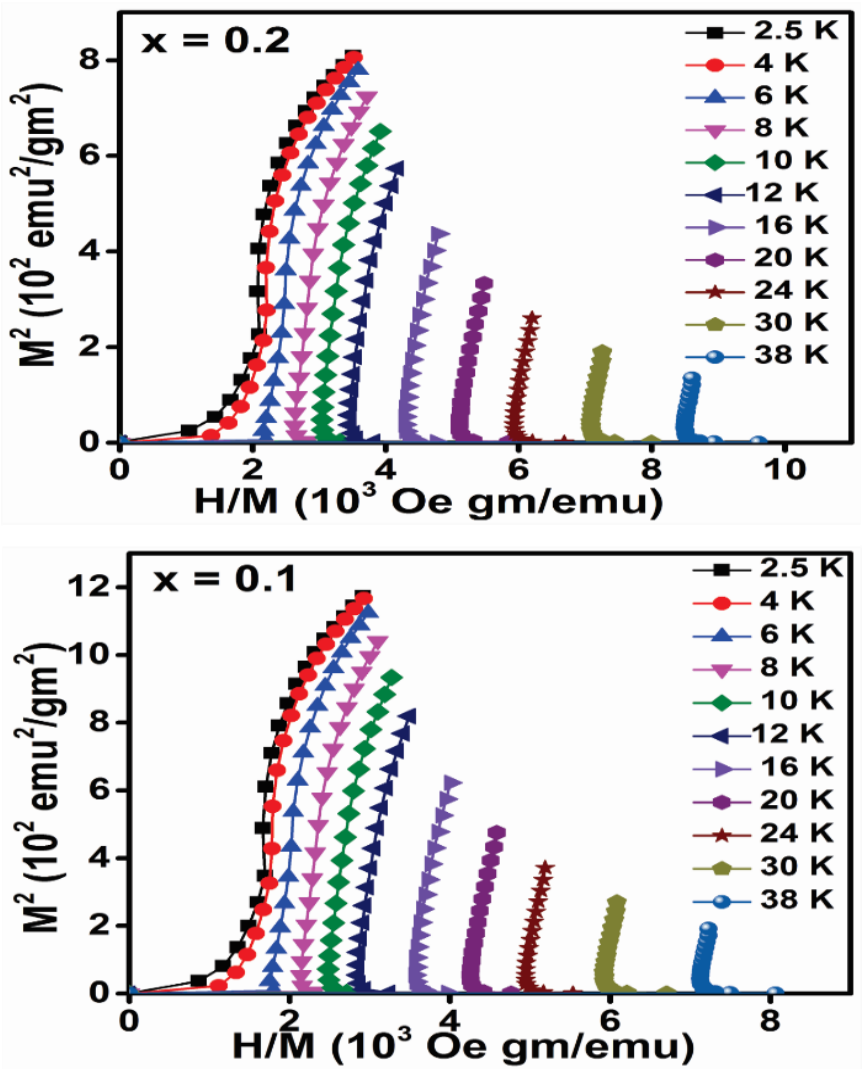


Figure.5.8: The Arrott plots of $M^2$ vs. H/M at various temperatures for $Yb_{1-x}Sc_xMnO_3$ (x = 0.1 and 0.2) samples.

The Arrott plots, H/M versus $M^2$ for the magnetization data are shown in fig. 5.8 [23]. Data of both samples show positive slopes in the full $M^2$ ranges, which is expected for a second-order phase transition [23, 24].

## 5. 3.3. Magnetocaloric behaviors

From the isothermal magnetization curves measured at different temperatures magnetic-entropy change $\Delta S_M$ can be obtained from Maxwell's thermodynamic relationship [25],

$$\left(\frac{\partial M}{\partial T}\right)_H = \left(\frac{\partial S}{\partial H}\right)_T \qquad (5.2)$$

The magnetic-entropy change $\Delta S_M$ due to the variation of the applied magnetic field from 0 to H is given by

$$\Delta S_M(T,H) = \int_0^H \left(\frac{\partial M}{\partial T}\right)_H dH \qquad (5.3)$$

The value of $\Delta S_M$ is determined using equation (2.3b) and the error/uncertainity in $\Delta S_M$ is calculated using equation of (2.4b) of Ref [26]. Calculations details of the same are explained in sec 4.3.3 in chapter 4. Using the given manufacturer data and following Ref. [26], errors of 0.5%, 0.1% and 0.25% were considered for uncertainties in magnetization, magnetic field and temperature values to calculate the error in $\Delta S_M$. The relative error in $\Delta S_M$ is 10-20 % for $\Delta H$ = 100 kOe and T around 10 K.

The magnetic entropy changes, $-\Delta S_M$ of $Yb_{1-x}Sc_xMnO_3$ (x = 0.1 and 0.2) samples, associated with the magnetic field variation (1 to 10 T), were calculated and the data for selected fields are shown in fig. 5.9. These curves present a characteristic shape with a broad maximum in the vicinity of the FM transition of Yb moment. The magnitude of the peak increases with increasing the value of $\Delta H$ for each composition and the position of the maximum shifts from 5 to 7.5 K when the magnetic field change increases from 1 to 10 T. The maximum entropy change,$-\Delta S_M^{max}$, corresponding to a magnetic field variation of 10 T is found to be 2.46 ± 0.40 J/mole-K and 1.87 ± 0.31 J/mole-K for x = 0.1 and 0.2, respectively. The magnitude of $|\Delta S_M^{max}|$ increases linearly with increasing magnetic field. The field induced metamagnetic transition contributes to the enhancement of $\Delta S_M$ .[27]. These values are in agreement with the reported values in the literature which are ~2.3 J $mole^{-1}K^{-1}$ at H = 8 T for single crystal $YbMnO_3$ [18]. For comparison, the data of various magnetic materials are listed in Table 3 which could be used as magnetic refrigerants.

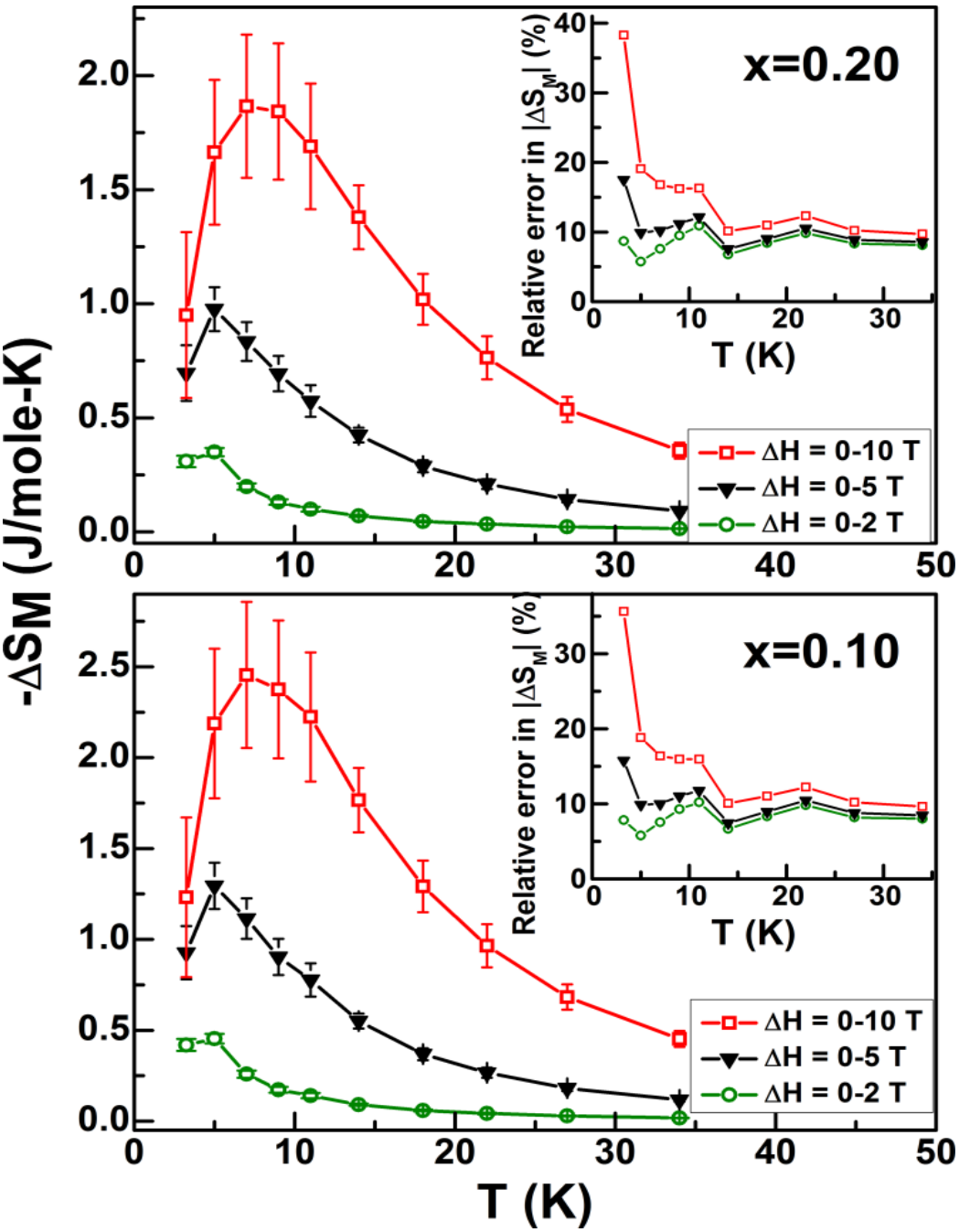


Figure.5.9: Temperature variation of magnetic entropy change for selected field change for $Yb_{1-x}Sc_xMnO_3$ (x = 0.1 and 0.2) samples.

When comparing different magneto-caloric materials, it is useful to calculate their relative cooling power (RCP) based on the magnetic entropy change. The relative cooling power is evaluated using equation 4.4.It is a measure of the quantity of heat transferred by the magnetic refrigerant between hot and cold sinks. The results of these calculations are shown in Fig. 5.10). We estimate a relative error of 15-30 % for the RCP values (as field increases from

low: 1 T to high: 10 T) considering the relative error of 10-20% in the value of $|\Delta S_M^{max}|$ and considering a 5-10% error in assigning the $\delta T_{FWHM}$ values. The RCP values show increase with increasing field for both compounds. RCP values are 38.5 ± 9 J /mol, and 30.1 ± 8 J/mol with ΔH = 10 T for samples with x = 0.1 and 0.2, respectively. These values are higher than those for single crystal $YbMnO_3$ (RCP = 26 J/mole with ΔH = 8 T) [18]. Thus, RCP values of these compounds indicate that these are potential candidates for applications at low temperatures.

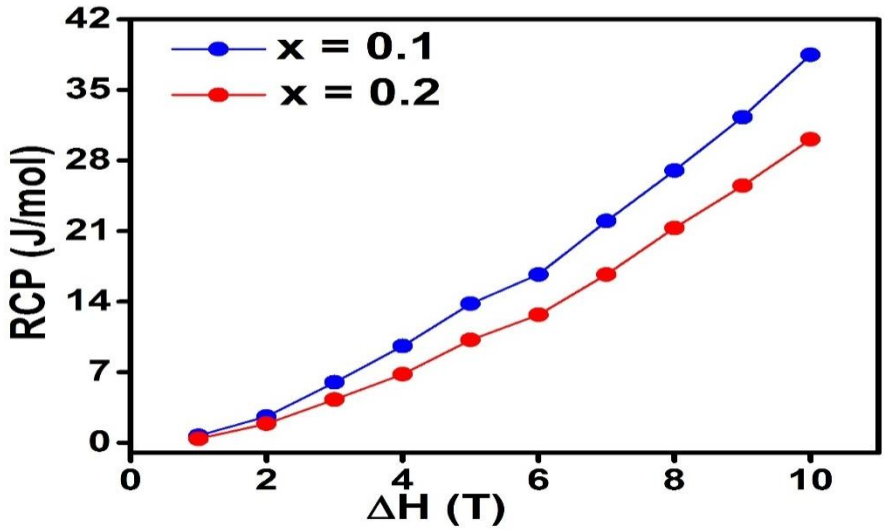


Figure.5.10: Relative cooling power as a function of field for $Yb_{1-x}Sc_xMnO_3$ (x = 0.1 and 0.2) samples.

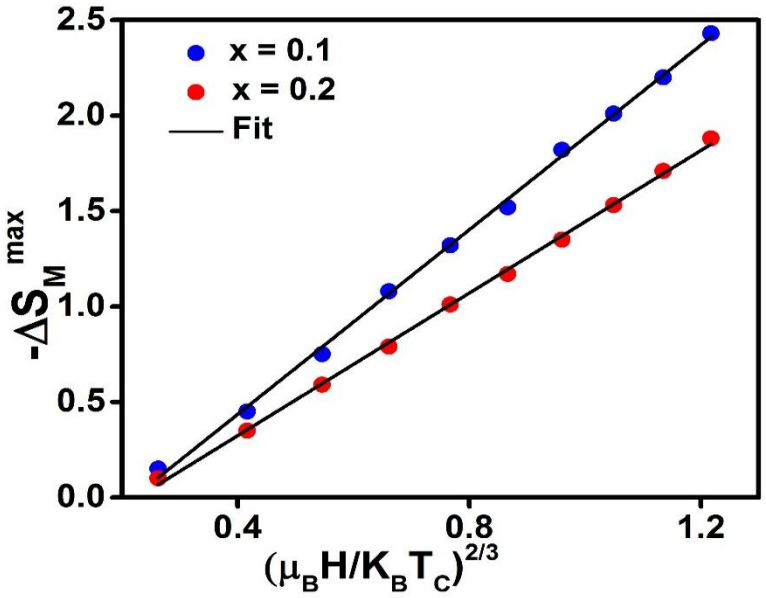


Figure.5.11: Temperature dependence of magnetic entropy change $\Delta S_M^{max}$ versus $h^{2/3}$for $Yb_{1-x}Sc_xMnO_3$ (x = 0.1 and 0.2) samples.

Figure 5.11 shows the dependence of the magnetic entropy change on the parameter$h^{2/3}$ [28,29] where $h$ is the reduced field just around $T_c$ and is given by $\left[h = (\mu_B H)/(K_B T_C)\right]$. The mean-field theory predicts that in the vicinity of second-order phase transitions, $\Delta S_M^{\max} = -kM_S(0)h^{2/3} - S(0,0)$, where k is a constant, Ms(0) is the saturation magnetization at low temperatures and S(0, 0) is the reference parameter, which may not be equal to zero [30,31]. Fig.5.11 shows the linear dependence of $\Delta S_M{}^{max}$ versus $h^{2/3}$ which implies the second order transition for $Yb_{1-x}Sc_xMnO_3$ (x = 0.1 and 0.2). The fact that $\Delta S_M{}^{max}$is estimated around $T_C$ and in fields larger than the critical field required for the metamagnetic transition, the conclusion about the second order transition is justified.

## 5. 3.4. Universal curve

The construction of the phenomenological universal curve is based on the collapse of the $\Delta S_M$ *(T,H)* points into one single point in the new curve corresponding to equivalent states of the system. Those equivalent states have the same height, in the ($-\Delta S_M/\ \Delta S_M{}^{max}$) curves. The collapse of the normalized entropy change curves can be then obtained by defining a new variable for the temperature axis, $\theta$, using equation 4.9(a) and 4.9(b) in chapter 4.

Fig.5.12 shows the dependence of ΔS* ($-\Delta S_M/\ \Delta S_M{}^{max}$) for $Yb1_{-x}Sc_xMnO_3$ (x = 0.1 and 0.2) for typical field changes. It can be clearly seen that the experimental points of the samples distribute on one universal curve of the magnetic entropy change (ranging from 4 T up to 10 T). The universal curve can be well fitted by a Lorentz function

$$\Delta S^* = \frac{a}{b+(\theta-c)^2}, \qquad (5.4)$$

where *a*, *b*, and *c* are the free parameters. A fit to this relation gives a =1.0246, b = 1.01, and c = -0.05. Where$T_{r1}$ and $T_{r2}$ are temperatures of the two reference points. In this work, $T_{r1}$ and $T_{r2}$ are selected such that $\Delta S_M$ $(T_{r1,2})$ =1/2 $\Delta S_M{}^{max}$ . The universal curve behavior is clearly observable in the figure, where the solid line in Fig.5.12 represents the curve corresponding to Eq. 5.4. The universal curve behavior with a Lorentz function like profile is a helpful tool for the evaluation of properties such as the refrigerant capacity RCP.

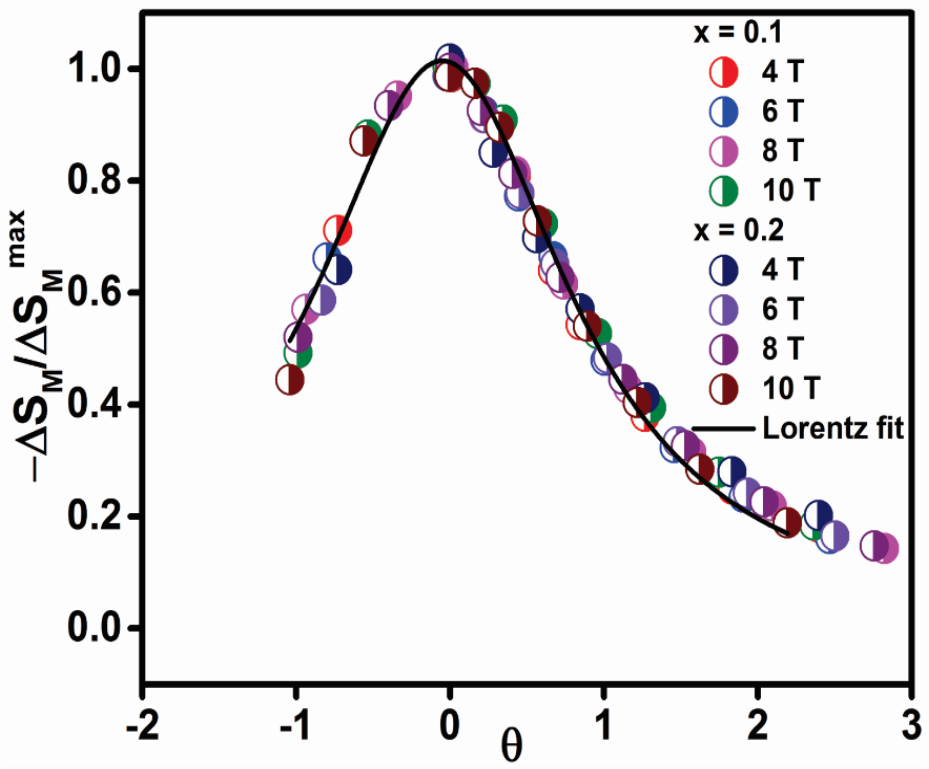


Figure.5.12: The universal curve behavior of the curves as a function of the rescaled temperature for different magnetic field for $Yb_{1-x}Sc_{0x}MnO_3$ (x = 0.1 and 0.2).

## 5.4 Conclusions

The effect of Sc doping on structural, magnetic and magnetocaloric properties of multiferroic $Yb_{1-x}Sc_xMnO_3$ (x = 0.1 and 0.2) have been investigated. X-ray powder diffraction shows that both samples crystallize in the hexagonal phase with $P6_3cm$ space group. The structural analysis shows decrease in lattice parameter *a*, decrease in cell volume of the hexagonal unit cell and decrease in the average bond length between Mn-O, with Sc substitution. Magnetic measurements show that the Néel temperature ($T_N$) increases from 90 *K* for $x = 0.1$ to 94 *K* for $x = 0.2$ sample. Isothermal magnetic curves show that the field variation in magnetization generates a metamagnetic transition. The maximum entropy change $-\Delta S_M^{max}$ and the relative cooling power (RCP)of $Yb_{1-x}Sc_xMnO_3$ are found to be 2.46± 0.40 J/mole-K and 38.5± 9 J /mol for $x = 0.1$ and 1.87 ± 0.31 J/mole-K and, 30.1± 8 J/mol for $x = 0.2$ with $\Delta H = 10$ T. The behavior of $\Delta S_M^{max}$ vs $h^{2/3}$curve confirm that present materials exhibit a second order transition. The rescaled magnetic entropy change curves for different applied fields collapse onto a single curve for materials with second-order phase transition.

## 5.5 References.

[1] M. Fiebig, J. Phys.D., **38,**(2005),R123–R152.

[2] W. Prellier, M.P. Singh, P. Murugavel, J. Phys. Condens. Matter.,**17**,(2005),R803–R832.

[3] N.A. Spaldin, M. Fiebig, Science.,**309** , (2005),391–392.

[4] X. Qi, J. Dho, R. Tomov, M.G. Blamire, J.L. MacManus-Driscoll, Appl.Phys.Lett., ,**86,**(2005), 062903(1)–062903(3).

[5] Z.J. Huang, Y. Cao, Y.Y. Sun, Y.Y. Xue, C.W. Chu, Phys. Rev. B., **56, (**1997),2623-2626.

[6] T. Katsufuji, S. Mori, M. Masaki, Y. Moritomo, N. Yamamoto, H. Takagi, Phys.Rev.B., ,**64**,(2001),104419(1)–104419(6).

[7] M. Fiebig, Th. Lottermoser, D. Frohlich, A.V. Goltsev, R.V. Pisarev, Nature ., ,419, (2002),818–820.

[8]T. Katsufuji, M. Masaki, A. Machida, M. Moritomo, K. Kato,E. Nishibori,M.Takata, M.Sakata, K. Ohoyama, K. Kitazawa, and H. Takagi, Phys. Rev. B.,**66**,(2002), 134434.

[9]. P. Schiffer and A. P. Ramirez, Condens. Matter Phys.,**18**,(1996),21.

[10]. Th. Lonkai,1, D. G. Tomuta, U. Amann, J. Ihringer, R. W. A. Hendrikx, D.M.To¨bbens, J. A. Mydosh, Phys.Rev.Lett.,**69**, (2004),134108.

[11]. K. A. Gschneidner Jr., V. K. Pecharsky, and A. O. Tsokol, Rep. Prog. Phys. ,**68**, (2005), 1479 and references therein.

[12]. A. M. Tishin in Handbook of Magnetic Materials, edited by K. H. Buschow(Elsevier Science B.V., New York) **12,(**1999), 395.

[13]. V. Provenzano, J. Li, T. King, E. Canavan, P. Shirron, M. DiPirro, and R. D. Shull, J. Magn. Magn. Mater.,,**266**,(2003), 185.

[14].A. Mun ˜oz, J. A. Alonso, M. J. Martı ´nez-Lope, M. T. Casa ´is, and J. L. Martı ´nez and M. T. Ferna ´ndez-Dı ´az Phys. Rev. B.,**62**, (2000),9498.

[15] Rodrı´guez-Carvajal, J., Hennion, M., Moussa, F. &Moudden, A. H..Phys. Rev. B.,**57**,(1998) R3189–R3192.

[16]. X. Fabre ´ges, I. Mirebeau, P. Bonville, S. Petit, G. Lebras-Jasmin, A. Forget, G. Andre, and S. Pailhes, Phys. Rev. B.,**78,(**2008), 214422.

17[17]. S.L. Samal , T. Magdaleno , K.V. Ramanujachary , S.E. Lofland , A.K. Ganguli, Journal of Solid State Chemistry., **183**,(2010), 643–648.

[18] A. Midya, S. N. Das, P. Mandal, S. Pandya and V. Ganesan, Phys. Rev. B.,**84**,(2011), 235127.

[19]. H. Sugie, N. Iwata, K. Kohn, J. Phys. Soc. Jpn., **71**, (2002),1558.

[20].M. Fiebig,C. Degenhardt,R. V. Pisarev, Phys. Rev. Lett. , **88**,(2002), 027203.

[21].M. Fiebig , Th. Lottermoser, R. V. Pisarev J. Appl. Phys., **93**,(2003),8194.

[22].N. Abramov, S. Lofland, and Ya. Mukovskii, phys. status solidi B, **1-3**,(2012),48318.

[23] A. Arrott and J. Noakes, Phys. Rev. Lett. , **19**, (1967), 786.

[24] S. K. Banerjee, Phys. Lett. **12**, (1964),16.

[25] A.H. Morrish, The Physical Principles of Magnetism Wiley, New York, 1965 (Chapter3).

[26] V.V. Pecharsky and K.A. Gschneidner, J. Appl. Phys. **86**,(1999), 565.

[27] A. Midya, P. Mandal,S. Das, S. Banerjee, L. S. Sharath Chandra, V. Ganesan and S,RoyBarman,Appl. Phys. Lett., **96**,(2010), 142514.

[28] Wang J L, Campbell S J, Zeng R, Poh C K , Dou S X J. Appl. Phys.,,**105,**(2009), 07A909.

[29] Oesterreicher H and Parker F T J. Appl. Phys.,,**55,**(1984),4334.

[30] V. Franco, A. Conde, V. K. Pecharsky and K. A. Gschneidner, EPL., **79**,(2007), 47009.

[31] N. Zaidi,S. Mnefgui, J. Dhahriaand E. K. Hlil, RSC Adv., **5**,(2015), 31901.

# Chapter 6

## *Structural, magnetic, and magnetocaloric effect of polycrystalline $Yb_{1-x}Ho_xMnO_3$*

## 6.1 Introduction:

For practical refrigeration applications, magnetocaloric materials are considered to be energetically efficient and environmentally friendly than the conventional refrigeration route based on the compression of a gas. Recent research in this area has been focused on identifying materials with large magnetocaloric effect (MCE) in two temperature regimes; either above 250 K for domestic and several technological applications, such as in air conditioning and commercial refrigeration, or below 80 K for specific technological applications, such as space science and liquefaction of hydrogen in fuel industry[1,2]. Consequently, magnetic refrigeration technology is building up with time and search for materials with large MCE is amplified in recent times. Rare earth manganites $RMnO_3$havebeen reasonably well studied for its crystal structure, dielectric and magnetic properties [3-5].These compounds exhibits interesting physical properties but most of the studies on these materials have been focused on their magnetic and ferroelectric behavior, but less work has been undertaken on exploring their MCE properties.

The magnetic phase diagram of $YbMnO_3$ is rather complex. Results of magnetic, dielectric and magnetoeolectric measurements on single crystals of $YbMnO_3$by H. Sugieet. al. [6] shows that below $T_{N2}$ ~ 3.5 K, long range ferromagnetic ordering of $Yb^{3+}$ moments develops and a magnetic field applied along the c-axis induces a first order metamagnetic transition at a critical field of H||c ~ 35 kOe, where the magnetic ordering along the c-axis becomes ferrimagnetic. They have identified the low temperature magnetic phase (H-T) diagram of $YbMnO_3$ with three different regions. Based on the neutron diffraction and Mossbauer spectroscopy studies on polycrystalline samples, Fabreges et. al. [7] have reported that the $Mn^{3+}$ moments aligned in the *ab*-plane order antiferromagnetically, at the Neel temperature ($T_{N1}$ = 85 K) and starts the Yb moments at the *4b* crystallographic site to order due to the Mn molecular field. The Yb(*4b*) moments aligned along the *c*-axis and are anitiferromagnetically (ferromagnetically) coupled along the ab-plane (c-axis).Below $T_{N2}$ ~ 3.5 K, $Yb^{3+}$ moments at the *2a* crystallographic site aligned along the ab-plane start long range ferromagnetic ordering through Yb-Yb interactions. They suggest a spin flip/reorientation of the Yb(2a) moments from *ab*-plane to *c*-axis as the

source/reason for the field induced metamagnetic transition[9].Based on the heat capacity and magnetization measurements on single crystals, N. Abramov et. al [8] also identified a three phase H-T phase diagram for this compound at low temperatures. However they have attributed the Yb(*4b*) moments spin flip as the reason for the field induced metamagnetic transition, rather than the spin flipping of Yb(*2a*) moments as suggested by Fabreges et. al. [7].

The above reported behavior of $YbMnO_3$ is very interesting and therefore, it was considered to be useful to investigate changes in the above behavior due to other rare-earth substitution for Yb. This chapter reports the effect of Ho substitution on the magnetic and magnetocaloric properties of $Yb_{1-x}Ho_xMnO_3$ system with x =0.1,0.2 and 0.3. Considering that the $Ho^{3+}$ion size is a little larger than that of $Yb^{3+}$ and also has higher magnetic moment than that of $Yb^{3+}$, it was considered interesting to study doping of Ho for Yb in $YbMnO_3$ on its magnetic behavior and magnetocaloric properties. The large field induced magnetization observed in $Yb_{1-x}Ho_xMnO_3$ has triggered interest us to investigate the magnetocaloric behavior in this system. Here a comprehensive study of the magnetocaloric effect of $Yb_{1-x}Ho_xMnO_3$(x =0.1,0.2 and 0.3) measured on polycrystalline compound near the Yb spin ordering transition is presented.

## 6.2 Experimental details

Polycrystalline samples of $Yb_{1-x}Ho_xMnO_3$ (x = 0.1, 0.2 and 0.3) were synthesized by the conventional solid state reaction method. High-purity (purity better than 99.9%) $Yb_2O_3$, $Ho_2O_3$ and $MnCO_3$, powders are obtained from M/s Sigma-Aldrich. The precursors$Yb_2O_3$ and $Ho_2O_3$ powders are preheated at 500 K for 5 h to remove moisture. Stoichiometric proportions of these oxides are thoroughly mixed, and then calcined in platinum crucibles at 1200 $^0$C in air for 30 h with an intermediate grinding for homogenization. The calcined mixture is cold pressed into pellets at approximately $5\times10^7$Pa pressure and then sintered at 1400 $^0$C in air for 24 hours. Finally, all samples were slowly cooled to room temperature for sufficient oxygenation. The phase purity of each sample was checked by powder x-ray diffraction (XRD) using a Bruker D8 Advance X-ray powder diffractometer operating with Cu-Kα radiation. Magnetizations (M) were measured as a function of temperature (T) using a cryogenic Inc. (UK) make 16T vibrating sample magnetometer(VSM).Magnetization isotherms were obtained in the range of

0–10 T and with a different temperature interval in the vicinity of low temperature ordering transition.

# 6.3 Results and discussion

## 6.3.1 X-ray diffraction

The X-ray diffraction patterns and the Rietveld refinement of the studied polycrystalline samples $Yb_{1-x}Ho_xMnO_3$ (x = 0.1,0.2 and 0.3) are shown in fig. 6.1.All the samples are in a single phase and the measured patterns can be indexed to the hexagonal phase with $P6_3cm$ space group, in agreement with a previous report [9]. Refined values of lattice parameters and discrepancy factors for $Yb_{1-x}Ho_xMnO_3$ (x = 0.1,0.2 and 0.3)are shown in table6.1.The increase in lattice constant *a* is due to the larger ionic radius of $Ho^{3+}$[Shannon radius = 1.015Å for coordination number (CN) = 8] than $Yb^{3+}$(Shannon radius = 0.985Å nm for CN = 8).

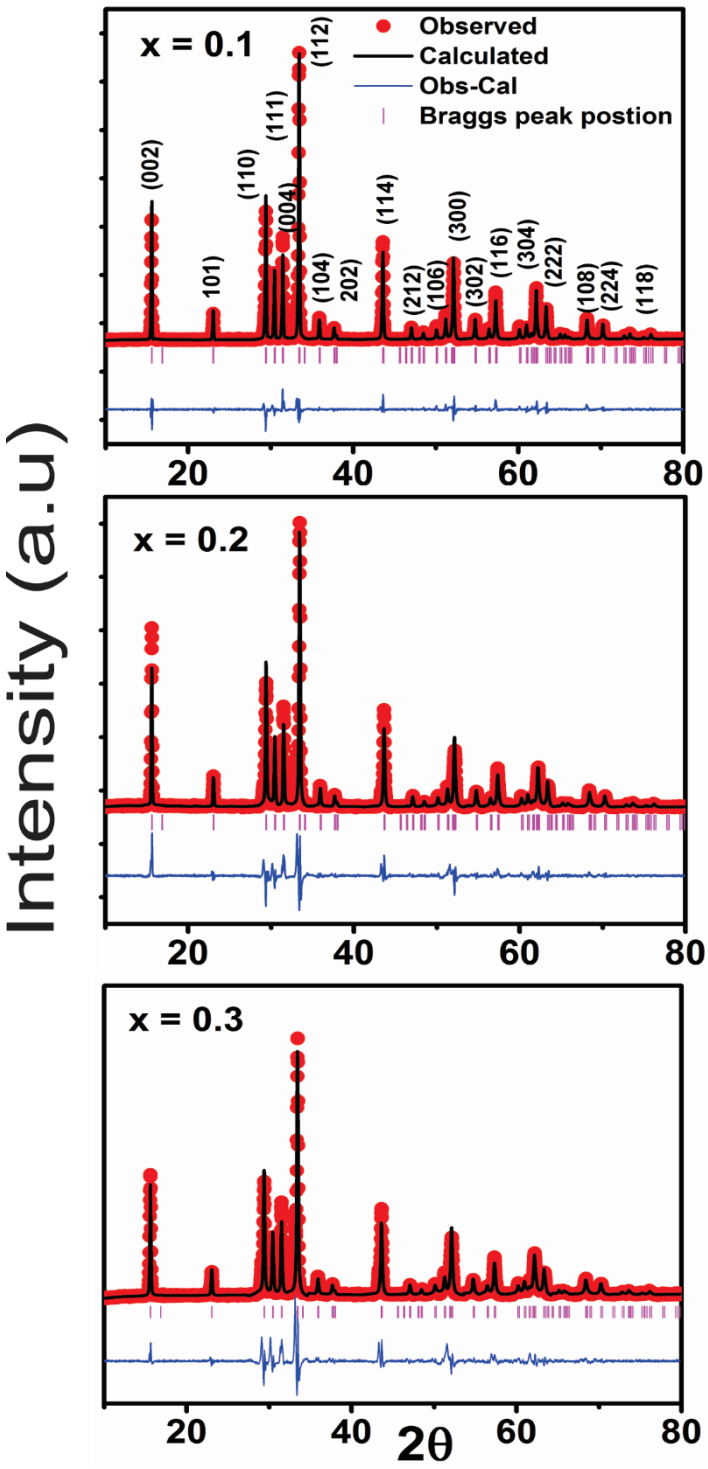


Figure.6.1: Room temperature XRD pattern of $Yb_{1-x}Ho_xMnO_3$ (x = 0.1,0.2 and 0.3)samples indexed in space group P63cm.

**Table.6. 1.** Refined crystallographic parameters, reliability factors and magnetic parameters of$Yb_{1-x}Ho_xMnO_3$ (x = 0.1,0.2 and 0.3)

| $Yb_{1-x}Ho_xMnO_3$ | ***x* = 0.1** | ***x* = 0.2** | ***x* = 0.3** |
|---|---|---|---|
| ***a* (Å)** | 6.0723(4) | 6.0732(4) | 6.0755(4) |
| ***c* (Å)** | 11.3712(4) | 11.3487(4) | 11.3534(4) |
| $R_F$ | 4.38 | 4.40 | 4.97 |
| ***Bragg R-factor*** | 5.66 | 7.84 | 8.12 |
| $\mu_{eff}^{Exp}(\mu_B)$ | 6.81 | 7.36 | 7.9 |
| $\mu_{eff}^{Theor}(\mu_B)$ | 7.32 | 7.9 | 8.49 |
| $\theta_{CW}$ **(K)** | -92 | -65 | -52 |

## 6. 3.2Magnetic behaviors

Temperature dependence of susceptibility χ (T) of $Yb_{1-x}Ho_xMnO_3$ (x = 0.1, 0.2 and 0.3)compounds under an applied magnetic field of 500 Oe in zero field cooled (ZFC) mode is shown in fig. 6.2.The magnetic susceptibility of each sample exhibits paramagnetic like behavior with most of the temperature range. No clear magnetic transition is observed over the whole temperature range. At low temperatures, around 5 K, a sudden rise inχfor all samples, is indicative of ferromagnetic ordering. The ferromagnetic ordering has been attributed to the ordering in the $Yb^{3+}$sublattice [7], It seems that the antiferromagnetic moments from Mn-Mn ordering are masked by the paramagnetic moments from the $Yb^{3+}$ and $Ho^{3+}$ions.Temperature variation of the inverse magnetic susceptibility is plotted in Fig.6.3(a) which shows that the Curie–Weiss (CW) law is well obeyed in temperature interval between 200 and 300 K and can be fitted by using the Curie-Weiss law $\chi = C/(T-\theta_{cw})$. Paramagnetic Curie temperatures ($\theta_{cw}$) and effective magnetic moments ($\mu_{eff}$) are calculated from the Curie-Weiss fits. The Curie-

Weiss temperatures are found to decrease with Ho doping as shown in table 6.1.The negative Weiss temperature indicates presence of antiferromagnetic interactions.

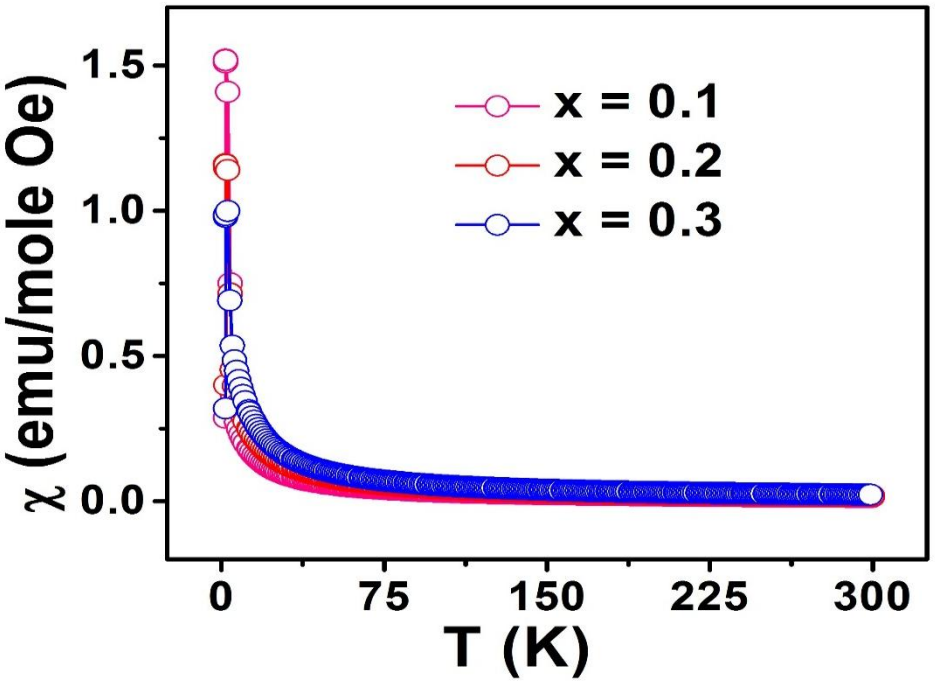


Figure.6.2:Temperature dependences of the zero-field-cooled (ZFC) magnetization for $Yb_{1-x}Ho_xMnO_3$( x = 0.1,0.2 and 0.3)samples under applied magnetic field 0.05 T,

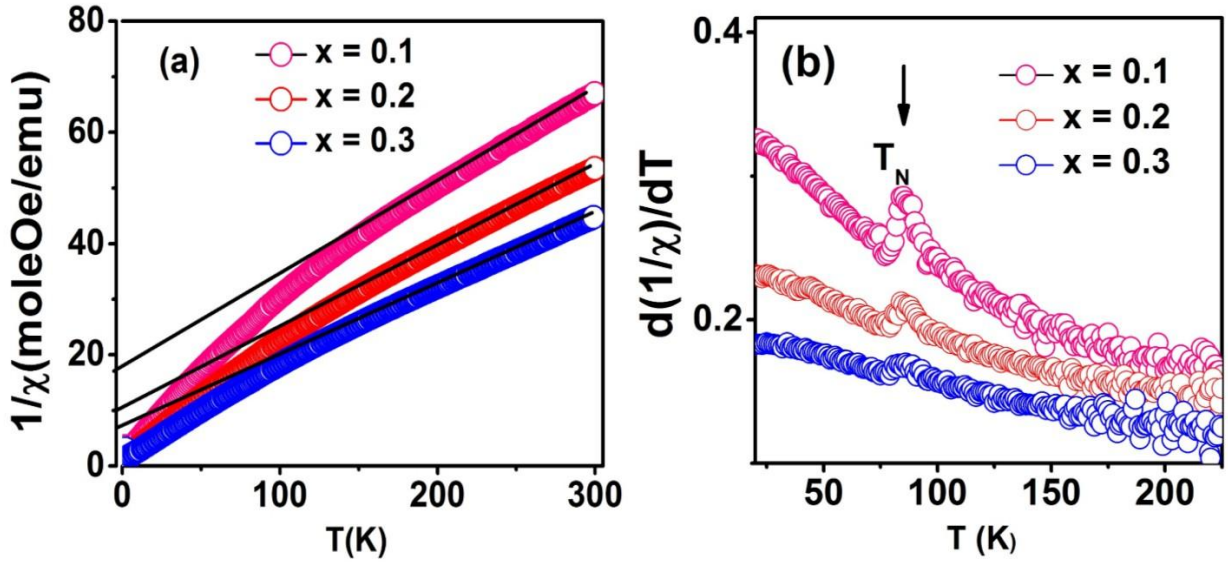


Figure.6.3: **(**a) Temperature dependent inverses susceptibility,$1/\chi(T)$ curves with Curie-Weiss fit. (b)First derivative of temperature dependent inverses susceptibility,$1/\chi(T)$for $Yb_{1-x}Ho_xMnO_3$ ( x = 0.1,0.2 and 0.3)samples.

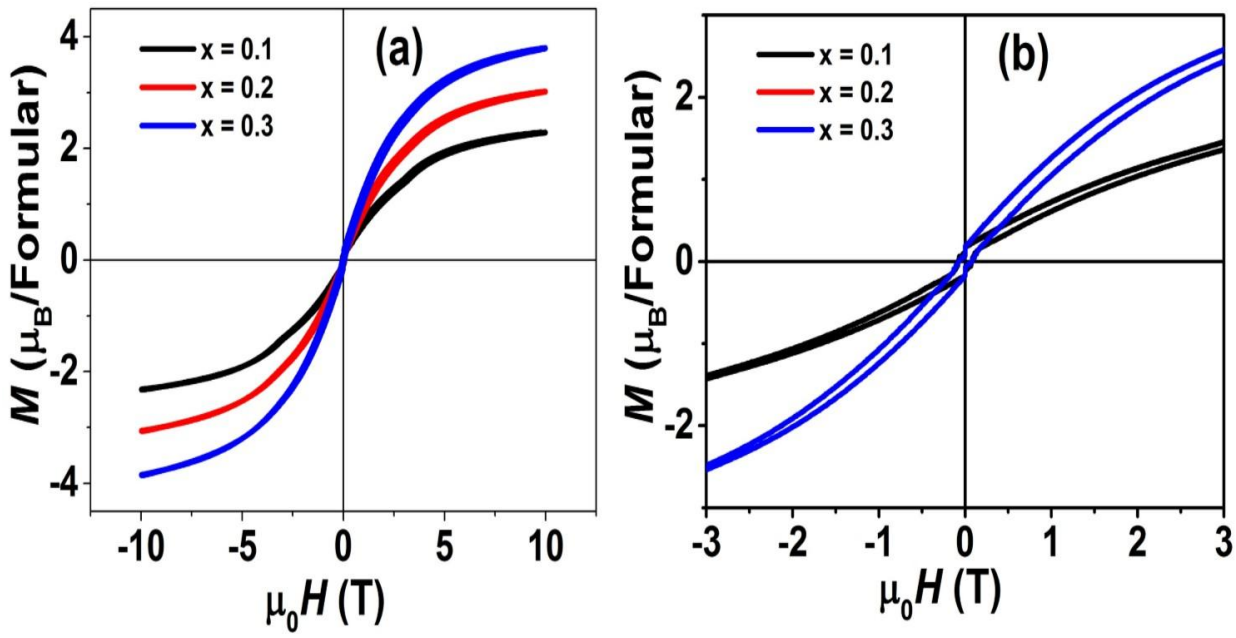


Figure.6.4:The magnetization behavior of $Yb_{1-x}Ho_xMnO_3$ ( x = 0.1, 0.2 and 0.3) at 2.5 K for all the samples (a) Magnetic fields strengths of 100 kOe.(b)Magnetic fields strengths of 3kOe.

The experimental effective magnetic moment of the $Yb_{1-x}Ho_xMnO_3$ (x = 0.1, 0.2 and 0.3) samples obtained from the equation $\mu_{eff} = (7.99C)^{0.5}$, where Cis Curie–Weiss constant. From Curie-Wiess fit the effective moment ($\mu_{eff}$) increases with Ho content shown in table 6.1.The experimental values of $\mu_{eff}$ are in good agreement with the calculated values using the following formula: $\mu_{eff}= ((1-x)\mu^2_{Yb} +x\mu^2_{Ho^{3+}} +\mu^2_{Mn^{3+}})^{1/2}$, where x is the Ho concentration while $\mu_{Yb}$, $\mu_{Ho}$ and $\mu_{Mn}$ are the effective magnetic moment of $Yb^{3+}$ ( $\mu_{Yb}= 4.53\mu_B$), $Ho^{3+}$($\mu_{Ho} = 10.6\mu_B$) and $Mn^{3+}$($\mu_{Mn} = 4.9\mu_B$), respectively. The $Mn^{3+}$ AFM ordering temperature is clearly visible in the derivative of $1/\chi$ vs temperature ($\frac{d(1/\chi)}{dT}$) plot shown in the figure 6.3(b).

The isothermal magnetization (M-H) curves of $Yb_{1-x}Ho_xMnO_3$ (x = 0.1, 0.2 and 0.3) measured at 2.5 K are shown in fig.6.4(a). All the samples show magnetic hysteresis loops representing ferromagnetic (FM) behavior due to $Yb^{3+}$.The FM component is more visible with increase of Ho content.. The magnetizations of these samples increase linearly with increasing magnetic field below 30 kOeand do not saturate up to 100 kOe. As for $Yb_{0.1}Ho_{0.9}MnO_3$ and $Yb_{0.7}Ho_{0.3}MnO_3$, the magnetization at 100 kOe is 2.2 $\mu_B$ and 3.8 $\mu_B$, respectively. The increasing magnetizations of these samples with increasing Ho concentration, is a result of the higher effective magnetic moment of $Ho^{3+}$(10.6 $\mu_B$) compared to that of $Yb^{3+}$(4.53$\mu_B$).

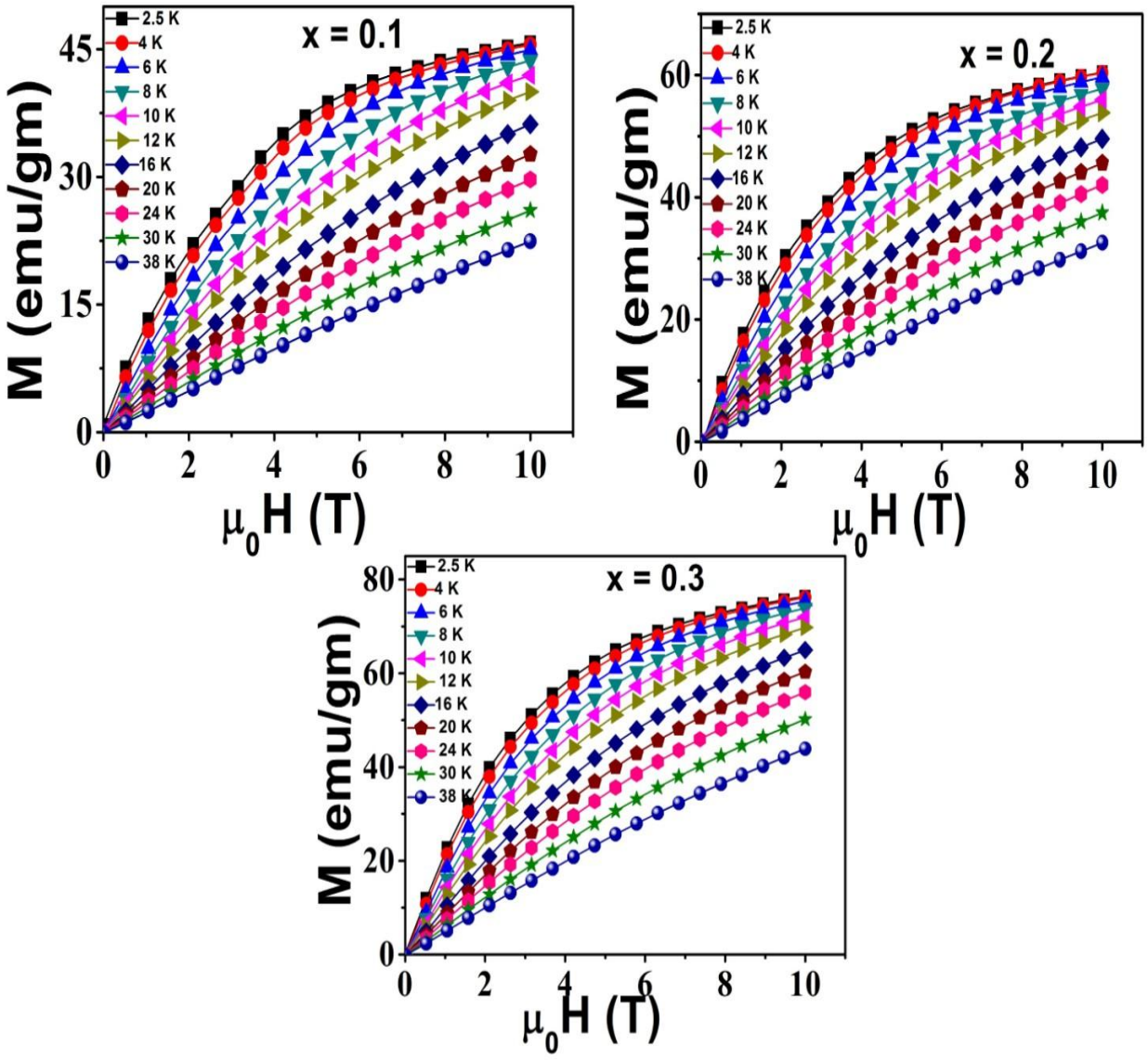


Figure.6.5: Field dependence of isothermal magnetization for $Yb_{1-x}Ho_xMnO_3$ (x = 0.1,0.2 and 0.3)at some selective temperatures.

The Arrott plots, H/M versus $M^2$ for the magnetization data are shown in fig. 5.8 [10]. Data of both samples show positive slopes in the full $M^2$ ranges, which is expected for a second-order phase transition [10, 11].

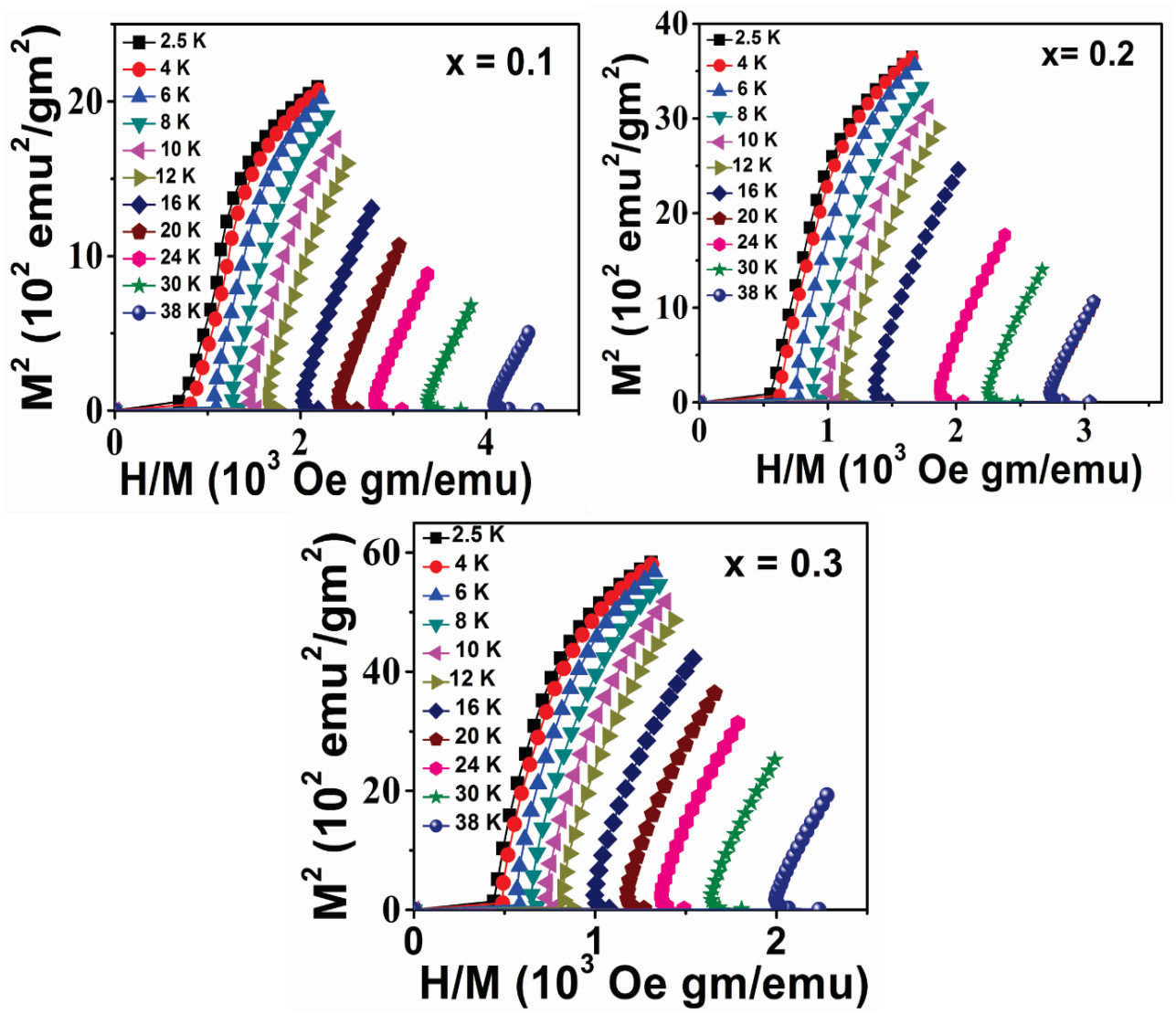


Figure.6.6The Arrott plots of $M^2$ vs. H/M at various temperatures for $Yb_{1-x}Ho_xMnO_3$ (x = 0.1,0.2 and 0.3) samples.

## 6.3.3Magnetocaloric behaviors

The magnetic entropy change $\Delta S_M$ associated with the magnetocaloric effect can be calculated from the magnetization data using the Maxwell relation.

$$\Delta S_M(T,H) = \int_0^H \left(\frac{\partial M}{\partial T}\right)_H dH \qquad (6.1),$$

The value of $\Delta S_M$ is determined from the isothermal magnetization curves measured at different temperatures with an appropriate interval of temperature $\Delta T$, using the equation (2.3b) and the error/uncertainity in $\Delta S_M$ is calculated using the equation of (2.4b) of ref [12].For the

calculation of relative error in the entropy change, following [14], the accuracy of magnetization measurements are taken as 0.5% and the accuracy of the magnetic field as 0.1%. The manufacturer quoted temperature stability of 0.25% is used as the error for temperatures. The values of $-\Delta S_M$ for different $\Delta H$ as a function of temperature is presented in fig.6.7. The inset shows the relative errors in $\Delta S_M$, calculated using (2.4b) of ref [12]. Except for very low temperatures and high fields the relative error is 10-20 %. $-\Delta S_M$ is positive in the entire temperature range for all the samples. The curves present a characteristic shape with a broad maximum in the vicinity of the FM transition of the Yb moment. The magnitude of the peak increases with increasing $\Delta H$ for each composition and the position of the maximum shifts from 5 to 10 K when the magnetic field change increases from 1 to 10 T. The values of the peak,$-\Delta S_M^{max}$ of $Yb_{1-x}Ho_xMnO_3$, are 2.85± 0.48J/mole-K for $x$ = 0.1,3.83±0.65J/mole-K for $x$ = 0.2 and 3.75±0.78J/mole-K for $x$ = 0.3 with $\Delta H$ = 10 T.

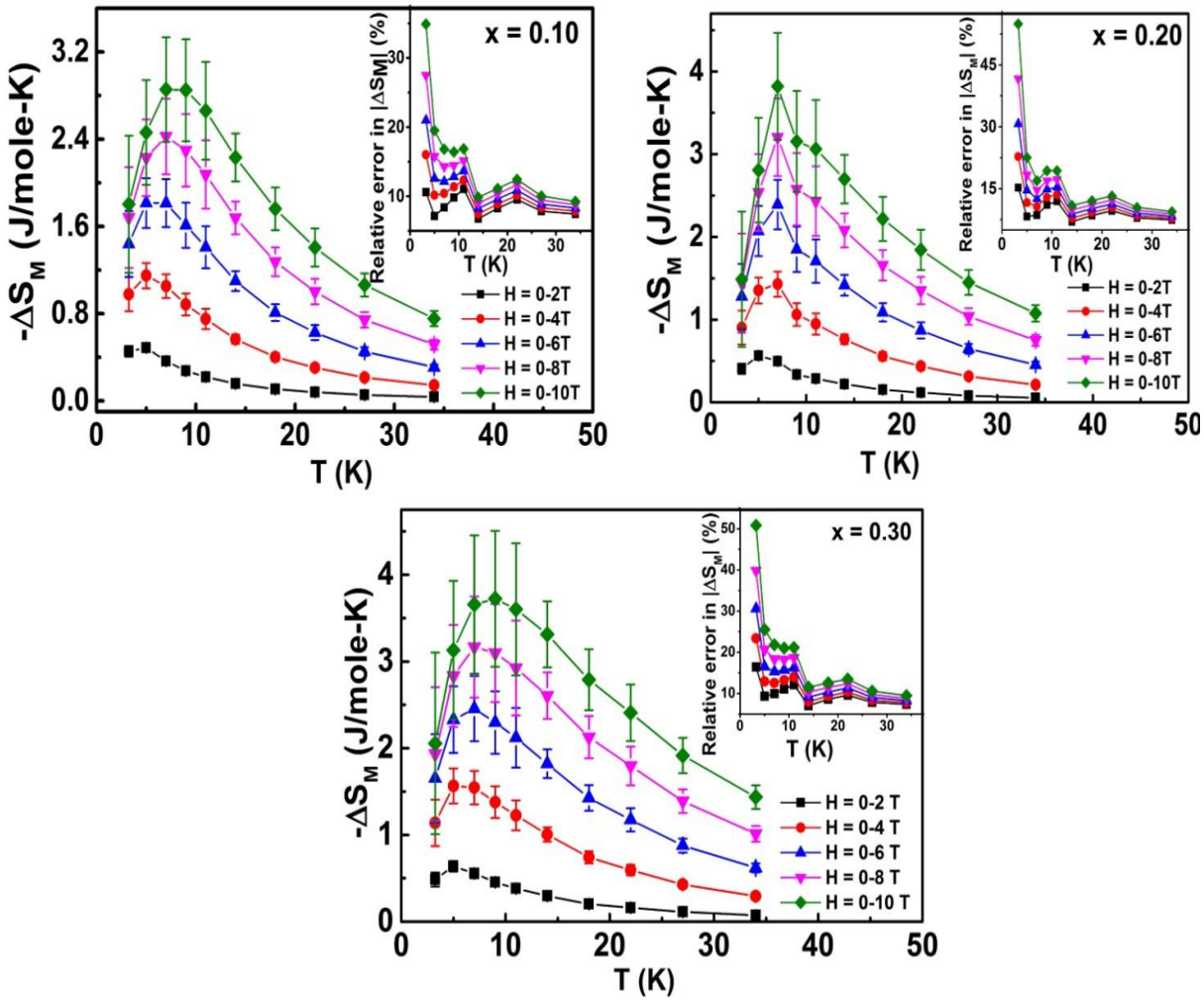


Figure.6.7: Temperature variation of magnetic entropy change for different field change for $Yb_{1-x}Ho_xMnO_3$ (x = 0.1, 0.2 and 0.3) samples.

The magnitude of $-\Delta S_M$ at maximum increases linearly with the increasing magnetic field, The field induced metamagnetic transition contributes to the enhancement of $\Delta S_M$[13].These values are large compared to other reported rare earth manganites [13-16].We can use $\Delta S_M^{max}$ and H to confirm that these materials exhibit a second order transition. The magnetic materials with a second order transition generally obey the relation, $\Delta S_M^{max} = -kM_S(0)h^{2/3} - S(0,0)$,where h is the reduced field just around $T_C$, $h = \mu_B H/k_B T_c$,k is a constant, Ms(0) is the saturation magnetization at low temperatures and S(0, 0) is the reference parameter, which may not be equal to zero[17]. Fig. 6.8(a) shows the linear dependence of $\Delta S_M^{max}$ versus $h^{2/3}$ which implies the second order transition for $Yb_{1-x}Ho_xMnO_3$ (x = 0.1,0.2 and 0.3).

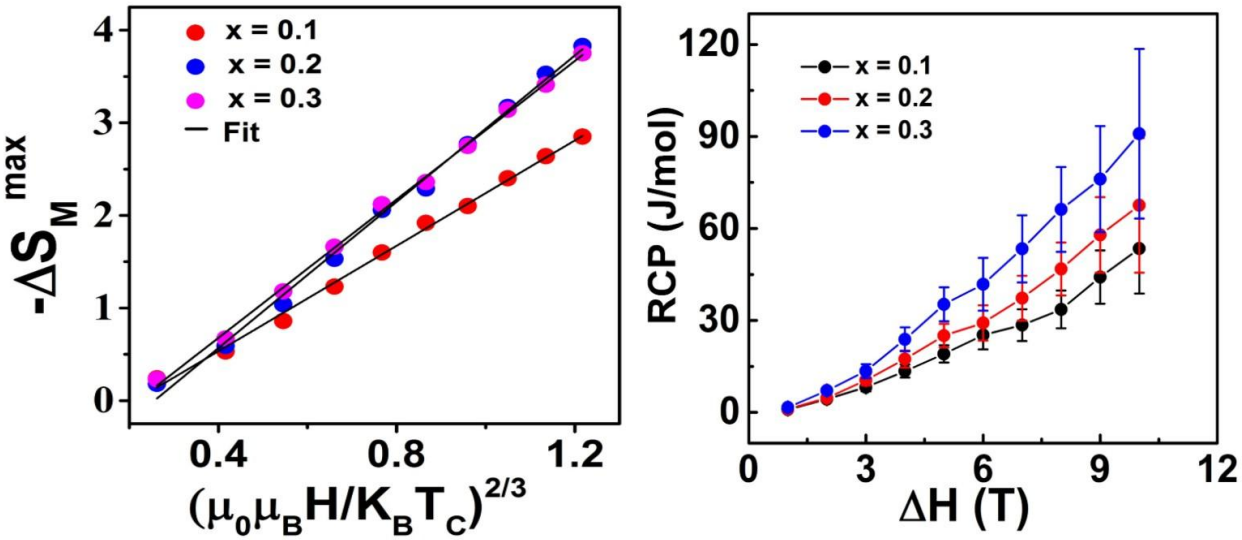


Figure.6.8 (a) Temperature dependence of magnetic entropy change $\Delta S_M^{max}$ versus $h^{2/3}$ (b)Relative cooling power as a function of field for$Yb_{1-x}Ho_xMnO_3$ (x = 0.1,0.2 and 0.3) samples.

For practical applications, not only the high value of-$\Delta S_M$, but also the temperature range over which it remains large is important. The characteristic parameter that determines the magnetic cooling efficiency of a magnetocaloric material is the relative cooling power (RCP) and is defined in equation 4.4.It is a measure of the quantity of heat transferred by the magnetic refrigerant between hot and cold sinks. Calculated values of RCP of $Yb_{1-x}Ho_xMnO_3$ are 53.43 ± 14 J /mol, 67.52 ± 21 J/mol and 90.0 ± 27 J/mol with ΔH = 10 T for x = 0.1, 0.2 and 0.3, respectively. Furthermore, the values of the RCP increase with increasing of the Ho content. These values are higher than single crystal $YbMnO_3$ (RCP = 26 J/mole with ΔH = 8

T) [14]and other rare earth manganites except for Ho/$DyMnO_3$[15].The RCP values exhibit a linear increase with increasing field for all compounds as shown in fig6.8(b). Thus, RCP of these compounds indicates that these materials can be considered as potential candidates applications for magnetic refrigeration at low temperature.

## 6.3.4 Universal curve

Franco and Conde [18] suggested the $\Delta S_M$ versus temperature curves for second order transition converges to a single universal after proper rescaling of the temperature axis. Thus ($-\Delta S_M/\ \Delta S_M{}^{max}$) versus the reduced temperature ($\theta$), defined in Eq.4.9, collapses to a single universal curve. Figure 6.9 shows the dependence of $\Delta S^*$ ($-\Delta S_M/\Delta S_M{}^{max}$) for typical field changes for $Yb_{0.7}Ho_{0.3}MnO_3$. It can be clearly seen that the experimental points of the samples distribute on one universal curve of the magnetic entropy change (ranging from 5 T to 10 T), demonstrating the predictions of universal curve behavior for different magnetic fields of the same sample. The universal curve can be well fitted by a Lorentz function [19]

$$\Delta S^* = \frac{a}{b+(\theta-c)^2}, \qquad (6.2)$$

where *a*, *b*, and *c* are the free parameters a, =1.28,b = 1.25, and c = -0.13.

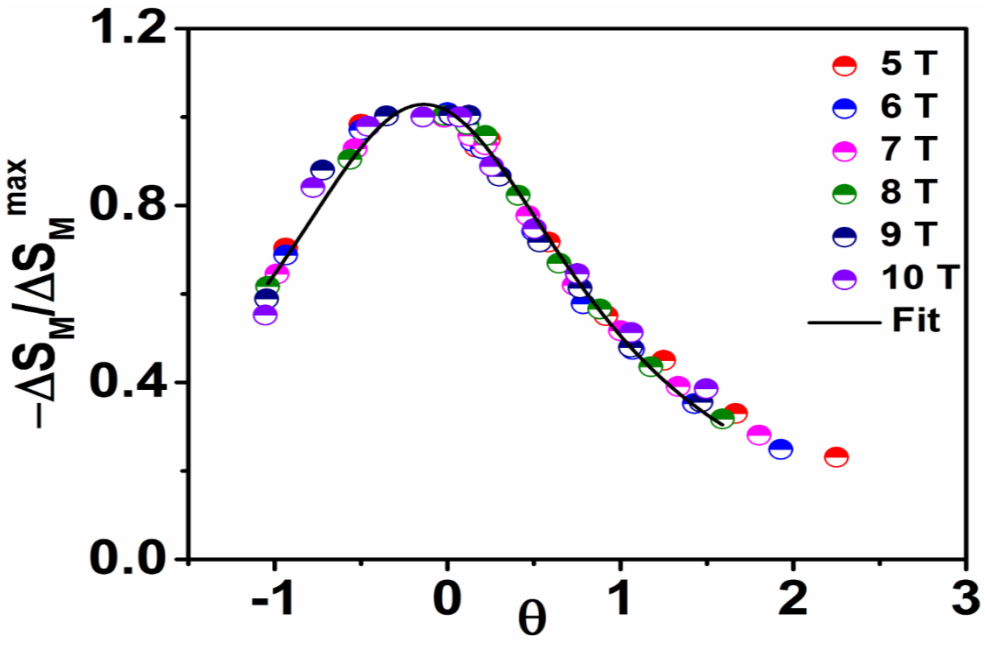


Figure.6.9: The universal curve behavior of the curves as a function of the rescaled temperature for different magnetic field for $Yb_{0.7}Ho_{0.3}MnO_3$.

The introduction of $Ho^{3+}$(10.6 $\mu_B$) at the $Yb^{3+}$(4.53$\mu_B$)resulted increased magnetization (figures6.5), increased magnetic entropy change and consequently enhanced the RCP values. Thus the higher moment of the doped Ho ion is responsible for the enhancement of the $\Delta S_M$ and RCP in the samples. This argument is supported by the fact that with non-magnetic Sc substitution at the Yb site the $|\Delta S_M|$ and RCP values decreased in chapter5. The $\Delta S_M$, RCP values at 10 T versus effective moment (theoretically calculated:$\mu_{eff} = ((1-x)\mu^2_{Yb} + \mu^2_{Mn})^{1/2}$ for Sc doping and $\mu_{eff}= ((1-x)\mu^2_{Yb^{3+}} + x\mu^2_{Ho^{3+}} + \mu^2_{Mn^{3+}})^{1/2}$ for Ho doping) and $\Delta S_M$,RCP values versus the maximum magnetization M (at 2.5K, 10 T) are shown in the figure.6.10 (c), (d), (e) and (f). The data points are shown in symbols with error bars and the solid line in the figures is linear fit to the data. There is a clear trend between the $\Delta S_M$, RCP and effective moment of the samples.

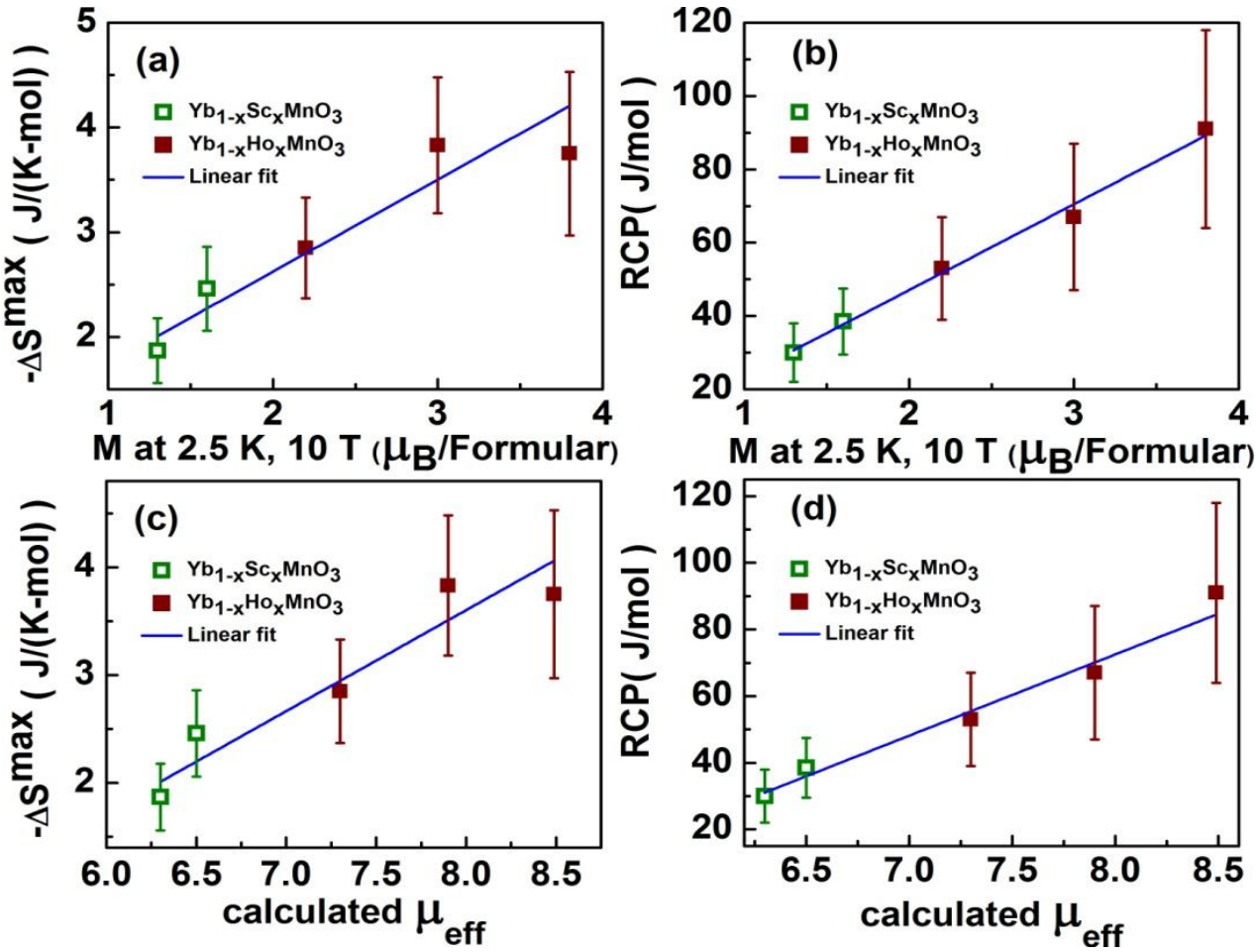


**Figure.6.10:(**a) and(b), $|\Delta S_M^{max}|$ and RCP at 10 T vs magnetization at 2.5 K, 10 T. (c) and (d), $|\Delta S_M^{max}|$ and RCP at 10 T vs effective moment for the $Yb_{1-x}Ho_xMnO_3$ and $Yb_{1-x}Sc_xMnO_3$ [chapter 5].

## 6.4 Conclusion

Polycrystalline hexagonal $Yb_{1-x}Ho_xMnO_3$ (x = 0.1, 0.2 and 0.3) compounds are prepared by solid state synthesis route. Magnetization measurements show $Mn^{3+}$ AFM ordering at the Néel temperature ($T_{N1}$) of ~ 83 K. Also the ferromagnetic (FM) ordering due to the Yb moments is observed at low temperatures ($T_{N2}$ ~ 5 K). Isothermal magnetization measurements at low temperatures ($T<T_{N2}$) show the field induced magnetic transition in the samples. The maximum entropy change $|\Delta S_M^{max}|$ and the relative cooling power (RCP) determined from the isothermal magnetization data of $Yb_{1-x}Ho_xMnO_3$ are 3.75 ± 0.78 J/ (mole K) and 90.0 ± 27 J/molfor $x$ = 0.3 at ΔH = 100 kOe. With increasing Ho content, both $|\Delta S_M^{max}|$ and RCP found to increase. $Yb_{1-x}Ho_xMnO_3$ seem to be potential materials for magnetic refrigeration in the low temperature region. The normalized entropy change vs the rescaled temperature for $Yb_{0.7}Ho_{0.3}MnO_3$ follows a universal curve behavior with a Lorentz function and the universal curve is a helpful tool for the evaluation of properties such as the refrigerant capacity RCP.

## 6.5 References:

[1]. V.K. Pecharsky, K.A. Gschneidner Jr, J. Magn. Magn. Mater.**200**, (1999).44–56

[2]. V. Provenzano, J. Li, T. King, E. Canavan, P. Shirron, M. DiPirro, J. Magn. Magn. Mater.**266**,(2003), 185–193.

[3]. Junghwan Park, Misun Kang, Jiyeon Kim, Seongsu Lee, Kwang-Hyun Jang, A. Pirogov, and J.-G. Park Phys. Rev. B,**79**,(2009), 064417.

[4]. Peng Liu, Xiao-Lin Wang, Zhen-Xiang Cheng, Yi Du, and Hideo Kimura Phys. Rev. B,**83**, (2011), 144404.

[5]. L. Chaix,S. de Brion, S. Petit, R. Ballou, L.-P. Regnault, J. Ollivier, J.-B. Brubach, P. Roy, J. Debray,P. Lejay,A. Cano, E. Ressouche, and V. Simonet Phys. Rev.Lett.**112**,(2014), 137201.

[6]. H. Sugie, N. Iwata, K. Kohn, J. Phys. Soc. Jpn., **71**, (2002), 1558.

[7]. X. Fabre ´ges, I. Mirebeau, P. Bonville, S. Petit, G. Lebras-Jasmin, A. Forget, G. Andre, and S. Pailhes, Phys. Rev. B. ,**78,**(2008), 214422.

[8].N. Abramov, S. Lofland, and Ya. Mukovskii, phys. status solidi B, **1**-**3**,(2012), 48318.

[9] M. C. Sekhar, S. Lee, G. Choi, C. Lee, and J.-G. Park, Phys. Rev. B, **72**,(2005),014402.

[10] A. Arrott and J. Noakes, Phys. Rev. Lett., **19**, (1967), 786.

[11] S. K. Banerjee, Phys. Lett.**12**,(1964),16.

[12] V.V. Pecharsky and K.A.Gschneidner, J. Appl. Phys., **86**,(1999), 565

[13] A. Midya, P. Mandal,S. Das, S. Banerjee, L. S. Sharath Chandra, V. Ganesan and S,Roy Barman, Appl. Phys. Lett, **96**, (2010), 142514.

[14] A. Midya, S. N. Das, P. Mandal, S. Pandya and V. Ganesan, Phys. Rev. B ,**84**,(2011), 235127

[15] Mingjie Shao, ShixunCao, Shujuan Yuan, Jin Shang, Baojuan Kang, Bo Lu, and JincangZhangAppl. Phys. Lett, **100**,(2012), 222404.

[16] Jin-Ling Jin, Xiang-Qun Zhang, Guo-Ke Li, and Zhao-Hua Cheng Phys. Rev. B ,**83**,(2011), 184431.

[17] V. Franco, A. Conde, V. K. Pecharsky and K. A. Gschneidner, EPL, **79**,(2007), 47009.

[18] Franco V,and Conde A. International. J Refrig. **33**, (2010), 465–73.

[19] Q. Y. Dong, H. W. Zhang,J. R. Sun, B. G. Shen, and V. Franco,J.Appl.Phys.**104**,(2008), 116101.

# Chapter 7

## *Structural, magnetic, and magnetocaloric effect of polycrystalline $Yb_{1-x}Er_xMnO_3$*

## 7.1 Introduction:

The hexagonal $RMnO_3$ compounds show ferroelectric transitions ($T_C$) at high temperatures in the range of 590–1000 K and antiferromagnetic transitions ($T_N$) at low temperatures from 70 to 130 K. [1, 2]. $T_N$ is ~ 85 K for YbMnO3 [3], and ferroelectric transition temperature is ~ 990 K [4], whereas $T_N$ is ~ 76 K for ErMnO3 [5] and ferroelectric transition temperature is ~880 K [4]. Since the crystal structures of $YbMnO_3$ and $ErMnO_3$ are quite similar, the Er doping in $YbMnO_3$ provides a chance to investigate additional contributions due to doping effects. Especially, the differences in ferroelectric transition temperatures make it significant to investigate how the ferroelectric and dielectric properties are modified through Er in $YbMnO_3$. The magnetic moment of Er is higher compare to Yb, so it is expected to effect ~~on~~ magnetic and magnetocaloric properties. In the present chapter, structural, magnetic, specific heat ($C_P$) and magnetocaloric properties of the Er doped $YbMnO_3$ compounds are discussed as the molecular field could be modified slightly by $Er^{3+}$doping since its ionic size is a little larger than that of $Yb^{3+}$ and has a higher magnetic moment

## 7.2 Experimental Detials

Polycrystalline samples of $Yb_{1-x}Er_xMnO_3$ (x = 0.1, 0.2 and 0.3) were prepared by the standard solid-state reaction method. Stoichiometric amounts of high-purity (purity better than 99.9%) $Yb_2O_3$, $MnCO_3$, and $Er_2O_3$ powders were thoroughly mixed and subsequently calcined in air at 1200 $^0$C for 24 h, with an intermediate grinding for homogenization. The calcined mixture was cold pressed into pellets, sintered at 1450 $^0$C in air for 24 hours. Finally, all the samples were slowly cooled to room temperature for sufficient oxygenation. The phase purity of each sample was checked by the powder x-ray diffraction (XRD) on Bruker D8 Advance X-ray powder diffractometer using Cu-Kα radiation. All the magnetization measurements were performed on a vibrating sample magnetometer (PPMS-VSM) in the temperature range 2 to 300 K in 10 KOe applied *dc* magnetic field in zero field cooled (ZFC) state of the samples. In addition, Specific heat was measured by the relaxation method using a PPMS (M/S Quantum Design, USA), having a superconducting magnet of 14 T, from 2 K to 160 K.

## 7.3 Results and Discussions

### 7.3.1 X-Ray diffraction

The X-ray diffraction patterns and the Rietveld refinement of the polycrystalline samples $Yb_{1-x}Er_xMnO_3$ (x = 0.1, 0.2 and 0.3) are shown in fig.7. 1. All the samples are in a single phase and the measured patterns can be indexed to the hexagonal phase with $P6_3cm$ space group, in agreement with a previous report [7]. Refined values of the lattice parameters of and discrepancy factors for $Yb_{1-x}Er_xMnO_3$ (x = 0.1, 0.2 and 0.3) are shown in Table 7.1. The variation of lattice parameters with the Er content are shown in fig.7.2 (a). The increase in lattice constant *a* and decrease in lattice constant *c* is observed which is due to the larger ionic radius of $Er^{3+}$ [Shannon radius = 1.003Å for coordination number (CN) = 8] than $Yb^{3+}$ (Shannon radius = 0.985Å nm for CN = 8). The unit cell volume increases too with increasing Er concentration, following roughly the Vegard law as shown in Fig. 7.2 (b).

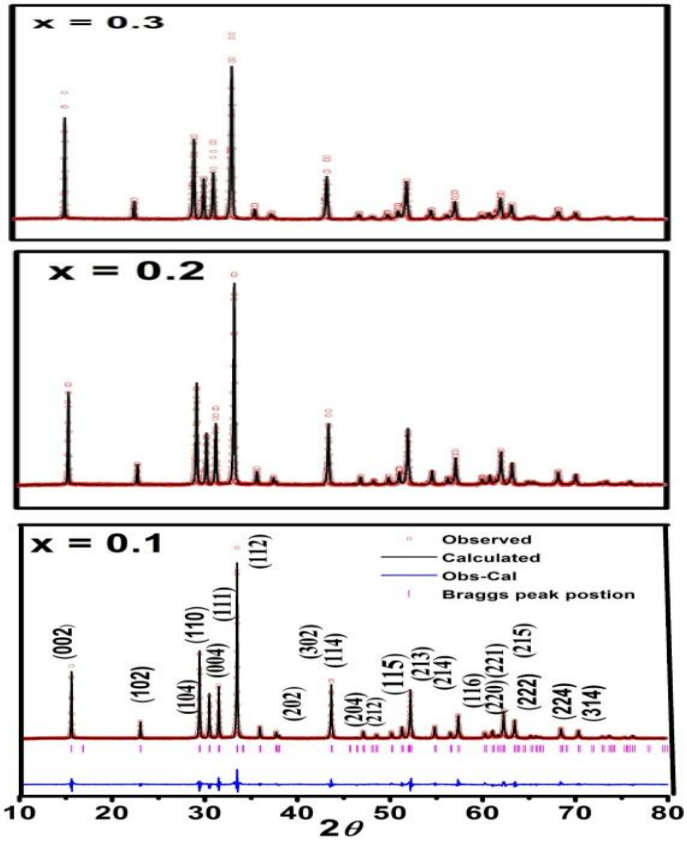


Figure. 7.1: Rietveld refinement of XRD patterns for $Yb_{1-x}Er_xMnO_3$ (x = 0.1, 0.2 and 0.3).

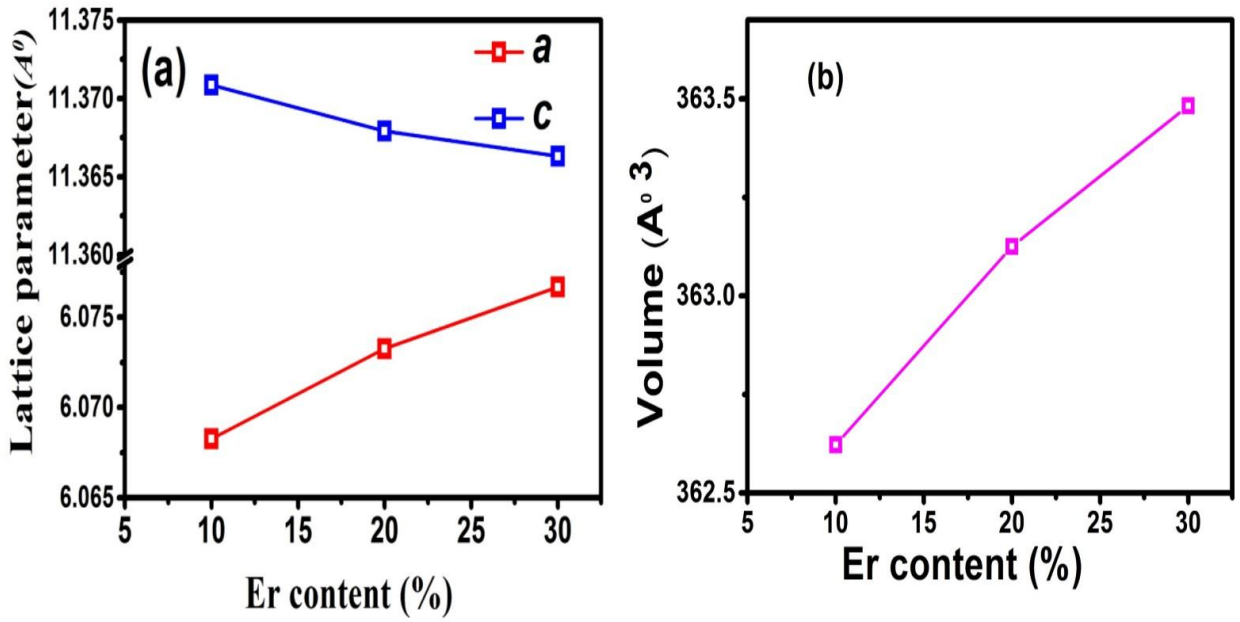


Figure.7.2: (a) Variation of lattice parameters a and c with the Er content. (b) Volume of the unit cell for $Yb_{1-x}Er_xMnO_3$ (x = 0.1, 0.2 and 0.3) as a function of the Er content.

Table7.1. Refined crystallographic parameters and reliability factors of $Yb_{1-x}Er_xMnO_3$ (x = 0.1, 0.2 and 0.3) as obtained by Rietveld analysis.

| **$Yb_{1-x}Er_xMnO_3$** | *x* = 0.1 | *x = 0.2* | *x = 0.3* |
|---|---|---|---|
| *a* (Å) | 6.0672 | 6.0726 | 6.0785 |
| *c* (Å) | 11.3686 | 11.3675 | 11.3673 |
| *V* (Å$^3$) | 362.416 | 363.034 | 363.740 |
| $R_P$ | 8.32 | 8.17 | 9.90 |
| $R_{wp}$ | 11.6 | 11.3 | 13.9 |
| $R_B$ | 4.92 | 5.30 | 6.62 |

Some selected bond distances and bond angles ~~is~~ are given in Table 7. 2. Mn-O3 and Mn-O4 bond lengths increases with the Er content, as parameter *a* increases with the Er content. Mn-O1 and Mn-O2 bond lengths along the c axis also increase lightly with the Er content. The

average Mn–O distances in $MnO_5$ units are significantly larger in the Er doped samples compared to those of pure $YbMnO_3$.

**Table7.2**. Main bond distances (A˚) and angles for $MnO_N$ polyhedra (N= 5) in $Yb_{1-x}Er_xMnO_3$ (x = 0.1, 0.2 and 0.3)

| **Parameter** | **x = 0.1** | **x = 0.2** | **x = 0.3** |
|---|---|---|---|
| Mn-O1 | 1.8452 | 1.8451 | 1.8450 |
| Mn-O2 | 1.8031 | 1.8030 | 1.8031 |
| <Mn-O1, O2> | 1.8241 | 1.8240 | 1.8240 |
| Mn-O3 | 1.9134 | 1.9150 | 1.9169 |
| Mn-O4 | 2,0961 | 2.0979 | 2.1000 |
| <Mn-O3, O4> | 2.0047 | 2.0064 | 2.0084 |
| <Mn-O> | 1.9144 | 1.9152 | 1.9162 |
| Mn-O3-Mn (°) | 118.647(9) | 118.649(6) | 118.652(7) |
| Mn-O4-Mn (°) | 119.028(9) | 119.058(6) | 119.059(9) |
| $\Delta(10^{-4})$ | 27.4 | 27.7 | 28.1 |

The distortion parameter is nearly constant with increasing Er content in hexagonal phases. In general, the Er doping does not notably affect the structure of the $MnO_5$ polyhedron, in agreement with the weak changes of the trigonal bipyramidal crystal field, which is proved by the fact that the $Mn^{3+}$ions ($3d^4$) remain in the high spin state (S=2) throughout the whole doping range.

## 7.3.2 Magnetic measurements

The temperature dependence of susceptibility χ (T) under an applied magnetic field of 1 T for $Yb_{1-x}Er_xMnO_3$ (x = 0.1, 0.2 and 0.3) in zero field cooled (ZFC) mode is shown in fig. 7.3. The magnetic susceptibility of each sample exhibits paramagnetic like behavior with temperature.

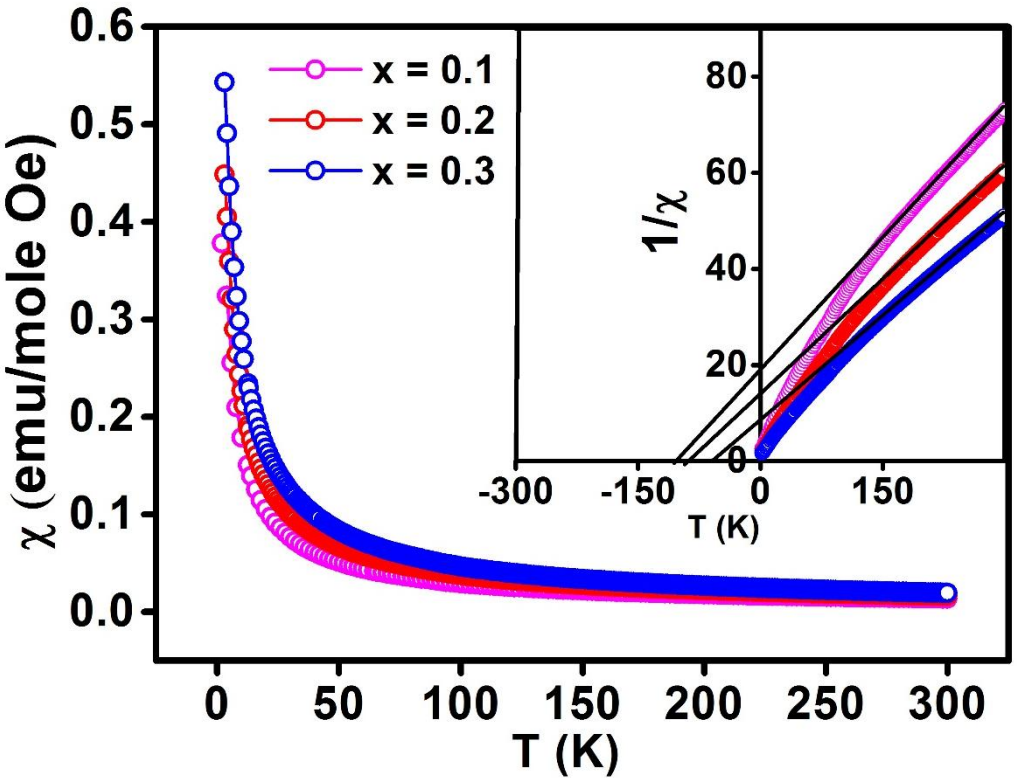


Figure. 7.3: Temperature dependence of the Zero Field Cooled (ZFC) magnetic susceptibility for $Yb_{1-x}Er_xMnO_3$ (x = 0.1, 0.2 and 0.3) at 1T. Insert shows Curie Weiss fit.

No clear magnetic transitions are observed over the whole temperature range in $\chi$ *vs* T data. The antiferromagnetic moments from Mn-Mn ordering are masked by the paramagnetic moments from $Yb^{3+}$ and $Er^{3+}$ ions. Temperature variation of the inverse magnetic susceptibility $\chi^{-1}$ *vs* T is shown as the inset in fig. 7.3 which shows that in the paramagnetic phase the the Curie–Weiss (CW) law is well obeyed in the temperature interval between 200 and 300 K. The Curie-Weiss temperatures are found to decrease with the Er doping i.e., $\theta_{CW}$ = -106 K for $Yb_{0.9}Er_{0.1}MnO_3$, -83 K for $Yb_{0.8}Er_{0.2}MnO_3$ and -66 K for $Yb_{0.7}Er_{0.3}MnO_3$. The negative Weiss temperature indicates that the antiferromagnetic interaction is dominating in these samples. The experimental effective magnetic moments of these samples were calculated using the equation $\mu_{eff} = (7.99C)^{0.5}$, where C is the Curie–Weiss constant.

The long range magnetic ordering temperatures are difficult to be defined clearly from the $\chi$(T) curves for some samples, so we show first derivative of susceptibility (d(1/$\chi$)/dT) *vs* T in fig.7.4. The d(1/$\chi$)/dT clearly shows a peak around 85 K due to a canted spin ordering of the $Mn^{3+}$ ions. $T_N$ slightly changes with change in x of hexagonal $Yb_{1-x}Er_xMnO_3$ (x = 0.1, 0.2 and 0.3). From the Curie-Wiess fit, the calculated effective moment ($\mu_{eff}$) increases with x. $\mu_{eff}$ is

6.40$\mu_B$ for $Yb_{0.9}Er_{0.1}MnO_3$ while it becomes 7.11, and 7.56$\mu_B$ for $Yb_{0.8}Er_{0.2}MnO_3$, and $Yb_{0.7}Er_{0.3}MnO_3$, respectively. We note that the experimental values of $\mu_{eff}$ are in good agreement with our calculations using the following formula: $\mu_{eff} = ((1-x)\mu^2_{Yb} + x\mu^2_{Er^{3+}} + \mu^2_{Mn^{3+}})^{1/2}$, where x is the Er concentration while $\mu_{Yb}$, $\mu_{Er}$ and $\mu_{Mn}$ are the effective magnetic moment of $Yb^{3+}$ ( $\mu_{Yb} = 4.53\mu_B$) , $Er^{3+}$ (Er = 9.6 $\mu_B$) and $Mn^{3+}$ (Mn = 4.9 $\mu_B$), respectively. The ratio $f = |\theta_{CW}/T_N|$, which is a measure of geometric frustration, is significantly reduced with increasing Er content as shown in table.7.2, which indicates the magnetic coupling between the Yb and the Mn moments might be relieve the frustration effects.. The magnitude of the magnetically coupling between Yb and Mn ions is the most important factors for the geometrical frustration.

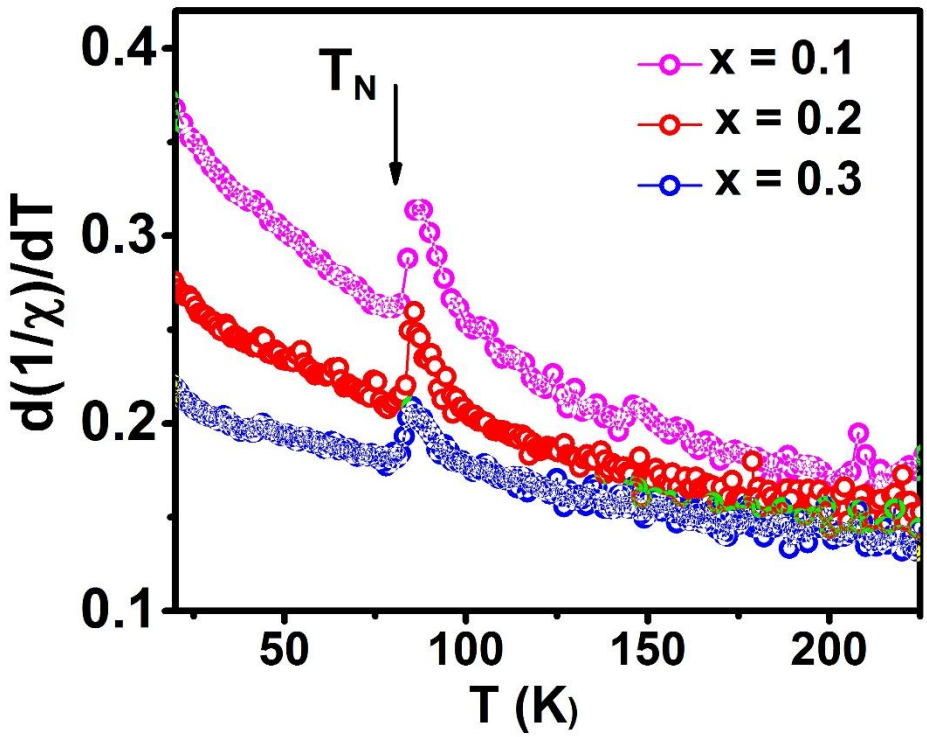


Fig7.4. d(1/χ)/dT as a function of temperature for $Yb_{1-x}Er_xMnO_3$ (x = 0.1, 0.2 and 0.3)

Table 7.3. Magnetic parameters from Curie-Wiess fit for $Yb_{1-x}Er_xMnO_3$ (x = 0.1, 0.2 and 0.3)

| **$Yb_{1-x}Er_xMnO_3$** | *x* = 0.1 | *x = 0.2* | *x = 0.3* |
|---|---|---|---|
| $\mu_{eff}^{Exp}(\mu_B)$ | 6.67 | 7.11 | 7.56 |
| $\mu_{eff}^{Theor}(\mu_B)$ | 7.18 | 7.43 | 8.12 |
| $\theta_{CW}$ (K) | -106 | -83 | -66 |
| $T_N$(K) | 86 | 85.5 | 85.2 |
| $f = \lvert\theta_{CW}/T_N\rvert$ | 1.2 | 0.9 | 0.8 |

The isothermal magnetization (M-H) curves of $Yb_{1-x}Er_xMnO_3$ (x = 0.1, 0.2 and 0.3), measured at 2.5 K, are shown in Fig.7.5 (a). All the samples show magnetic hysteresis loops representing weak ferromagnetic (FM) behavior due to rare earth elements. The FM component is more visible for the Er doped samples. The weak ferromagnetic (FM) behavior is observed in these samples with corresponding coercivity (Hc) around 500 Oe, with change in Er concentration slightly changes coercivity but retentivity increases with the Er content as shown in fig 7.5(b). The magnetizations of these samples increase linearly with increasing magnetic field below 30 kOe and do not saturate up to 100 kOe. As for $Yb_{0.9}Er_{0.1}MnO_3$ and $Yb_{0.7}Er_{0.3}MnO_3$, the magnetization at 100 kOe is 2.1 $\mu_B$ and 3.0 $\mu_B$, respectively. Moreover, the magnetizations of these samples increase according to the increasing erbium concentration, as a result of the higher effective magnetic moment of $Er^{3+}$(9.6 $\mu_B$) compared to that of $Yb^{3+}$(4.53$\mu_B$) .

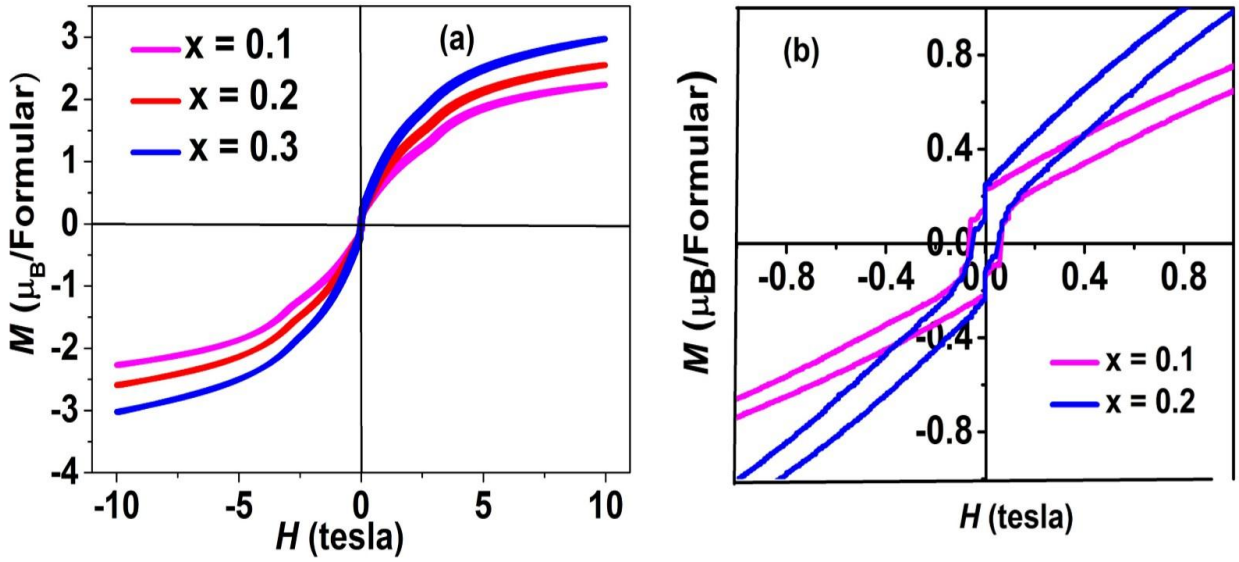


Figure 7.5: (a) Isothermal magnetization curves of $Yb_{1-x}Er_xMnO_3$ (x = 0.1, 0.2 and 0.3) at 2.5 K. Inset shows of (b) M *vs* T for $Yb_{0.9}Er_{0.1}MnO_3$ and $Yb_{0.7}Er_{0.3}MnO_3$ up to 1 tesla.

### 7.3.3 Specific heat measurements

Data of specific heat ($C_P$) of $Yb_{1-x}Er_xMnO_3$ (x =0.1 and 0.2) *vs* T with zero magnetic field are shown in the fig 7.6 together with the estimates for phonon contributions using the Debye model with two Debye temperatures. A good fit is only obtained when two Debye temperatures, $\theta_{D1}$= 370 K and $\theta_{D2}$= 705 K are used for the fitting, which is similar to the values in Mg doped $YbMnO_3$ discuss in chapter 4. Magnetic specific heat $C_{mag}/T$ is shown in fig 7.7 after subtracting off the phonon contribution. (Details of these calculations are given in earlier Chapter …). It displays a clear peak at the antiferromagnetic transition ($T_N$) ~83 K for both samples and is independent of the magnetic field.

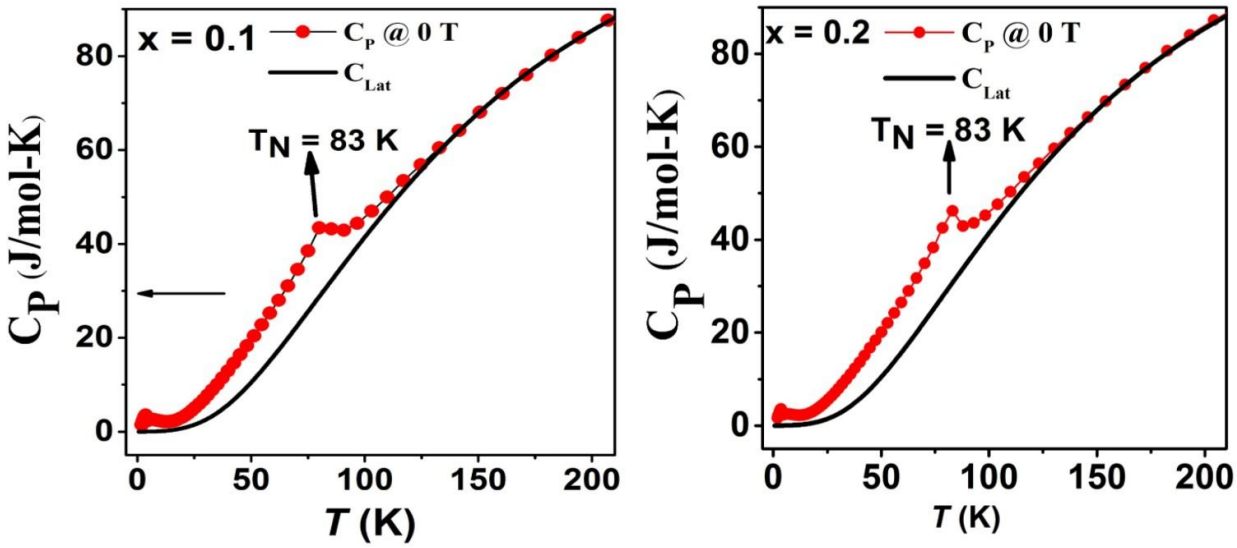


Figure.7.6: Specific heat of $Yb_{1-x}Er_xMnO_3$ (x = 0.1 and 0.2) at zero magnetic field with phonon estimate lines using Debye temperatures.

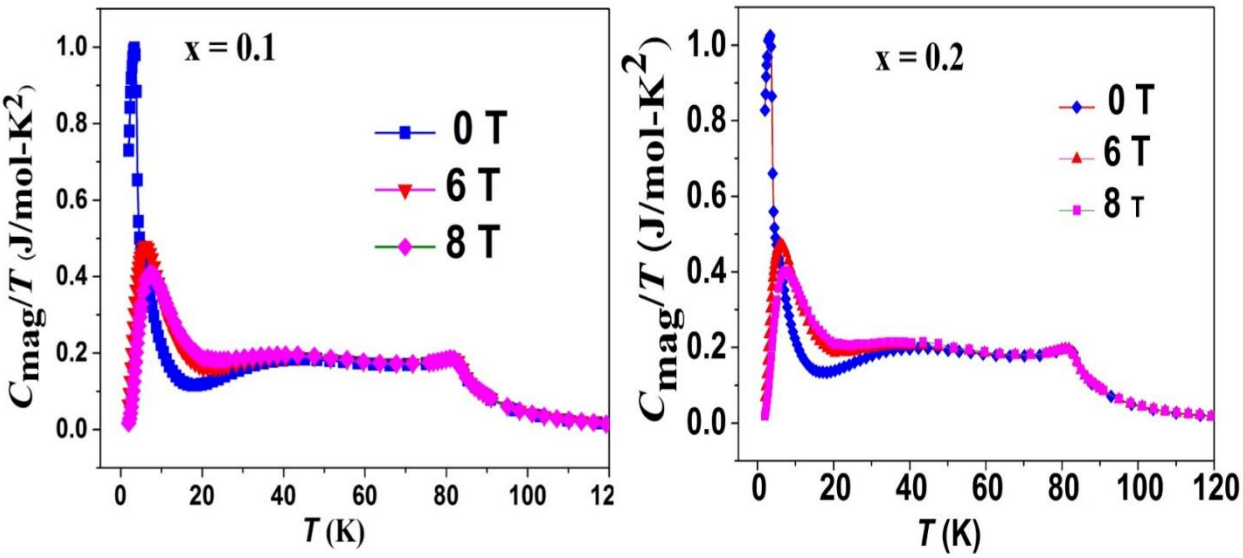


Figure. 7.7: Temperature dependence of $C_{mag}/T$ with different magnetic fields for $Yb_{1-x}Er_xMnO_3$ (x = 0.1 and 0.2)

By subtracting off the phonon contribution from the raw data, we have obtained the total magnetic entropy of 15.5 J/mol K for $Yb_{0.9}Er_{0.1}MnO_3$, and 16.0J/mol K for $Yb_{0.8}Er_{0.2}MnO_3$ at $T_N$~ 83 K., which are shown in fig 7.8. A pronounced peak in $C_P$ (measured in zero magnetic field), seen in fig 7.9 at 3.7 K, is identified with the long range ferromagnetic

ordering due to Yb(Er) at the 2a site [3] This peak disappears in applied magnetic field. Fig 7.9 shows a strong Schottky anomaly in $C_p$ below 20 K for $Yb_{1-x}Er_xMnO_3$ due to Yb (Er) in site 4b due to the Mn molecular field. This anomaly shifts to higher temperature and smears out on application of a magnetic field. The Mn molecular field at the Yb 4b site is rather high, while it is absent at the 2a site. The value of the energy splitting is $\Delta_{sch}= 2\mu_{Yb}H_{mf}$, where $\mu_{Yb}$ is the magnetic moment of Yb in the site 4b, and $H_{mf}$ is the effective molecular field at the Yb 4b site. Only the concentration of Yb ions is taken into account to calculate the Schottky energy. A contribution from a two level Schottky function should be appropriate to fit the excess specific heat at low temperatures.

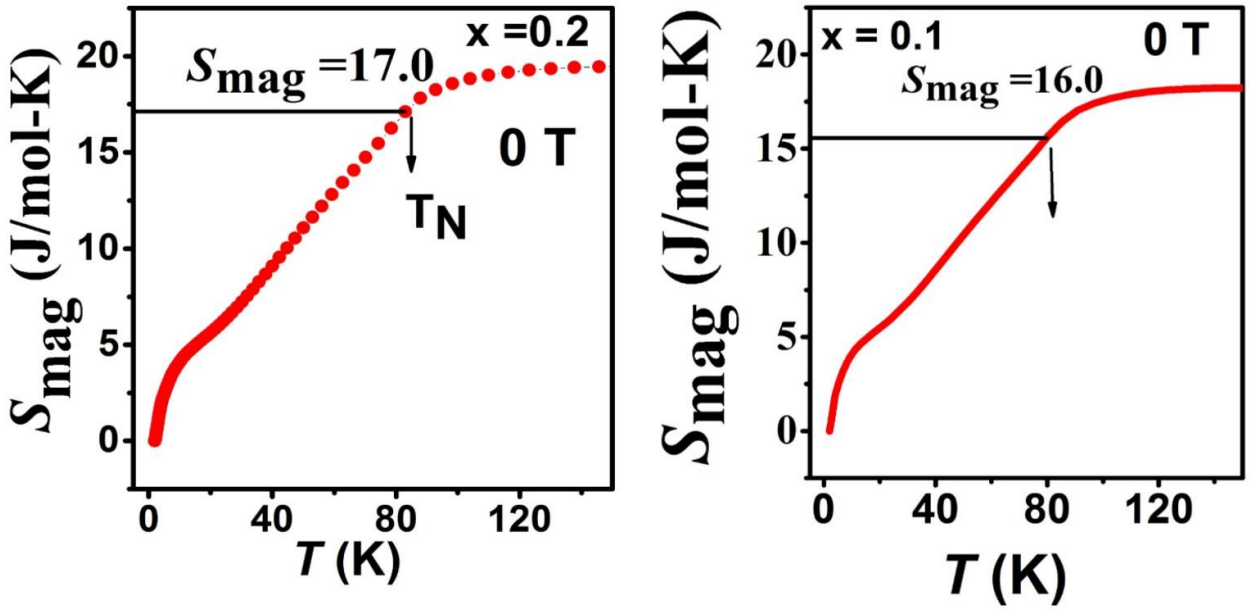


Figure.7.8: Magnetic entropy (S) with zero magnetic field for $Yb_{1-x}Er_xMnO_3$ (x = 0.1 and 0.2)

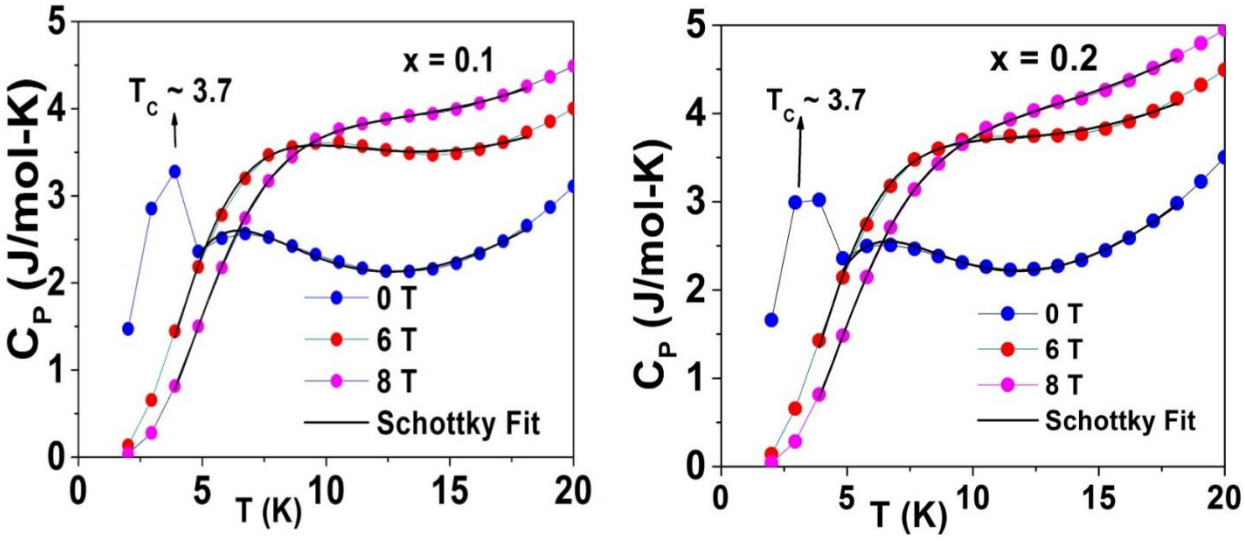


Figure 7.9: Schottky fitting with different magnetic fields for $Yb_{1-x}Er_xMnO_3$ (x = 0.1 and 0.2)

We have used the Schottky function for the two level system as,

$$C_p(T) = C_S(T, \Delta_{Sch}) + C_0(T), \qquad (7.1)$$

Where $C_{Sch}(T, \Delta_{Sch}) = nN_A k_B \left(\frac{\Delta_{Sch}}{k_B T}\right)^2 \left[\frac{\exp\left(\frac{\Delta_{Sch}}{k_B T}\right)}{\left(1+\exp\left(\frac{\Delta_{Sch}}{k_B T}\right)\right)^2}\right]$

is the Schottky contribution with $n$ = 2/3 for Yb 4b sites taken from the literature [7] with $N_a$ being Avogadro's number and $k_B$ Boltzmann's constant. We have chosen $C_0(T) = aT + bT^2 + cT^3$ to describe the phonon and magnon contributions. We obtain values of $\Delta_{sch}$ and $H_{mf}$ at Yb 4b sites from Schottky fit with different magnetic fields which is shown in table.7.3. We observe that the magnitude of the Schottky gap $\Delta_{sch}$ is higher for larger concentration of $Yb^{3+}$ ions. That is, the molecular field experienced by the Yb ion is the strongest for $Yb_{0.9}Er_{0.1}MnO_3$. The Schottky gap and molecular field increase with the magnetic field. In $NdMnO_3$ and $PrMnO_3$ crystals, Schottky energy increases as H increases similar to reported earlier [8].

It is to be noted that due to a breakdown in the heat capacity equipment, sample with x = 0.3 could not be run but trend is expected to be similar.

**Table.7.3**.Values of $\Delta_{sch}$ and $H_{mf}$ with different magnetic fields. Also listed are magnetocaloric effect (MCE) parameters: $\Delta T_{ad}$,$^{max}$, $\Delta S_M{}^{max}$ and RCP.

| **$Yb_{1-x}Er_xMnO_3$** | | | | | | | | |
|---|---|---|---|---|---|---|---|---|
| | **From Schottky Fit** | | | | **MCE** | | | |
| | **H (T )** | **$\Delta_{sch}$ (mev or K)** | **$H_{mf}$ (T)** | | **$\Delta H$ (T)** | **$\Delta S_M{}^{max}$ (J mol$^{-1}$ K$^{-1}$)** | **$\Delta T_{ad}{}^{max}$ (K)** | **RCP J mol$^{-1}$** |
| **X= 0.1** | 0 | 1.1 or ~13 | 3.3 | | 2 | 0.5 | 0.7 | 1.7 |
| | 6 | 1.3 or ~15 | 3.8 | | 4 | 0.9 | 1.7 | 6 |
| | 8 | 1.6 or ~18.7 | 4.8 | | 6 | 1.5 | 3.4 | 13.8 |
| | | | | | 8 | 2 | 5.4 | 23.1 |
| **X= 0.2** | 0 | 1.2 or 13.3 | 3 | | 2 | 0.5 | 0.7 | 1.5 |
| | 6 | 1.3\ or 15 | 3.6 | | 4 | 1 | 1.8 | 6 |
| | 8 | 1.57 or 18.3 | 4.1 | | 6 | 1.6 | 3.5 | 13.9 |
| | | | | | 8 | 2.1 | 5.6 | 23.8 |
| **Reported values for $YbMnO_3$** | | | | | | | | |
| **Ref 9** | - | - | - | | 8 | 2.3 | 15 | 26 |
| **Cha 4** | 0 | 0.87 or 10 | 3.0 | | 10 | 2 | 6.4 | 26 |
| **Ref 7** | 0 | 0.73 | 3.6 | | - | - | - | - |

## 7.3.4 Magnetocaloric effect

The magnetocaloric effect (MCE) is also calculated for these samples using the specific heat data. The total entropy of a sample, S (T,H) is calculated using the following relation [10].,

$$S(T,H) = \int_0^T \frac{C(T,H)}{T} dT \qquad (7.2)$$

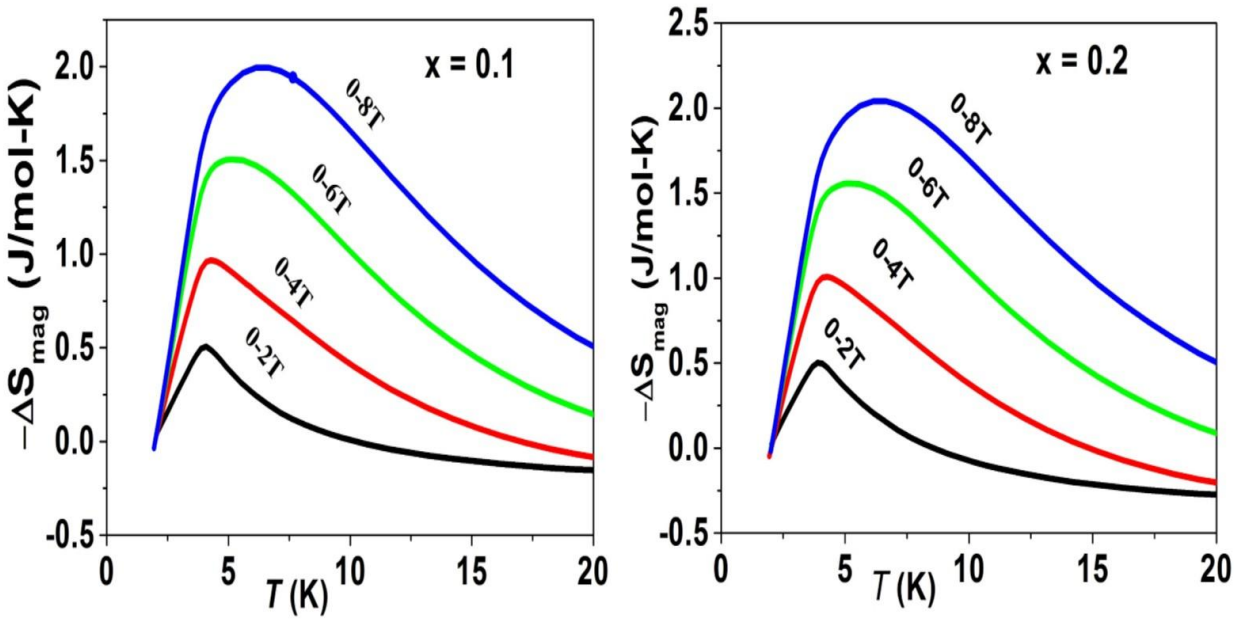


Figure 7.10: Temperature variation of magnetic entropy change for different field change of $Yb_{1-x}Er_xMnO_3$ (x = 0.1 and 0.2)

$\Delta S_{mag}$ (H,T), change in magnetic entropy is S(H,T) – S (H,0). $-\Delta S_M$ vs T, at different magnetic field changes is shown in fig 7.10 for both samples Maximum values of $\Delta S_{mag}^{max}$ are 2 $J.mol^{-1}.K^{-1}$ for $Yb_{0.9}Er_{0.1}MnO_3$ and 2.1 $J.mol^{-1}.K^{-1}$for $Yb_{0.8}Er_{0.2}MnO_3$, with 8 T magnetic field change. $\Delta S_{mag}^{max}$ values increase with the magnetic field change and shift to higher temperature as shown table 7.3 and show agreement with earlier reported values [9]

$\Delta T_{ad}^{max}$ caused by magnetic field change, is obtained by an equation $\Delta T(H,T) = T(S,H) – T (S,0)$, whereT(S,H) and T(S,0) are temperatures in field H and H = 0 at constant S. The plots of $\Delta T_{ad}$ vs. T are shown in fig 7.11 with different field changes for both samples. For $\Delta H$ = 8 T, $\Delta T_{ad}^{max}$ values for $Yb_{0.9}Er_{0.1}MnO_3$ and $Yb_{0.8}Er_{0.2}MnO_3$ are found to be 5.4 and 5.6 K

respectively. $\Delta T_{ad}^{max}$ values increase with ΔH and shift to higher temperature and are in agreement with the reported values in the literature (Table 7.3).

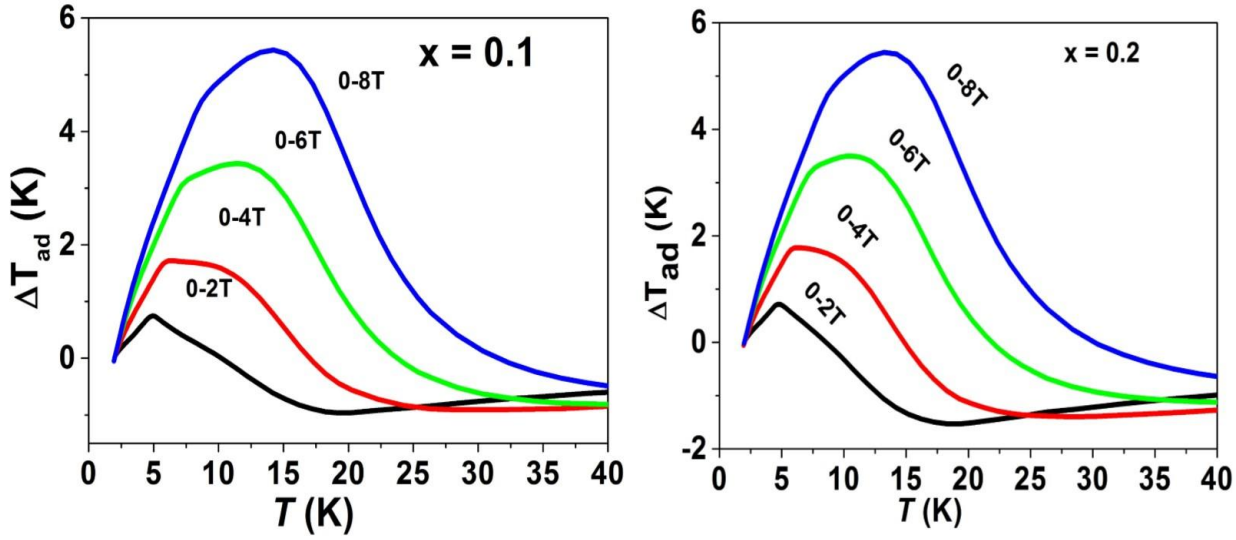


Figure 7.11: Temperature variation of adiabatic temperature change for different field change of $Yb_{1-x}Er_xMnO_3$ (x = 0.1 and 0.2)

Relative cooling power (RCP) is evaluated to determine cooling efficiency of a magnetocaloric material. RCP is given by $\left|\Delta S_{mag}^{max}\right| \times \left|\delta T_{FWHM}\right|$, where $\delta T_{FWHM}$ is full width at half maximum of $\Delta S_M(T)$ curve. RCP values of both samples are listed in Table 7.3 with different ΔH. RCP values are 23.1 J.mol$^{-1}$for $Yb_{0.9}Er_{0.1}MnO_3$ and 23.8 J.mol$^{-1}$ for $Yb_{0.8}Er_{0.2}MnO_3$, with ΔH = 8 T. These values are in agreement with the RCP value of 26 J.mol$^{-1}$ for $YbMnO_3$ single crystal [9]. This shows that polycrystalline Er doped $YbMnO_3$ is equally good for magnetocaloric applications.

## 7.4 Conclusions

Single-phase $Yb_{1-x}Er_xMnO_3$ (x = 0.1, 0.2 and 0.3) compounds were synthesized by the solid-state reaction method. The increases in the *a* lattice parameter with increasing Er content are caused by the small higher radius of the $Er^{3+}$ions. The distortion parameter nearly constant with increasing Er content in hexagonal phases, which is proved by the fact that the $Mn^{3+}$ ions ($3d^4$) remain in the high spin state (S = 2) throughout the whole doping range. The magnetizations of these compounds gradually increases with increasing Er content. Specific heat, $C_P$ *vs* T for $Yb_{0.9}Er_{0.1}MnO_3$ and $Yb_{0.8}Er_{0.2}MnO_3$ show three bumps with zero magnetic

field: one is associated with the antiferromagnetic transition of the $Mn^{3+}$ sublattice, second is due to Schottky anomaly because of the $Yb^{3+}/Er^{3+}$ ground state doublet splitting and other is ferromagnetic ordering due to $Yb^{3+}$ at 2a site. Schottky gap and molecular field increase with magnetic field. These materials exhibit large change in magnetic entropy, adiabatic temperature and RCP values, therefore, these may be exploited for possible magnetic refrigerant applications at low temperatures.

## 7.5 References

[1] W. C. Koehler, H. L. Yakel, E. O. Wollan, and J. W. Cable,Phys.Lett.9, (1964), 93.

[2] B. Lorenz, A. P. Litvinchuk, M. M. Gospodinov, and C. W. Chu, Phys.Rev.Lett.92, (2004), 087204

[3] X. Fabre´ges, I. Mirebeau, P. Bonville, S. Petit, G. Lebras-Jasmin, A. For-get, G. Andre, and S. Pailhes,Phys. Rev. B **78**, (2008), 21442.

[4] Th. Lonkai,1, D. G. Tomuta, U. Amann, J. Ihringer, R. W. A. Hendrikx, D. M. To¨bbens,and J. A. Mydosh, Phys.Rev.Lett. 69, (2004), 134108

[5] Peng Liu, Xiao-Lin Wang, Zhen-Xiang Cheng, Yi Du, and Hideo Kimura, Phys. Rev. Lett. 83 (2011) 14404.

[6] M. C. Sekhar, S. Lee, G. Choi, C. Lee, and J.-G. Park, Phys. Rev. B72, (2005), 014402

[7]. N. Abramov, S. Lofland, and Ya. Mukovskii, phys. status solidi B **1-3,** (2012), 48318.

[8].J.-G. Cheng, Y. Sui, Z. N. Qian, Z. G. Liu, J. P. Miao, X. Q. Huang, Z.Lu, Y.Li, X.J.Wang, and W.H. Su, Solid State Commun **134**, (2005), 381.

[9].A. Midya, S.N. Das, P. Mandal, S. Pandya, V. Ganesan, Phys. Rev. B **84,** (2011), 235127.

[11]. N. Pavan Kumar, and P. Venugopal Reddy, Materials Letters **122**, (2014), 292–295.

# Chapter 8

# Conclusions and future scope of the present thesis

## 8.1 Conclusions

This chapter summarizes key findings of this thesis and brief ideas for future work. In this thesis, the doping effects on the crystal structure, magnetic properties, specific heat properties and magnetocaloric properties of hexagonal manganites are $YbMnO_3$ system, including $Yb_{1-x}Mg_xMnO_3$ (x = 0.0, 0.05 and 0.1), $Yb_{1-x}Sc_xMnO_3$ (x = 0.1 and 0.2), $Yb_{1-x}Ho_xMnO_3$ (x = 0.1, 0.2 and 0.3) and $Yb_{1-x}Er_xMnO_3$ (x = 0.1, 0.2 and 0.3). All these samples were prepared by the solid state reaction. Important points from the investigation are the following:

In chapter 3, the structural, magnetic and magnetoelastic properties of $Yb_{1-x}Mg_xMnO_3$ (x = 0.00 and 0.05) using neutron diffraction and magnetization measurements were investigated. Room temperature neutron diffraction studies were carried out on these samples to determine phase formation as well as cation distribution and structural properties such as bond length and bond angles. The structural analysis shows that with Mg substitution, there is a marginal change in a and c parameters of the hexagonal unit cell, c/a ratio remains constant for x = 0 and 0.05 samples. Due to changes in bond angle and bond lengths on substituting Mg, there is a slight decrease in the distortion of $MnO_5$ polyhedra.

Temperature dependent neutron diffraction studies were carried out on polycrystalline $Yb_{1-x}Mg_xMnO_3$ ($x$ = 0.00 and 0.05) samples. For the magnetic refinement of the present ND data, the structure described by the basis vectors of the irreducible representations $\Gamma_6$ for $Yb^{3+}$ (at Wyckoff site 2*a*), $\Gamma_2$ for $Yb^{3+}$ at 4b site and $\Gamma_2$ representation for Mn at 6*c* site were used. From the Rietveld refinement of temperature dependent ND data, the structural and magnetic properties of the samples were extracted. The temperature dependence of the lattice parameters (*a* and c/*a* ratio) and unit cell volume *V* show anomalous behavior near $T_{N1}$ ~ 85 K (The Mn ordering temperature) due to the magnetoelastic effect. Also all the Mn-O bond distances display considerable variation at $T_{N1}$. Magnetic measurements show that the Néel temperature ($T_N$) increases marginally from 85 *K* for $x$ = 0.00 to 89 *K* for $x$ = 0.05 sample, respectively and also studied structural magnetic properties of $Yb_{0.9}Mg_{0.1}MnO_3$ sample.

In continuation, specific heat and magnetocaloric properties of $Yb_{1-x}Mg_xMnO_3$ ($x$ = 0.00 and 0.05) samples were discussed in chapter 4. The temperature variation of specific heat (Cp) of single phase $Yb_{1-x}Mg_xMnO_3$ (x = 0 and 0.05) has been studied. A peak in $C_p$ is obtained for both samples, it is at ~83 K for x = 0 and at ~86 K for x = 0.05 samples and is attributed to the antiferromagnetic ordering indicating a small increase in Neel temperature due to Mg substitution. The broad feature in $C_p$ vs T at ~6.5 K is attributed to the Schottky anomaly. The estimated effective molecular fields were derived from the Schottky analysis are $H_{mf}$ = 3.0 and 3.5 T for $YbMnO_3$ and $Yb_{0.95}Mg_{0.05}MnO_3$, respectively. High temperature shift of Schottky anomaly with Mg doping indicates increase in effective molecular field of Mn at the Yb 4*b* site. The data supports that the idea that although molecular field is mainly responsible for the Schottky anomaly in $Yb_{1-x}Mg_xMnO_3$ and $Mn^{3+}$ spin ordering also affects it. Specific heat data also shows that the ferromagnetic transition is taking place at 2.7 K for x = 0.0 and T = 3.3 K for x = 0.05 samples due to Yb 2*a* site, thus these compounds show multiple transitions. The data has also been analyzed to determine magnetocaloric properties of these materials. Magnetic part of the specific heat is obtained by subtracting the lattice contribution estimated using two Debye temperatures. The magnetic entropy change ($\Delta S_{mag}$) for pure and doped samples are 2.0 J $mol^{-1}K^{-1}$ and 2.1 J $mol^{-1}K^{-1}$ respectively, while the relative cooling power (RCP ) calculate 26.1 J/mol, 27.2 J/mol for a field change of 10 T.

Polycrystalline hexagonal $Yb_{0.9}Mg_{0.1}MnO_3$ is examined for its magnetic, and magnetocaloric properties. Antiferromagnetic ordering of the Mn sublattice occurs at $T_N$ = 88 K. At low temperature (~3.5 K), the compound shows ferromagnetic (FM) ordering attributed to Yb in site 2a. A Schottky anomaly was observed related to the Yb moments due to Mn molecular field at temperature ~6.7 K. The values of isothermal magnetic entropy change 1.98 J $mol^{-1}K^{-1}$, adiabatic temperature change 16 K and relative cooling power 26 J/mol for a field change of 10 T are also appreciable so as to consider $Yb_{0.9}Mg_{0.1}MnO_3$ as a magnetic refrigerant at low temperatures.

Isothermal magnetization curves measured near the Yb long range ordering temperatures indicate a field induced magnetic transition with applied field. Isothermal magnetic entropy change ($-\Delta S_M$) is calculated from the magnetization curves measured for different temperatures. Values of maximum entropy change ($-\Delta S_M^{max}$), the adiabatic temperature change ($\Delta T_{ad}$) and the relative cooling power (RCP) for these compounds are found to be 3.02 ± 0.37 J/(mol-K), 8.6 ± 0.95 K and 41 ± 9 J/mol for x = 0.00, and 2.63 ± 0.36 J/(mol-K), 9.06 ± 0.96 K and 40.0 ± 10 J/mol for x = 0.05, respectively, for ΔH = 100 kOe. $\Delta S_M^{max}$ versus $h^{2/3}$ shows a linear behavior indicates that these compounds exhibit a second order transition. The

universal curve for the normalized entropy change vs the rescaled temperature for the $Yb_{1-x}Mg_xMnO_3$ constructed.

In chapter 5, the effect of Sc doping on structural, magnetic and magnetocaloric properties of multiferroic $Yb_{1-x}Sc_xMnO_3$ (x = 0.1 and 0.2). X-ray powder diffraction shows that both samples crystallize in the hexagonal phase with $P6_3cm$ space group. The structural analysis shows decrease in lattice parameter *a*, decrease in cell volume of the hexagonal unit cell and decrease in the average bond length between Mn-O, with Sc substitution. Magnetic measurements show that the Néel temperature ($T_N$) increases from 90 *K* for $x = 0.1$ to 94 *K* for $x = 0.2$ sample. Isothermal magnetic curves show that the field variation in magnetization generates a metamagnetic transition. The maximum entropy change $-\Delta S_M^{max}$ and the relative cooling power (RCP)of $Yb_{1-x}Sc_xMnO_3$ are found to be 2.46 ± 0.40 J/mole-K and 38.5 ± 9 J /mol for $x = 0.1$ and 1.87 ± 0.31 J/mole-K and, 30.1± 8 J/mol for $x = 0.2$ with $\Delta H = 10$ T. The behavior of $\Delta S_M^{max}$ vs $h^{2/3}$curve confirm that present materials exhibit a second order transition. The rescaled magnetic entropy change curves for different applied fields collapse onto a single curve for materials with second-order phase transition.

In chapter 6, Magnetocaloric properties of polycrystalline hexagonal $Yb_{1-x}Ho_xMnO_3$ (x = 0.1, 0.2 and 0.3) compounds are studied through magnetization measurements. Temperature dependence of Zero Field Cooled (ZFC) magnetic moment measurements show Néel temperature ($T_{N1}$) of ~ 83 K, corresponding to the $Mn^{3+}$ AFM ordering. At low temperatures ($T_{N2}$ ~ 5 K), all compounds show ferromagnetic (FM) ordering due to alignment of the Yb moments and the field induced magnetic transition is observed in the isothermal magnetization measurements. The maximum entropy change $|\Delta S_M^{max}|$ and the relative cooling power (RCP) of $Yb_{1-x}Ho_xMnO_3$ are 3.75 ± 0.78 J/ (mole K) and 90.0 ± 27 J/mol for $x = 0.3$ at $\Delta H = 100$ kOe. Values of both $|\Delta S_M^{max}|$ and RCP found to increase with increasing Ho content. $Yb_{1-x}Ho_xMnO_3$ seem to be potential materials for magnetic refrigeration in the low temperature region. The normalized entropy change vs the rescaled temperature for $Yb_{0.7}Ho_{0.3}MnO_3$ follows a universal curve behavior with a Lorentz function and the universal curve is a helpful tool for the evaluation of properties such as the refrigerant capacity RCP.

In chapter 7, the effect of Er doping on structural, magnetic and specific heat properties of multiferroic $Yb_{1-x}Er_xMnO_3$ (x = 0.1, 0.2 and 0.3). X-ray powder diffraction shows that both samples crystallize in the hexagonal phase with $P6_3cm$ space group. The structural analysis shows the increase in lattice constant *a* and decrease in lattice constant *c* is due to the larger

ionic radius of $Er^{3+}$, The inverse susceptibility of these compounds observed that the magnetic Neel temperature ($T_N$) slightly change with increasing Er content. The magnetizations of these compounds increases with Er content. Isothermal magnetization (M-H) plots indicated ferromagnetic (FM) character due to the presence of $Yb^{3+}$ ions. Specific heat $C_P$ of polycrystalline hexagonal $Yb_{1-x}Er_xMnO_3$ (x =0.1 and 0.2) samples is measured over a temperature range 2–160 K in different magnetic fields. From the Schottky analysis, Estimated effective molecular fields $H_{mf}$ are 3.3 and 3.0T for samples with x = 0.1 and 0.2, respectively, in zero field. Maximum values of $\Delta S_M^{max}$ are found to be 2 $J.mol^{-1}.K^{-1}$ for $Yb_{0.9}Er_{0.1}MnO_3$ and 2.1 $J.mol^{-1}.K^{-1}$ for $Yb_{0.8}Er_{0.2}MnO_3$, with 8 T field change in the vicinity of ferromagnetic ordering temperature of $Yb^{3+}$.The values of adiabatic temperature change and relative cooling power are calculated to be 5.4 K ,23.1 $J.mol^{-1}$ and 5.6 K, 23.8 $J.mol^{-1}$with a field change of 8 T for$Yb_{0.9}Er_{0.1}MnO_3$ and $Yb_{0.8}Er_{0.2}MnO_3$, respectively, which are appreciable enough to consider these samples as magnetic refrigerants at low temperature.

## 8.2 Comparison of physical properties of Mg, Sc, Ho and Er doped $YbMnO_3$

The following table gives comparison of magnetic and magnetocaloric properties of $YbMnO_3$ due to various doping

| **Compounds** | $\mu_{eff}^{Exp}(\mu_B)$ | $\mu_{eff}^{Theor}(\mu_B)$ | $\theta_{CW}$ **(K)** | $T_N$ | **MCE** | |
|---|---|---|---|---|---|---|
| | | | | | $\Delta S^{max}$ at 10 T (J/mole- K) | **RCP (J/mole)** |
| $YbMnO_3$ | 5.91 | 6.68 | -219 | 85 | 3.02 ± 0.37 | 41 ± 9 |
| $Yb_{0.95}Mg_{0.05}MnO_3$ | 5.66 | 6.6 | -182 | 89 | 2.63 ± 0.36 | 40.0 ± 10 |
| $Yb_{0.9}Sc_{0.1}MnO_3$ | 6.1 | 6.52 | -182 | 90 | 2.46 ± 0.40 | 38.5 ± 9 |
| $Yb_{0.8}Sc_{0.2}MnO_3$ | 5.6 | 6.36 | -193 | 94 | 1.87 ± 0.31 | 30.1±8 |
| $Yb_{0.9}Ho_{0.1}MnO_3$ | 6.81 | 7.33 | -92 | 84 | 2.85 ± 0.48 | 53.43±14 |
| $Yb_{0.8}Ho_{0.2}MnO_3$ | 7.36 | 7.94 | -65 | 84 | 3.83 ± 0.65 | 67.52±21 |
| $Yb_{0.7}Ho_{0.3}MnO_3$ | 7.9 | 8.49 | -52 | 84 | 3.75 ± 0.78 | 90.0±27 |
| $Yb_{0.9}Er_{0.1}MnO_3$ | 6.67 | 7.18 | -106 | 85 | | |
| $Yb_{0.8}Er_{0.2}MnO_3$ | 7.11 | 7.43 | -83 | 85 | | |
| $Yb_{0.7}Er_{0.3}MnO_3$ | 7.56 | 8.12 | -66 | 85 | | |

Among above compounds $Yb_{0.7}Ho_{0.3}MnO_3$ shown high magnetocaloric properties. The $|\Delta S_M^{max}|$, RCP values are higher for samples having high effective moment. Sc doped samples have shown higher antiferromagnetic ordering temperature.

## 8.3 Future scope of work

It would desirable to study whether higher concentration of Er and Ho can be introduces at the Yb sites. If yes, then similar studies, are reported in this work should be carried out. Another important investigation will be low temperature neutron diffraction work on $YbMnO_3$ with dopings as done in this work in order to investigate magnetic structure and magnetic properties.

More heat capacity measurements on all above samples need to be carries out to compare MCE properties obtained by heat capacity and magnetic measurements.

Most important investigation should be study of dielectric and ferroelectric properties of these samples as $YbMnO_3$ is a multiferroic and an overall better understanding of all these properties is required.